ROVIRA I VIRGILI UNIVERSITY
FUEL CELL MODELING AND CONTROL FOR FUEL CONSUMPTION OPTIMIZATION
Carlos Andres Ramos Paja
ISBN:978-84-692-6902-2/ DL:T-1848-2009

**Carlos Andrés Ramos Paja**

# Fuel Cell Modeling and Control for Fuel Consumption Optimization

Doctoral Thesis

Supervised by
Dr. Alfonso Romero and Dr. Roberto Giral

Department of Electronics, Electric and Automatic Engineering

UNIVERSITAT ROVIRA I VIRGILI

Tarragona
2009

ROVIRA I VIRGILI UNIVERSITY
FUEL CELL MODELING AND CONTROL FOR FUEL CONSUMPTION OPTIMIZATION
Carlos Andres Ramos Paja
ISBN:978-84-692-6902-2/ DL:T-1848-2009

ROVIRA I VIRGILI UNIVERSITY
FUEL CELL MODELING AND CONTROL FOR FUEL CONSUMPTION OPTIMIZATION
Carlos Andres Ramos Paja
ISBN:978-84-692-6902-2/ DL:T-1848-2009

Departament d'Enginyeria Electrònica, Elèctrica i Automàtica
Escola Tècnica Superior d'Enginyeria
Edifici L-1, 3a planta despatx 331
Avda. Paisos Catalans, 26
Campus Sescelades
43007 Tarragona SPAIN
Tel.: + 34 977 559 610
Fax:+ 34 977 559 605

We, Alfonso Romero and Roberto Giral, associate professors in the Department of Electronics, Electric and Automatic Engineering of the Rovira i Virgili University,

CERTIFY:

That the present study, entitled "Fuel Cell Modeling and Control for Fuel Consumption Optimization", presented by Carlos Andrés Ramos Paja for the award of the degree of Doctor, has been carried out under our supervision at the Department of Electronics, Electric and Automatic Engineering of this university, and that it fulfils all the requirements to be eligible for the European Doctorate Label.

Tarragona, April the 15th, 2009.

| | |
|---|---|
| ..... | ..... |
| Alfonso Romero, PhD. | Roberto Giral, PhD. |

ROVIRA I VIRGILI UNIVERSITY
FUEL CELL MODELING AND CONTROL FOR FUEL CONSUMPTION OPTIMIZATION
Carlos Andres Ramos Paja
ISBN:978-84-692-6902-2/ DL:T-1848-2009

ROVIRA I VIRGILI UNIVERSITY
FUEL CELL MODELING AND CONTROL FOR FUEL CONSUMPTION OPTIMIZATION
Carlos Andres Ramos Paja
ISBN:978-84-692-6902-2/ DL:T-1848-2009

*To my beautiful wife...Claudia Patricia*

*A mi bella esposa...Claudia Patricia*

ROVIRA I VIRGILI UNIVERSITY
FUEL CELL MODELING AND CONTROL FOR FUEL CONSUMPTION OPTIMIZATION
Carlos Andres Ramos Paja
ISBN:978-84-692-6902-2/ DL:T-1848-2009

ROVIRA I VIRGILI UNIVERSITY
FUEL CELL MODELING AND CONTROL FOR FUEL CONSUMPTION OPTIMIZATION
Carlos Andres Ramos Paja
ISBN:978-84-692-6902-2/ DL:T-1848-2009

# Acknowledgments

I thank to God by the strength and faith that give me, which allow me to accomplish this and others achievements. Also, I thank to my beautiful wife, the light of my life, who shares my difficulties and give me the strength to achieve this objective, which one is a success of both because we are one.

In the professional field, I want to thank to my supervisors, professors Alfonso Romero and Roberto Giral, by their guide and knowledge sharing that allow the fulfillment of this thesis, and without their support this work would not be possible. Similarly, I give my thanks to professor Luis Martinez Salamero by his guide, corrections, writing collaboration and attention.
I also like to thank to professor Carlos Bordons Alba (Departamento de Ingeniería de Sistemas y Automática, Universidad de Sevilla) by his help and guide on my research stay in his laboratory. In the same way, I thank to professor Giovanni Spagnuolo (Dipartimento di Ingegneria dell'Informazione ed Ingegneria Elettrica, University of Salerno) by his support, concern, help, guide and co-work in personal and professional fields in the course of the research stay that I perform in his laboratory.
In the Automatic Control and Industrial Electronics Group laboratory, I want to thank to Josep Maria Bosque by his collaboration in the boards construction, and also thank to my laboratory partners Adolfo Andrés Jaramillo, Carlos Eduardo Carrejo, Carlos Olalla and Eliana Isabel Arango by their collaboration in multiple papers.
In this collaboration line, I want to give a special mention to Jenny Romano, master student of the Dipartimento di Ingegneria dell'Informazione ed Ingegneria Elettrica, University of Salerno, who design with me the fuel cell model described in chapter 2. Also, to professor Giovanni Spagnuolo, by his collaboration and useful advices in that and other works.

In the personal field, I thank to my mother and grandmother by their support in all the ways, by their love and concern. Similarly, I thank to my father by his support, example and love. Without my family this achievement would not be possible.
Personally, I also thank to my friends Adolfo Andrés and Carlos Eduardo by their invaluable companion, and thank to Alfonso and Roberto by their comprehension, advice and help in difficult moments. My incalculable thanks to Adolfo Andrés by his friendship and concern, which comes from more than twelve years.

Thanks to all of you.

ROVIRA I VIRGILI UNIVERSITY
FUEL CELL MODELING AND CONTROL FOR FUEL CONSUMPTION OPTIMIZATION
Carlos Andres Ramos Paja
ISBN:978-84-692-6902-2/ DL:T-1848-2009

ROVIRA I VIRGILI UNIVERSITY
FUEL CELL MODELING AND CONTROL FOR FUEL CONSUMPTION OPTIMIZATION
Carlos Andres Ramos Paja
ISBN:978-84-692-6902-2/ DL:T-1848-2009

# Agradecimientos

Agradezco a Dios por la fuerza y la fe que me ha dado, las cuales me permitieron cumplir este y muchos otros objetivos en mi vida. Así mismo, agradezco a mi bella esposa, la luz de mi vida, quien compartió mis dificultades y me dio la fuerza para finalizar este objetivo, el cual es un logro de los dos porque ella y yo somos uno.

En el campo profesional, quiero agradecer a mis directores, profesores Alfonso Romero y Roberto Giral, por su guía y enseñanza que me permitieron realizar esta tesis, y quienes sin su apoyo este trabajo no habría sido posible. Igualmente, le doy gracias al profesor Luis Martínez Salamero por su guía, correcciones, colaboración y atención. También le doy gracias al profesor Carlos Bordons Alba (Departamento de Ingeniería de Sistemas y Automática, Universidad de Sevilla) por su ayuda y guía en la estancia de investigación que realicé en su laboratorio. De igual forma, le agradezco al profesor Giovanni Spagnuolo (Dipartimento di Ingegneria dell'Informazione ed Ingegneria Elettrica, Universidad de Salerno) por su apoyo, preocupación, guía y colaboración, tanto en el campo personal como profesional, durante el tiempo que estuve en su laboratorio realizando una estancia de investigación. En el laboratorio del Grupo de Automática y Electrónica Industrial, quiero agradecer a Josep María Bosque por su colaboración en la construcción de prototipos. Así mismo, agradezco a mis compañeros de laboratorio Adolfo Andrés Jaramillo, Carlos Eduardo Carrejo, Carlos Olalla y Eliana Isabel Arango, por su colaboración en la escritura de diferentes artículos. En esta línea de colaboración, quiero dar una mención especial a Jenny Romano, estudiante de master del Dipartimento di Ingegneria dell'Informazione ed Ingegneria Elettrica, Universidad de Salerno, quien diseñó conmigo el modelo de pila de combustible descrito en el capítulo 2. Esta mención es extendida al profesor Giovanni Spagnuolo, por su colaboración y consejos en ese y otros trabajos.

En el campo personal, agradezco a mi madre y abuela por su apoyo en todo momento, por su amor y su preocupación. Igualmente, agradezco a mi padre por su apoyo, ejemplo y amor. Sin mi familia este logro no habría sido posible. Personalmente, también agradezco a mis amigos Adolfo Andrés y Carlos Eduardo por su invaluable compañía, y a Alfonso y Roberto por su comprensión, consejos y ayuda en los momentos difíciles. Mis incalculables agradecimientos a Adolfo Andrés por su amistad y preocupación, la cual viene desde hace más de doce años.

Gracias a todos.

ROVIRA I VIRGILI UNIVERSITY
FUEL CELL MODELING AND CONTROL FOR FUEL CONSUMPTION OPTIMIZATION
Carlos Andres Ramos Paja
ISBN:978-84-692-6902-2/ DL:T-1848-2009

ROVIRA I VIRGILI UNIVERSITY
FUEL CELL MODELING AND CONTROL FOR FUEL CONSUMPTION OPTIMIZATION
Carlos Andres Ramos Paja
ISBN:978-84-692-6902-2/ DL:T-1848-2009

# Fuel Cell Modeling and Control for Fuel Consumption Optimization

by

Carlos Andrés Ramos Paja

Department of Electronics, Electric and Automatic Engineering
Rovira i Virgily University
Tarragona, 2009

## Abstract

This thesis describes the theoretical and practical background necessary to design and implement fuel cell based power systems. The state of the art of fuel cell modeling and emulation is analyzed, and shortcomings in modeling are identied and emulation requirements are dened. One of the shortcomings in modeling is addressed by designing a fuel cell model intended to support simulations and power electronics designs, where important internal states are predicted and circuit based load interaction is analyzed by fuel cell impedance reproduction. Similarly, the design and implementation of a fuel cell emulator are described, which supports the evaluation of power electronic devices and control systems intended to interact with real prototypes. During the emulator design process the second modeling shortcoming is reported: an accurate model suitable for real-time applications is required. This problem is addressed by designing a fuel cell fuzzy-based modeling technique. The models and emulator validations are based on experimental results and analysis.

This thesis also studies fuel cell mechanical considerations and load restrictions in the definition of control objectives, and makes a theoretical analysis of common fuel cell-auxiliary storage device hybrid topologies so that selection criteria can be proposed that depend on load profile. It then goes on to describe control approaches for these hybrid topologies in which fuel cell safety and efficient operation are the main objectives. In order to validate the control structures, an experimental setup based on a Ballard 1.2 kW Nexa power system, a four boost-module DC/DC converter and a capacitive bus is theoretically designed and experimentally evaluated. Also, theoretical background, design guidelines and practical considerations for implementing fuel cell power interface systems are given.

A methodology for identifying the optimal operating points of fuel cells is proposed and experimentally validated. This methodology denes the experimental setup control proles that minimize fuel consumption for a given load prole. Using the minimum consumption strategy, the control structure of the fuel cell-based power system is experimentally validated and also contrasted with the manufacturers default control system. Finally, the control and power electronic systems developed are analyzed and conclusions are drawn.

Thesis Supervisors: Alfonso Romero and Roberto Giral

ROVIRA I VIRGILI UNIVERSITY
FUEL CELL MODELING AND CONTROL FOR FUEL CONSUMPTION OPTIMIZATION
Carlos Andres Ramos Paja
ISBN:978-84-692-6902-2/ DL:T-1848-2009

ROVIRA I VIRGILI UNIVERSITY
FUEL CELL MODELING AND CONTROL FOR FUEL CONSUMPTION OPTIMIZATION
Carlos Andres Ramos Paja
ISBN:978-84-692-6902-2/ DL:T-1848-2009

# Contents

ROVIRA I VIRGILI UNIVERSITY
FUEL CELL MODELING AND CONTROL FOR FUEL CONSUMPTION OPTIMIZATION
Carlos Andres Ramos Paja
ISBN:978-84-692-6902-2/ DL:T-1848-2009

ROVIRA I VIRGILI UNIVERSITY
FUEL CELL MODELING AND CONTROL FOR FUEL CONSUMPTION OPTIMIZATION
Carlos Andres Ramos Paja
ISBN:978-84-692-6902-2/ DL:T-1848-2009

ROVIRA I VIRGILI UNIVERSITY
FUEL CELL MODELING AND CONTROL FOR FUEL CONSUMPTION OPTIMIZATION
Carlos Andres Ramos Paja
ISBN:978-84-692-6902-2/ DL:T-1848-2009

ROVIRA I VIRGILI UNIVERSITY
FUEL CELL MODELING AND CONTROL FOR FUEL CONSUMPTION OPTIMIZATION
Carlos Andres Ramos Paja
ISBN:978-84-692-6902-2/ DL:T-1848-2009

# List of Figures

ISBN:978-84-692-6902-2/ DL:T-1848-2009

ISBN:978-84-692-6902-2/ DL:T-1848-2009

ROVIRA I VIRGILI UNIVERSITY
FUEL CELL MODELING AND CONTROL FOR FUEL CONSUMPTION OPTIMIZATION
Carlos Andres Ramos Paja
ISBN:978-84-692-6902-2/ DL:T-1848-2009

ROVIRA I VIRGILI UNIVERSITY
FUEL CELL MODELING AND CONTROL FOR FUEL CONSUMPTION OPTIMIZATION
Carlos Andres Ramos Paja
ISBN:978-84-692-6902-2/ DL:T-1848-2009

# List of Tables

ROVIRA I VIRGILI UNIVERSITY
FUEL CELL MODELING AND CONTROL FOR FUEL CONSUMPTION OPTIMIZATION
Carlos Andres Ramos Paja
ISBN:978-84-692-6902-2/ DL:T-1848-2009

ROVIRA I VIRGILI UNIVERSITY
FUEL CELL MODELING AND CONTROL FOR FUEL CONSUMPTION OPTIMIZATION
Carlos Andres Ramos Paja
ISBN:978-84-692-6902-2/ DL:T-1848-2009

# Preface

This thesis reports the results of my Ph.D. study at the Departament dEnginyeria Electrònica, Elèctrica i Automàtica, Escola Tècnica Superior d'Enginyeria, Universitat Rovira i Virgili. It documents the work I carried out between December 2005 and December 2008, which was funded by the Universitat Rovira i Virgili in the first year and subsequently by the Spanish Ministry of Education and Science, under project ENE2005-06934 and the FPI scholarship BES-2006-11637. I made the study as a Ph.D student of the Automatic Control and Industrial Electronics Group, to which I have been affiliated since December 2005.

The thesis contains results that have been accepted or are to be submitted for publication as papers in international journals or conference proceedings (see appendix D), but the thesis format makes it easier for the reader to gain a better understanding of the overall work and of the improvements in the state of the art.

The thesis follows common publishing guidelines given by international journals. Color figures have been used only when strictly necessary, such as is the case of simultaneous plots of a high number of signals. Similarly, the bibliographical citations have been numbered in order of appearance, as have the equations, figures and tables.
Both roman and *italic* fonts appear in the text, the latter being used in particular to highlight important issues, differentiate nouns and mark non-English words. Similarly, in the mathematical expressions the common nomenclature for time and frequency variables has also been respected: lowercase variables correspond to the time domain and uppercase to the frequency domain. This is not true only for the fundamental time and frequency variables: the $t$ variable corresponds to the continuous time domain, the $s$ variable to the continuous frequency domain, the $k$ variable to the discrete time domain, and the $z$ variable to the discrete frequency domain.

In fuel cell-based power systems, the mechanical device that provides air to the fuel cell can be designated like *air pump* or *air compressor*, it depending on the physical implementation of the particular experimental system. In this way, in this thesis that device is referenced like *air compressor* or *air pump* indistinctly, being used one term or the another mainly depending on the context: for electrical purposes in the literature is commonly used *air compressor*, and for mechanical purposes is more habitual the use of *air pump*.
Finally, the simulations of the fuel cell power system and power electronics circuits have been carried out by using Matlab/Simulink and PSIM software.

ROVIRA I VIRGILI UNIVERSITY
FUEL CELL MODELING AND CONTROL FOR FUEL CONSUMPTION OPTIMIZATION
Carlos Andres Ramos Paja
ISBN:978-84-692-6902-2/ DL:T-1848-2009

ROVIRA I VIRGILI UNIVERSITY
FUEL CELL MODELING AND CONTROL FOR FUEL CONSUMPTION OPTIMIZATION
Carlos Andres Ramos Paja
ISBN:978-84-692-6902-2/ DL:T-1848-2009

# Chapter 1

# Introduction

Fuel cells are efficient electric energy sources that produce minimal pollutant emissions. They are therefore called *low emission power sources*. Fuel cells transform chemical energy into electrical energy, as long as the reagents and the conditions are appropriate and, unlike batteries, the reagents are stored outside the system, which gives higher autonomy. The main drawback of fuel cells compared with batteries is that their safe bandwidth is low, and it is mainly due to the mechanical interactions in the fuel cell, thus requiring an additional energy storage device to supply high-frequency electrical loads.

Different types of fuel cells use different technologies, electrolytes or membranes: for example, alkaline fuel cells (AFC), molten carbonate fuel cells (MCFC), phosphoric acid fuel cells (PAFC), solid oxide fuel cells (SOFC) and polymer electrolyte membrane (PEM) fuel cells. PEM fuel cells are currently the subject of significant research, and are particularly useful in portable applications, small-distributed generation and vehicle propulsion. The most important advantages are its high efficiency, low operating temperature, high power density, solid electrolytes, relatively low corrosion and fast start-up compared with other generation systems and other fuel cell types [1]. PEM fuel cells consume hydrogen and oxygen to produce electrical energy.

The principle of PEM fuel cell operation is depicted in figure 1-1. The hydrogen reaches the anode under a defined pressure, and then goes to the anode catalytic layer where it is dissociated in electrons and protons, as described in (1.1).

$$2H_2 \rightarrow 4H^+ + 4e^- \tag{1.1}$$

The protons flow through an electrolytic membrane, which blocks the electrons, to the catalytic layer of the cathode. The electrons travel through an external circuit to the cathode, generating electric current in this process. Simultaneously, oxygen flows to the catalytic layer of the cathode,

ISBN:978-84-692-6902-2/ DL:T-1848-2009

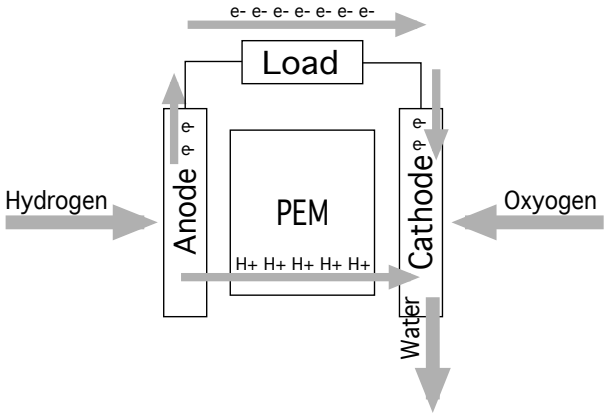


Figure 1-1: PEM fuel cell operation principle.

where oxygen, protons and electrons react to produce water and heat on the surface of catalytic particles:

$$O_2 + 4H^+ + 4e^- \rightarrow 2H_2O + \text{heat} \tag{1.2}$$

The global reaction in the fuel cell [2] is summarized in (1.3).

$$H_2 + \frac{1}{2}O_2 \rightarrow H_2O + \text{heat} + \text{electricity} \tag{1.3}$$

The fuel cell has a characteristic voltage-current relation called the *polarization curve*. Figure 1-2 shows the polarization and power curves for different fuel flows (normalized in terms of percentage of the maximum fuel flow allowed), obtained by interpolation of experimental data taken on a fuel cell with an active area of 14.4 $cm^2$, a maximum output power of 6.5 W and a theoretical cell voltage of 1.2 V.

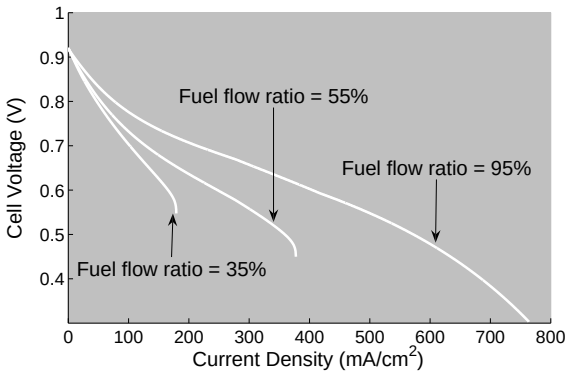


(a) Polarization curves.

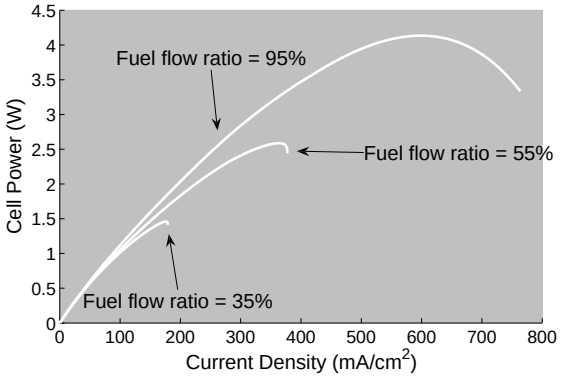


(b) Power curves.

Figure 1-2: Fuel cell static electric behavior for fuel flows between 95 % and 35%.

ISBN:978-84-692-6902-2/ DL:T-1848-2009

The polarization and power curves describe non-linear relations that depend on the fuel flow ratio, cell current, thermal effects, reactant pressures, etc. The cell voltage is affected by losses in the electrochemical system, and those losses increase with the current degrading the effective power of the cell. Also, because of construction deciencies and the lack of optimal operation conditions the theoretical maximum cell voltage is not achieved even when there is no cell current.

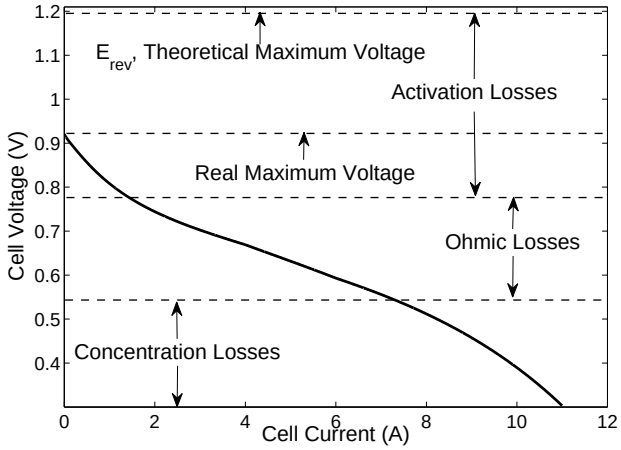


Figure 1-3: Fuel cell polarization curve zones.

The losses in the cell voltage generate different zones in the polarization curve as is depicted in figure 1-3. The theoretical maximum cell voltage $E_{rev}$ is called *thermoneutral* or *reversible potential*, which corresponds to the maximum possible energy resulting from the electrochemical reaction [3] as follows:

$$E_{rev} = -\frac{\Delta G}{n\mathsf{F}} \tag{1.4}$$

where $\Delta G$ represents the Gibbs free energy, $n$ is the number of transferred electrons and $\mathsf{F}$ is the Faraday constant. The difference between $E_{rev}$ and the cell voltage ($V_{st}$) gives the fuel cell losses. Barbir et al. define the fuel cell efficiency as [3]:

$$\eta_{fc} = \frac{V_{st}}{E_{rev}} \tag{1.5}$$

The losses in the cell voltage are classified according to their cause: activation losses, ohmic losses and concentration losses. Figure 1-3 illustrates the losses and also the theoretical and real maximum voltages. The difference between them is mainly caused by electrons flow in the membrane, which theoretically only transports positive ions, but in a real prototype even at null output current electrons flow occurs. Activation losses are caused by delays in the electrodes surface reactions,

ISBN:978-84-692-6902-2/ DL:T-1848-2009

which generate voltage drops. These losses are at the top of the polarization curve (figure 1-3). Ohmic losses are caused by resistance to positive ions flow in the membrane and to the ohmic effect in the cell current. Both voltage drops increase with the current density and are proportional to the cell current. This effect is dominant in the middle zone of the polarization curve (figure 1-3). Finally, concentration losses are caused by a decrease in the reagent concentration on the electrodes active layers. This effect is considerable at the bottom of the polarization curve (figure 1-3), where high currents cause high reagent consumptions and therefore low concentrations.

Another important effect that must be taken into account in the operation of a fuel cell is its sensitivity to current changes [4], [5]. This effect also causes voltage drops and, therefore, reduces the electric power generated and, in critical cases, degrades the fuel cell stack and causes membrane perforation.

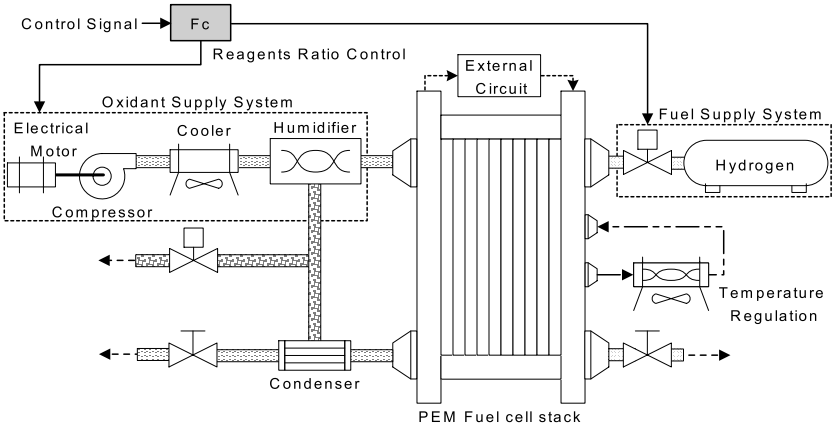


Figure 1-4: PEM fuel cell-based electrical power generation system (PEMFC).

A single PEM fuel cell produces low voltages ($E_{rev}$ theoretical maximum voltage) at high current profiles and, in order to provide useful voltage levels, single cells are connected in series to form fuel cell stacks, which can provide electric power with a higher voltage. These PEM fuel cell stacks require support systems in order to produce electric power with safe operating conditions. These systems provide the reagents and regulate their temperature and pressure ratio. They also regulate the stack temperature, manage the water produced and inject water vapor to regulate the membrane humidity. The optimization and control of these ancillary systems are subjects of intense research and development. The solutions nowadays available allow the production of electric power in a useful form. A scheme of a PEM fuel cell electric power generation system (PEMFC) is presented in figure 1-4 [6], showing the presence of several subsystems: the oxidant supply system consists of an electrical motor, a compressor, a cooler, a humidifier and manifolds. The fuel supply system that provides pressurized hydrogen to the stack is also shown. The PEMFC presented in figure 1-4 considers water management and humidity regulation systems to so that the membrane can be correctly wetted.

ISBN:978-84-692-6902-2/ DL:T-1848-2009

The reagents and stack temperature regulation systems are also shown. The PEMFC presented has a feedforward control strategy for the reagent ratio that ensures the appropriate oxidant-fuel mass ratio and prevents undesired effects such as oxygen starvation [1]. This topology is commonly used in electrical and hybrid automobiles, such as Ford P2000 [7], and in experimental PEMFC prototypes. Some of them are commercially available as the Nexa Power Modules from Ballard or the PowerPEMTM-PS250 PEMFC system from Hpower Co. Other PEMFC systems, such as that one presented by Friede et al. in [8], are user-designed implementations.

PEMFC systems require power electronic devices to be interfaced with electrical loads and control strategies to regulate the power electronics, the mechanical systems and the fuel cell itself. The design of the power electronics and control strategies for PEMFC requires parameterized models that describe both static and dynamic behaviors, and constraints. The electrical constraints on the power electronic systems also need to be identified. In the control approach, the specific control restrictions need to be synthesized to provide a safe operation, identifying also the optimal operation conditions.

This thesis develops some analytical tools and devices intended to support the analysis and experimentation on fuel cell power systems: an experimentally developed and validated fuel cell physical model is proposed in chapter 2 to support power electronics and control strategy designs for PEMFC. The same chapter analyzes such physical behaviors of fuel cell as voltage ripple and membrane water content estimation. In order to support power electronics tests and evaluations, in chapter 3 an experimentally validated fuel cell emulator is presented, and its design and implementation are described. This chapter presents also a comparison of different numerical methods and considerations about power electronics design that are mandatory for the fuel cell emulator design. This device allows to evaluate any hardware intended to interact with fuel cells before to be used with PEMFC prototypes, allowing the tuning of the under-test hardware to avoid PEMFC degradation. The emulator design requires a new modeling approach that optimizes the calculation time. Therefore, a new fuzzy-based emulation technique for PEMFC systems is proposed and validated.

In chapter 4, theoretical and practical considerations for the design and control of fuel cell power systems are proposed, and a practical example of a DC/DC converter-based power system design, implementation and validation is described. This chapter also presents a DC bus design for load interaction, and gives an analysis of the typical architectures including PEMFC and auxiliary storage devices (capacitor banks, super capacitors, batteries, etc.). A selection criteria for those architectures, depending on the load power profile, is proposed and evaluated. Then, control restrictions required for safe and efficient fuel cell operation are analyzed, and experimentally validated optimal operation conditions are defined. Control strategies for regulating the PEMFC system are also presented for different fuel cell-storage architectures, and an optimal control system to minimize the

ROVIRA I VIRGILI UNIVERSITY
FUEL CELL MODELING AND CONTROL FOR FUEL CONSUMPTION OPTIMIZATION
Carlos Andres Ramos Paja
ISBN:978-84-692-6902-2/ DL:T-1848-2009

fuel consumption, which increases the operation efficiency and autonomy, is proposed and validated in a benchmark prototype. Finally, the conclusions are given in chapter 5, where possible future developments are also proposed.

ROVIRA I VIRGILI UNIVERSITY
FUEL CELL MODELING AND CONTROL FOR FUEL CONSUMPTION OPTIMIZATION
Carlos Andres Ramos Paja
ISBN:978-84-692-6902-2/ DL:T-1848-2009

# Chapter 2

# Fuel Cell Modeling and Simulation

This chapter presents an experimentally developed and validated physical fuel cell model, intended to support power electronics simulation and design. The proposed model is also useful for evaluating PEMFC control systems and defining safety policies. It reproduces the behavior of a fuel cell system, and it is experimentally validated using a 1.2 kW Nexa Power Module. The main characteristic of the model is its simplicity compared with complex electrochemical models, but it can still predict critical internal states in fuel cell control design. The model combines electrochemical equations and experimentally identified relations, and considers thermal effects in order to reproduce a general behavior. The fuel cell electrical impedance is also modeled using a non-linear circuit in order to allow a realistic circuital connection with electrical loads.

Additional analyses are made to complement the model in greater depth: the stack voltage ripple in non-ripple current conditions is studied and the number of sensors required to estimate the membrane water content is defined.

## 2.1 Introduction

In the literature are reported many models that describe fuel cell both static and dynamic behaviors. These models can be classified into electrical equivalents and mathematical models [9]. Of the latter, the most widely accepted is the dynamic model proposed by Larminie [10], in which each electrode is represented by means of a capacitor in parallel with a resistor and a voltage source. The resistors and the capacitors are associated with anode and cathode Faraday resistances and capacitances. An independent voltage generator also reproduces the fuel cell open circuit voltage. In [11] a more complex model was presented, which reproduces the different areas of the fuel cell polarization curve. In this model, a diode, two transistors and a resistor represent the static response. The diode reproduces the activation losses and its parasitic resistance models the ohmic effect in the cell.

ISBN:978-84-692-6902-2/ DL:T-1848-2009

The transistors and the resistor reproduce the concentration losses and a capacitor and an inductor together with the transistors model the dynamic behavior. Capel presents an electrical equivalent that reproduces the polarization curve of the fuel cell [12]. This model uses the electrical effects of the semiconductor devices to reproduce the different zones of the polarization curve. The activation effect is modeled by a diode, the concentration effect by an electrical network composed by a diode and a voltage source, and the ohmic effect is modeled by a resistor.

A different approach of electrical equivalent was presented by Famouri [13], in which the fuel flow dynamics were taken into account in the output power calculation. The circuit models the transient effects caused by variation in the hydrogen flow, the partial pressures of the reactants and the mechanical losses inside the fuel cell. This model is a circuital implementation of the electrochemical equations in which the fuel cell and the humidifier dynamics are taken into account through mass conservation equations. The model calculates the cell voltage as function of partial pressures, load current and mechanical losses, but considers the stack temperature to be constant (77 $^o$C).

Mathematical models represent electrochemical and physical equations, and build linear or non-linear models in state space representations, block diagrams, etc. In the literature several models have been proposed and validated: detailed non-linear models in state space (Hernández [14]), empirical approaches implemented with polynomial approximations (Xue [15]), models of efficiency based on interpolation and experimental characterization (Ogaji [16]), control-oriented models (Golbert [17]-[18]), models that consider the stack with its auxiliary systems (Khan [19]-[20]), and also models that includes a power converter for specific applications (Choe [21]). Another interesting model is the one proposed by Correa [22] which analyzes the electrochemical reactions and gives the stack voltage as output. The analysis focuses on the activation, concentration and ohmic losses, and the fuel cell dynamics are modeled by a first order delay with a time constant, where C and R are the equivalent capacitance and resistance of the system. This model is useful for electrical simulations in low calculation power environments. The fuel cell behavior was also described in terms of chemical and physical relations by Real et al. [23], and experimentally validated using a Ballards 1.2 kW Nexa Power Module. This fuel cell system is representative of the state of the art in PEM fuel cell prototypes, and the literature reports that it is used by many research groups.

The model proposed in this chapter shares the internal state prediction of complex physical models, but the fuel cell polarization is modeled in terms of impedance, thus giving more realistic interaction between the PEMFC and the load, and making it possible to evaluate power electronic designs and control strategies in power electronic simulators.

The stack voltage ripple observed in fuel cell operation is also analyzed in this chapter. The

main ripple source is identified in order to complement the model and the behavior of the system is described. Finally, the information required to estimate the membrane water content is analyzed using signal processing techniques, in particular Principal Components Analysis (PCA) and Artificial Neural Network (ANN) estimators. This because the membrane water content is an important, but even difficult variable to be measured, for the safe operation of fuel cells.

## 2.2 Model overview

The model proposed is control-oriented and considers experimentally measurable inputs and outputs in order to fit it to the real prototype. The model interacts with the electrical load (DC/DC converter, battery charger, inverter and so on) through an electrical circuit that models the fuel cell output impedance. The thermal effects on the stack voltage are also taken into account and the main internal state predicted in the model is the oxygen excess ratio $\lambda_{O_2}$, which is an important variable in FC control and safety [1].

The modeling procedure is supported by experimental data for identifying physical relations and simplify complex equations derived from the involved models [23]. The model, then, includes physical and electrochemical equations as well as behavioral relations obtained by interpolating experimental data. The experimental setup used is the Ballard 1.2 kW NEXA Power Module (see figure 2-1(a)), which is composed of a stack of 46 cells with membranes with a surface area of 110 $\mathsf{cm}^2$. The physical configuration of the fuel cell NEXA module can be seen in figure 2-1(b), which shows the interaction between the stack, the air compressor, the humidifier, the cooling system, the hydrogen supply and the anode purge valve.

The NEXA module also has a control board that implements strategies aimed at regulating the anode-cathode pressure ratio and the stack temperature and humidity to ensure safe operation conditions. Similarly, the control board executes safe start-up, load connection and shutdown sequences, and allows command and monitoring procedures in a PC through the NEXA module control interface. Finally, the control board includes regulation strategies for the anode purge valve and the air compressor voltage that are intended to avoid undesired phenomena like flooding and oxygen starvation. The flooding phenomenon occurs when the water generated and the inert gases supplied with the hydrogen get stuck in the anode producing a decrease in the stack voltage and power [24]. The oxygen starvation phenomenon occurs when the oxygen supplied to the fuel cell is not enough to react in agreement with the demand of stack current, causing degradation of the fuel cell and decrement of the output power, thus frequently requiring to shut-down the fuel cell to avoid severe damages [25].

ISBN:978-84-692-6902-2/ DL:T-1848-2009

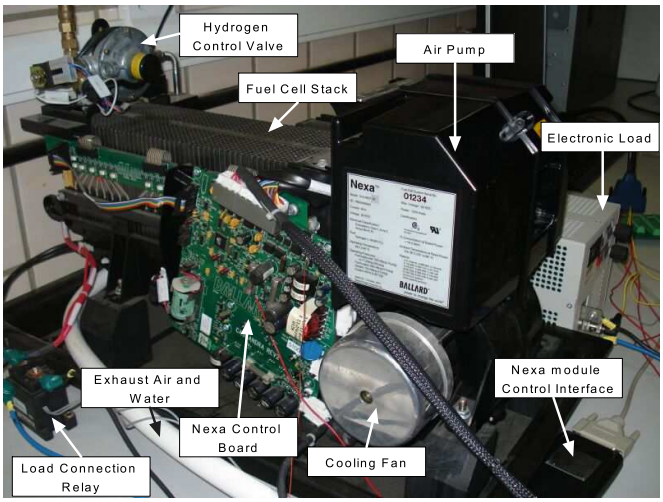


(a) Nexa power module.

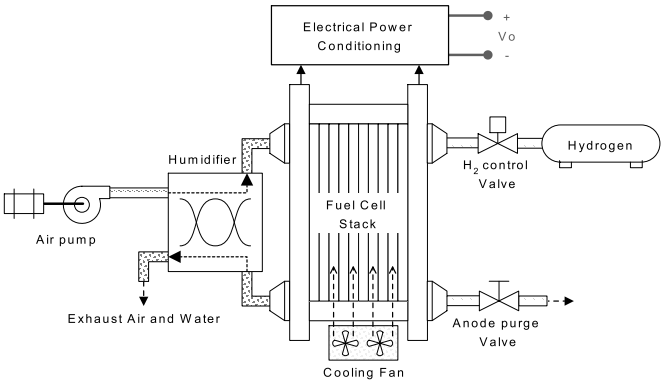


(b) Nexa power module diagram.

Figure 2-1: Ballard 1.2 kW Nexa power module.

The model inputs are the load current $I_{net}$ and the ambient temperature $T_{ca,in}$, and the main outputs are the oxygen excess ratio $\lambda_{O_2}$ and the stack voltage $V_{st}$. The stack temperature $T_{st}$ is calculated in a thermal model used to estimate the voltage deviation caused by stack temperature changes, but it can be also used for prediction purposes.

The FC dynamics, included in $\lambda_{O_2}$ and thermal models, have been also considered. The FC-load interaction is performed by a non-linear circuit, being the voltage at the FC terminals dependent on the oxygen excess ratio and load current. Finally, the output voltage deviation $dV_T$ caused by changes in the stack temperature is also modeled, reproducing in this way the non-linear fuel cell electrical impedance. The proposed model structure is given in figure 2-2, which shows the compressor dynamics, its losses and NEXA board control structure, where the effective stack current depends on the load current and on the compressor consumption.

The model is intended to test power electronic circuits and control strategies, being used in power

ISBN:978-84-692-6902-2/ DL:T-1848-2009

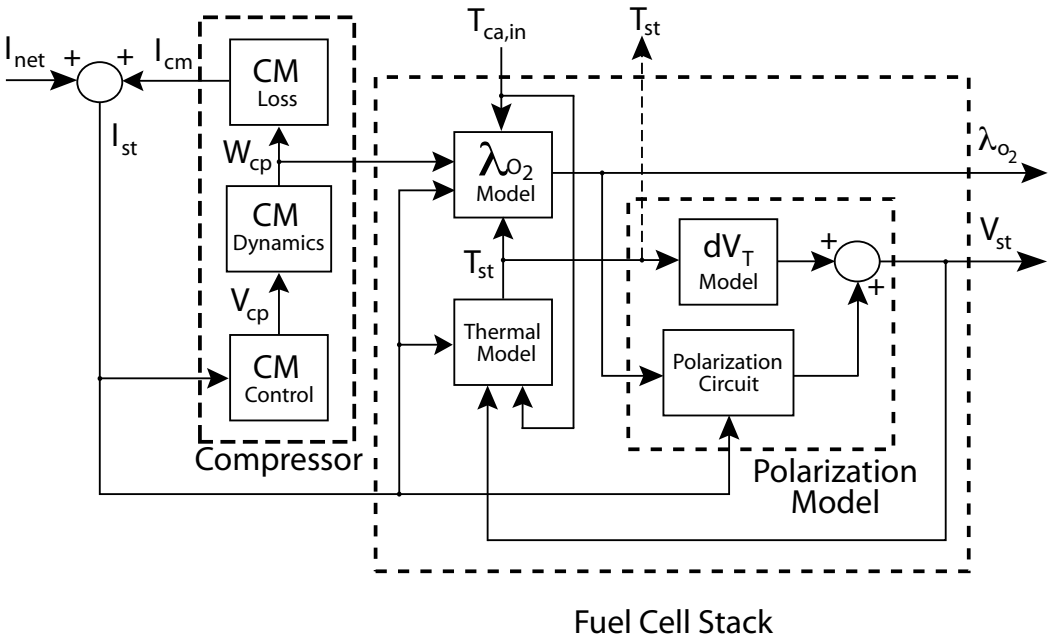


Figure 2-2: Proposed model structure.

electronic simulation environments. Consequently, the model implementation has been performed using the power electronics simulation software PSIM [26], which allows to use electrical circuits for the polarization and thermal models, and continuous and discrete transfer functions for $\lambda_{O_2}$ and compressor models.

The next sections describe $\lambda_{O_2}$, thermal, compressor and polarization models and their implementations.

## 2.3 Oxygen excess ratio ($\lambda_{O_2}$)

In order to prevent membrane stress, the anode-cathode pressure ratio is regulated in a safe relation, it being usually a small constant difference. This implies that hydrogen and oxygen flows are correlated, the oxygen flow being the main variable for control objectives [27].

The cathode oxygen flow $W_{O_2,ca,in}$ available in the air flow $W_{ca,in}$ supplied by the FC compressor is given in (2.1), where $\omega_{ca,in}$ is the humidity ratio [1]:

$$W_{O_2,ca,in} = \frac{y_{O_2,ca,in} \cdot \mathsf{M}_{\mathsf{O}_2}}{y_{O_2,ca,in} \cdot \mathsf{M}_{\mathsf{O}_2} + (1 - y_{O_2,ca,in}) \cdot \mathsf{M}_{\mathsf{N}_2}} \cdot \left( \frac{1}{1 + \omega_{ca,in}} \right) \cdot W_{ca,in} \tag{2.1}$$

ISBN:978-84-692-6902-2/ DL:T-1848-2009

$$\left.\begin{aligned} \omega_{ca,in} = \frac{\mathsf{M_v}}{M_{a,ca,in}} \cdot \frac{p_{v,ca,in}}{p_{a,ca,in}} = \frac{\mathsf{M_v}}{M_{a,ca,in}} \cdot \frac{\phi_{ca,in} \cdot p_{sat}(T_{ca,in})}{p_{ca,in} - \phi_{ca,in} \cdot p_{sat}(T_{ca,in})} \\ M_{a,ca,in} = y_{O_2,ca,in} \cdot \mathsf{M_{O_2}} + (1 - y_{O_2,ca,in}) \cdot \mathsf{M_{N_2}} \end{aligned}\right\} \quad (2.2)$$

Here $y_{O_2,ca,in}$ is the oxygen mole fraction (0.21 for atmospheric air); $M_{a,ca,in}$, $\mathsf{M_{O_2}}$, $\mathsf{M_{N_2}}$ and $\mathsf{M_v}$ are the air, oxygen, nitrogen and water vapor molar mass, respectively. $p_{v,ca,in}$ and $p_{a,ca,in}$ are the vapor and dry air partial pressures; $\phi_{ca,in}$ is the inlet humidity; $T_{ca,in}$ is the inlet flow temperature and $p_{sat}(T)$ is the saturation pressure, which depends on the temperature as [1, 28]:

$$\begin{aligned} log_{10}(p_{sat}) = (-1.69 \times 10^{-10}) \cdot T^4 + (3.85 \times 10^{-7}) \cdot T^3 - (3.39 \times 10^{-4}) \cdot T^2 \\ +0.143 \cdot T - 20.92 \end{aligned} \quad (2.3)$$

A set of experimental measurements taken on the Ballard-NEXA 1.2kW system has allowed to obtain the cathode inlet flow total pressure, which has been modeled by the following linear regression:

$$p_{ca,in} = 1.0033 + (2.1 \times 10^{-3}) \cdot W_{cp} - (475.7 \times 10^{-6}) \cdot I_{st} \quad (2.4)$$

$W_{ca,in}$ in (2.1) has to be set in [kg/s], but the output of the air compressor $W_{cp}$ is expressed in standard liters per minute [SLPM]. To convert [SLPM] into [kg/s] the following expressions are used:

$$\left.\begin{aligned} W_{ca,in} = \frac{W_{cp}}{22.4 \times 60} \cdot M_{am} \\ M_{am} = (1 - x_v) \cdot y_{O_2,ca,in} \cdot \mathsf{M_{O_2}} + (1 - x_v)(1 - y_{O_2,ca,in}) \cdot \mathsf{M_{N_2}} + x_v \cdot \mathsf{M_v} \\ = 0.02884 - 0.01084 \cdot x_v \\ x_v = \frac{\phi_{ca,in} \cdot p_{sat}(T_{st})}{1 - \phi_{ca,in} \cdot p_{sat}(T_{st})} \end{aligned}\right\} \quad (2.5)$$

In (2.5), the air flow expressed in [SLPM] is converter to molar flow (moles per second) by using the ideal gas law and mol definition (mol volume equal to 22.4 liters), and also dividing by 60 seconds per minute. Next, the inlet air flow in [kg/s] is obtained by multiplying the molar flow by the inlet air molar mass $M_{am}$, which depends on the oxygen-nitrogen relation in the inlet dry air (given by $y_{O_2,ca,in}$), and on the water vapor fraction in the inlet air $x_v$ that depends on the cathode (stack) temperature according to the saturation pressure [1].

The oxygen and hydrogen flows consumed in the reaction ($W_{O_2,reac}$ and $W_{H_2,reac}$, respectively)

ISBN:978-84-692-6902-2/ DL:T-1848-2009

depends on the stack current and it are defined by electrochemistry principles as follows [1, 23]:

$$W_{O_2,reac} = \mathsf{M}_{\mathsf{O}_2} \frac{\mathsf{n} \cdot I_{st}}{4\mathsf{F}} \tag{2.6}$$

$$W_{H_2,reac} = \mathsf{M}_{\mathsf{H}_2} \frac{\mathsf{n} \cdot I_{st}}{2\mathsf{F}} \tag{2.7}$$

The parameters $\mathsf{M}_{\mathsf{H}_2}$, $\mathsf{n}$ and $\mathsf{F}$ are the hydrogen molar mass, the number of cells in the stack and the Faraday constant, respectively.

The water vapor flow $W_{v,gen}$ generated in the electrochemical reaction also depends on the stack current and it is defined by (2.8).

$$W_{v,gen} = \mathsf{M}_{\mathsf{v}} \frac{\mathsf{n} \cdot I_{st}}{2\mathsf{F}} \tag{2.8}$$

The relation between the oxygen flow provided to the stack and the one required to supply the current demand is normally expressed by the *oxygen excess ratio* $\lambda_{O_2}$ [1]:

$$\lambda_{O_2} = \frac{W_{O_2,ca,in}}{W_{O_2,reac}} \tag{2.9}$$

A high oxygen excess ratio, and thus high oxygen partial pressure, improves the power of the stack; however, after an optimum value is reached, a further increase of its value causes an excessive increase in air compressor losses, thus degrading the system efficiency.

The control of oxygen flow is critical because a oxygen concentration lower than the one required to supply the stack current generates the oxygen starvation effect, which leads to the FC degradation [25]. Therefore, the oxygen excess ratio must be regulated to $\lambda_{O_2} \geq 1$ in order to prevent the starvation phenomena. In [29, 30] the authors propose to track $\lambda_{O_2} = 2$, because this value prevents the oxygen starvation effect and ensures a high efficiency in its experimental system.

The possibility of predicting the $\lambda_{O_2}$ value, together with thermal effects and the reproduction of the electric power generated by the fuel cell, gives a useful tool to evaluate the efficiency and safety of power electronics and control systems interacting with the FC.

## 2.4 Thermal model

The thermal model can be obtained by an energy balance: defining $\dot{H}_{reac}$ as the energy produced in the chemical reaction of water formation, $P_{elec}$ as the electric power supplied and $\dot{Q}_{rad,B2amb}$ and $\dot{Q}_{conv,B2amb}$ as the amount of heat evacuated by radiation and both natural and forced convection,

ISBN:978-84-692-6902-2/ DL:T-1848-2009

respectively, the energy balance is the following [23]:

$$m_{st} \cdot C_{st} \frac{dT_{st}}{dt} = \dot{H}_{reac} - P_{elec} - \dot{Q}_{rad,B2amb} - \dot{Q}_{conv,B2amb} \tag{2.10}$$

$$\left.\begin{aligned} \dot{H}_{reac} = \dot{m}_{H_2,reac} \cdot \Delta h_{H_2} + \dot{m}_{O_2,reac} \cdot \Delta h_{O_2} - \\ W_{H_2O,gen(g)}(h^0_{f,H_2O(g)} + \Delta h_{H_2O(g)}) \\ \Delta h_{H_2} = c_{p,H_2} \cdot (T_{anch,in} - T^0) \\ \Delta h_{O_2} = c_{p,O_2} \cdot (T_{cach,in} - T^0) \\ \Delta h_{H_2O(g)} = c_{p,H_2O(g)} \cdot (T_{st} - T^0) \end{aligned}\right\} \tag{2.11}$$

$$P_{elec} = P_{st} = V_{st} \cdot I_{st} \tag{2.12}$$

where $h^0_{f,H_2O(g)}$ is the mass specific enthalpy of formation of water steam and $c_{p,H_2}$, $c_{p,O_2}$ and $c_{p,H_2O(g)}$ are the specific heats of hydrogen, oxygen and water steam respectively. $T^0$ is the reference temperature for the enthalpy, $T_{anch,in}$ and $T_{cach,in}$ the inlet temperature of anode and cathode respectively, $T_{st}$ is the stack temperature, $m_{st}$ is the mass of the fuel cell stack and $C_{st}$ is its heat capacity. $\dot{m}_{O_2,reac}$, $\dot{m}_{H_2,reac}$ are the mass flow rate reacted of oxygen and hydrogen, respectively, and $W_{H_2O,gen(g)}$ the water mass flow rate. Finally, $V_{st}$ and $I_{st}$ are the voltage and the current of the fuel cell stack.

The amount of radiated heat depends on the exchange area $A_{B2amb,rad}$ and the emissivity $\varepsilon$ as given in (2.13), where $\sigma$ is the Stefan-Boltzmann constant. $\dot{Q}_{rad,B2amb}$ can be also approximated by the linear expression (2.14) obtained by means of a polynomial regression.

$$\dot{Q}_{rad,B2amb} = \sigma \cdot \varepsilon \cdot A_{B2amb,rad} \cdot (T^4_{st} - T^4_{cach,in}) \tag{2.13}$$

$$\dot{Q}_{rad,B2amb} \approx 0.81249 \cdot T^4_{st} - 0.81262 \cdot T^4_{cach,in} \tag{2.14}$$

The heat extracted by means of natural and forced convection (2.15) includes two terms: $\dot{Q}_{conv,B2amb,nat}$ that corresponds to natural convection (2.16) and $\dot{Q}_{conv,B2amb,forc}$ that corresponds to forced convection (2.17) [23].

$$\dot{Q}_{conv,B2amb} = \dot{Q}_{conv,B2amb,nat} + \dot{Q}_{conv,B2amb,forc} \tag{2.15}$$

$$\dot{Q}_{conv,B2amb,nat} = (h_{B2amb,nat} \cdot A_{B2amb,conv}) \cdot \Delta T_{ca,in} \tag{2.16}$$

$$\dot{Q}_{conv,B2amb,forc} = (h_{B2amb,forc} \cdot A_{B2cool,conv}) \cdot \Delta T_{ca,in} \tag{2.17}$$

$$\Delta T_{ca,in} = T_{st} - T_{cach,in} \tag{2.18}$$

$$h_{B2amb,forc} = K_{h1} \cdot (W_{cool})^{K_{h2}} \tag{2.19}$$

ISBN:978-84-692-6902-2/ DL:T-1848-2009

In each term, the convective heat transfer coefficients ($h_{B2amb,nat}$ and $h_{B2amb,forc}$) are different, just as the exchange areas ($A_{B2amb,conv}$ and $A_{B2cool,conv}$) are, this because natural convection takes place in the fuel cell lateral walls, and forced convection occurs across the internal walls of the cells, which are constructed as a radiator. $K_{h1}$ and $K_{h2}$ are the heat transfer coefficients. In the NEXA system, the air flow supplied by the cooling fan $W_{cool}$ has been identified as follows [23]:

$$W_{cool} = 36 \cdot u_{cool} \tag{2.20}$$

where the input $u_{cool}$ is the control signal of the fan. The new final energy balance expressed by means of the polynomial regression is:

$$\frac{dT_{st}}{dt} = \frac{1}{5500}[57.64 \cdot I_{st} + 0.0024 \cdot I_{st} \cdot (T_{cach,in} - 298) - 8.13807 \cdot (T_{st} - T_{cach,in}) \\ -(0.81249 \cdot T_{st} - 0.81262 \cdot T_{cach,in}) - V_{st} \cdot I_{st}] \tag{2.21}$$

where the stack current is in amperes, the temperatures in kelvin and the stack voltage in volts.

This thermal model has been implemented in the PSIM environment by using electrical equivalents [13], so that a capacitor voltage models the stack temperature. Figure 2-3 shows the model scheme, and table 2.1 helps the reader in relating the different blocks with the equations discussed.

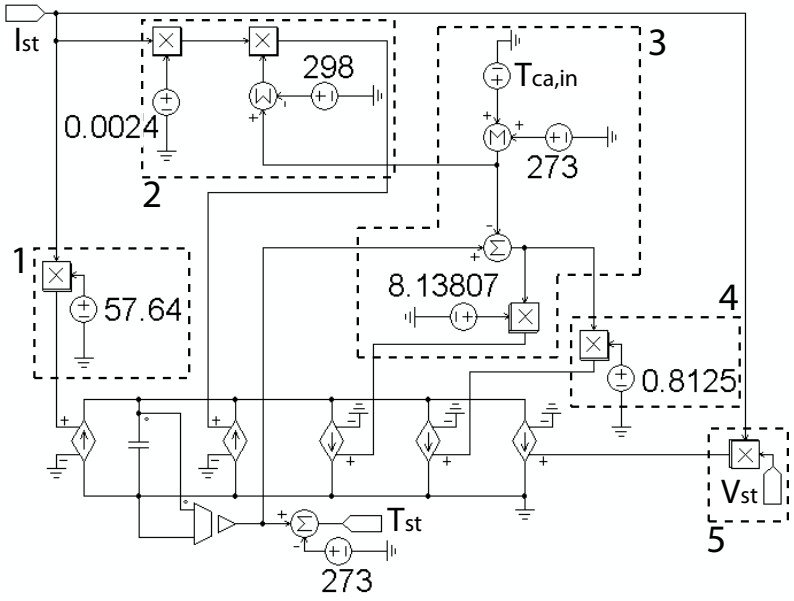


Figure 2-3: PSIM schematic subsystem simulating the thermal model.

ROVIRA I VIRGILI UNIVERSITY
FUEL CELL MODELING AND CONTROL FOR FUEL CONSUMPTION OPTIMIZATION
Carlos Andres Ramos Paja
ISBN:978-84-692-6902-2/ DL:T-1848-2009

Table 2.1: Blocks and corresponding equations in the subsystem simulating the thermal model (figure 2-3).

| Block | Equations |
|---|---|
| 1-3 | (2.11) |
| 2 | (2.15), (2.16), (2.17), (2.18), (2.19) and (2.20) |
| 4 | (2.14) |
| 5 | (2.12) |

## 2.5 Modeling the air compressor dynamics and losses

The air compressor is usually modeled by using mechanical and electrical relations: an example is proposed in [1]. Nevertheless, a simplified model that allows a low computational effort and, at the same time, a good accuracy can be based on a Laplace representation of its dynamic behavior. The following transfer function has been identified from experimental data taken on the Ballard-NEXA 1.2 kW system:

$$\left.\begin{aligned} W_{cp} &= G_{cm}(s)\cdot V_{cp} - 45 \\ G_{cm}(s) &= \frac{0.1437s^2 + 2.217s + 8.544}{s^3 + 3.45s^2 + 7.324s + 5.745} \end{aligned}\right\} \tag{2.22}$$

where $V_{cp}$ is the compressor control signal (0% - 100%) and $W_{cp}$ is the air mass flow supplied to the FC stack.

The compressor control law implemented in the NEXA control board has been identified experimentally as:

$$V_{cp} = 0.99873 \cdot I_{st} + 46.015 \tag{2.23}$$

In order to account for the power consumption due to FC system ancillaries, and especially to the air compressor, the stack current $I_{st}$ must be obtained by the sum of the net current $I_{net}$ requested by the load and the compressor current $I_{cm}$. The parasitic consumption and losses of the ancillaries have been identified experimentally from the prototype in order to obtain the following relation between the air mass flow $W_{cp}$ and $I_{cm}$:

$$I_{cm} = -3.231 \times 10^{-5} \cdot W_{cp}^2 + 0.018 \cdot W_{cp} + 0.616 \tag{2.24}$$

ISBN:978-84-692-6902-2/ DL:T-1848-2009

## 2.6 Polarization curve modeling by circuital equations

In order to obtain a reproduction of the FC polarization curve by using an equivalent circuit that includes linear and non-linear components, the electrochemical processes that take place at each electrode and between them have been studied. This was performed by following the modeling procedures proposed by Capel et al. [12] and Buasri et al. [31]. In this way, it is defined an electrical representation of the electrochemical processes that take place on each electrode and between them, where their contributions have different influences and depend on the operating point [32]. The effects modeled are:

- *the activation of both electrodes.* The voltage contributions of each electrode depend on species and electrode materials. According to the Butler and Volmer law [12], the relationship between the voltage $v_A$ and the cell current $i$ for a given electrode is:

$$i = i_a + i_c = i_o \left[ e^{\left( \frac{\alpha_a n \mathsf{F} v_A}{\mathsf{R} T} \right)} - e^{\left( \frac{-\alpha_c n \mathsf{F} v_A}{\mathsf{R} T} \right)} \right] \tag{2.25}$$

  where $i_a$ and $i_c$ are the currents of the electrode involved in the oxidation or the reduction processes when it operates as an anode or as a cathode. The current $i_0$ is the cell current at steady state, and parameters $\alpha_a$ and $\alpha_c$ are the charge transfer coefficients of the generated species at the electrode, in the oxidation (fuel cell area or anode operation) and in the reduction (water electrolysis or cathode operation) processes respectively; $n$ is the number of electrons, $\mathsf{F}$ the Faraday constant, $\mathsf{R}$ the gas constant and $T$ the FC temperature.

- *the charge transfer from electrode to electrode* according to Ficks first law of diffusion, related to the carrier concentration, which states that the voltage drop $v_D$ due to the current $i$ is given by [12]:

$$v_D = \frac{\mathsf{R} T}{n \mathsf{F}} \cdot \ln \left( 1 - \frac{i}{i_L} \right) \tag{2.26}$$

  where $i_L$ is the maximum current produced by the fuel cell for a given flow of hydrogen. This limit condition corresponds to the short circuit point of the fuel cell characteristic.

- *the voltage drop* $v_R$ introduced by the Ohm's law applied to all resistive parts of the cell, that is the ohmic losses due to the circulation of current $i$ through the connectors, the electrodes

ISBN:978-84-692-6902-2/ DL:T-1848-2009

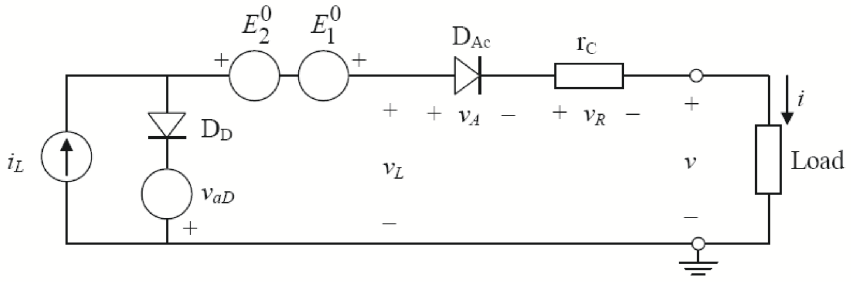


Figure 2-4: Equivalent electrical circuit of the fuel cell impedance.

and the electrolyte, representing a total resistance $r_c$:

$$r_c = \frac{v_R}{i} \tag{2.27}$$

Modeling the electrical characteristic of a cell consists in representing these three effects in order to define an electrical equivalent circuit with the same behavior. This circuit exhibits the same $v(i)$ characteristic of the cell, that is, at any time $t$:

$$v(i,t) = \Delta E^0 + v_A(i,t) + v_D(i,t) + v_R(i,t) \tag{2.28}$$

where $\Delta E^0$ is the open circuit voltage, i.e. the difference of the standard potentials of the electrodes.

The electrical circuit, which represents an electrochemical system and behaving as a fuel cell, has to assemble the three different contributions of the chemical reaction on each electrode. As shown in [12], the activation process is equivalent to a diode connected in series with a voltage source that represents the standard potential of the electrode; the diffusion is represented by a current source with a diode in series with a negative voltage source and the ohmic effect is represented by a series resistance.

The equivalent electrical circuit is depicted in figure 2-4. It is composed by a current source $i_L$ feeding at the same time two branches, one constituted by a diode $D_D$ in series with a negative voltage source $v_{aD}$, and the second consisting of the series connection of a resistance $r_c$, one diode $D_A$ and two voltage sources $E_2^0$, $-E_1^0$. This branch is connected to the external network (*Load*) and represent the positive terminal of the cell. The relationships of the activation and diffusion processes imply three voltage sources $E_2^0$, $-E_1^0$ and $v_{aD}$, and one current source $i_L$. These voltage sources can be suppressed by fulfilling the following condition, which imposes that the difference between the

ISBN:978-84-692-6902-2/ DL:T-1848-2009

standard reference potentials sets the open circuit voltage of the cell, that is:

$$v_{aD} = E_2^0 - E_1^0 \tag{2.29}$$

The cell characteristic $v(i)$ becomes:

$$v = v_L - v_A - v_R \tag{2.30}$$

that is

$$v = \frac{A_D \mathsf{k} T}{\mathsf{q}} \cdot \ln\left(1 + \frac{i_L - i}{i_{RD}}\right) - \frac{A_A \mathsf{k} T}{\mathsf{q}} \cdot \ln\left(1 + \frac{i}{i_{RA}}\right) - r_c \cdot i \tag{2.31}$$

In the case of a stack consisting in the series connection of $m$ cells, some parameters in the equivalent circuit multiplies by $m$. The final equation of the proposed stack impedance model is:

$$V_{st} = m \cdot \frac{A_D \mathsf{k} T}{\mathsf{q}} \cdot \ln\left(1 + \frac{I_{sc} - I_{st}}{i_{RD}}\right) - m \cdot \frac{A_A \mathsf{k} T}{\mathsf{q}} \cdot \ln\left(1 + \frac{I_{st}}{i_{RA}}\right) - R_C \cdot I_{st} \tag{2.32}$$

where $m = 46$ for the Ballard-NEXA is the number of individual cells connected in series, $R_C = m \cdot r_C$ is the overall stack resistance, $\alpha = A_D \mathsf{k} T/\mathsf{q}$ and $\beta = A_A \mathsf{k} T/\mathsf{q}$ are the products of the diodes ideal factor $A_D$ and $A_A$, the Boltzmann constant $\mathsf{k}$, the electron charge $\mathsf{q}$ and the temperature $T$ in Kelvin that is equal to 35 $^o$C, i.e. the reference temperature. The experimental data of different polarization curves for different $\lambda_{O_2}$ were taken regulating the stack to the reference temperature. In this circuit some non-linear elements have been used to model the diodes to define the complete non-linear equations shown below:

$$i_{Dd} = i_{RD}\left[e^{\left(\frac{v}{m \cdot \alpha}\right)} - 1\right] \tag{2.33}$$

$$i_{Da} = i_{RA}\left[e^{\left(\frac{v}{m \cdot \beta}\right)} - 1\right] \tag{2.34}$$

where $i_{RA}$ and $i_{RD}$ are the diode saturation currents. The voltage-controlled current source gives the short-circuit current $I_{sc}$ that corresponds to a given $\lambda_{O_2}$ condition. The circuit has been parameterized by using experimental polarization curves with $\lambda_{O_2}$ values between 3.0 and 6.5, obtaining the identified relation given in (2.35).

$$I_{sc} = -0.45 \cdot \lambda_{O_2}^2 + 8.5 \cdot \lambda_{O_2} + 35 \tag{2.35}$$

ISBN:978-84-692-6902-2/ DL:T-1848-2009

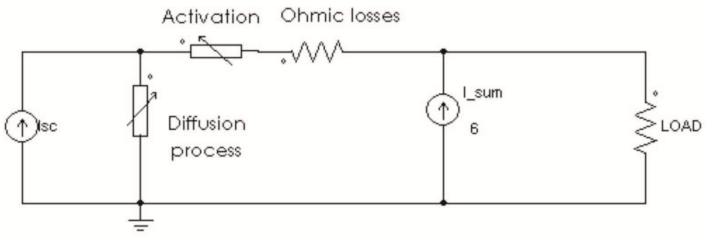


Figure 2-5: Equivalent electrical circuit of the polarization curve.

The polarization model and its corresponding voltage-current characteristic have been identified by means of experimental measurements, thus obtaining: $i_{RA} = 3.9$ mA, $i_{RD} = 790.8$ mA, $\alpha = 199.9$ mV, $\beta = 6.9$ mV and $R_C = 92.6$ mΩ.

In the experimental setup the stack current was limited to the desired operating range of $I_{st} \geq 6$ A where the compressor dynamics are linear with respect to the air flow and control signal. The fitting was performed using a new current axis $(I_{st} - 6)$ to reproduce the behavior using the diodes-resistor network. This was implemented in the model circuit using a current source of 6 A (I_sum) to obtain the new stack current axis.

The stack voltage predicted by the circuit shown in figure 2-5 is valid for the modeling reference temperature. In order to consider the effect of the temperature on the stack voltage, the deviation of the polarization curve $dV_T$ depending on the changes of the stack temperature from the reference temperature has been modeled. In the experimental prototype the reference temperature is set to $T_0 = 35\ ^oC$ and the following deviation law has been experimentally identified [23]:

$$\begin{aligned} dV_T &= k_{dV} \cdot (T_{st} - T_0), \\ k_{dV} &= \begin{cases} T_{st} > T_0 \rightarrow k_{dV} = 0.138 \\ T_{st} \leq T_0 \rightarrow k_{dV} = 0.250 \end{cases} \end{aligned} \tag{2.36}$$

The polarization curves obtained by means of the model presented in this chapter (lines) have been compared with the experimental data (symbols): figure 2-6 shows the model prediction as well as the experimental measurements data for different $\lambda_{O_2}$ values.

## 2.7 Experimental validation of the model

The model described above has been implemented in the PSIM environment as depicted in figure 2-7. Table 2.2 helps the reader in relating the different blocks with the equations discussed in the previous sections. The inputs of the model are the load current $I_{net}$ and the ambient temperature $T_{ca,in}$, and

ISBN:978-84-692-6902-2/ DL:T-1848-2009

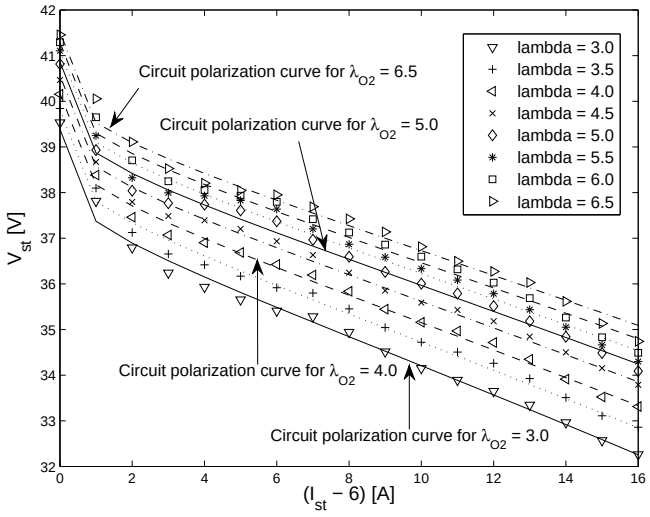


Figure 2-6: Polarization curves for different $\lambda_{O_2}$ values obtained by fitting and experimental data.

the outputs are the oxygen excess ratio $\lambda_{O_2}$ and the stack voltage $V_{st}$. The stack temperature $T_{st}$ is calculated in the thermal model and can be also used for prediction purposes, but it is not a main output variable.

Numerical results obtained by means of the developed model have been validated by means of experimental measurements on a 1.2 kW Ballard Nexa FC system. The model parameters used in this validation process are given in table 2.3.

The comparison between the experimental data and the model response is presented in figure 2-8. The physical variables externally imposed to the real system and to the model have been the load current $I_{net}$ and ambient temperature $T_{ca,in}$. The applied $I_{net}$ profile shown in figure 2-8(a) exhibits high and low frequency transients that allow a realistic validation of the model. The $T_{ca,in}$ behavior measured during the experiments is depicted in figure 2-8(b).

The air compressor dynamics and losses models have been compared with the experimental measurements: figure 2-8(c) shows the comparison between the losses predicted by the model and the measured current consumption of the auxiliary systems, with the model reproducing the main consumption only. Figure 2-8(d) shows that the compressor dynamic model reproduces the experimental air mass flow in a satisfactorily way.

The good agreement between the model and the experimental results also holds for the oxygen excess ratio $\lambda_{O_2}$ (figure 2-8(e)). Experiments have been also allowed to identify the $\lambda_{O_2}$ profile followed by the control law implemented in the NEXA control board (2.37), which presents a static

ISBN:978-84-692-6902-2/ DL:T-1848-2009

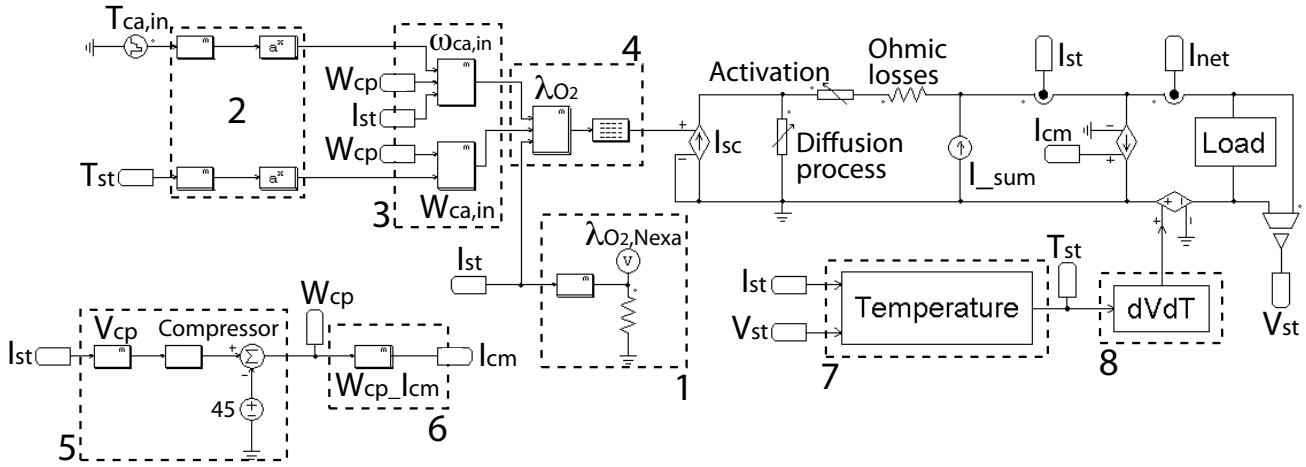


Figure 2-7: PSIM schematic of the Ballard Nexa 1.2 kW fuel cell model.

Table 2.2: Blocks and corresponding equations in the FC model (figure 2-7).

| Block | Equations |
|---|---|
| 1 | (2.37) |
| 2 | (2.3) |
| 3 | (2.1), (2.2), (2.4) and (2.5) |
| 4 | (2.6), (2.9) and (2.35) |
| 5 | (2.22) and (2.23) |
| 6 | (2.24) |
| 7 | Thermal model subsystem |
| 8 | (2.36) |

relation between the desired $\lambda_{O_2,Nexa}$ and the stack current $I_{st}$. This relation gives a safe $\lambda_{O_2}$ reference against oxygen starvation phenomenon only in steady state conditions but not during transient behavior. The NEXA board controller parameters are given in table 2.4.

$$\lambda_{O_2,Nexa} = \frac{a_3 \cdot I_{st}^3 + a_2 \cdot I_{st}^2 + a_1 \cdot I_{st} + a_0}{b_1 \cdot I_{st} + b_0} \tag{2.37}$$

Finally, figure 2-8(f) shows the comparison between the stack voltage values obtained from both simulations and experimental measurements: a satisfactory fitting of both results is evident.

In order to provide an estimation of the model accuracy, an error analysis has been carried out by using the mean relative error criteria [33] given in (2.38), where $m_j$ and $f_j$ represent the experimental and estimated data sets, respectively, and $N$ the number of samples.

$$MRE(\%) = 100 \times \frac{1}{N} \sum_{j=1}^{N} \left| \frac{m_j - f_j}{m_j} \right| \tag{2.38}$$

ISBN:978-84-692-6902-2/ DL:T-1848-2009

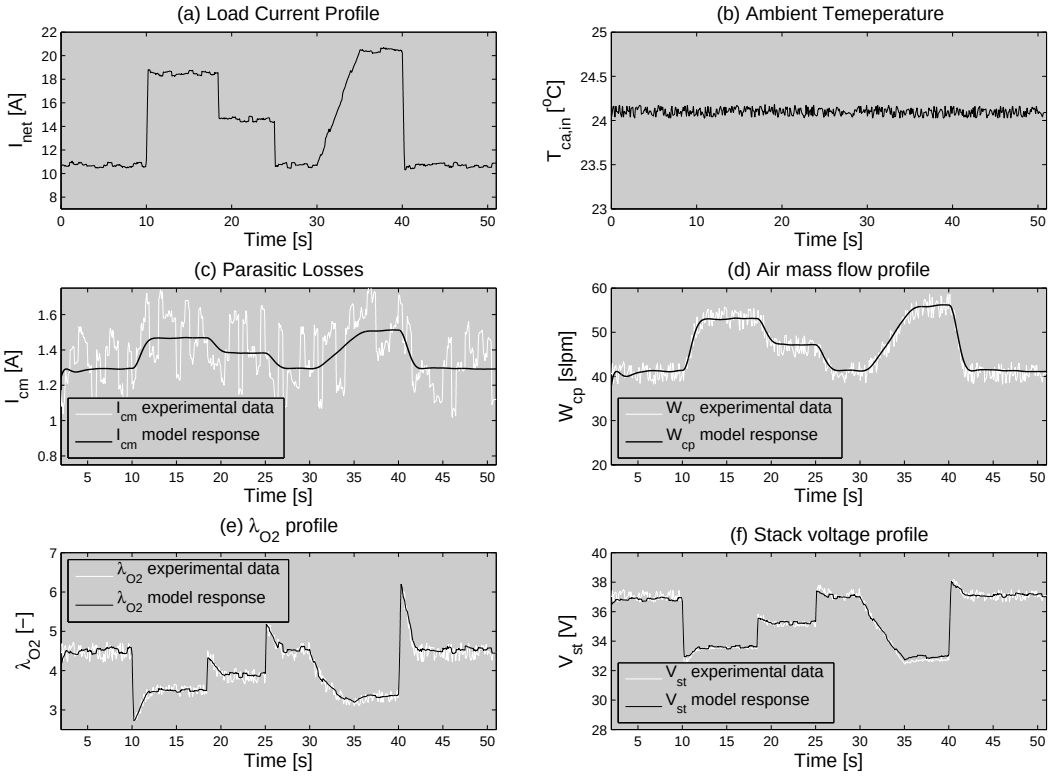


Figure 2-8: Fuel cell model experimental validation.

The MRE criteria was applied to the static and dynamic model validation. The model reproduction of the polarization curves, depicted previously in figure 2-6, reports a relative mean error equal to 0.34 %. In the dynamic behavior, the MRE criteria was also applied to the estimated states depicted in figure 2-8, obtaining the relative mean errors given in table 2.5. From these MRE values it is evident the satisfactory model reproduction of the static and dynamic fuel cell behavior, where the higher error is reported in the estimation of the auxiliary systems consumption and losses, which prediction is constrained to its mean value. Finally, the errors in the compressor air flow, oxygen excess ratio and stack voltage are mainly due to the non-modeled ripple in those signals.

ISBN:978-84-692-6902-2/ DL:T-1848-2009

Table 2.3: Model parameters.

| Parameter | | Value |
|---|---|---|
| $A_{B2amb,rad}$ | $[\mathsf{m}^2]$ | 0.1410 |
| $A_{B2amb,conv}$ | $[\mathsf{m}^2]$ | 0.0720 |
| $A_{B2cool,conv}$ | $[\mathsf{m}^2]$ | 1.2696 |
| $C_{st}$ | $[\mathsf{J}\cdot\mathsf{kg}^{-1}\cdot\mathsf{K}^{-1}]$ | 1100 |
| $\mathsf{F}$ | $[\mathsf{C}\cdot\mathsf{mol}^{-1}]$ | 96485 |
| $K_{h1}$ | $[-]$ | 0.0156 |
| $K_{h2}$ | $[-]$ | 1 |
| $\mathsf{M}_{\mathsf{N}_2}$ | $[\mathsf{kg}\cdot\mathsf{mol}^{-1}]$ | 0.028 |
| $\mathsf{M}_{\mathsf{O}_2}$ | $[\mathsf{kg}\cdot\mathsf{mol}^{-1}]$ | 0.032 |
| $\mathsf{M}_{\mathsf{v}}$ | $[\mathsf{kg}\cdot\mathsf{mol}^{-1}]$ | 0.018 |
| $c_{p,H_2}$ | $[\mathsf{J}\cdot(\mathsf{kg}\cdot\mathsf{K})^{-1}]$ | 14420 |
| $c_{p,O_2}$ | $[\mathsf{J}\cdot(\mathsf{kg}\cdot\mathsf{K})^{-1}]$ | 918.75 |
| $c_{p,H_2O}$ | $[\mathsf{J}\cdot(\mathsf{kg}\cdot\mathsf{K})^{-1}]$ | 1865 |
| $h_{B2amb,nat}$ | $[\mathsf{W}\cdot\mathsf{kg}^{-1}]$ | 14 |
| $\mathsf{k}$ | $[\mathsf{J}\cdot\mathsf{kg}^{-1}]$ | $1.380650\times10^{-23}$ |
| $m_{st}$ | $[\mathsf{kg}]$ | 5 |
| $m,\ n$ | $[-]$ | 46 |
| $\mathsf{q}$ | $[\mathsf{C}]$ | $1.602176\times10^{-19}$ |
| $y_{O_2,ca,in}$ | $[-]$ | 0.21 |
| $\varepsilon$ | $[-]$ | 0.9 |
| $\sigma$ | $[\mathsf{W}\cdot\mathsf{m}^{-2}\cdot\mathsf{K}^{-4}]$ | $5.678\times10^{-8}$ |
| $\phi_{ca,in}$ | $[-]$ | 1 |

Table 2.4: $\lambda_{O_2,Nexa}$ controller identified parameters.

| Parameter | Value |
|---|---|
| $a_0$ | 402.4 |
| $a_1$ | $8.509\times10^{-5}$ |
| $a_2$ | - 0.8387 |
| $a_3$ | 0.027 |
| $b_0$ | 61.4 |
| $b_1$ | 1.0 |

Table 2.5: Dynamical validation error analysis (MRE)

| Variable | MRE [%] |
|---|---|
| $I_{cm}$ | 8.77 |
| $W_{cp}$ | 2.35 |
| $\lambda_{O_2}$ | 2.36 |
| $V_{st}$ | 0.49 |

ROVIRA I VIRGILI UNIVERSITY
FUEL CELL MODELING AND CONTROL FOR FUEL CONSUMPTION OPTIMIZATION
Carlos Andres Ramos Paja
ISBN:978-84-692-6902-2/ DL:T-1848-2009

## 2.8 Fuel cell voltage ripple analysis

PEMFC systems exhibit voltage ripple even in null-ripple load current conditions, and the analysis of this phenomenon is mandatory for reproducing the fuel cell behavior in real-time simulators and emulators, and also it is important for the power electronics design process. In this analysis the validated physical model proposed by Real et al. [23] was used. That model was selected instead of the model previously proposed in this chapter because the last one is oriented to power electronics interactions, and therefore it is difficult to extract the voltage components since it models the fuel cell output impedance. The model from Real et al., in the other hand, provides a physical modeling of the stack as a voltage source where its components are easily differentiable.

The Real et al. model considers the auxiliary systems dynamics and power consumption, stack humidity, temperature effects and fluid dynamics, gas diffusion and electrochemical reactions inside the stack. Also, the model is tuned to the 1.2 kW fuel cell Nexa module considered in this work using experimental data, taking four operating points to fit the polarization curve. The stack voltage is governed by equation (2.39):

$$\begin{aligned} V_{fc} = x_1 + x_2(T_{st} - T_{st}^0) + x_3(0.5\ ln(p_{O_2,ca}) + ln(p_{H_2})) \\ -x_4(1 - exp(-j/x_5)) - x_6 \cdot j - x_7 \cdot j^{(1+x_8)} \end{aligned} \tag{2.39}$$

whose parameters $\{\ x_k\ , k = 1..8\ \}$ are given by

$$x_8 = (1 + p_{4i}^2)/(0.25\ p_{4i}) \tag{2.40}$$

$$x_7 = \frac{(p_{4v} - p_{3v}) + (p_{2v} - p_{3v})((p_{4i} - p_{3i})/(p_{3i} - p_{2i}))}{-p_{4i}^{(1+x_8)} + p_{3i}^{(1+x_8)}((p_{4i} - p_{3i})/(p_{3i} - p_{2i}))} \tag{2.41}$$

$$x_6 = \left((p_{2v} - p_{3v}) - x_7\ p_{3i}^{(1+x_8)}\right)/(p_{3i} - p_{2i}) \tag{2.42}$$

$$x_5 = (p_{2i} - p_{1i})/4 \tag{2.43}$$

$$x_4 = p_{1v} - p_{2v} - x_6\ p_{2i} \tag{2.44}$$

$$x_3 = 2\ p_{O_2,ca}^0\ (\Delta V_{fc}/\Delta p_{O_2,ca}) \tag{2.45}$$

$$x_2 = \Delta V_{fc}/\Delta T_{st} \tag{2.46}$$

$$x_1 = p_{1v} - x_3\ (0.5\ ln(p_{O_2,ca}^0) + ln(p_{H_2}^0)) \tag{2.47}$$

while the current density $j$ is defined by

$$j = I_{st}/A_{fc} = I_{st}/(A_{fc}^0(1 - \alpha_1 m_{1,anch})) \tag{2.48}$$

ISBN:978-84-692-6902-2/ DL:T-1848-2009

and the stack power is given by

$$P_{fc} = V_{fc} \cdot I_{st} \tag{2.49}$$

$V_{fc}$, $I_{st}$, $P_{st}$ and $T_{st}$ represent the fuel cell Nexa module voltage, current, power and temperature, respectively. $p_{O_2,ca}$ and $p_{H_2}$ are the oxygen cathode and hydrogen anode pressures. $A_{fc}$ is the effective fuel cell area, which depends on the nominal fuel cell area $A^0_{fc}$ and on a mass fraction of the liquid water present in the anode $\alpha_1 m_{1,anch}$. This value is included to consider the effect of the anode water accumulation on the voltage. $\{ (p_{ki}, p_{kv}) , k = 1..4 \}$ are the currents and voltages of the experimental operating points used to model the fuel cell, and also $p^0_{O_2,ca}$, $p^0_{H_2}$, $T^0_{st}$ define a nominal operating point where $\Delta V_{fc}/\Delta T_{st}$, $\Delta V_{fc}/\Delta p_{O_2,ca}$ and $\alpha_1$ are measured quantities. The stack current considered in the model is that one requested by both load and auxiliary systems and, therefore, the stack power corresponds to the total system consumption. The thermal and fluid dynamics are also taken into account, and a detailed description and validation of this physical model can be found in [23].

From (2.39)-(2.49) it is concluded that at constant current and temperature, the stack voltage varies according to the current density change and the oxygen and hydrogen partial pressures. The water particles and inert gases accumulation in the anode causes voltage drops, which are compensated with the anode purge process. This effect depends on the stack current and it is also present at constant current profiles. Also, from the oxygen and hydrogen reacted (2.6)-(2.7), it is concluded that the control system that regulates the oxygen flow suffers disturbances due to the air compressor current demand, and this regulation affects the partial pressures that govern the stack voltage. In fuel cell systems the regulation of oxygen flow is important because insufficient reactants flow to supply current demands ($\lambda_{O_2} < 1$) causes the oxygen starvation phenomenon. This causes a fast stack degradation and low power generation [25]. In the literature concerning this undesired phenomenon, it is proposed to regulate $\lambda_{O_2} > \lambda_{O_2,min}$ [34]-[35], where $\lambda_{O_2,min}$ depends on the compressor dynamics, system mechanical structure and load profile. In this way, Arce et al. [27] proposes a $\lambda_{O_2,min} = 4$ in order to provide safety to the fuel cell and maximize the fuel cell net power output, this analysis being based on a 1.2 kW Nexa power module.

The regulation strategies of the oxygen flow to prevent oxygen starvation and to control the anode purge process affect the reagents partial pressures and therefore the stack voltage. Analyzing (2.6)-(2.7), (2.22)-(2.24), (2.39)-(2.49) and the $\lambda_{O_2}$ definition (2.9), it is concluded that in constant load current conditions, variations on the compressor current demand cause variations on the air flow generated by the compressor. This air flow can be approximated to the oxygen flow because

ISBN:978-84-692-6902-2/ DL:T-1848-2009

the Nexa power module does not consider humidification of the inlet air, and also because the oxygen fraction in the air can be considered constant. Therefore, compressor current variations cause oxygen flow changes that affect the stack voltage.

In conclusion, the model analysis shows that the voltage ripple, in ripple free load current conditions, mainly depends on the air flow variations. The experimental data depicted in figure 2-8(c) shows a significant ripple in the compressor current demand (approximately 15 %), and also in figure 2-8(d) air flow variations are observed (approximately 5 %). This can be compared with the simulation results presented in the same figures, where ripple free compressor currents generate ripple free air flows. Finally, the air flow changes generate reactant partial pressure changes yielding voltage ripple. There are other sources that contribute to the voltage ripple like stack temperature variations, anode purge process and noise induction from the cooling fan and compressor motor, which might be the subject of future works.

## 2.9 Sensors analysis for membrane water content estimation

Membrane water content ($\lambda$) is an important variable in PEMFC power generation, but its value cannot be measured or estimated easily. $\lambda$ gives information about the membrane hydration condition, this being useful in membrane resistance reduction. Also, an uniform $\lambda$ distribution contributes positively in the membrane health because reduce the hot-points and flood-points formation that stress and degrade the membrane [36].

In the physical non-linear model proposed by Pukrushpan et al. [28], the calculation of $\lambda$ is performed using the states considered in the model (nine states). Also, the water flow and water mass in the cathode must be calculated to finally obtain $\lambda$ [37]. Figure 2-9 shows the simulation of the stack current and voltage, cathode pressure, cathode water flow and mass, and membrane water content for a 50 kW fuel cell, carried out with the Pukrushpan non-linear model.

In order to analyze the redundancy of information in the signals used to calculate $\lambda$, a Principal Components Analysis (PCA) [38]-[39] was performed, which allows to compress the information given by the sensors (used signals) and evaluate the additional information that each one contribute to the desired data ($\lambda$). The analysis was performed by using the *PLS Toolbox* for MATLAB [40]. Figure 2-10(a) shows the compression of the information given by the five sensors considered (stack current $I_{st}$, stack voltage $V_{st}$, cathode pressure $P_{ca}$, water flow in the cathode $W_{w,ca}$ and water mass in the cathode $m_{w,ca}$) into two principal components ($PC\#1$ and $PC\#2$), which represent 97.6 % of the overall information. This figure is a new dimensional representation of the information where the

ISBN:978-84-692-6902-2/ DL:T-1848-2009

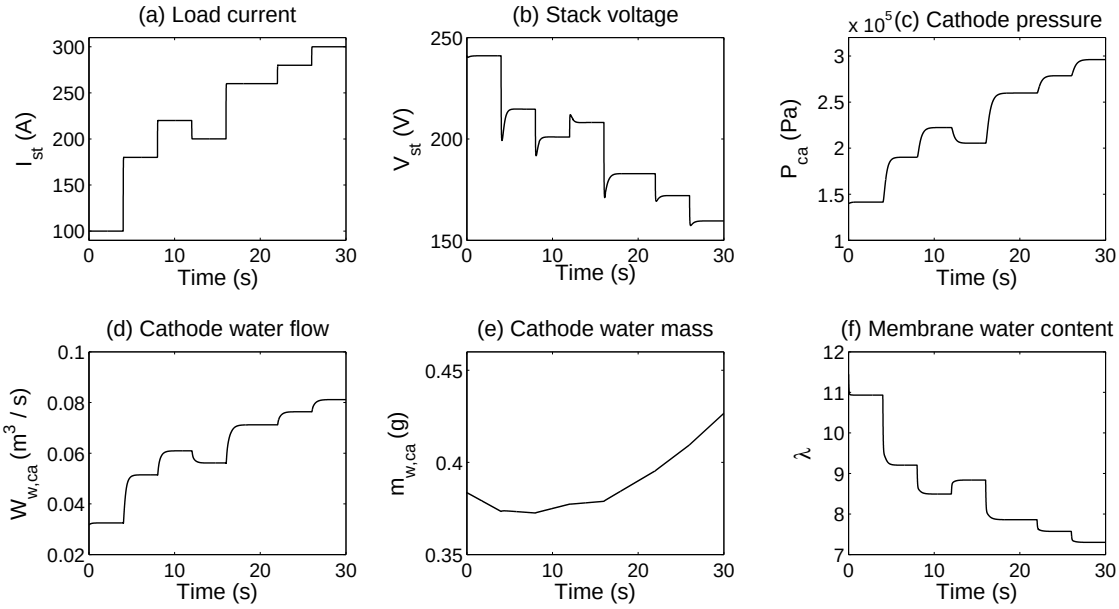


Figure 2-9: Membrane water content and states profiles.

principal components are the new coordinate axis. These principal components were obtained by the analysis of the stack current and voltage, cathode pressure and finally cathode water flow and mass (full sensors set). Figure 2-10(b) presents the loads of each sensor into the principal components, where the stack current and voltage, and cathode pressure are representative in the construction of the components, but the cathode water flow and mass do not give additional information to them (loads near to zero), instead they provide redundant information. Based on this, it was proposed to use only the information provided by the stack current, voltage, and cathode pressure (reduced sensors set) to obtain the principal components. Figure 2-10(c) shows the compression of the information given by the reduced sensors set into the same number of principal components ($PC\#1$ and $PC\#2$), which represent 99.1 % of the reduced information. Also, figure 2-10(d) presents the loads of each sensor into the components, where now it is observed that does not exist redundant sensors information. The correlation between the compressed information of the full and reduced sensors sets (figures 2-10(a) and 2-10(c)) also confirms that the reduced set gives an acceptable representation of the system behavior.

From the above analysis, it can be concluded that the reduced sensors set allows to reproduce the $\lambda$ behavior. In order to confirm this, Artificial Neural Networks estimators were developed: ANN5, which was trained with the full sensors set, and ANN3 that was trained with the reduced sensors set. Each estimator has a tree layer ANN with back-propagation training algorithm, where the input layer has the number of neurons equal to inputs, and has a single output ($\lambda$). The time response of

ISBN:978-84-692-6902-2/ DL:T-1848-2009

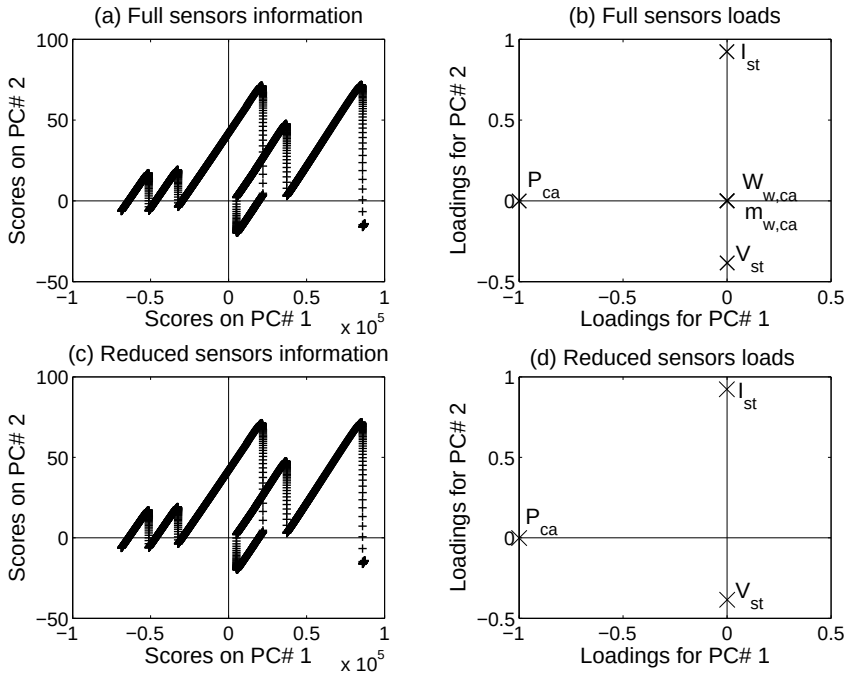


Figure 2-10: Sensors Principal Component Analysis (PCA).

both estimators and physical model are shown in figure 2-11(a), where it is observed an acceptable agreement between the physical model and the ANN estimators. Also, the difference between ANN3 and ANN5 is not perceptible. This is also observed in the relative errors between each ANN estimator and the physical model given in figure 2-11(b), where the errors were calculated using (2.50), being $\lambda_{physical}$ the physical model calculation and $\lambda_{ANN}$ the estimators approximations.

$$e_\lambda = 100 \times \frac{\lambda_{physical} - \lambda_{ANN}}{\lambda_{physical}} \tag{2.50}$$

$$E_\lambda = \frac{1}{N} \sum_{k_E=1}^{N} |e_{\lambda,k_E}| \tag{2.51}$$

The absolute average errors (2.51) of the ANN3 and ANN5 estimators are 2.5 % and 1.8 %, respectively. Also, it is observed that ANN5 instantaneous errors are mainly constrained in a 2 % error band, and the ANN3 in a 5 % band, which confirms the satisfactory reproduction of $\lambda$ by the reduced sensors set ANN estimator.

Finally, the physical model and ANN3 estimator were implemented in a real-time system intended to estimate $\lambda$. This was performed using the MATLAB Real-time Windows Target [41] and executed in a Personal Computer with an Intel Pentium 4 processor at 2.0 GHz, 1 GByte of Ram

ISBN:978-84-692-6902-2/ DL:T-1848-2009

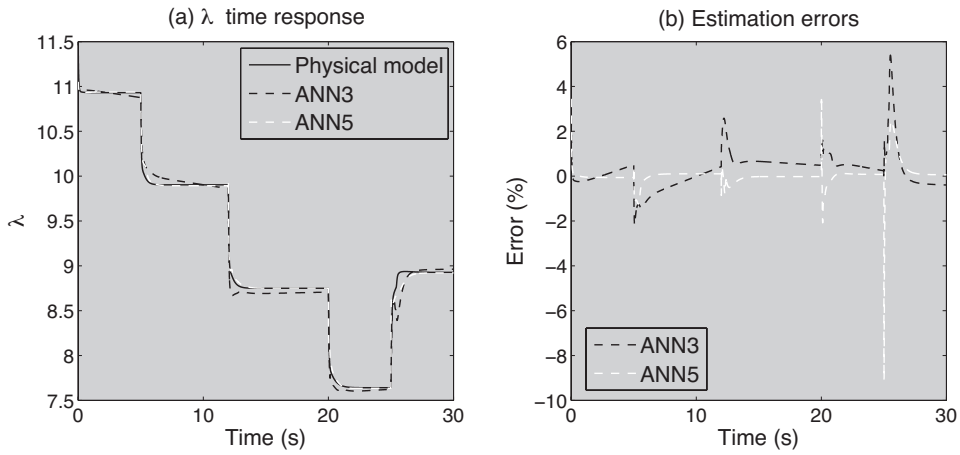


Figure 2-11: ANN estimator evaluation.

Table 2.6: Physical model and ANN3 processor loads.

| Sample time | Physical model load | ANN3 load |
|---|---|---|
| 0.2 ms | 36.2 % | 3.9 % |
| 0.4 ms | 19.7 % | 2.8 % |
| 0.6 ms | 13.2 % | 2.2 % |
| 0.8 ms | 9.8 % | 1.6 % |
| 1.0 ms | 7.4 % | 0.9 % |

memory and Microsoft Windows 2000 operating system. It was used the Runge-Kutta differential equation solution method [42] with sample times between 0.2 ms and 1.0 ms, obtaining the processor load profile given in table 2.6. The processor load data makes evident the ANN3 estimator advantage in terms of calculation power requirements, it being ideal for real-time implementations like process estimators.

## 2.10 Conclusions

In this chapter a novel PEM fuel cell dynamic model has been introduced. It is useful to design new strategies for controlling the oxygen excess ratio and it is also suitable for simulating power electronic circuits dedicated to fuel cell systems. The model includes experimentally derived behavioral relations, electrochemical equations and a non-linear circuit reproducing the fuel cell polarization curve. The model has been implemented in PSIM environment, and also validated by means of experimental data, referred to a Ballard NEXA 1.2 kW fuel cell power system.

The main characteristic of the proposed model is the interaction of electrochemical equations and circuital-based models, this in order to provide an estimation of the oxygen excess ratio together

ISBN:978-84-692-6902-2/ DL:T-1848-2009

with an electrical interaction with the load, this based on the modification of the output impedance of the model. This makes the proposed model suitable for oxygen excess ratio estimation in power electronics design, control and simulation. The model is also useful for on-line estimation of the oxygen excess ratio, since it is possible to adjust the model parameters to real prototypes, and run it in real-time systems measuring the fuel cell net current. Also, using other variables like stack voltage and temperature, the fidelity of the oxygen excess ratio estimation can be evaluated, allowing in this way the design of an oxygen excess ratio virtual sensor, which can be very useful for fuel cell safe experimentation and optimal operation. Finally, the model evaluation shows a satisfactory agreement with the experimental measurements.

This chapter also presents a stack voltage ripple analysis validated by means of the same experimental prototype: it assesses that the main source of ripple is the air flow control system. This information is useful to improve control strategies and power electronics in fuel cells, and therefore to reduce the current ripple components caused by resistive effects in the loads that degrade the fuel cell output power. Finally, the analysis of the sensors required to estimate the membrane water content ($\lambda$) was performed, and a reduced sensors set that allows the reproduction of $\lambda$ behavior without the need of measure all the fuel cell states has been proposed. This is useful in order to design systems for on-line estimation of $\lambda$ that allows protecting the fuel cell and improving its operation. Later, the real-time processing advantage of a neural network estimator was evaluated by using real-time implementations that makes evident the reduction of calculation power requirements of this type of systems, this being ideal for embedded implementations and autonomous systems.

ROVIRA I VIRGILI UNIVERSITY
FUEL CELL MODELING AND CONTROL FOR FUEL CONSUMPTION OPTIMIZATION
Carlos Andres Ramos Paja
ISBN:978-84-692-6902-2/ DL:T-1848-2009

ROVIRA I VIRGILI UNIVERSITY
FUEL CELL MODELING AND CONTROL FOR FUEL CONSUMPTION OPTIMIZATION
Carlos Andres Ramos Paja
ISBN:978-84-692-6902-2/ DL:T-1848-2009

# Chapter 3

# Fuel Cell Emulation

This chapter presents the concepts, analyses and implementations involved in a dynamic fuel cell emulation system, intended to support fuel cell control systems and hardware design and tests. Such a system is necessary because of the high PEMFC costs and the restrictive safe operation conditions, which make evaluating the non-tested control strategies or power electronics a dangerous and, maybe, costly procedure.

## 3.1 Introduction

To develop control systems required by either the application or fault detection strategies in mechanical systems, electrical power interfaces and high level energy management, experimentation needs to be carried out on physical systems. Some of these systems are expensive, and the required equipment and safety procedures are not easily provided by most control and power electronics laboratories. These difficulties have been addressed using emulators. In this way, Mosskull et al. [43] evaluated the responses of a stabilization strategy for induction motor drives with poorly damped input filters using a Hardware-In-The-Loop (HIL) simulator because it allows faster and more flexible experiments then when a real motor-inverter system is used. In electric systems, Koizumi et al. [44] used a reduced-scale distribution network simulator and a commercial solar cell array hardware simulator to evaluate the performance of a microcontroller for grid-connected photovoltaic systems because these simulators allow to define work and loading conditions.

Emulators are the object of considerable research because they make it possible to carry out reproducible experiments that control the *uncertain conditions* which affect real systems. Also, emulators do not require start-up/turn-off sequences or specialized environments. Arellano-Padilla et al. developed a dynamic emulator of mechanical loads [45] that allow electrical drives and motion-control

ISBN:978-84-692-6902-2/ DL:T-1848-2009

techniques to be tested and experimentally validated. Their work was an enhanced development of the emulator presented by Hakan et al. [46] seven years before, and shows the importance of emulation systems. Similarly, Rodic et al. reported the development of a dynamic emulator of mechanical loads using an induction motor [47] intended to evaluate the operation of electrical drives for specific mechanical load profiles.

Emulators are also a valuable resource for testing control strategies in industrial environments because the evaluation of controllers in a real system implies that production has to stop. Bettendorf [48] developed an emulator to test the programmable logic controller (PLC) software that controls a paper winding machine. It made it possible to test and optimize control strategies before their online implementation in the industrial process.

Similarly, emulators are also important for developing, testing and controlling of power electronics systems. Bin Lu et al. reported a low-cost real-time HIL system that does not need costly hardware in the design process of power electronic controllers [49]. Their system emulates either a power electronic plant that is controlled externally by the device being tested, or both the plant and the controller in different pc-based emulation platforms. A similar real-time simulator was presented by Dinavahi et al. [50] with the objective of verifying digital control systems before they were applied to real systems. They focused on the emulation of Voltage-Source-Converted-based Distribution STATic COMpensator (D-STATCOM) power systems, and validated their implementation in a 5 kVA D-STATCOM power system.

Emulators have been intensively used in renewable energy systems, because these systems are expensive, may require safety protocols, consume chemical reagents or have a non-predictable source of energy. One example of this use is the unified design, test and research platform for wind energy systems based on a real-time HIL simulator reported by Li et al. in [51]. This platform uses dynamometers and variable voltage and frequency converters to emulate realistic dynamic mechanical and electrical behaviors.

In the field of fuel cells, emulation has been used by the automobile industry to evaluate the performance of real devices in a controlled environment. With this objective, Vath et al. [52] reported a HIL system for PEM fuel cells. Their emulator represents the fuel cell and other systems of an automobile and makes it possible to evaluate control strategies, performance profiles and test of new hardware.

Other developments in fuel cell emulators and real-time simulators are focused in testing power systems designed to be connected to real fuel cells, thus making possible the a priori evaluation of systems performance and the detection of problems of connection and synchronization. Prabha et al. [53] presented a real-time simulator designed to reproduce the fuel cell behavior in different operation conditions and to evaluate the performance of DC/DC and DC/AC converters powered by

ISBN:978-84-692-6902-2/ DL:T-1848-2009

fuel cells. The authors justified using the simulator for the easy of the configuration process, the safe operation and the efficiency of the fault evaluation. Likewise, Dufour et al. [54] presented a fuel cell emulator based on real-time hardware. The emulator supports the evaluation of control strategies for hybrid automobile applications by providing an accurate and user-friendly platform. This approach was followed by Lim et al. [55] in their fuel cell dynamic simulator based on a programmable DC power supply and a LabVIEW graphical user interface. These emulators enable experiments to be carried out safely and easily without consuming any reagents. The main drawback is that these emulators require computational equipment that restricts portability, and increases the overall cost of the emulation system.

Similar developments have been reported by Tae-Won et al. [56] [57]. They describe a simple fuel cell emulator based on a DC/DC buck converter, which is digitally controlled by a DSP, and define the emulator output voltage with a lineal current-voltage relation (I-V). Ordonez et al. follows this same approach in [58]. They consider a static I-V relation and model the charge double layer effect by using a first order delay. In [59], Cirrincione et al. report a similar development. They model the polarization curve and charge double layer effect and use a power stage based on a DC/DC buck converter. Sirisukprasert et al. [60] follow the same simple modeling-DC/DC buck converter based power stage approach, mainly intended to support DC/AC inverter design. A slightly different approach was reported by Gebregergis et al. [61], who modeled the static characteristic of a solid oxide fuel cell (SOFC) and considered the thermal effects on the output voltage. This emulator uses a commercially available linear power amplifier to interact with electrical loads, thus making it easy to reproduce but at the price of an increased overall cost. The main drawback of these developments are that the fuel cell models implemented are simple, and any clarification in the benefits of using switching or linear implementations is given.

In [62], a different fuel cell emulator approach was proposed by Ordonez et al., who used a low power fuel cell to emulate high-power prototypes. This approach was also implemented by Parker-Allotey et al. in [63], where the emulator load current is scaled and applied to a low power prototype, the output voltage of which is also scaled to a high-power stack in order to interact with electrical loads. This is an interesting solution since is based on real fuel cell systems, but it still requires safety procedures and reagents, so it is costly and non-portable.

This chapter presents the development of digital emulators of PEM fuel cells based on a dynamic model validated by means of experimental measurements. Its main objectives are to test power systems designed to interact with PEMFC and to evaluate the performance of fuel regulation strategies in different electrical power profiles. The emulator was designed to be portable and a low-cost digital device was used to process the fuel cell model and output stage control, so the calculation

ISBN:978-84-692-6902-2/ DL:T-1848-2009

requirements of both the model and the controllers must be reduced. The model proposed in chapter 2, then, is not the best choice because its numerous calculation loops require highly time-consuming operations. The dynamic impedance output circuit will also require differential equation solutions and circuit analysis, thus generating a processing time that is not suitable for real time implementations. This issue was addressed by developing a novel fuzzy-based modeling technique that provided accurate reproduction of the behavior with low calculation requirements. This modeling technique has been applied to a PEMFC prototype, obtaining a fuzzy-based model that enabled the PEMFC emulator to be implemented using a low-cost digital processing device which, in spite of its computational limitations, satisfies the real-time processing requirements. Finally, the advantages and disadvantages of using switching or linear power stages in the emulation of fuel cells to interact with electrical loads are analyzed in terms of voltage ripple, energy efficiency and thermal consideration for the implementation.

## 3.2 Fuel cell models in emulation

PEMFC experimental prototypes can be classified in two groups: commercially available and user-designed implementations. Some of these prototypes are used in research and development of power electronic interface systems required between the PEMFC and the electric loads. Examples of this use are reported by Wai et al. in [64], [65] and [66] for high-efficiency DC/DC converters intended to operate with fuel cells. Other uses are reported in the three-phase high-power converter for low voltage fuel cell applications presented by Liu et al. in [67], and in the DC-DC boost converter designed for a fuel cell vehicle presented by Anzicek et al. in [68]. Many physical models of commercial and user-designed PEMFCs have been developed. As examples, the PEMFC models presented by Pukrushpan et al. in [6] and Real et al. in [23] are control-oriented, and are validated in the most common operating conditions. Likewise, the physical model proposed by Friede et al. in [8] is analytic-oriented, but since the model does not considers the current and humidity distribution over the cell surface and other parameters, the model cannot be fitted for all the operating conditions. Other modeling developments are application-oriented. For example, the model proposed by Kong et al. in [69] is a combination of an empirical model and an electric circuit model, and uses parameter identification to provide a good reproduction of experimental data. Similarly, the power electronics design-oriented model proposed by Stanton et al. in [70] is devised to model a PEMFC for power electronics simulation programs in an easy way, representing the physical phenomena as electrical components. Compared with more complex physical models, this type of PEMFC models are simpler, easier to implement and simulate, and correlate well with the experimental behavior of modeled systems with a small calculation time. More recently, the model proposed in chapter 2 of

ISBN:978-84-692-6902-2/ DL:T-1848-2009

this thesis presents a physical description that takes into account the electrochemical and thermal equations, and gives an impedance implementation of the polarization curve. This model provides accuracy and it is intended to be implemented in power electronics simulators, but it requires circuit analysis and differential equations processing for its solution.

Fuzzy and artificial neural network (ANN) based models, such as the ANN-based model for supercapacitor thermal and electrical behaviors reported by Marie-Francoise et al. [71], are another alternative for modeling complex systems from complex model-generated or experimentally measured data. These techniques were also used to model the behavior of PEMFCs. One example is the model proposed by Jemei et al. in [72], where a whole fuel cell system for automotive applications is modeled using ANN. Other fuel cell types and behaviors have also been modeled using such methodologies as the solid oxide fuel cell performance model based on ANN proposed by Ogaji et al. in [73]. Likewise, the fuzzy modeling of fuel cells is illustrated by the dynamic-nonlinear fuzzy model proposed by Yang et al. in [74], applied to molten carbonate fuel cells. Yang's fuzzy model is restricted to the operating conditions considered. Another interesting use of fuzzy models was presented by Entchev et al. in [75], where an application of adaptive neuro-fuzzy inference system techniques and ANNs is used to predict the performance of fuel cells in residential microgeneration installations.

Their simplicity, short processing time and consolidated implementation techniques makes fuzzy and ANN models appropriate choices not only for developing and simulating control strategies, but also for implementing simulators and emulators of fuel cells and, in particular, of PEMFCs whose physical models are very complex and require long calculation times.

As result of active research in fuel cell power conditioning for electric power applications [76], many real-time simulators and emulators of PEMFC have been developed to test the behavior of power systems that interact with PEMFC, thus making it possible to evaluate systems performance, detect problems of connection and synchronization early, etc. One of the main aspects to consider in the development of these emulators is the mathematical model of the emulated system. Depending on the complexity of the model and the accuracy of the integration algorithms, the calculation times can be very high, which is especially critical when a real-time implementation is required.

The *Adaptive-Network-Based Fuzzy Inference System (Anfis)* is a processing option that approximates the responses of complex-nonlinear systems and accurately reproduces a function or mathematical model. In the Fuzzy-Anfis modeling procedure, the *hybrid-Anfis* learning algorithm is used to obtain the parameters of a *Takagi-Sugeno (T-S) fuzzy system* [77] [78]. The hybrid-Anfis algorithm trains a five-layer neural network to generate known output values as response to defined input data. This network is implemented in a T-S fuzzy reasoning algorithm [77]. Due to the T-S fuzzy structure, the process for calculating the fuzzy model output has a constant number of math-

ISBN:978-84-692-6902-2/ DL:T-1848-2009

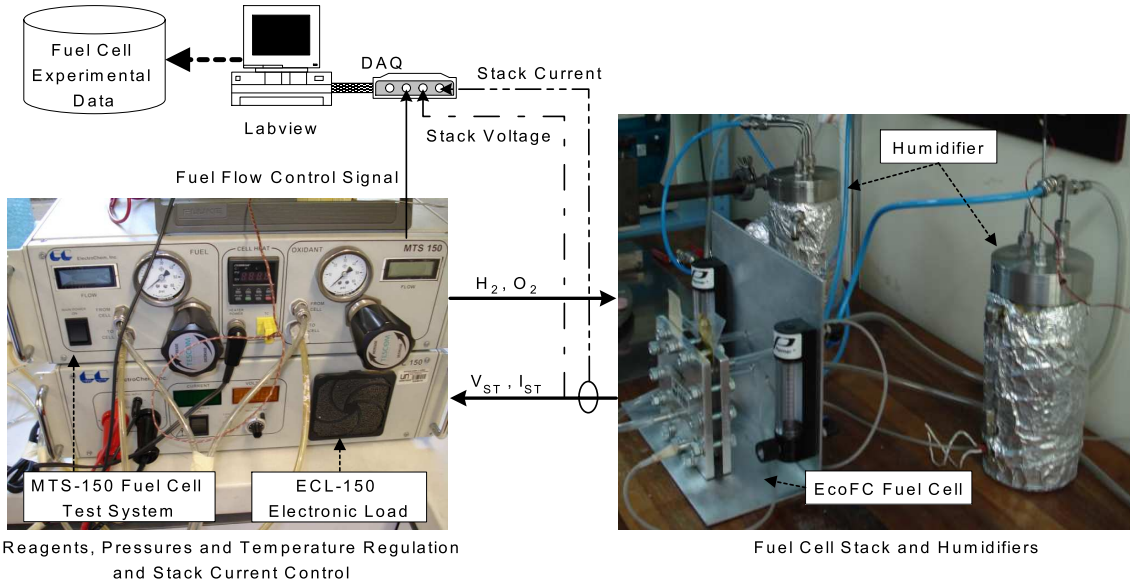


Figure 3-1: *$H_2$Economy EcoFC* Fuel Cell Test System Topology.

ematical operations for any combination of input variables, and this makes it possible to predict the resulting computational load, which makes it suitable for real-time implementations. Following the fuzzy-based models reviewed and the Fuzzy-Anfis theory described in appendix A, this chapter presents a fuzzy-based technique for modeling the dynamic and static behavior of a PEMFC's output voltage. This type of model requires large amounts of data to train the model networks, and the fuzzy model train procedure reported in [74] was used to parameterize the models proposed by Pukrushpan et al. and Real et al. in [1], [6], [23] and [79] to reproduce a real prototype behavior with the objective of generating the required training data for the Fuzzy-Anfis systems. Those models were selected because they represent the fuel cell as a voltage source and are normalized to a single cell. In turn, the model presented in chapter 2 describes the fuel cell as a variable impedance circuit.

### 3.2.1 PEMFC physical model parameterization

In order identify the fuzzy-based model in the usual operation conditions, the physical model was parameterized using experimental data of a user-designed PEMFC, the *$H_2$Economy-EcoFC* fuel cell of which produces a power of 3.5 W at a voltage of 0.6 V when $H_2$ is supplied at a pressure of 1 bar, $O_2$ at 1.2 bar, and the temperature of the cell is regulated to 80 $^oC$. This cell, which can produce a maximum electrical power of 5 W, is shown in figure 3-1. The PEMFC has two humidifiers (one for the oxidant and another for the fuel), and a *MTS-150* fuel cell test system that regulates the stack temperature and controls the anode-cathode pressure ratio according to the manufacturer's specifications.

ISBN:978-84-692-6902-2/ DL:T-1848-2009

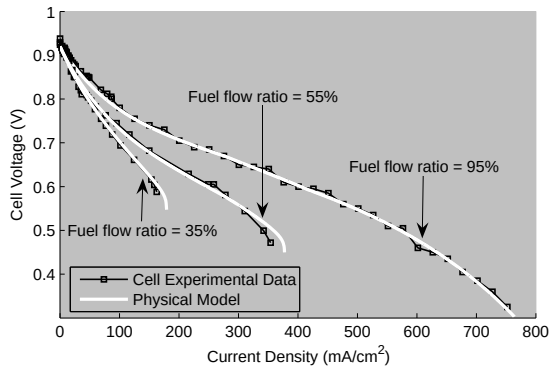


(a) Polarization Curves for fuel flows between 95 % and 35%.

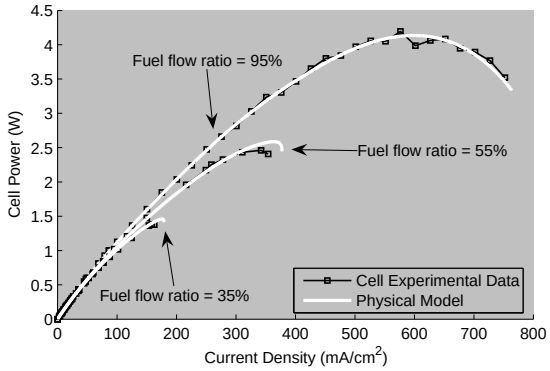


(b) Power Curves for fuel flows between 95 % and 35%.

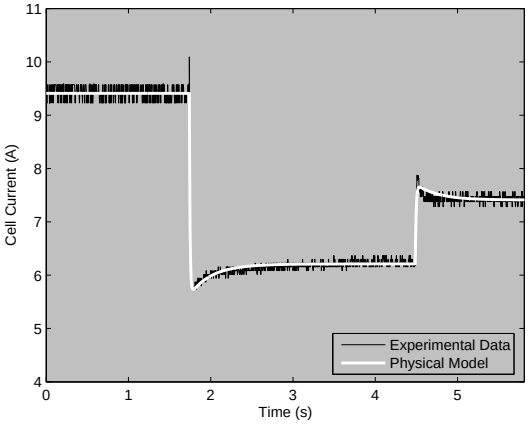


(c) Dynamic cell current response.

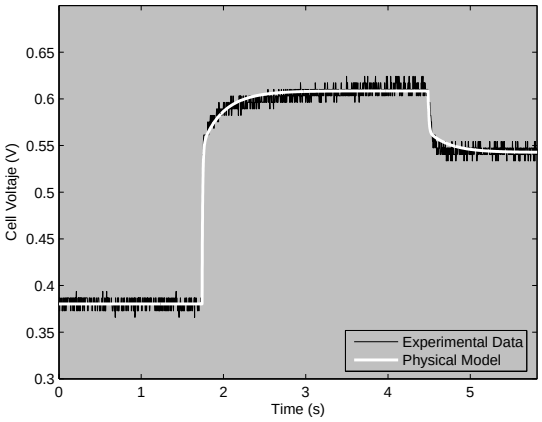


(d) Dynamic cell voltage response.

Figure 3-2: Fuel Cell model behavior evaluation.

Several experiments were made to evaluate the static and dynamic PEMFC behaviors at the desired operating points using the test topology of figure 3-1. The stack temperature, humidity and pressures were regulated to guarantee that the reagents ratio would allow correct reactions and safe operation. The stack current was controlled using an *ECL-150* electronic load [80]. The PEMFC fuel flow control signal, current and voltage values were recorded for the tasks of identification and validation. The fuel and oxidant fed to the PEMFC is presented in a standardized format called the fuel flow ratio like a percentage of the maximum flow of reagents that the fuel cell can process.

Figures 3-2(a) and 3-2(b) present the polarization and power curves of the PEMFC and the parameterized physical model for 95 %, 55 %, and 35 % fuel flow ratios. Figures 3-2(c) and 3-2(d) show the behavior of the PEMFC and the parameterized physical model in response to resistive load variations. In this experiment, the electrical resistance connected to the fuel cell was varied, and the fuel flow ratio, current and voltages values were recorded. Subsequently, Matlab simulations of the parameterized physical model were performed and compared with the experimental data, which reports a satisfactory performance in the desired operation conditions.

ROVIRA I VIRGILI UNIVERSITY
FUEL CELL MODELING AND CONTROL FOR FUEL CONSUMPTION OPTIMIZATION
Carlos Andres Ramos Paja
ISBN:978-84-692-6902-2/ DL:T-1848-2009

## 3.3 Fuzzy-based modeling technique for PEMFC

The PEMFC voltage behavior mainly depends on the activation, ohmic and concentration effects. According to the models proposed by Correa et al. [2], Real et al. [23] and Pukrushpan et al. [28], these effects generate the respective voltage losses described by:

$$v_{act} = v_0 + v_a \left(1 - e^{-c_1 \cdot i}\right) \tag{3.1}$$

$$v_{ohm} = i(R_M + R_C) \tag{3.2}$$

$$v_{con} = \left(c_2 \frac{i}{i_{max}}\right)^{c_3} \tag{3.3}$$

where $v_0$ is the voltage drop at zero current density and $v_a$ and $c_1$ are constants. $R_M$ represents the equivalent resistance of the membrane, and depends on the current density, the structure of the membrane and the temperature. $R_C$ represents the resistance to the proton flow in the membrane, and is normally considered constant. Finally $c_2$, $i_{max}$ and $c_3$ are parameters that depend on the temperature and on the partial pressures of the reagents.

The PEMFC voltage is affected by a phenomenon called *charge double layer* which, as Pukrushpan, Correa and Zenith [81] propose, shows a capacitor-like charge/discharge dynamics. In addition, a change in the load current causes an immediate change in the PEMFC voltage due to the ohmic effects.

The dynamic behavior of the PEMFC voltage in response to a current transient is presented in figure 3-3, which shows the effects considered in the modeling. These effects are modeled independently in a functional form: a static model, which determines PEMFC voltage in steady-state conditions, an instantaneous ohmic effect model and a *charge double layer* effect model.

The static model affects the PEMFC voltage at any instant, determines its initial and final conditions in current and/or flow transients, and depends on the stable values of the model inputs. The instantaneous ohmic effect is a high-frequency phenomenon that only affects the PEMFC voltage when a current transient occurs. When the current reaches a new steady state, the instantaneous ohmic effect disappears and the static model determines the voltage for the new current condition. The relationship that describes the instantaneous ohmic effect is given in (3.4).

$$v_{ohmic\_inst}(t) = R_{ohmic\_inst} \cdot \Delta i_{st}(t) \tag{3.4}$$

where $v_{ohmic\_inst}(t)$ is the instantaneous voltage drop caused by this effect, $R_{ohmic\_inst}$ is the electrical resistance that models the effect, and $\Delta i_{st}(t)$ is the instantaneous PEMFC current variation. In

ROVIRA I VIRGILI UNIVERSITY
FUEL CELL MODELING AND CONTROL FOR FUEL CONSUMPTION OPTIMIZATION
Carlos Andres Ramos Paja
ISBN:978-84-692-6902-2/ DL:T-1848-2009

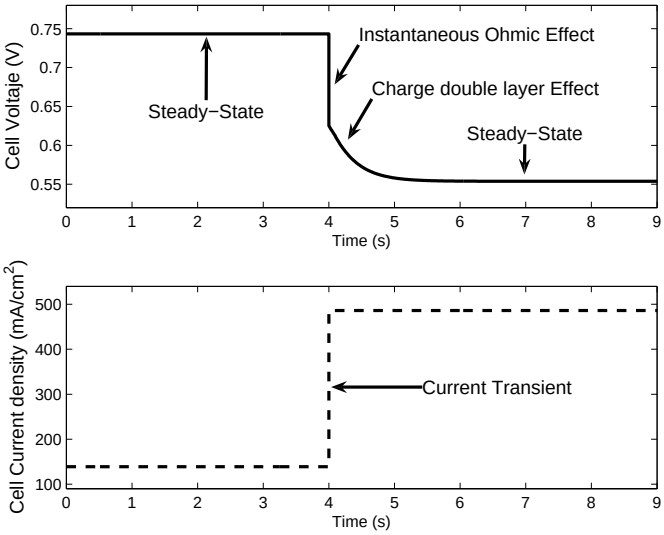


Figure 3-3: PEMFC voltage dynamic Effects.

the desired digital implementation, the stack current variation in the $k$-th sampling period $\Delta i_{st}(k)$ can be expressed in the discrete time domain as presented in (3.5).

$$\Delta i_{st}(k) = i_{st}(k) - i_{st}(k-1) \tag{3.5}$$

From (3.4) and (3.5), the discrete complex frequency-domain (or z domain) [82] representation of the instantaneous ohmic effect as a discrete transfer function $G_{ohmic\_inst}(z)$ is obtained as follows:

$$V_{ohmic\_inst}(z) = R_{ohmic\_inst} \cdot \Delta I_{st}(z) \tag{3.6}$$

$$V_{ohmic\_inst}(z) = R_{ohmic\_inst} \cdot \frac{z-1}{z} \cdot I_{st}(z) \tag{3.7}$$

$$G_{ohmic\_inst}(z) = \frac{V_{ohmic\_inst}(z)}{I_{st}(z)} = R_{ohmic\_inst} \cdot \frac{z-1}{z} \tag{3.8}$$

where $V_{ohmic\_inst}(z)$, $\Delta I_{st}(z)$ and $I_{st}(z)$ are the z domain representation of the instantaneous voltage loss, the instantaneous PEMFC current variation and the PEMFC stack current, respectively.

The capacitive effect represents the transient behavior of the PEMFC voltage in response to a current and/or fuel flow ratio transient. This capacitive effect has been modeled using a first order delay, expressed in (3.9) as a continuous-domain transfer function $G_{delay}(s)$.

$$G_{delay}(s) = \frac{V_{st}(s)}{V_{static}(s)} = \frac{1}{\tau s + 1} \tag{3.9}$$

ISBN:978-84-692-6902-2/ DL:T-1848-2009

As expressed in (3.9), $G_{delay}(s)$ gives the relationship between the PEMFC output voltage, $V_{st}(s)$, and the static model output voltage, $V_{static}(s)$, in terms of a delay time-constant $\tau$. In order to make a digital implementation, the first order delay has been expressed in the z domain using the bilinear transformation [82], [83]. The resulting discrete-domain transfer function $G_{delay}(z)$ is

$$G_{delay}(z) = \frac{V_{st}(z)}{V_{static}(z)} = K_c^* \cdot \frac{1}{\tau} \cdot \frac{z}{z - e^{-T_s/\tau}} \tag{3.10}$$

where $T_s$ is the sampling time for the processing of the discrete implementation of the fuzzy-based model, $V_{st}(z)$ and $V_{static}(z)$ are, respectively, the sampled PEMFC output voltage and the sampled static model output voltage in the z domain. $K_c^*$ is the correction factor due to the continuous-to-discrete domain transformation, which can be calculated by evaluating the transfer functions in steady state, $s \to 0$ (or $t \to \infty$) for the continuous domain and $z \to 1$ (or $k \to \infty$) for the discrete domain as follows:

$$\lim_{s\to 0} \frac{1}{\tau s + 1} = \lim_{z\to 1} K_c^* \cdot \frac{1}{\tau} \cdot \frac{z}{z - e^{-T_s/\tau}} \tag{3.11}$$

$$K_c^* = \tau \left(1 - e^{-T_s/\tau}\right) \tag{3.12}$$

$$K_c = K_c^*/\tau \tag{3.13}$$

$$G_{delay}(z) = \frac{V_{st}(z)}{V_{static}(z)} = K_c \frac{z}{z - P_d} \tag{3.14}$$

$$P_d = e^{-T_s/\tau}$$

$$K_c = 1 - e^{-T_s/\tau} = 1 - P_d$$

The discrete transfer function pole [82], $P_d$, defines the discrete delay behavior in (3.14), and depends on the time-constant $\tau$ of the continuous delay transfer function and on the sampling-time $T_s$ of the discrete implementation. A normalized gain compensation factor $K_c$ is defined in (3.13) with the convenient characteristic of being a simple function of the discrete transfer function pole, as is expressed in (3.14). This property is important, since it reduces the required number of calculations and makes it possible to omit this discrete gain compensation from the identification process.

It should be pointed out that the PEMFC voltage is only affected by the instantaneous ohmic effect for a current transient, and not for a fuel flow ratio transient. Summarizing the effects modeled, the discrete transfer function for the PEMFC voltage in the z domain is presented in (3.15).

$$V_{st}(z) = G_{delay}(z) \cdot V_{static}(z) - G_{ohmic}(z) \cdot I_{st}(z) \tag{3.15}$$

ISBN:978-84-692-6902-2/ DL:T-1848-2009

For a practical implementation, a discrete time domain difference equation is required as follows:

$$v_{st}(k) = P_d \cdot v_{st}(k-1) + K_c \cdot v_{static}(k) - R_{ohmic\_inst} \cdot \Delta i_{st}(k) \tag{3.16}$$
$$K_c = 1 - P_d$$
$$\Delta i_{st}(k) = i_{st}(k) - i_{st}(k-1)$$

where $v_{st}(k)$ is the PEMFC voltage, $v_{static}(k)$ is the after-transient static model output voltage, $i_{st}(k)$ is the current in the present sampling period and $i_{st}(k-1)$ is the current in the immediate previous sampling period, respectively.

The difference equation presented in (3.16) describes the behavior of the PEMFC voltage in the transitions between steady-states determined by a static model. Likewise, the delay model and the instantaneous ohmic effect model have parameters that depend on the operating conditions of the PEMFC. Both the model and its parameters change dynamically as non-linear functions of the physical variables that affect the PEMFC behavior. Some of the common physical variables considered in this analysis are the operating temperature, the fuel and oxidant stoichiometric ratio, humidity, etc. This study proposes three Fuzzy-Anfis models to model the steady-state behavior of the PEMFC, and the variation of the dynamic model parameters in response to changes in the physical variables that govern its behavior.

The first one models the steady-state (or static) behavior of the PEMFC (3.17), and uses the temperature, humidity and other conditions to predict the polarization curves. The second one models the time-constant $\tau$ of the first-order delay model in terms of the pole $P_d$ (3.18), and the third one models the instantaneous ohmic effect with the resistance $R_{ohmic\_inst}$ (3.19).

$$v_{static}(k) = Fm_{static}(mi_1, mi_2, ...mi_n) \tag{3.17}$$
$$P_d = Fm_{delay}(mi_1, mi_2, ...mi_n) \tag{3.18}$$
$$R_{ohmic\_inst} = Fm_{ohmic\_inst}(mi_1, mi_2, ...mi_n) \tag{3.19}$$

$Fm_{static}$, $Fm_{delay}$ and $Fm_{ohmic\_inst}$ are the Fuzzy-Anfis models for the static behavior, the pole delay and the ohmic effect resistance, respectively. The model inputs are represented by the signals $mi_1, mi_2, ...mi_n$.

The block diagram of the proposed PEMFC voltage fuzzy-based technique is presented in figure 3-4, where the three Fuzzy-Anfis models described in (3.17), (3.18) and (3.19), and the implementation of the difference equation (3.16) can be observed. It is also noteworthy that the PEMFC current is taken as an input, because it defines the steady-state of the polarization curve and affects the other fuzzified parameters. The other model inputs depend on the implementation of the PEMFC and ancillary regulation systems considered (temperature regulation, humidity control, etc.).

ISBN:978-84-692-6902-2/ DL:T-1848-2009

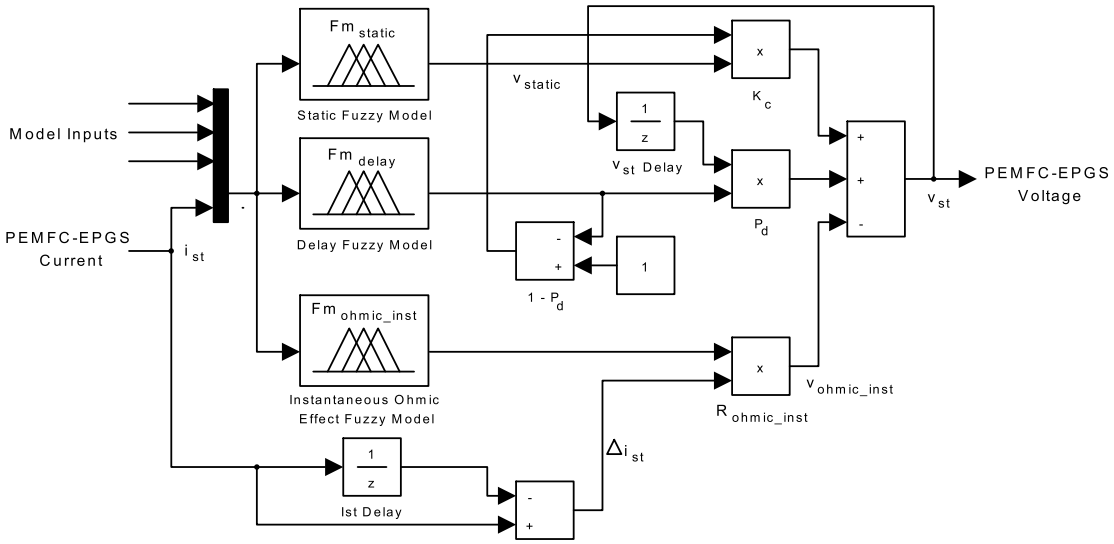


Figure 3-4: Fuzzy-based model Block Diagram.

### 3.3.1 Example of an application of the fuzzy-based modeling technique to a user-designed PEMFC

The proposed fuzzy-based modeling technique has been applied to the user-designed PEMFC presented in section 3.2.1. The operating conditions of this PEMFC consider a temperature regulation strategy, humidity control, and the regulation of the reagent pressure ratio. Therefore, only variations in the fuel flow ratio and electric current have been considered in this example.

The ANFIS training and evaluation iterative processes used to identify the three T-S fuzzy models was based on the procedures presented by Yang et al. [74] and Entchev et al. [75], who used a physical model to generate the data sets required. To evaluate the performance of the fuzzy-based model, the *root mean square error (RMSE)* [84] given in (3.20) and the previously presented *mean relative error (MRE)* (2.38) were used, where $m_j$ and $f_j$ represents the data sets compared and $N$ the number of samples.

$$RMSE(\%) = 100 \times \sqrt{\frac{1}{N}\sum_{j=1}^{N}(m_j - f_j)^2} \tag{3.20}$$

The size of the training sets was increased until both criteria reached performances under 10 % in the static and dynamic behavior. The training and validation of the static Fuzzy-Anfis model was the most demanding. It required a matrix of 130000 static data, of which 75000 were used to train the static Fuzzy-Anfis model $Fm_{static}$ and 55000 were used for the validation step. A small matrix of 200 first-order-delay poles and instantaneous-ohmic resistances pair values were required. From

ISBN:978-84-692-6902-2/ DL:T-1848-2009

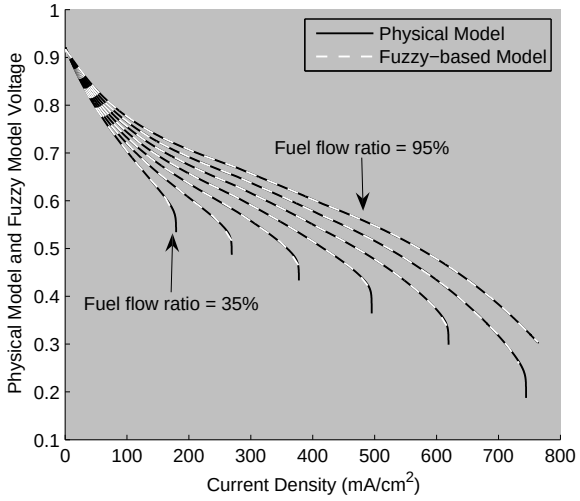


Figure 3-5: Fuzzy-based model polarization curves for 95 %, 85 %, 75 %, 65 %, 55 %, 45 % and 35 % fuel flow ratios.

this matrix, 110 data sets were used to train the $Fm_{delay}$ and $Fm_{ohmic\_inst}$ Fuzzy-Anfis models and 90 were used for validation purposes. The RMSE and MRE obtained are presented in table 3.1.

Table 3.1: Fuzzy-based model performance evaluation.

| Criteria | Static Data | Dynamic Data |
|---|---|---|
| *RMSE* | 3.15 % | 9.93 % |
| *MRE* | 0.29 % | 9.07 % |

### 3.3.2 Simulation Results

To complete the performance evaluation given by the RMSE and MRE criteria, several simulations were made of the user-designed PEMFC voltage model obtained with the proposed fuzzy-based technique. Subsequently, the fuzzy-based and physical models responses to current and fuel flow ratio transients were compared.

The response of the static Fuzzy-Anfis model $Fm_{static}$ has a RMSE of 3.15 % and a MRE of 0.29 %, and this results in the indistinguishable difference between the polarization curves of the parameterized physical and fuzzy-based models (see figure 3-5), which take into account several fuel flow ratios.

The dynamic behavior of the fuzzy-based model was evaluated with the performance criteria of table 3.1, and completed with the simulations presented in figure 3-6. The current profile presented in figure 3-6(a) was used to evaluate the response of the model. This current profile has step, ramp and stable zones, which make it possible to evaluate the fuzzy-based model response in a wide frequency range of current transients. The fuzzy-based and physical model responses are compared

ROVIRA I VIRGILI UNIVERSITY
FUEL CELL MODELING AND CONTROL FOR FUEL CONSUMPTION OPTIMIZATION
Carlos Andres Ramos Paja
ISBN:978-84-692-6902-2/ DL:T-1848-2009

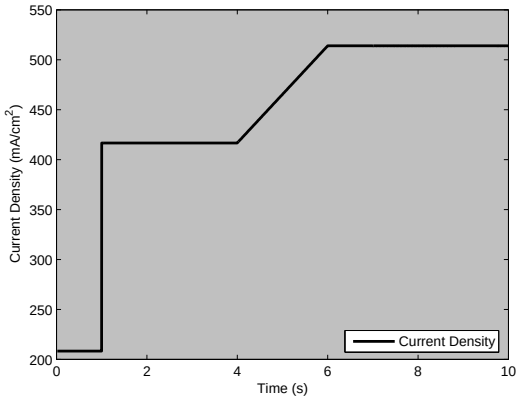


(a) Current density transients.

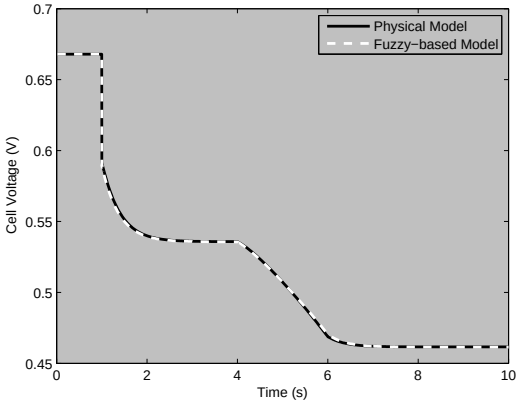


(b) Fuzzy-based model response to current transients in (a).

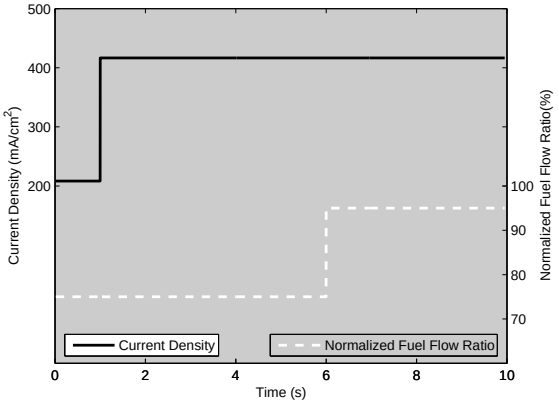


(c) Current density and fuel flow transients.

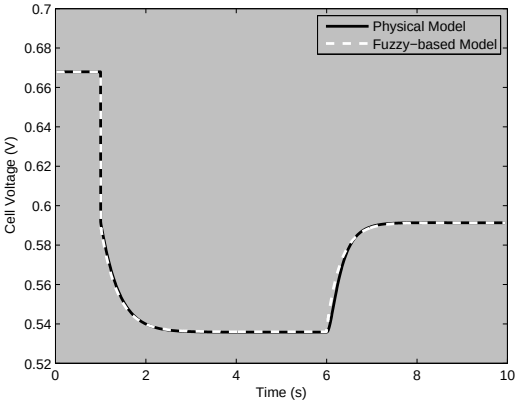


(d) Fuzzy-based model response to transients in (c).

Figure 3-6: Fuzzy-based model dynamic behavior evaluation.

in figure 3-6(b). The proposed fuzzy-based model performs satisfactorily in all the current transient conditions.

The step changes in the current and fuel flow ratio in figure 3-6(c) were used to demonstrate that the instantaneous ohmic effect only affects the PEMFC voltage in current transients (see figure 3-6(d)). When the fuel flow ratio changes and the current remains constant, the fuzzy-based model exhibits a slightly increase in the prediction error, but the approximation to the physical model remains satisfactory.

ISBN:978-84-692-6902-2/ DL:T-1848-2009

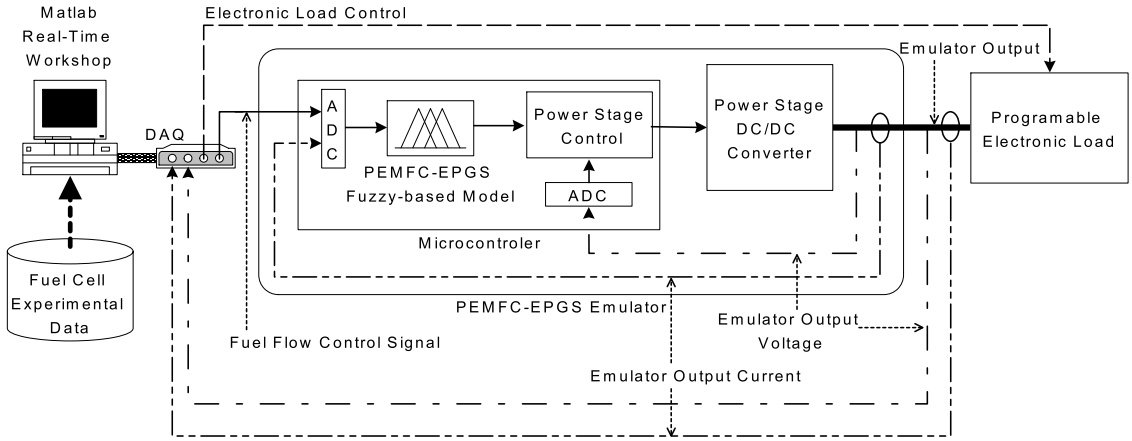


(a) PEMFC Emulator and Test System Structure.

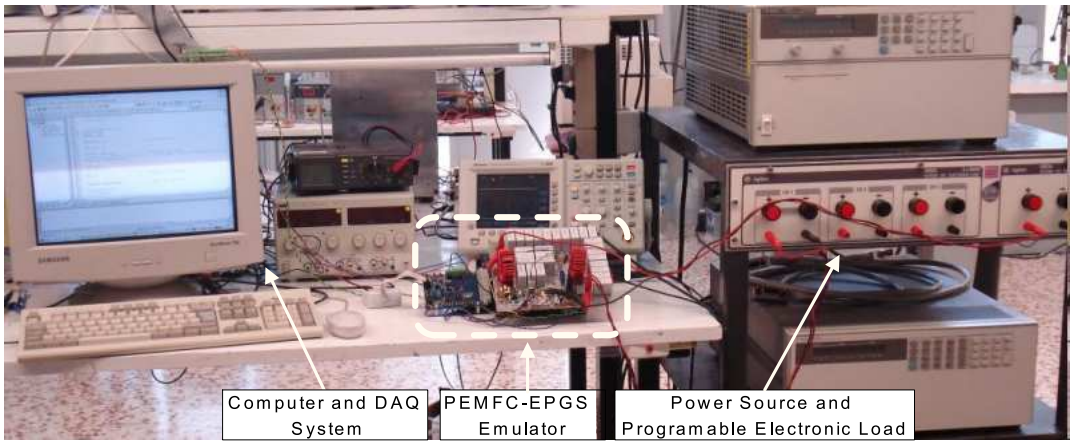


(b) PEMFC Emulator and Test System photography.

Figure 3-7: PEMFC Emulator and Test Equipment.

## 3.4 Fuel cell emulator

One of the main objectives of the fuzzy-based modeling technique proposed is to develop low-cost PEMFC emulators. The particular application of the fuzzy-based modeling technique presented in section 3.3.1 is implemented in an emulator, and its real-time behavior is validated by means of experimental data.

### 3.4.1 Fuzzy-based emulator structure and test system

In this implementation, the fuzzy-based model defines the output voltage of a PEMFC Electrical Power Generation System (PEMFC-EPGS) emulator, which is presented with the emulation test system in figure 3-7. The experimental system scheme and a photograph are shown in figures 3-7(a) and 3-7(b), respectively. This topology uses experimental data recorded by the fuel cell test system presented in section 3.2.1 (figure 3-1) in order to excite the emulator with the same

ISBN:978-84-692-6902-2/ DL:T-1848-2009

physical magnitudes measured in the fuel cell prototype. This makes it possible to perform a realistic comparison of the output voltages.

The emulator was developed using a low-cost microcontroller and a power stage. The PEMFC fuzzy-based model was implemented in the microcontroller, and it defines the voltage reference for the digital control system of the power stage. Also, the Fuzzy-Anfis systems of the fuzzy-based model were implemented using three look-up tables, and the model inputs and feedback signals were acquired through analog-to-digital converters (ADC) available in the microcontroller. The numerical methods for the real-time implementation of the model states and control systems were selected following the evaluation of fixed-step differential equations solution methods for real-time simulation and emulation described in appendix B.

**Power Stage**

The power stage was implemented using a step-down two-inductors DC/DC switching converter introduced by Tymerski et al. in [85]. This DC/DC converter makes it possible to drive the output voltage to positive and negative levels using a unipolar power source, which reduces the size of the emulator and its requirements without a considerable increment in the complexity of the control design. In this converter, high voltage-low current conditions are achieved with duty cycles near to 50 %, and in a nominal condition of 12 V input voltage and 5 V output voltage, defined in the middle of the desired emulator voltage range, the duty cycle is approximately 63 % (switching frequency of 100 kHz).

Figure 3-8 shows the circuit scheme of the proposed switching power stage, which is based on an unipolar output voltage implementation of the two-inductor step-down DC/DC switching converter. This switching converter is able to provide high currents at voltages near to zero volts, and low currents at voltages close to the input supply $V_g$, and is regulated by a common designed linear controller. Disregarding losses, the set of differential equations that describes the DC/DC converter dynamics are

$$\frac{di_{L_r}}{dt} = \frac{V_g \cdot (1-D) - v_{C_r} \cdot D}{L_r} \tag{3.21}$$

$$\frac{di_L}{dt} = \frac{-v_{Cr} \cdot (1-D) + V_g \cdot D - v_C}{L} \tag{3.22}$$

$$\frac{dv_{C_r}}{dt} = \frac{i_L \cdot (1-D) + i_{L_r} \cdot D}{C_r} \tag{3.23}$$

$$\frac{dv_C}{dt} = \frac{i_L - v_C/(R_{Load})}{C} \tag{3.24}$$

$$v_o = v_C \tag{3.25}$$

where $D$ represents the duty cycle. Due to the unipolar implementation of the converter, the steady-

ISBN:978-84-692-6902-2/ DL:T-1848-2009

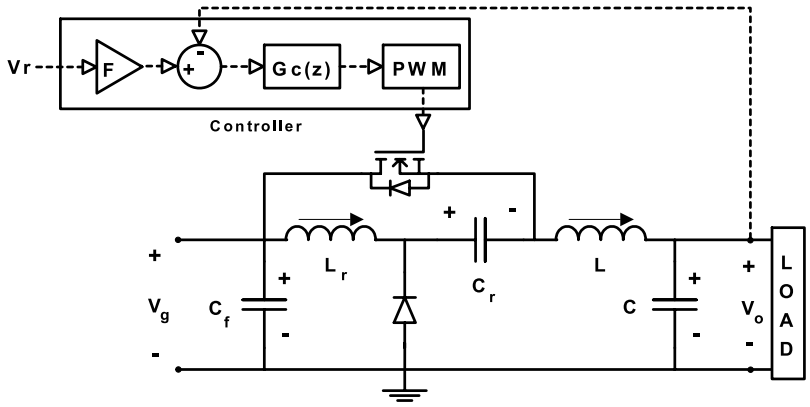


Figure 3-8: Circuit scheme of the step-down two-inductor DC/DC converter used in the power stage.

state voltage gain in continuous conduction mode is

$$V_o = \frac{2D-1}{D} V_g, \quad 0.5 \leq D \leq 1 \tag{3.26}$$

The electrical parameters of the implemented DC/DC switching converter are $\mathsf{C_f} = 400\ \mu\mathsf{F}$, $\mathsf{L} = 140\ \mu\mathsf{H}$, $\mathsf{C} = 15\ \mu\mathsf{F}$, $\mathsf{L_r} = 140\ \mu\mathsf{H}$, $\mathsf{C_r} = 200\ \mu\mathsf{F}$, and its switching frequency is $100\ \mathsf{kHz}$. The supply voltage range required is between 14 V and 18 V, and the maximum output current, voltage and power are restricted to 12 A, 12 V and 100 W, respectively, with a conversion efficiency of 80 %.

Table 3.2: Operating point specifications.

| Specification | Value |
|---|---|
| $V_g$ | 12 V |
| $V_o$ | 5 V |
| Output power | 100 W |
| Switching frequency | 100 kHz |
| D | 63 % |
| Sampling time | 10 $\mu$s |

From equations (3.21) to (3.25), the discrete control-to-output transfer function [82] [86] for the DC/DC converter, at the operating point described in table 3.2 and with the previous set of parameters, can be expressed as

$$G_p(z) = \frac{0.756z^3 - 0.8185z^2 - 0.571z + 0.6513}{z^4 - 3.584z^3 + 4.843z^2 - 2.929z + 0.6703} \tag{3.27}$$

From this model, a digital control system for the power stage was designed and implemented in the same emulator microcontroller to regulate the DC/DC switching converter output voltage. The digital controller $G_c(z)$ given in (3.28) defines the duty cycle applied to the MOSFET by a microcontroller PWM module (see figure 3-8). This controller was designed to achieve a phase

ROVIRA I VIRGILI UNIVERSITY
FUEL CELL MODELING AND CONTROL FOR FUEL CONSUMPTION OPTIMIZATION
Carlos Andres Ramos Paja
ISBN:978-84-692-6902-2/ DL:T-1848-2009

margin of 61.8° and a gain margin of 10.9 dB.

$$G_c(z) = \frac{0.7636z - 0.4416}{z + 0.7323} \tag{3.28}$$

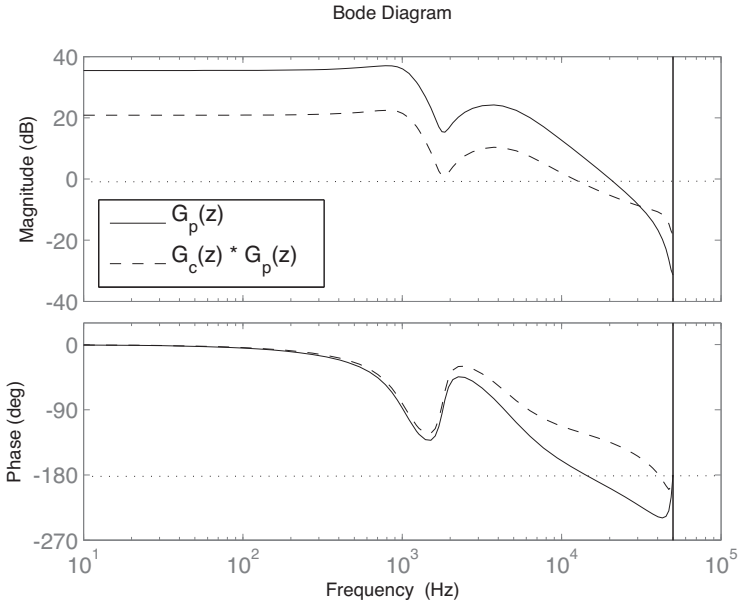


Figure 3-9: DC/DC Converter open loop and control loop frequency response.

The frequency responses of the open loop ($G_p(z)$) and control loop ($G_c(z) \cdot G_p(z)$) are depicted in figure 3-9: they confirm the closed loop stability. The digital control system also incorporates a prefilter F, which was adjusted to F=1.0907 to achieve a closed loop DC gain equal to one and, therefore, null steady state error. The controller also generates a closed loop power stage bandwidth of 1.82 kHz, which ensures that the fuel cell model reference can be tracked, since from the parameterized simulation model and prototypes experimental data, a 700 Hz bandwidth in the fuel cell voltage dynamics was identified. It can be mainly attributed to the air compressor time constant. This compressor time constant oscillates between 1.5 ms and 1 s according to the mathematical models and experimental measurements, this depending on the compressor power, technology and load. Also, from the model proposed in chapter 2, and Pukrushpan and Real models, it is deduced that the main fuel cell dynamics are caused by the compressor and manifolds.

Therefore, this controlled power stage makes it possible to follow the voltage reference defined by the fuzzy-based model with an output voltage ripple of 100 mV.

ISBN:978-84-692-6902-2/ DL:T-1848-2009

**Computational Load Analysis**

Because the fuzzy-based model was implemented using look-up tables, fewer calculations are needed than for computing the physical model. This means that computation is faster and the microcontroller, which process the control system of the power stage and the PEMFC fuzzy-based voltage model, is used efficiently. The power stage control system takes 23 $\mu$s of processing time and the fuzzy-based model computation requires 96 $\mu$s. To give a comparison, the computation of the physical model takes a minimum of 1.32 ms and its calculation time depends on the internal states of the physical model, which makes it non predictable and unsuitable for real-time applications.

### 3.4.2 Experimental Validation

To evaluate the behavior of the emulator, an electronic load controlled by a computer with Matlab's Real-Time Workshop and a data acquisition system (DAQ) was used to modify the emulator output current. The computer also defines the control signal for the fuel flow ratio of the emulator, thus controlling the fuzzy-based model inputs. The output current and voltage of the emulator have been stored in a database for analysis and comparison with previously recorded PEMFC experimental data.

The emulator can reach voltage values between 0 V and 12 V and current values between 0 A and 12 A. Because of these specifications, the emulator can represent PEMFC with stack sizes between 1 and 12 parameterized cells. The emulator dynamics were evaluated by simulations and emulations of a PEMFC with a stack of 12 cells in series. This configuration was selected because it demands maximum power from the emulator and makes it possible to evaluate its behavior in the most critical conditions.

The behaviors of the physical model and the emulator in response to current transients are presented in figure 3-10(a), which shows satisfactory emulator dynamics in the real-time processing of the fuzzy-based model. In figure 3-10(b), the performance of the emulator in response to variations in the current and fuel flow ratio is presented and, again, it is observed that the behavior of the fuzzy-based emulator is in agreement with the physical model, the only difference being a 100 mV voltage ripple in the emulator output caused by the switching component in the power stage.

To validate the emulator, its behavior was compared with static and dynamic PEMFC experimental data corresponding to 12 cells in series ($Cellx12$). The $Cellx12$ and emulator polarization curves of figure 3-10(c) show a good correlation between plots. To evaluate the dynamic behavior of the emulator, its current was adjusted to reproduce that which had been recorded in the dynamic experiment made with the real PEMFC. Figure 3-10(d) shows the experimental current (bottom,

ISBN:978-84-692-6902-2/ DL:T-1848-2009

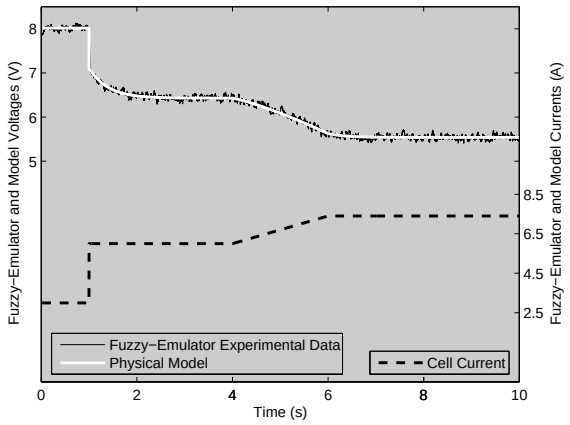


(a) Fuzzy-Emulator dynamic response to current transient.

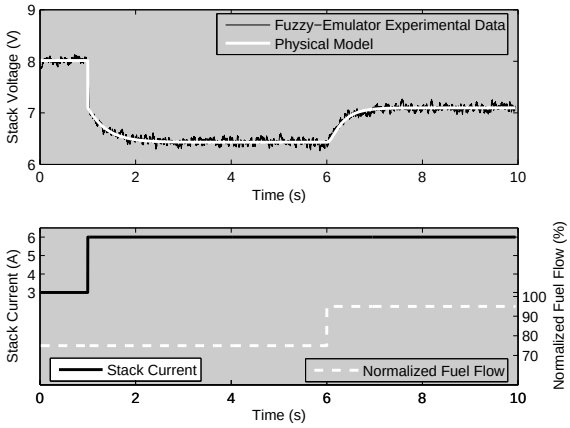


(b) Fuzzy-Emulator dynamic response to current and fuel flow transients.

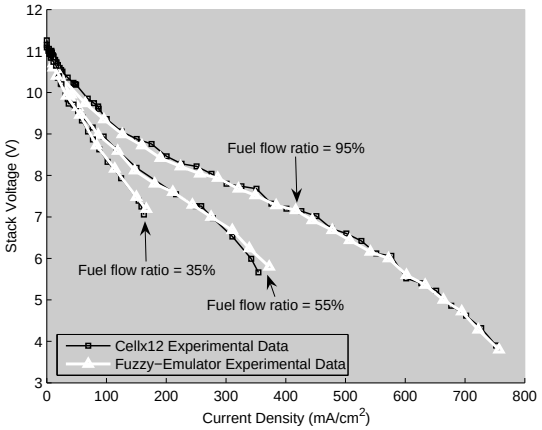


(c) Fuzzy-Emulator Polarization Curve.

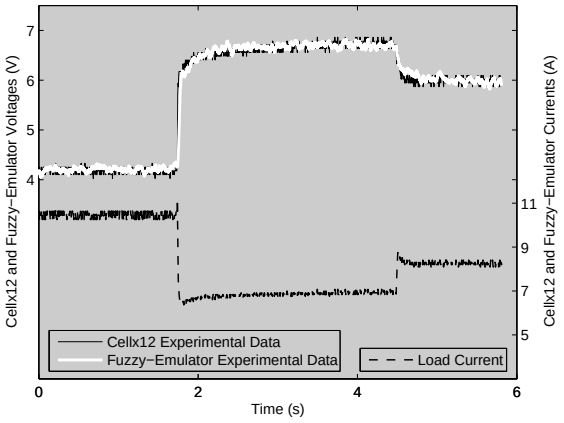


(d) Fuzzy-Emulator dynamic response to experimental current data.

Figure 3-10: Fuzzy-Emulator static and dynamic evaluation.

dashed-black trace), the experimental voltage (top, black trace) and the emulated output voltage (top, white trace). Again, the reproduction of the real PEMFC output voltage by the emulator is excellent.

The experiments carried out demonstrate that the fuzzy-based model designed with the proposed technique reproduces the physical model's behavior quite accurately and that its implementation in a low-cost microcontroller is a practical option to develop a PEMFC emulator. Also, the small-calculation implementation of the fuzzy-based model, based on a discrete representation, do not produce significant discrepancies.

ROVIRA I VIRGILI UNIVERSITY
FUEL CELL MODELING AND CONTROL FOR FUEL CONSUMPTION OPTIMIZATION
Carlos Andres Ramos Paja
ISBN:978-84-692-6902-2/ DL:T-1848-2009

## 3.5 Evaluation of switching and linear power stages for PEMFC emulation

The first step in the emulation of physical systems is to define the implementation characteristics of the emulator by taking into account the application and objective. A choice must also be made about the emulator actuator or power stage implementation, which interacts with electrical loads: the two options are switching or linear power systems. In fuel cell emulation, switching power stages are commonly used because they have high electrical efficiency [87], but in the emulation of such other electrical systems as batteries [88] linear power systems are chosen due to their simplicity. This section presents power stages intended to interact with the electrical loads being tested, each of which exhibiting low cost, energy efficiency or power scalability characteristics; the advantages and drawbacks of switching and linear power stages in fuel cells emulation are also analyzed.

### 3.5.1 Emulator structure revision

The hardware structure of the PEMFC emulator mixes a digital processing system and an electrical power stage. In this new implementation, the emulation algorithm is implemented in a Silabs C8051F120 low-cost microcontroller, which processes in real-time the PEMFC model and generates the control signal for the power stage.

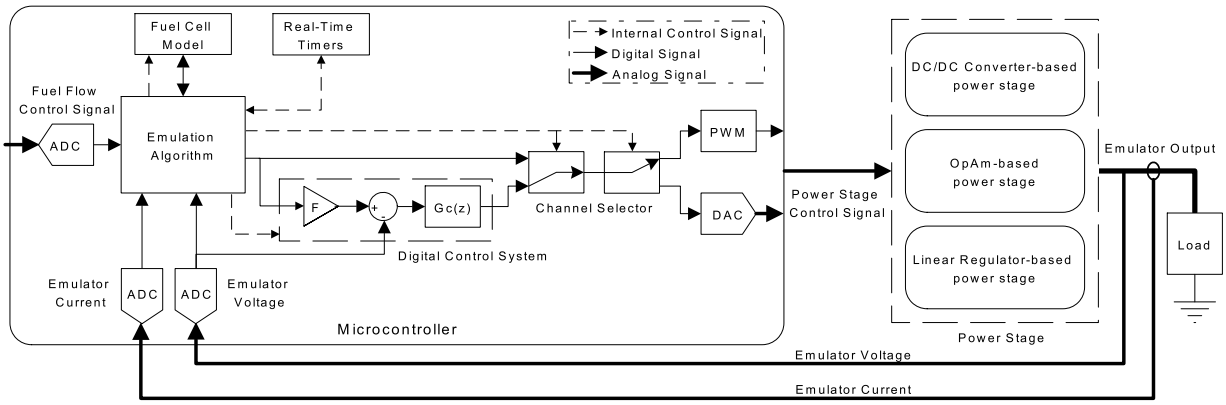


Figure 3-11: Revised PEMFC emulation system structure.

Figure 3-11 depicts a revision of the PEMFC emulator structure presented in section 3.4 in great detail. The requirements for processing the model responses and the power stage control in real-time involve restricting the calculation time so that the sampling time can be guaranteed. This problem was solved by using real-time timers to control the execution period of the digital loops. The system has an emulation algorithm that controls the acquisition of the emulator inputs, the processing of

ISBN:978-84-692-6902-2/ DL:T-1848-2009

the fuel cell model and the power stage, and it also allows to choose the right power stage driver. The emulation algorithm initializes the real-time timers that generate interruptions when the execution periods have been completed. This implementation has two different sampling periods: one for the power stage control system and the other for the emulator output voltage refresh. The emulation algorithm also controls a channel selector that permits to avoid the digital control system in order to interact with power stages that could have their own control system. The emulation system also makes it possible to produce an analog control signal or a pulse width modulated (PWM) control signal. This is useful for controlling different implementations of switching or linear power stages.

In the emulation system linear and non-linear digital control strategies can be implemented. The power stage control signal (analog or PWM) is generated by using two control algorithms. First, an internal loop is implemented with a digital control system designed to track the voltage reference generated by the emulation algorithm, which in figure 3-11 consists of a prefilter (F) and a linear compensator ($G_C(z)$), but the emulator allows the use of any linear and non-linear discrete control approach. Second, the emulation algorithm acts as a supervisory control loop that generates the voltage reference for the internal loop using the emulator inputs and fuel cell model.

The emulation algorithm is processed inside the microcontroller with a sampling time of 10 $\mu$s, where the power stage controller sampling time is automatically adjusted to 10 $\mu$s or 100 $\mu$s depending on the output channel (PWM or analog, respectively) because of the maximum sampling time allowed by the digital-to-analog converter (DAC). The fuel cell model is also computed with a fixed step of 100 $\mu$s, and the stack internal states and ancillary systems are satisfactorily reproduced.

From the analyses of the model proposed in section 2, and Pukrushpan and Real models, it is deduced that the main fuel cell dynamics are due to the compressor and manifolds (constraining the fuel cell voltage dynamics up to 700 Hz), and that the electrochemical reactions have time constants between 10 and 20 orders of magnitude less than the compressor and manifolds ones [28]. Therefore, they are considered to be static relations in the models. Likewise, the hydrogen and air manifold equations exhibit time constants in the order of milliseconds, so the water membrane content dynamics depends on the electrochemical static equations and on the oxygen and hydrogen mass flow dynamics, which also depends on the compressor and manifold time constants. The effectiveness of different fixed-step differential equations solution methods for fuel cell model real-time processing have been analyzed in appendix B, and the relation between sampling time and processing load has been evaluated. The fuel cell model inside the microcontroller, then, is processed with a sampling time of 100 $\mu$s using the Euler integration method, and the agreement with the Matlab variable-step simulation results and with the experimental measurements is satisfactory.

ISBN:978-84-692-6902-2/ DL:T-1848-2009

### 3.5.2 Power stage analysis

Switching and linear power stages have been designed with different characteristics, and compared in fuel cell emulation conditions. The first power stage is the one described in section 3.4.1. It is based on a two-inductor step-down DC/DC converter, while the second and third power stages are based on operational amplifiers and integrated linear regulators, respectively.

#### DC/DC converter-based power stage

The DC/DC converter-based power stage, described in section 3.4.1, has an output voltage ripple of 100 mV. It affects the voltage defined by the fuel cell model that does not predict voltage ripple in free ripple load current. It should be pointed out that experimental fuel cell voltage exhibits ripple caused by the air supply regulation system (see section 2.8), but the high frequency voltage ripple caused by this switching power stage is not directly comparable with the fuel cell voltage ripple in terms of frequency components and power.

#### Operational amplifier-based power stage

This linear power stage was designed using power operational amplifiers (OpAm). The OpAm selected for this implementation was the OPA549 from Texas Instruments. It supports a maximum continuous output current of 8 A and current peaks up to 10 A. This OpAm can also be supplied with one polarity voltage and has a wide range of output voltage. To make this linear power stage comparable with the switching power stage, a nominal output current of 14 A is required, which means that two OpAms must be parallelized. Although the connection was made using the configuration recommended by the manufacturer, the practical implementation had some problems in current sharing due to differences in the impedances of the paths. The electrical resistance of the connectors and cables also affects the current paths and, therefore, the current balance. To solve this problem, a practical voltage follower in master-slave configuration with equalization resistances was used. The scheme of the linear power stage based on the OPA549 OpAm is given in figure 3-12.

In this circuit, the equalization resistors $R_z$ guarantee current sharing whereas the variable resistors $R_s$ minimize the unbalance in each individual current. On the other hand, the equalization resistances cause a steady-state error in the output voltage. Although $R_z$ is small (0.1 $\Omega$), it generates voltage drops at high currents when the emulator voltage is low and comparable with that undesired drops.

The OPA549 has an open loop voltage gain of 110 dB and a Gain Bandwidth Product equal to 0.9 MHz, and from its frequency response [89], the continuous poles $P_1 = 1.351 \times 10^7$ rad/s and $P_2 = 32.26$ rad/s that model its open loop voltage response were defined. The pole $P_1$ is out of

ISBN:978-84-692-6902-2/ DL:T-1848-2009

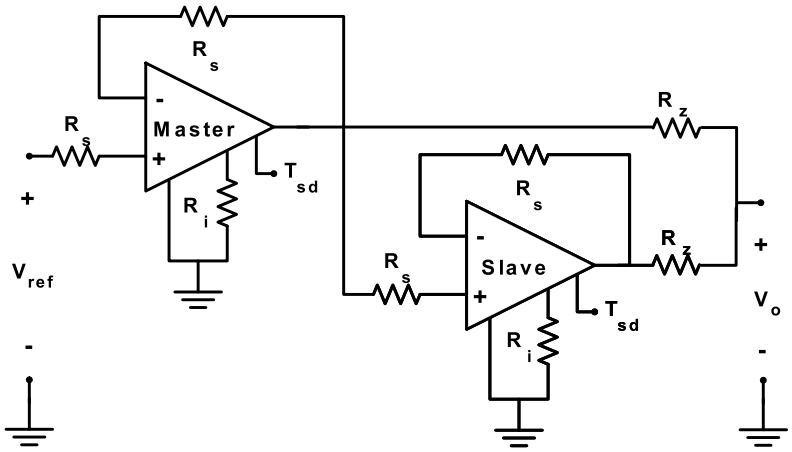


Figure 3-12: OpAm-based power stage scheme.

the frequency range of interest ([0, 100] kHz), and therefore the continuous model of the OPA549 open loop voltage response can be approximated by (3.29), where $V_i(s)$ and $V_o(s)$ are the input and output voltages, respectively.

$$G_{OPA549}(s) = \frac{V_o(s)}{V_i(s)} = \frac{1.566 \times 10^7}{s + 32.26} \tag{3.29}$$

In order to design a control strategy to compensate the voltage losses caused by the equalization resistors $R_z$, the maximum $R_z$ voltage drop was calculated by taking into account the OPA549 voltage supply ($V_g$) and the maximum allowed load current $I_{Lm}$ and power dissipation $W_m$. The relation $K_{vd}$ between the $R_z$ voltage drop $v_{Rz}$ and the OPA549 output voltage $v_o$ is calculated as follows:

$$K_{vd} = \frac{v_{Rz}}{v_o} = \frac{R_z \cdot I_{Lm}}{V_g - \dfrac{W_m}{I_{Lm}}} \tag{3.30}$$

Considering the specifications of the OPA549 ($W_m = 90$ W, $I_{Lm} = 8$ A), a supply voltage of 15 V, and the selected Rz (0.1 Ω), the maximum voltage drop allowed in the equalization resistors $R_z$ is equal to 21.33 % of the OPA549 output voltage ($K_{vd} = 0.2133$).

The transfer function of the OPA549 closed loop configuration in figure 3-12 is given in (3.31), and considering the $R_z$ voltage drop, the steady state error of the OPA549 - $R_z$ loop ($G_{OPA549_{CL}}(s) - K_{vd}$) is equal to $K_{vd}$.

$$G_{OPA549_{CL}}(s) = \frac{G_{OPA549}(s)}{1 + G_{OPA549}(s)} = \frac{1.566 \times 10^7}{s + 1.566 \times 10^7} \tag{3.31}$$

ISBN:978-84-692-6902-2/ DL:T-1848-2009

A Proportional-Integral (PI) controller was designed to compensate the $R_z$ voltage drop (null steady state error) and to obtain a closed loop bandwidth of 2 kHz, which ensures the capability to track the fuel cell model reference. This controller was digitized with a sampling time of 100 $\mu$s so that it could be implemented in the emulation topology of figure 3-11, and its transfer function is given in (3.32). The prefilter F in figure 3-11 was set to F=1.

$$G_c(z) = \frac{1.285}{z-1} \tag{3.32}$$

In this implementation, the electric currents requested by the load and by the OpAms operation are provided in series by the power supply, and because of the input-output voltage difference, this means that the electrical efficiency of the power stage is low and the power supply requirement is high. The most critical limitation occurs in the thermal behavior of the OpAms when high current at low voltages are requested because high power must be dissipated in the devices. The OPA549 has a thermal shutdown protection that disables the output power when the junction temperature reaches 160 $^o$C and re-enables it at 140 $^o$C, thus providing a safety margin below the maximum junction temperature recommended of 150 $^o$C. This thermal shutdown system has a digital signal ($T_{sd}$ in figure 3-12) that drops to 200 mV when the shutdown occurs, and this was used in the experiments to determine the dissipation limits.

Considering an operating point of 28 W output power, a 15 V supply voltage and 2 V output voltage at 14 A of load current, this linear power stage will require 210 W of input power. This means that the power stage must dissipate 182 W in thermal energy, which is large enough to damage the OpAms.

Using the safe operating area for dissipation provided by the manufacturer it is possible to solve these critical cases by means of a heat sink that maintains the OpAms at low temperature. This results in a large size device which can be minimized by a forced air system, which increases the rate of air flow over the heat sink and maintains a larger temperature gradient by replacing warmed air faster than using the heat sink alone. The heat sink selected for the implementation has a nominal thermal resistance of 0.5 $^o$C/W. In order to verify the effect of the forced air system on its thermal resistance, the voltage supply of the power stage was set to 14 V and the load current to 4 A, which led to a supply current of 4.15 A and an input power of 58.1 W. Then, the output voltage ($V_o$) was sequentially changed, thus modifying the dissipated power ($DP$). This is done with the heat sink by itself and with the forced air system. The experiments recording the heat sink temperature working by itself ($T_{hsa}$) and with the forced air system ($T_{hsfa}$), as well as the ambient temperature ($T_a$). This information was used to calculate the experimental thermal resistance of the heat sink either by itself ($\theta_{hsa}$) and with the forced air system ($\theta_{hsfa}$), and to obtain the change factor of these

ISBN:978-84-692-6902-2/ DL:T-1848-2009

thermal resistances ($K_{Rt}$) so that the effect of the forced air system can be standardized. These measurements and calculations are presented in table 3.3.

Table 3.3: Effect of the forced air system in the thermal resistance of the heat sink in the OpAm-based power stage.

| $V_o$ (V) | $DP$ (W) | $T_{hsa}$ ($^o$C) | $T_{hsfa}$ ($^o$C) | $T_a$ ($^o$C) | $\theta_{hsa}$ ($^o$C/W) | $\theta_{hsfa}$ ($^o$C/W) | $K_{Rt}$ |
|---|---|---|---|---|---|---|---|
| 2.00 | 50.10 | 54.00 | 37.60 | 22.60 | 0.63 | 0.30 | 0.48 |
| 5.20 | 37.30 | 48.00 | 36.00 | 25.00 | 0.62 | 0.29 | 0.48 |
| 7.20 | 29.30 | 40.70 | 31.00 | 22.70 | 0.61 | 0.28 | 0.46 |
| 10.00 | 18.10 | 33.60 | 27.60 | 22.60 | 0.61 | 0.28 | 0.45 |

The thermal data shows that the thermal resistance of the heat sink can be reduced to 48 % or less of its value when the forced air system is used. In a practical low-voltage/high-current polarization point of a 12 cell $H_2Economy - EcoFC$ PEM fuel cell stack, the voltage is 4.78 V and the current is 9.89 A. Using the OpAm-based linear power stage with a voltage source of 15 V to emulate this electrical behavior, 101 W (50.5 W in each OpAm) needs to be dissipated. The devices have a junction-to-case thermal resistance ($\theta_{JC}$) of 1.4 $^o$C/W, and in the implementation a thermally conductive insulator providing a case-to-heat-sink thermal resistance ($\theta_{CH}$) of 0.28 $^o$C/W was used. Assuming an ambient temperature ($T_A$) of 25 $^o$C, the heat-sink-to-ambient thermal resistance ($\theta_{HA}$) needed to dissipate the required power ($PD$) at a recommended safety temperature ($T_J$) of 125 $^o$C is calculated as follows:

$$\theta_{HA} = \frac{T_J - T_A}{PD} - \theta_{JC} - \theta_{CH} \tag{3.33}$$

Expression (3.33) leads to $\theta_{HA} = 0.3$ $^o$C/W, which can be reached with the forced air system ($\theta_{hsfa}$), thus avoiding a bigger, heavier and more expensive heat sink.

Although the OpAm-based power stage has an almost zero voltage ripple, a small ripple appears (between 5 mV and 15 mV) when the power stage operates in the emulation system. This ripple is caused by noise induction in both output voltage and current sensing and affects the calculation of the fuel cell model. However, this ripple is a small portion of the ripple generated by the switching power stage (between 5 % and 15 %).

### Linear regulator-based scalable power stage

The two power stages presented above have the capacity to provide the electric power required to emulate a fuel cell system, but have a fixed maximum power. This is an important limitation when the emulator has to represent fuel cell stacks with different numbers of cells because in some cases the power stage will be over-dimensioned causing an excessively energy and space consumption,

ISBN:978-84-692-6902-2/ DL:T-1848-2009

and, in other cases, the output power will not be enough. This issue is taken into account in the design of this linear regulator-based power stage (LinReg), which shares the small voltage ripple advantage and the low electrical efficiency disadvantage of the OpAm-based power stage presented above. However, in this linear power stage its maximum output power, size and consumption can be modified. These modifications are useful when the emulator represents fuel cell stacks with different numbers of cells, and are carried out with the design of a scalable power system. The power stage has a master circuit and several slave boards so that the maximum output power can be increased depending on the application. Since this topology involves current sharing, the same master-slave technique presented in the OpAm-based power stage was used. Also, an analog control strategy regulates the output power stage voltage to track the voltage reference. Note that an analog control system is selected to test the performance of a regulation loop that does not require excessive additional hardware because it only needs a single low-power OpAm, and because it is possible to implement the master board with dual or quad OpAm chips.

Figure 3-13 shows the circuit scheme of the LinReg-based power stage, where the master and slave circuits can be observed. It should be pointed out that the circuits are simple and that standard integrated linear regulators are used, which contrast with either the specialized OpAm required in the OpAm-based power stage or with the less common two-inductor step-down DC/DC converter used in the switching power stage. The topology used in this linear power stage is based on the circuit proposed by the manufacturer of the integrated linear regulator LM338, which can drive currents up to 5 A. In this topology, equalization resistors were used in the regulator inputs in order to share the current requested by the load. This structure enables slaves to be aggregated when necessary, and the maximum output current increases by 5 A with each added slave stage. The parameters of the circuit are: $R_z = 0.1\ \Omega$, $R_a = 2\ \mathsf{k}\Omega$, $C_i = 3.3\ \mu\mathsf{F}$, $C_o = 4.7\ \mu\mathsf{F}$, $C_{si} = 1000\ \mu\mathsf{F}$, $R_{ci} = 10\ \mathsf{k}\Omega$, $R_{fb} = 10\ \mathsf{k}\Omega$ and $C_{fb} = 10\ \mathsf{nF}$.

The master and slave circuits have few components and they are all commonly-used, which makes this power stage easy and fast to replicate and modify, and a low-cost option for a linear power stage in fuel cell emulation. Also, because additional components are required for current sensing and conditioning, the analog controller for the output voltage presented in figure 3-13 is simple to implement. A dual-OpAm chip in the master board is used for this purpose, i.e., one OpAm for the current sensing conditioning and another one for the controller. An additional element introduced in this circuit is the output diode $D_o$, the functions of which is to prevent undesired current flow between the linear regulators, and to drop the output voltage below the linear regulator limit of 1.2 V. With these characteristics, the emulation algorithm shapes the channel selector of figure 3-11 to avoid the effect of the digital controller $G_c(z)$ and to drive the power stage control signal directly from the fuel cell model to the DAC.

ISBN:978-84-692-6902-2/ DL:T-1848-2009

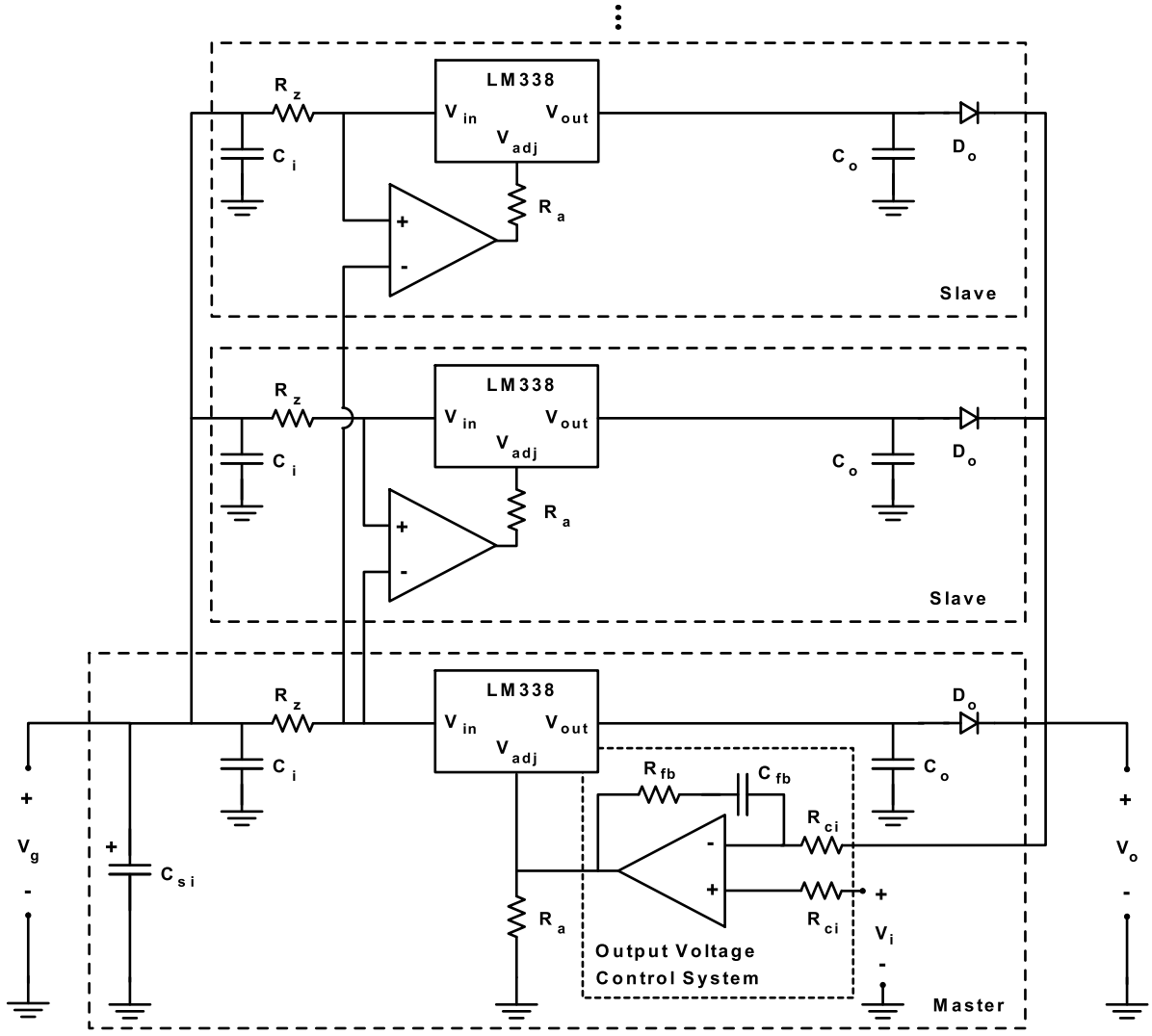


Figure 3-13: LinReg-based power stage scheme.

This linear power stage has the same disadvantage of power dissipation present in the OpAm-based power stage, and this problem can be addressed using forced air systems or current sharing until the power dissipated in each slave stage is safe. To evaluate the convenience of these possible solutions, the power dissipation capability was experimentally tested with a selected heat sink working by itself and with a forced air system. Using a heat sink with a nominal thermal resistance of 1.0 $^{o}$C/W, a voltage source of 14 V, and a load current of 2 A that generates an input current of 2.1 A (input power of 29.4 W), the output voltage was sequentially changed to modify the dissipated power ($DP$) and to measure the performance of the solutions tested. The experimental data are summarized in table 3.4 and the nomenclature is that used in table 3.3.

ISBN:978-84-692-6902-2/ DL:T-1848-2009

Table 3.4: Effect of the forced air system in the thermal resistance of the heat sink in the LinReg-based power stage.

| $V_o$ (V) | $DP$ (W) | $T_{hsa}$ ($^o$C) | $T_{hsfa}$ ($^o$C) | $T_a$ ($^o$C) | $\theta_{hsa}$ ($^o$C/W) | $\theta_{hsfa}$ ($^o$C/W) | $K_{Rt}$ |
|---|---|---|---|---|---|---|---|
| 1.00 | 27.40 | 57.20 | 35.80 | 23.20 | 1.24 | 0.46 | 0.37 |
| 3.00 | 23.40 | 52.10 | 33.70 | 23.10 | 1.24 | 0.45 | 0.37 |
| 5.00 | 19.40 | 47.40 | 32.00 | 23.40 | 1.24 | 0.44 | 0.36 |
| 7.20 | 15.00 | 41.40 | 29.90 | 23.20 | 1.21 | 0.45 | 0.37 |
| 10.00 | 9.40 | 33.20 | 26.40 | 22.60 | 1.13 | 0.40 | 0.36 |

Table 3.4 describes the same behavior observed in table 3.3, and here the forced air system reduces the thermal resistance of the heat sink to 37 % of its nominal value. Taking the same example used in the OpAm-based power stage thermal analysis, a 12 cell-stack low-voltage/high-current polarization point of 4.78 V and 9.89 A can be emulated using the heat sink either by itself or with a forced air system, and sharing the load current to ensure that each linear regulator dissipates a safe thermal power. This example considers a 15 V power source, so the electric power that must be dissipated is 101 W. To calculate the number of slave stages required the equation (3.33) is used, replacing the values of the junction-to-case thermal resistance ($\theta_{JC} = 1$ $^o$C/W) of the linear regulator, the case-to-heat-sink thermal resistance ($\theta_{CH} = 0.28$ $^o$C/W) provided by the thermally conductive insulator used in the implementation, the recommended safety junction temperature ($T_J = 125$ $^o$C) and the ambient temperature ($T_a = 25$ $^o$C). This analysis results in two possible solutions: a) for the thermal resistances of the heat sink by itself ($\theta_{hsa} = 1.24$ $^o$C/W) and b) for the forced air system ($\theta_{hsfa} = 0.46$ $^o$C/W). If the heat sink is working by itself, the system can dissipate a maximum power of 39.68 W when it reaches the maximum junction temperature recommended, which means that three linear regulators are required, each of which should be at the 85 % of its maximum junction temperature. The second option considers the use of the forced air system, so that each linear regulator can dissipate a maximum power of 57.47 W before it reaches its maximum junction temperature recommended, which means that two linear regulators need to be used, each one working at 88 % of its maximum junction temperature. This example illustrates the advantage of using the forced air system in this kind of power stage, which supplies the desired power with fewer linear regulators and, therefore, with a lower power consumption.

This LinReg-based power stage also has a small voltage ripple between 5 mV and 16 mV, which is similar to the ripple generated in the OpAm-based power stage, and just a small part of the one generated by the switching power stage (between 5% and 16%).

ISBN:978-84-692-6902-2/ DL:T-1848-2009

### 3.5.3 Power supply requirements and analysis of characteristics

An important electrical specification derived from the electrical efficiency is the power supply requirement. A critical condition in linear power regulation systems occurs when the output voltage is far from the supply voltage, because the input and output currents are similar and the difference between the input and output powers is high. This is dissipated in the device. Thus, in the emulation of a fuel cell polarization point of 2 V stack voltage and 14 A stack current, with a supply voltage of 15 V in the power stage, the output power will be approximately 28 W (disregarding losses). At this operating point, a linear power stage will require an input current approximately equal to the load current, which requires to the supply an electrical power of 210 W and results in an electrical efficiency of 13.24 %. In contrast, assuming the worst electrical efficiency of the switching power stage (60 %), the power requested from the supply by the switching power stage will be 46.67 W with an input current of 3.12 A. The difference in the electrical efficiency represents the excess power supply required by the linear power stages over the switching power stage, which in this example is 450 %, and its therefore being bigger, heavier and more expensive.

The OpAmp-based and LinReg-based power stages provide the same model tracking and output ranges as the switching power stage. The linear options require a higher power supply, but the output voltage does not exhibit appreciable voltage ripple. This is an interesting characteristic when different physical models are used in the emulator, or when different air supply systems and control strategies are emulated, each of which has its own voltage ripple pattern. Also, the voltage ripple frequency and amplitude change from one fuel cell prototype to another. The linear power stages, then, can reproduce the fuel cell voltage ripple by modeling approaches. In contrast, the switching power stage exhibits a high frequency voltage ripple, the amplitude of which is comparable with the fuel cell voltage ripple. It is, therefore, difficult to emulate the fuel cell voltage ripple with common switching power systems. This can be confusing because, in the time scale of the fuel cell dynamic response, the difference between the voltage ripples of the fuel cell and the switching power stage can be indistinguishable, but the ripple frequencies and powers are not comparable. This problem can be observed in other reported fuel cell emulators based on switching power stages [56][57][59][87][90], where their dynamic responses are considered satisfactory because the fuel cell and emulator voltage profiles are approximated equal in the time scale of the fuel cell dynamic response, but the voltage ripple is not analyzed. In the fuel cell emulators reported, the switching voltage ripple is regarded as being acceptable since it is less than 2 % of the output voltage. The switching and linear power stages proposed in this study have maximum voltage ripples of 2.5 % and 0.4 %, respectively. These conditions make it possible to compare the proposed switching power stage with other reported options in terms of electrical efficiency and fuel cell dynamic reproduction. They also reveal the improvement of the linear power stages in the capability of reproduction of the

ISBN:978-84-692-6902-2/ DL:T-1848-2009

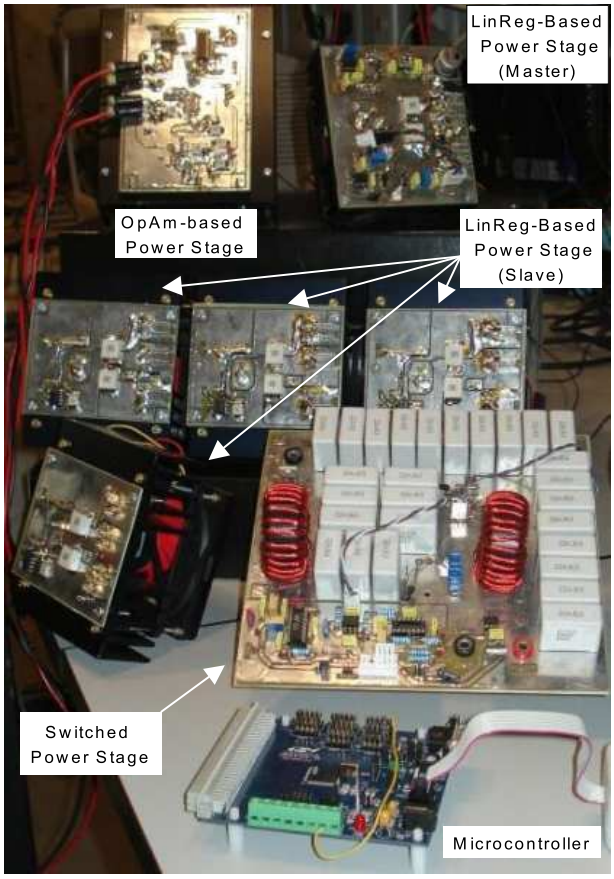


Figure 3-14: Implemented power stages and microcontroller used in the emulator.

fuel cell voltage ripple present in ripple free current conditions, this by using modelling approaches.

The LinReg-based power stage can also change its maximum output power, size and weight, which is an attractive characteristic in variable-cell stack emulation applications required in research and teaching environments. This power stage has been developed using common, low-cost electronic devices, which makes it easily reproducible, and a scalable and low-cost alternative.

In summary, the power stages presented provide the output power required to emulate a fuel cell stack with a variable number of cells. Each power stage has advantages and disadvantages, and will be selected or not depending on the application and emulation considerations. The switching, OpAmp-based and LinReg-based power stages implemented are shown in figure 3-14, which also shows the heat sinks sizes, the forced air systems and the microcontroller used in the fuel cell emulation system implementation. It can be noted that four slaves were developed for the LinReg-based power stage and, therefore, it can provide up to 25 A of load current. However, since the switching and OpAmp-based power stages can, respectively, work below 14 A and 16 A, only two slave stages have been used in the electrical behavior evaluation presented in the subsection below.

ISBN:978-84-692-6902-2/ DL:T-1848-2009

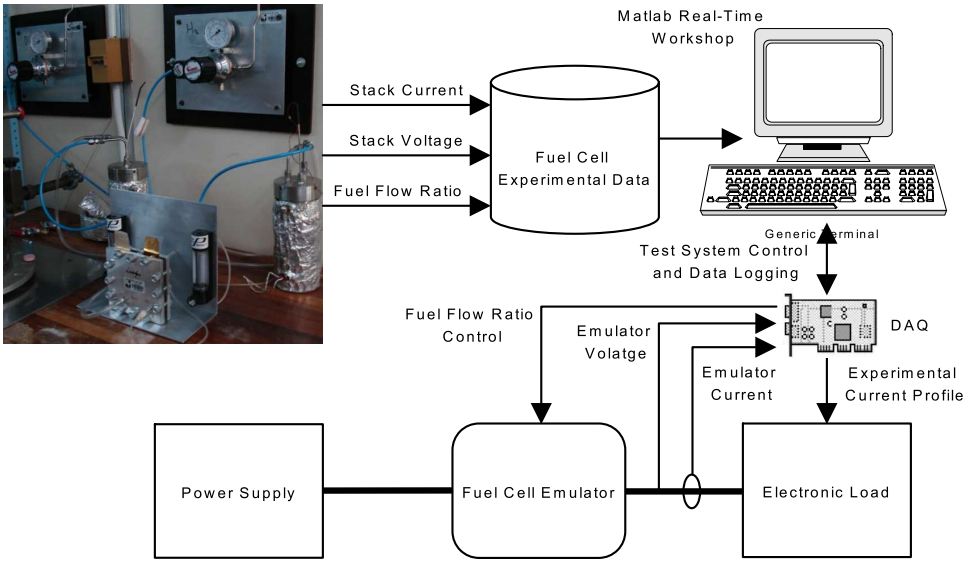


Figure 3-15: Emulator power stages test system.

### 3.5.4 Evaluation of electrical behavior

The power stage circuit schemes, design considerations and power dissipation analysis of the power stages have been presented above. The distinctive characteristics of each one have also been described and some selection guidelines have been given. But the most important characteristics of the power stages are the static and dynamic electrical behavior in the emulation of fuel cells. This electrical behavior was evaluated using the test system presented in figure 3-15.

The test system used experimental data measured from a real PEM fuel cell stack, and stored the stack current profile requested by an ECL-150 electronic load, the voltage profile from the stack and the fuel flow ratio control signal of the MTS-150 fuel cell test station. Next, using the Matlab Real-Time Workshop and a data acquisition card (DAQ), an Agilent 6050A electronic load was controlled to request the experimental current profile from the emulator and its power stages. The test system also reproduces the experimental fuel flow ratio signal so the emulator is controlled in the same conditions as in the real fuel cell prototype. The emulator voltage, current and fuel flow ratio data were stored so that the static and dynamic behavior of the emulator and its power stages could be evaluated. This system can also test the emulator and power stages under other conditions using the parameterized fuel cell model to generate current and fuel flow profiles so that the distortion in the output voltage caused by both real-time calculation of the model and power stage operation can be calculated.

ISBN:978-84-692-6902-2/ DL:T-1848-2009

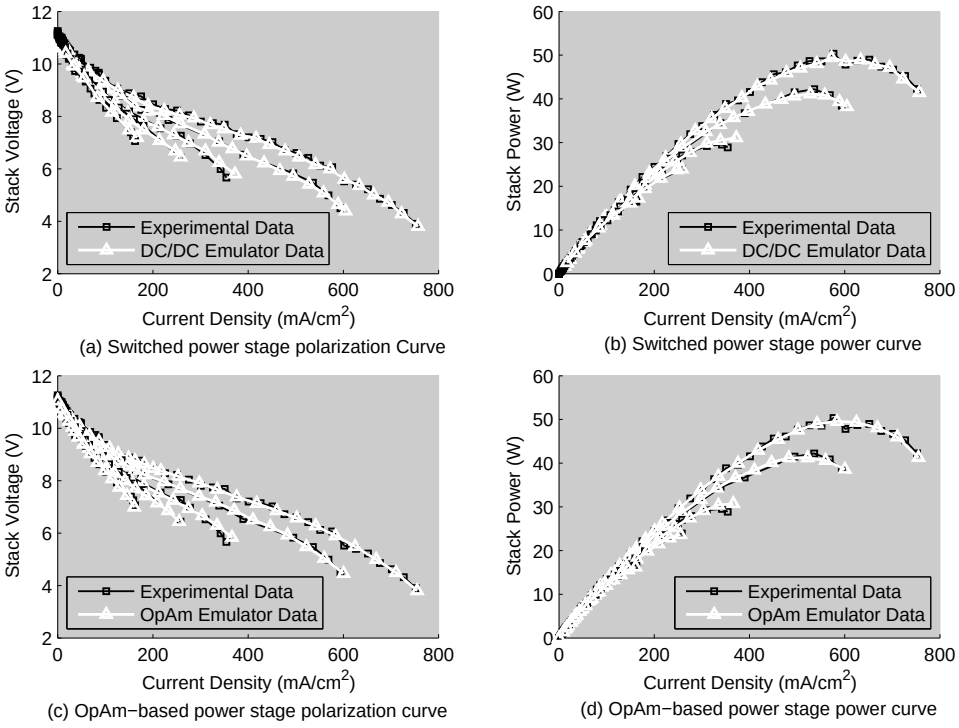


Figure 3-16: Static behavior of the switching and OpAm-based power stages.

Figure 3-16 compares the static behavior of the switching and OpAm-based power stages with the measurements of a real 12 cell stack. No difference can be seen between the polarization and power curves of the two power stages, whereas it can be observed a satisfactory similarity of both power stages responses with the polarization and power curves of the real fuel cell prototype. The performance of the LinReg-based power stage is the same as that of the OpAm-based power stage, which confirms that the proposed power stages can reproduce the steady-state behavior of the modeled PEM fuel cell power system.

Then, to evaluate the dynamic responses of the power stages and their effects on the emulator output, the emulator and its power stages were tested with different current and fuel flow ratio profiles, and their responses compared with the expected output voltages. Figure 3-17 shows the responses of the switching (top-left), OpAm-based (top-right) and LinReg-based (bottom-left) power stages to a dynamic current profile (bottom-right) with a fuel flow ratio of 85 %. In this experiment, the tracking of the fuel cell model reference signal by the power stages is satisfactory. The outputs of both linear power stages, presenting a small voltage ripple, are very similar. In contrast, the switching power stage exhibits a notable voltage ripple that is not predicted by the model. Similarly, figure 3-18 presents the response of the power stages to changes in the fuel flow ratio signal with a load current of 6 A. Again, the power stages follow the model signal with a satisfactory dynamic

ISBN:978-84-692-6902-2/ DL:T-1848-2009

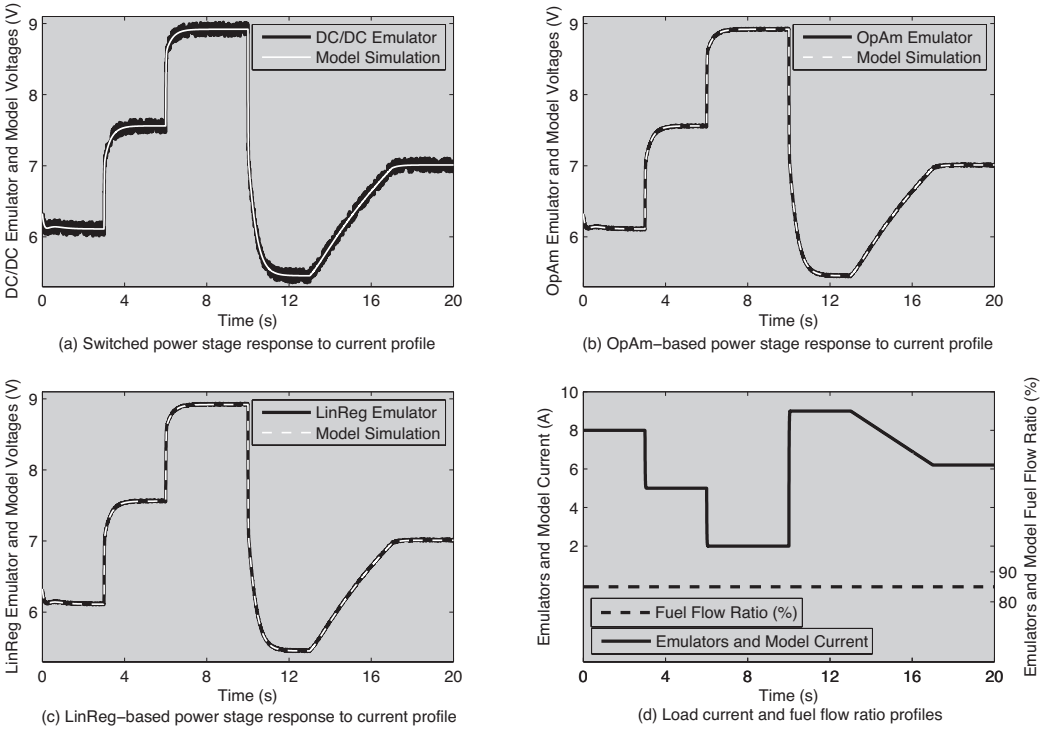


Figure 3-17: Power stages responses to dynamic current profile.

response and the switching power stage presents a bigger output ripple. These experiments are also useful for confirming the performance of the emulation algorithm and control strategies of the power stages. Comparing figures 3-17 and 3-18 confirms the accurate real-time computation of the emulation algorithm and fuel cell physical model inside the microcontroller. The tests also verify the digital controllers performance of the switching and OpAm-based power stages and show the satisfactory operation of the analog controller of the LinReg-based power stage.

The last evaluations of the power stages and emulation system were performed using an experimental current profile measured from a real PEM fuel cell prototype, the fuel flow ratio of which was set to 90 %. Figure 3-19 presents the responses of the emulation system with the different power stages to a real load profile (bottom-right). The performance of the emulation system using the switching power stage (top-left) is satisfactory because the mean values of the real and emulated voltages are very similar, which makes it possible to reproduce the fuel cell behavior. This same condition is observed in the OpAm-based (top-right) and LinReg-based (bottom-left) power stages operation, but their voltage ripple is lower. However, in other fuel cell systems, like the 1.2 kW Nexa power module, the voltage ripple exhibits a more complex profile, with high and low frequency voltage ripple components of 20 mV and 200 mV, which can also be reproduced by modelling approaches in the emulation algorithm.

ISBN:978-84-692-6902-2/ DL:T-1848-2009

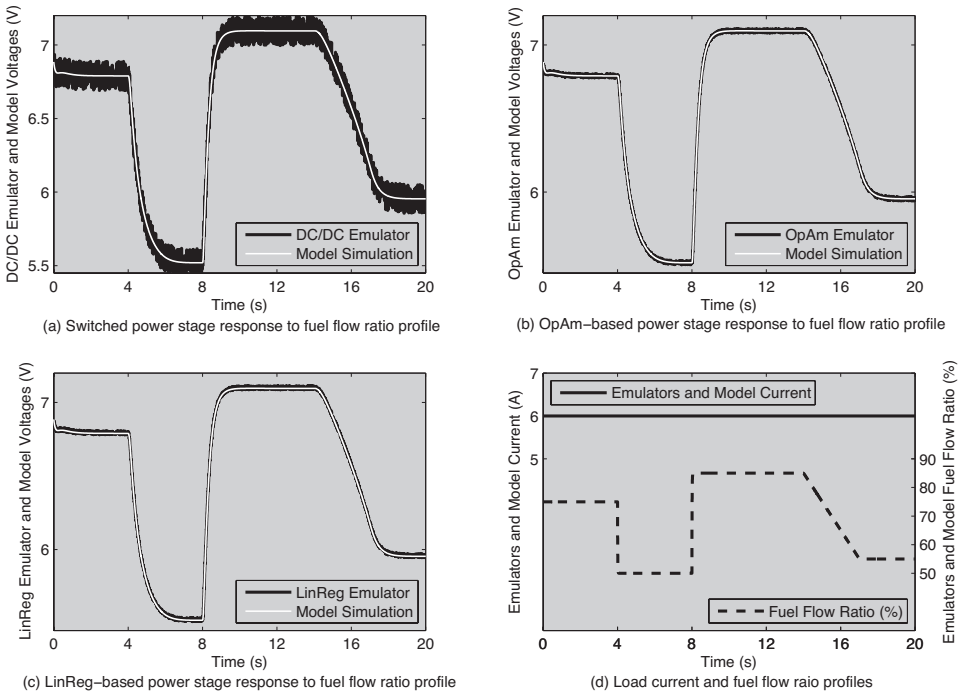


(a) Switched power stage response to fuel flow ratio profile
(b) OpAm–based power stage response to fuel flow ratio profile
(c) LinReg–based power stage response to fuel flow ratio profile
(d) Load current and fuel flow raio profiles

Figure 3-18: Power stages responses to dynamic fuel flow profile.

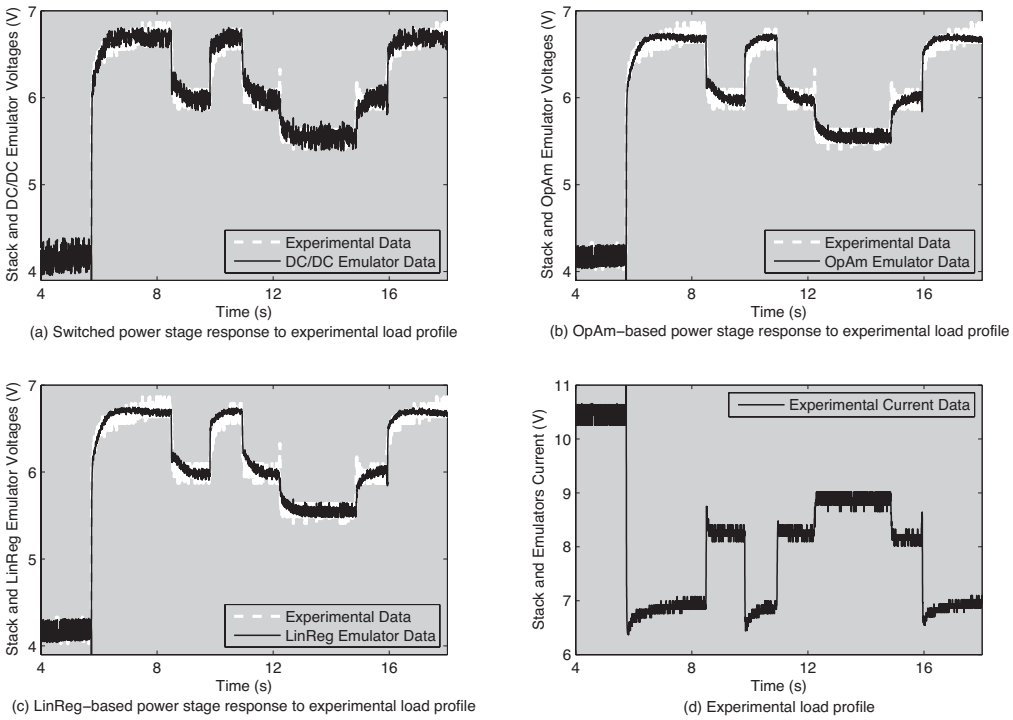


(a) Switched power stage response to experimental load profile
(b) OpAm–based power stage response to experimental load profile
(c) LinReg–based power stage response to experimental load profile
(d) Experimental load profile

Figure 3-19: Power stage responses to an experimental load profile.

ISBN:978-84-692-6902-2/ DL:T-1848-2009

## 3.6 Conclusions

This chapter presents a fuzzy-based modeling technique for PEM fuel cell electric power generation systems. The implementation of the technique proposed requires a short computation time, and it is suitable for use in real-time and embedded systems such as emulators. This fuzzy-based modeling technique gives a simple description of the dynamic effects that affects the PEMFC voltage and power. As a consequence of the simplicity, the data required for identifying the fuzzy models are easily generable. The technique has been applied to a particular system, where the temperature, humidity and pressure ratio have been regulated. This technique is currently being applied to more general cases.

Using the fuzzy-based technique, a model of a user-designed PEMFC has been developed and compared with a previously parameterized physical model and experimental data. The results validate the fuzzy-based modeling technique proposed. This model was used to implement a fuel cell emulator, which satisfactorily reproduces the behavior of the experimental prototype. The emulator can be used in a preliminary step to develop control strategies and electronic power systems that will subsequently be used in more expensive real PEMFC systems. The proposed switching and linear power stages allow to emulate fuel cell systems, and the impact of using switching or linear power stages in the emulation performance to be evaluated. A recursive problem has been identified in the switching DC/DC converter-based fuel cell emulators reported in the literature: its dynamic responses are considered satisfactory since the fuel cell and emulator voltage profiles are approximately equal in the time scale of the fuel cell dynamic response, but the voltage ripple is not analyzed. The emulation system proposed in this chapter improves this aspect by providing not only the traditional switching alternative, but also linear options that enable the fuel cell voltage ripple to be reproduced by modeling approaches. This characteristic means that it can be used to emulate the behavior of a wide range of fuel cells prototypes with detailed or simplified models.

Finally, the experiments performed confirm that the emulation system behaves satisfactory in the reproduction of fuel cell power systems. The proposed power stages also exhibit satisfactory electrical responses, and their characteristics make the emulation system a useful tool for testing power electronic systems designed to interact with real fuel cell prototypes.

ROVIRA I VIRGILI UNIVERSITY
FUEL CELL MODELING AND CONTROL FOR FUEL CONSUMPTION OPTIMIZATION
Carlos Andres Ramos Paja
ISBN:978-84-692-6902-2/ DL:T-1848-2009

# Chapter 4

# Fuel Cell Power Systems

This chapter analyzes the power system structure required to operate PEMFCs in safe and optimal conditions. First it analyzes the dynamic restrictions of the load that ensures the regulation of $\lambda_{O_2}$ and prevents oxygen starvation, and it also gives the control objectives in a fuel cell power system. Then different hybrid topologies for fuel cell and auxiliary storage interaction are evaluated, and control strategy designs are proposed in these environments and tested in simulation. Finally, the fuel cell optimal operating points are studied and a power electronics system is designed to experimentally evaluate the proposed strategy.

## 4.1 Introduction

The use of PEMFC systems in real applications requires control strategies for fuel cell and power electronics systems, and the power electronics interface itself presents design problems because of the dynamic restrictions of the fuel cell. The specialized literature contains numerous control strategies that have been proposed to ensure that the fuel cell operates correctly for the application objectives, i.e., Wishart et al. [91] propose a semi-empirical model and mathematical algorithms for the optimization of the electric power. Wishart uses simulations, genetic algorithms and sequential quadratic programming to obtain the optimal temperature and pressure conditions so that fuel cell operation generates the maximum power. Similarly, Zenith et al. [81] states that it is always possible to extract the maximum power from the fuel cell, but recommends stack current control to prevent fuel cell degradation. Zenith proposes theorems that describe fuel cell behavior as an electric power generation system, and presents an analysis of the interaction between fuel cells and DC-DC converters oriented to power converter control design. Other authors have proposed different control objectives. Kim et al. [92] presents an analysis to obtain the optimal fuel cell-battery-power converter configuration for automobile applications, where the optimization objectives are cost and

ISBN:978-84-692-6902-2/ DL:T-1848-2009

performance. Other examples of specific control objectives are presented by Muller et al. [93] where the load power is supplied in interaction with a battery in order to reduce the fuel cell heating. Similarly, Vega-Leal et al. [94] control of a portable fuel cell system to reduce the air compressor consumption without producing oxygen starvation.

The numerous fuel cell power systems reported in the literature show that control implementation depends on the objective and the application environment, but almost all the implementations use a power electronics interface. The one commonly used here is a switching interface for high conversion efficiency. The effects of the fuel cell interaction with switching converters have been analyzed by Gemmen et al. [4], Choi et al. [5] among other authors: they conclude that the fuel cell is sensitive variations in the stack current, which reduce electric power and degrade the fuel cell. In order to support the DC-DC converter selection, Choi et al. [95] present a useful evaluation of DC-DC converters for hybrid fuel cell-battery topologies. Another common approach reported is the design of new DC-DC converter topologies for fuel cell applications, i.e., the new topology proposed by Rong-Jong et al. [96], which has a high efficiency and low current ripple, but it is a non-conventional converter with complex control requirements. In stationary applications is also required to avoid the low frequency oscillation caused by the inverter operation since this phenomenon affects the performance of the fuel cell, and in fact, Ballard gives a maximum value for the 120 Hz current ripple with respect to the DC component (35 % peak-to-peak) for the operation of the 1.2 kW Nexa power system. For this aspect different solutions concerning the bulk capacitor design and power system control have been reported in the literature [97][98].

This chapter analyzes the mechanical considerations that must be taken into account in the fuel cell control design and in the definition of the power load restrictions. This was done by simulation analysis of the model proposed in chapter 2, which defined the safe load restrictions and therefore the power electronics structure required. The control objectives for the fuel cell are proposed in order to obtain an efficient power system. Next, common hybrid topologies for fuel cell and auxiliary storage interaction are analyzed, so that the most appropriate one can be selected for the load profile. Subsequently, several control approaches for these hybrid topologies are proposed, and the load restriction and control robustness are evaluated under simulation. Finally, the optimal operating points for the fuel cell are investigated in order to minimize hydrogen consumption, and an experimental fuel cell power system for a 48 VDC bus implementation is described, and the proposed optimization strategy validated.

ISBN:978-84-692-6902-2/ DL:T-1848-2009

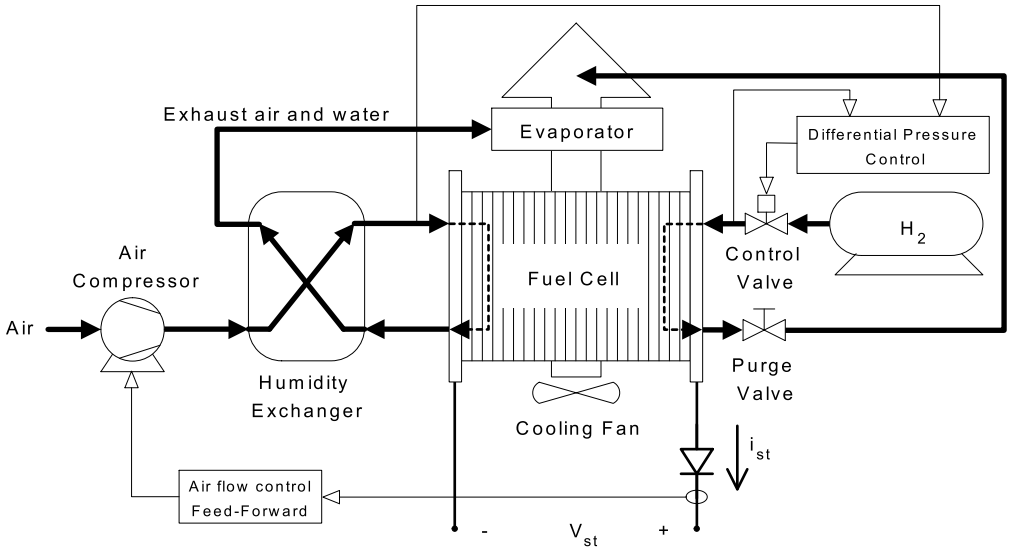


Figure 4-1: Ballard 1.2 kW Nexa power module scheme and manufacturer default control systems.

## 4.2 Mechanical considerations and control objectives

In PEMFC systems the main mechanical delays are caused by the air compressor, which is also the actuator in the $\lambda_{O_2}$ regulation strategies. Figure 4-1 shows the mechanical scheme of the Ballard 1.2 kW Nexa power module with the manufacturer default control systems, which are designed to ensure a safe anode-cathode differential pressure and enough air flow to supply the load current. This last control strategy was identified as a feed-forward control system and its equivalent $\lambda_{O_2}$ control behavior was described in chapter 2 - equation (2.37), which represents a static relation between the stack current and the desired $\lambda_{O_2}$. Nevertheless, the real implementation is a static non-linear relation (or look-up table interpolation) between the measured stack current and the air pump voltage control applied as expressed in (2.23). Following the control structure given in figure 4-1, and using the compressor dynamics identified in (2.22) and the $\lambda_{O_2}$ equations (2.6)-(2.9), the closed loop oxygen excess ratio dynamics can be simplified as:

$$\lambda_{O_2} = \frac{W_{O_2,ca,in}}{W_{O_2,reac}} = \frac{K_{W_{O2,ca}}}{K_{W_{O2,reac}}} \cdot \frac{W_{cp}}{I_{st}} = K_{\lambda_{O2}} \cdot \frac{G_{cm}(s) \cdot V_{cp} - 45}{I_{st}} =$$
$$K_{\lambda_{O2}} \cdot \frac{G_{cm}(s) \cdot (0.99873 \cdot I_{st} + 46.015) - 45}{I_{st}} = K_{\lambda_{O2}} \cdot [G_{cm}(s) \cdot F_1(I_{st}) + F_2(I_{st})] \quad (4.1)$$

where $K_{W_{O2,ca}}$ corresponds to the humidity, temperature and pressure conditions in a specific operating point, $K_{W_{O2,reac}}$ represents the oxygen molar mass and Faraday constant ratio and $K_{\lambda_{O2}}$ the ratio between the two constants. $F_1(I_{st})$ and $F_2(I_{st})$ are static non-linear relations that depend on the stack current and which define the $\lambda_{O_2}$ value, and $G_{cm}(s)$ is the linearized transfer function of the compressor given in (2.22).

ISBN:978-84-692-6902-2/ DL:T-1848-2009

From (4.1) it is deduced that the main dynamics in $\lambda_{O_2}$ are imposed by the air compressor. This implies that stack current transients cause almost instantaneous $\lambda_{O_2}$ disturbances (disregarding the cathode capacitance and electrochemical dynamics) that will be compensated according to the compressor dynamics, i.e., in a step-up stack current transient the oxygen excess ratio decreases and it is regulated by the compressor according with its time delay. In order to constraint the $\lambda_{O_2}$ deviations from the desired value in short and high current transitions, the stack current dynamics must be constrained to a slew-rate that can be followed by the compressor. By simulating the fuel cell model and the step responses of equation (4.1), a balance between $\lambda_{O_2}$ deviations and the PEMFC power system dynamic response (lower current slew-rate implies lower dynamic response) was obtained, where the stack current slew-rate is limited to a maximum of 10 A/s with an instantaneous $\pm 1.2$ $\lambda_{O_2}$ variation as result of the compressor manufacturer compensation system delay.

The main objective of the PEMFC power system proposed in this chapter is the efficient supply of the power requested by the load. Therefore, the load dynamics restriction can also be expressed as the maximum fuel cell power slew-rate, which depends on the stack voltage, load current and DC-DC converter efficiency. When the stack current is highest (that is to say, when the stack voltage is the lowest experimentally recommended of 26 V), the average fuel cell power slew-rate is 280 W/s, but due to mechanical non-linearities and other effects that are not discussed here, in this study is proposed a recommended maximum fuel cell slew-rate of 250 W/s. In the sections below in this chapter the effect of this power slew-rate is analyzed by modifying its value by $\pm 20$ % depending on the robustness of the controller implemented, using a higher value for robust controllers and a lower value for common linear strategies. This approach is used because robust controllers can compensate quickly and safe for the oxygen excess ratio by allowing a higher bandwidth.

The main design constrains and objectives of the proposed PEMFC power system are:

- To avoid the oxygen starvation phenomenon, which means restricting the fuel cell power slew-rate.

- To provide the load with a regulated DC bus, the regulation parameters of which are defined according to the load considerations.

- To minimize hydrogen consumption in order to increase autonomy and reduce operating cost.

The sections below analyze the power electronics structure, the design of the DC-DC converter interface and the control strategies used to accomplish the above constrains and objectives.

ISBN:978-84-692-6902-2/ DL:T-1848-2009

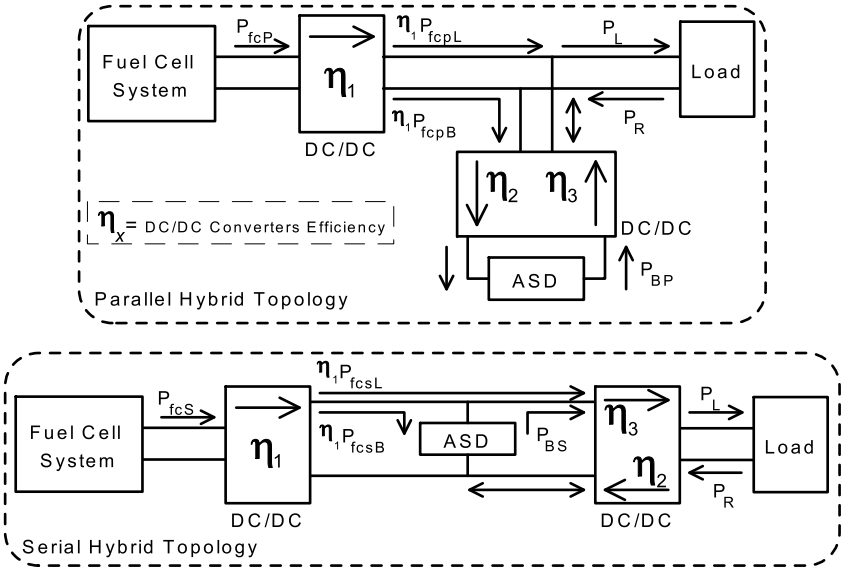


Figure 4-2: Fuel cell-ASD hybrid topologies.

## 4.3 Mathematical Analysis of Hybrid Topologies Efficiency for Fuel Cell Power Systems Design

The fuel cell bandwidth constraint imposed to avoid oxygen starvation limits the load transient frequencies that can be supplied by the fuel cell-based power system. In this way, the use of Auxiliary Storage Devices (ASD) to supply the high frequency transients is a common technique, where capacitor banks, supercapacitors and batteries are the most typical ASD used.

In the literature different fuel cell-ASD hybrid topologies are reported [99] [100] [101] [102] [103]. The most used fuel cell-ASD hybrid topologies are the parallel and serial [76]. The parallel topology, shown in the top of figure 4-2, uses an unidirectional DC/DC converter to isolate the fuel cell from the load DC bus, and a bidirectional DC/DC converter that exchanges energy between the ASD and the load DC bus. The serial topology shown in the bottom of figure 4-2 uses an unidirectional DC/DC converter to isolate the fuel cell from the ASD bus, and a bidirectional DC/DC converter to exchange energy with the load DC bus. These topologies support *regenerative brake-like* operations, and therefore their *topology efficiencies* are higher than those obtained in applications where the load is only a passive one-port.

In the same way, the use of batteries to support fuel cell energy generation systems is widely accepted due to the advantages in DC bus voltage regulation and overload capability [104] [105]. Also, the use of batteries allows cold start without the pre-charge step, which could be required depending on the storage capacity in supercapacitor-based systems [106] [107].

ISBN:978-84-692-6902-2/ DL:T-1848-2009

The topologies used in the reported fuel cell-ASD hybrid applications [99]-[107] have been selected taking into account different criteria such as common use, simplicity in the DC/DC converters control design, application restrictions, etc. However, the majority of the references have not considered the topology efficiency as the main design criteria. Therefore, it is not clear which topology must be selected in order to obtain the highest efficiency in the paths for the power that flows through the power electronics system that interfaces the fuel cell, the ASD and the load. High topology efficiency implies a lower electrical power required from the fuel cell in order to supply the load and regulate the ASD state-of-charge (SOC), and according to equation (2.7), lower hydrogen consumption generating lower operating cost and an increase in the autonomy. This topologies efficiency evaluation has been addressed by Moore et al. [108] for hydrogen fuel cell vehicles, considering a battery like ASD. Moore used simulation-based results in order to analyze the efficiency of different topologies, but his results depend on the particular load profiles considered for the simulations, and therefore are not easily extendible to other load profiles and applications.

In order to compare the efficiencies of the parallel and serial topologies, the same conditions in terms of DC/DC converters efficiency have been considered, this with the objective of obtaining conclusions depending on the load profile characteristics. In this way, a generic consumption power profile $P_L$ is considered, and the conditions where one topology is more efficient than the other are determined. Following the nomenclature of figure 4-2, it is assumed the same efficiency $\eta_1$ for the DC/DC converters that interact with the fuel cell in the serial and parallel topologies, efficiencies $\eta_2$ for the bidirectional DC/DC converters in the ASD charge direction (parallel) and load-to-ASD direction (serial). Finally, efficiencies $\eta_3$ for the discharge direction of the bidirectional converters are considered.

The efficiency of a topology is calculated depending on the power extracted from the fuel cell ($P_{fc_P}$ for the parallel and $P_{fc_S}$ for the serial) and on the net power consumed by the load ($P_L$) in the requested profile, which is the difference between the powers consumed and regenerated by the load. The efficiencies of the parallel and serial topologies are calculated in (4.2) and (4.3), respectively,

$$\eta_P = \frac{(1-k_R)\cdot P_L}{P_{fc_P}} \tag{4.2}$$

$$\eta_S = \frac{(1-k_R)\cdot P_L}{P_{fc_S}} \tag{4.3}$$

where $k_R$, denominated *regenerative ratio*, is the ratio between the power flows consumed $P_L$ and returned $P_R$ by the load. $P_R$ can be expressed as in (4.4).

$$P_R = k_R \cdot P_L \tag{4.4}$$

ISBN:978-84-692-6902-2/ DL:T-1848-2009

Table 4.1: Nomenclature for the mathematical analysis of hybrid topologies efficiency.

| | |
|---|---|
| **Abbreviations:** | |
| FC | Fuel cell |
| ASD | Auxiliary storage device |
| SOC | State of charge |
| **Variables:** | |
| $I_{st}$ | Fuel cell stack current |
| $\lambda_{O_2}$ | Oxygen excess ratio |
| $\eta_1$, $\eta_2$, $\eta_3$ | Switching DC/DC converters efficiency |
| $P_L$ | Load consumption power profile |
| $P_R$ | Load regenerative power profile |
| $P_{fc_PL}$ | FC power delivered directly to the load (parallel top.) |
| $P_{fc_SL}$ | FC power delivered directly to the load (serial top.) |
| $P_{fc_PB}$ | FC power delivered to the ASD (parallel top.) |
| $P_{fc_SB}$ | FC power delivered to the ASD (serial top.) |
| $P_{BP}$ | ASD power delivered directly to the load (parallel top.) |
| $P_{BS}$ | ASD power delivered directly to the load (serial top.) |
| $k_R$ | Regenerative ratio |
| $P_{BO_0}$ | ASD power profile for equal topologies efficiency |
| $P_{BO_x}$ | ASD power profile for generic load profile |
| $k_B$ | Relative equalization power factor |
| $k_x$ | Relative ASD power factor |
| $\eta_P$ | Parallel topology efficiency |
| $\eta_S$ | Serial topology efficiency |
| $f_x$ | Efficiency ratio |
| **Physical intervals:** | |
| *(Interesting ranges)* | |
| $\eta_1$, $\eta_2$, $\eta_3$, $\eta_P$, $\eta_S$ | $(0\ ,\ 1)$ |
| $k_R$ | $[0\ ,\ 1)$ |
| $k_B$ | $[0\ ,\ \frac{1}{\eta_3}]$ |
| $k_x$ | $[0\ ,\ \frac{P_L}{\eta_3 \cdot P_{BO_0}}]$ |
| $f_x$ | $[0\ ,\ \infty)$ |
| **Constants:** | |
| $\mathtt{F}$ | Faraday constant |
| $\mathtt{M}_{\mathtt{O}_2}$ | Oxygen molar mass |
| $\mathtt{M}_{\mathtt{N}_2}$ | Nitrogen molar mass |
| **Additional subindex:** | |
| *num* | Numerical calculation result |
| *sim* | Numerical simulation result |

The efficiency comparison is based on the fuel cell power required to supply the same load power profile and to regulate the SOC of the ASD. Also, in this analysis it is considered a *regenerative* power flow from the load ($0 < k_R < 1$). The topologies have three main operating modes: In the fist mode the load is supplied by the fuel cell and the ASD, this represented by equation (4.5) for the parallel topology and (4.6) for the serial one, where $P_{fc_PL}$ represents the power required from

ISBN:978-84-692-6902-2/ DL:T-1848-2009

the fuel cell in the parallel topology and $P_{fc_SL}$ in the serial topology. Similarly, $P_{BP}$ is the power required to the ASD in the parallel topology and $P_{BS}$ in the serial.

$$P_L = \eta_1 \cdot P_{fc_PL} + \eta_3 \cdot P_{BP} \tag{4.5}$$

$$P_L = \eta_3 \left(\eta_1 \cdot P_{fc_SL} + P_{BS}\right) \tag{4.6}$$

The second operating mode corresponds to the charge of the ASD (SOC regulation) by the fuel cell, this modeled by equations (4.7) and (4.8), where $P_{fc_PB}$ represents the power extracted from the fuel cell in the parallel topology and $P_{fc_SB}$ in the serial topology:

$$P_{BP,fc} = \eta_1 \cdot \eta_2 \cdot P_{fc_PB} \tag{4.7}$$

$$P_{BS,fc} = \eta_1 \cdot P_{fc_SB} \tag{4.8}$$

In the third mode, the ASD is charged using the power feed-back from the load $P_R$. The $P_R$ power flow is affected by the DC/DC convert efficiency $\eta_2$, and the effective power flows that charge the ASD in both parallel and serial topologies are given in (4.9).

$$P_{BP,R} = P_{BS,R} = \eta_2 \cdot P_R \tag{4.9}$$

These *regenerative brake-like* power flows (4.9) can be analyzed in terms of common feed-back power in both topologies that affects the power demanded from the fuel cell in order to restore the SOC of the ASD:

$$P_{BP} = \eta_2 \left(\eta_1 \cdot P_{fc_PB} + k_R \cdot P_L\right) \tag{4.10}$$

$$P_{BS} = \eta_1 \cdot P_{fc_SB} + \eta_2 \cdot k_R \cdot P_L \tag{4.11}$$

From equations (4.5)-(4.11) the power requested to the fuel cell in both topologies can be calculated as: $P_{fcP} = P_{fc_PL} + P_{fc_PB}$ in (4.12) for the parallel topology, and $P_{fcS} = P_{fc_SL} + P_{fc_SB}$ in (4.13) for the serial one.

$$P_{fcP} = \frac{\eta_2 \left(1 - k_R\right) P_L + \left(1 - \eta_2 \cdot \eta_3\right) P_{BO}}{\eta_1 \cdot \eta_2} \tag{4.12}$$

$$P_{fcS} = \frac{1 - \eta_2 \cdot \eta_3 \cdot k_R}{\eta_1 \cdot \eta_3} P_L \tag{4.13}$$

In (4.12), $P_{BO}$ represents the power required from the ASD to supply the load. Also, it is remarkable that the power required to the fuel cell in the serial topology (4.13) does not depend on the amount of power exchanged with the ASD.

ISBN:978-84-692-6902-2/ DL:T-1848-2009

In order to compare the efficiency of both topologies, the first step is to find the conditions where the power requested from the fuel cell in both topologies is the same, and therefore their efficiencies are equal. From (4.12)-(4.13) it is concluded that, by assuming the same converters efficiency, the same load consumption power profile and regenerative ratio, the condition for having the same efficiencies depends on the power extracted from the ASD:

$$P_{fcP} = P_{fcS} \tag{4.14}$$

$$P_{BO_0} = \frac{\eta_2}{\eta_3} \cdot \frac{(1-\eta_3) + \eta_3 (1-\eta_2) k_R}{1 - \eta_2 \cdot \eta_3} P_L \tag{4.15}$$

$$k_B = \frac{P_{BO_0}}{P_L} = \frac{\eta_2}{\eta_3} \cdot \frac{(1-\eta_3) + \eta_3 (1-\eta_2) k_R}{1 - \eta_2 \cdot \eta_3} \quad , \quad 0 \leq k_B \leq 1/\eta_3 \tag{4.16}$$

where the minimum and maximum values of $k_B$ are calculated from the function analysis in different $\eta_2$ and $\eta_3$ conditions. This aspect is discussed below.

In (4.14)-(4.16) it is calculated the power $P_{BO_0}$ exchanged with the ASD that makes the power requested to the fuel cell in both topologies ($P_{fcP}$ and $P_{fcS}$) and the topologies efficiencies equal. $k_B$ correlates $P_{BO_0}$ with the load consumption power.

The next step is to analyze the behavior of both topologies efficiency far from $P_{BO_0}$, and this is done by considering a generic ASD power profile $P_{BO_x}$, defined in (4.17), where $k_x$ correlates the generic ASD power profile with the $P_{BO_0}$ power that makes equal both serial and parallel topologies efficiency.

$$P_{BO_x} = k_x \cdot P_{BO_0} \quad , \quad 0 \leq k_x \leq \frac{P_L}{\eta_3 \cdot P_{BO_0}} \tag{4.17}$$

In order to compare the efficiencies, an efficiency ratio $f_x$ is proposed in (4.18)-(4.19).

$$f_x = \frac{\eta_S}{\eta_P} = \frac{P_{fcP}}{P_{fcS}} \tag{4.18}$$

$$f_x = \frac{[\eta_3 + k_x (1-\eta_3)] - [1 - k_x (1-\eta_2)] \eta_3 \cdot k_R}{1 - \eta_2 \cdot \eta_3 \cdot k_R} \quad , \quad f_x \geq 0 \tag{4.19}$$

The conditions where each topology is more convenient can be obtained from equations (4.16) and (4.19). $k_B$ gives information about the fraction of load power extracted from the ASD that makes the topologies efficiency equal. A mathematical analysis of this parameter gives valuable information about its behavior. First, the influence of changes on $\eta_2$ is investigated, where the limit values of $\eta_2$ are used to evaluate the range of variation of $k_B$ in function of $\eta_2$:

$$\left.\begin{array}{l} \lim\limits_{\eta_2 \to 0^+} k_B = 0 \\ \lim\limits_{\eta_2 \to 1^-} k_B = \dfrac{1}{\eta_3} \end{array}\right\} \tag{4.20}$$

ISBN:978-84-692-6902-2/ DL:T-1848-2009

Also, examining the partial derivative of $k_B$ with respect to $\eta_2$ (4.21), and taking into account the physical restrictions of the efficiencies and regenerative ratio ($\{0 < \eta_i < 1, i = 1, 2, 3\}$, $0 \leq k_R < 1$), it is concluded that $k_B$ and its partial derivative with respect to $\eta_2$ are continuous. But due to the structure of (4.21) it is difficult to determine its behavior, and therefore it is proposed to examine this partial derivative in the $\eta_2$ limits and also investigate the second partial derivative with respect to $\eta_2$ (4.22).

$$\frac{\partial k_B}{\partial \eta_2} = \frac{1 - \eta_3 (1 - k_R) - \eta_2 \cdot \eta_3 (2 - \eta_2 \cdot \eta_3) k_R}{\eta_3 (1 - \eta_2 \cdot \eta_3)^2} \tag{4.21}$$

$$\left.\begin{array}{r} \lim\limits_{\eta_2 \to 0^+} \left( \dfrac{\partial k_B}{\partial \eta_2} \right) = \dfrac{1 - \eta_3 (1 - k_R)}{\eta_3} > 0 \\ \lim\limits_{\eta_2 \to 1^-} \left( \dfrac{\partial k_B}{\partial \eta_2} \right) = \dfrac{1 - \eta_3 \cdot k_R}{\eta_3 (1 - \eta_3)} > 0 \\ \dfrac{\partial^2 k_B}{\partial \eta_2^2} = \dfrac{2 (1 - k_R)(1 - \eta_3)}{(1 - \eta_2 \cdot \eta_3)^3} > 0 \end{array}\right\} \tag{4.22}$$

Due to the continuity of $k_B$ in $\eta_2$, and since the second partial derivative and limit values in (4.22) are positive, it can be concluded that $k_B$ partial derivative with respect to $\eta_2$ is also positive, and taking into account the positive $k_B$ limit values, it is concluded that increments in $\eta_2$ cause increments in $k_B$ and vice versa, which is expressed in (4.23).

$$\eta_2 + \Delta\eta_2 \Rightarrow k_B + \Delta k_B \quad , \quad \left\{ \begin{array}{l} \Delta\eta_2 \geq 0 \Rightarrow \Delta k_B \geq 0 \\ \Delta\eta_2 < 0 \Rightarrow \Delta k_B < 0 \end{array} \right. \tag{4.23}$$

In a similar analysis the behavior of $k_B$ with respect to $\eta_3$ is investigated in (4.24)-(4.26).

$$\left.\begin{array}{r} \lim\limits_{\eta_3 \to 0^+} k_B \to +\infty \\ \lim\limits_{\eta_3 \to 1^-} k_B = \eta_2 \cdot k_R \end{array}\right\} \tag{4.24}$$

$$\frac{\partial k_B}{\partial \eta_3} = -\frac{\eta_2 \cdot \left[1 - \eta_2 \cdot \eta_3^2 (1 - \eta_2) k_R - \eta_2 \cdot \eta_3 (2 - \eta_3)\right]}{\eta_3^2 (1 - \eta_2 \cdot \eta_3)^2} \tag{4.25}$$

$$\left.\begin{array}{r} \lim\limits_{\eta_3 \to 0^+} \left( \dfrac{\partial k_B}{\partial \eta_3} \right) \to -\infty < 0 \\ \lim\limits_{\eta_3 \to 1^-} \left( \dfrac{\partial k_B}{\partial \eta_3} \right) = -\eta_2 \dfrac{1 - \eta_2 \cdot k_R}{1 - \eta_2} < 0 \end{array}\right\} \tag{4.26}$$

The structure of (4.25) is also difficult to be analyzed, but its limits are negative (4.26) and also it is continuous in the range of interest of $\eta_3$ ($0 < \eta_3 < 1$). In order to investigate if $\partial k_B / \partial \eta_3$ exhibits a sign change, the solutions $\eta_{3(S1,S2)}$ of $\partial k_B / \partial \eta_3 = 0$ given in (4.27) were calculated.

$$\eta_{3(S1,S2)} = \frac{\eta_2 \pm \sqrt{-\eta_2 (1 - \eta_2)(1 - k_R)}}{\eta_2 (1 + \eta_2 \cdot k_R - k_R)} \tag{4.27}$$

The physical restrictions of $\eta_2$ and $k_R$ ($0 < \eta_2 < 1$, $0 \leq k_R < 1$) guarantee that does not exist a real $\eta_3$ value having a physical meaning for $\partial k_B / \partial \eta_3 = 0$. From this $\partial k_B / \partial \eta_3 \neq 0$ condition,

ISBN:978-84-692-6902-2/ DL:T-1848-2009

the continuity of $\partial k_B/\partial \eta_3$ in $\eta_3$, and the negative limit values given in (4.26), it is concluded that $\partial k_B/\partial \eta_3 < 0$.

The above mathematical relations indicate that increments in $\eta_3$ cause decrements in $k_B$ and vice versa, which is expressed in (4.28).

$$\eta_3 + \Delta\eta_3 \Rightarrow k_B + \Delta k_B \quad , \quad \begin{cases} \Delta\eta_3 \geq 0 \Rightarrow \Delta k_B \leq 0 \\ \Delta\eta_3 < 0 \Rightarrow \Delta k_B > 0 \end{cases} \tag{4.28}$$

Finally, a similar analysis of $k_B$ is performed on $k_R$ in (4.29)-(4.30), which is an interesting variable since it represents the fraction of power feed-back from the load.

$$\left.\begin{array}{l} \lim\limits_{k_R \to 0^+} k_B = \dfrac{\eta_2 (1-\eta_3)}{\eta_3 (1-\eta_2 \cdot \eta_3)} > 0 \\ \lim\limits_{k_R \to 1^-} k_B = \dfrac{\eta_2}{\eta_3} > 0 \end{array}\right\} \tag{4.29}$$

$$\frac{\partial k_B}{\partial k_R} = \eta_2 \frac{1-\eta_2}{1-\eta_2 \cdot \eta_3} > 0 \tag{4.30}$$

The influence of $k_R$ on $k_B$ is summarized in (4.31), where increments in $k_R$ cause increments in $k_B$ and vice versa.

$$k_R + \Delta k_R \Rightarrow k_B + \Delta k_B \quad , \quad \begin{cases} \Delta k_R \geq 0 \Rightarrow \Delta k_B \geq 0 \\ \Delta k_R < 0 \Rightarrow \Delta k_B < 0 \end{cases} \tag{4.31}$$

The mathematical relations presented in (4.23), (4.28) and (4.31) describe the behavior of $k_B$. This is graphically illustrated in figure 4-3, where $k_B$ profiles for different $\{\eta_2, \eta_3, k_R\}$ conditions are depicted. In the figure it is observed that increments in $\eta_3$ reduce the $k_B$ value and therefore the ASD power that generates equal topologies efficiency is reduced. This same effect is caused by decrements in $\eta_2$ and by decrements in the regenerative ratio $k_R$. The figure also presents the $k_B$ profiles under the usual design condition $\{\eta_2 = \eta_3\}$. Finally, the physical limit $k_B = 1/\eta_3$ is plotted.

The next analyses required are related to the efficiency ratio $f_x$, which gives the final information about the comparison of the topologies efficiency. The first evaluation is made on variations of $k_R$:

$$\left.\begin{array}{l} \lim\limits_{k_R \to 0^+} f_x = (1-\eta_3)\, k_x + \eta_3 > 0 \\ \lim\limits_{k_R \to 1^-} f_x = k_x > 0 \end{array}\right\} \tag{4.32}$$

$$\frac{\partial f_x}{\partial k_R} = -\eta_3 (1-\eta_2 \cdot \eta_3) \frac{1-k_x}{(1-\eta_2 \cdot \eta_3 \cdot k_R)^2} \tag{4.33}$$

Due to the range of $k_x$, which can be grater or lower than 1 ($0 \leq k_x \leq P_L/(\eta_3 \cdot P_{BO_0})$), the

ISBN:978-84-692-6902-2/ DL:T-1848-2009

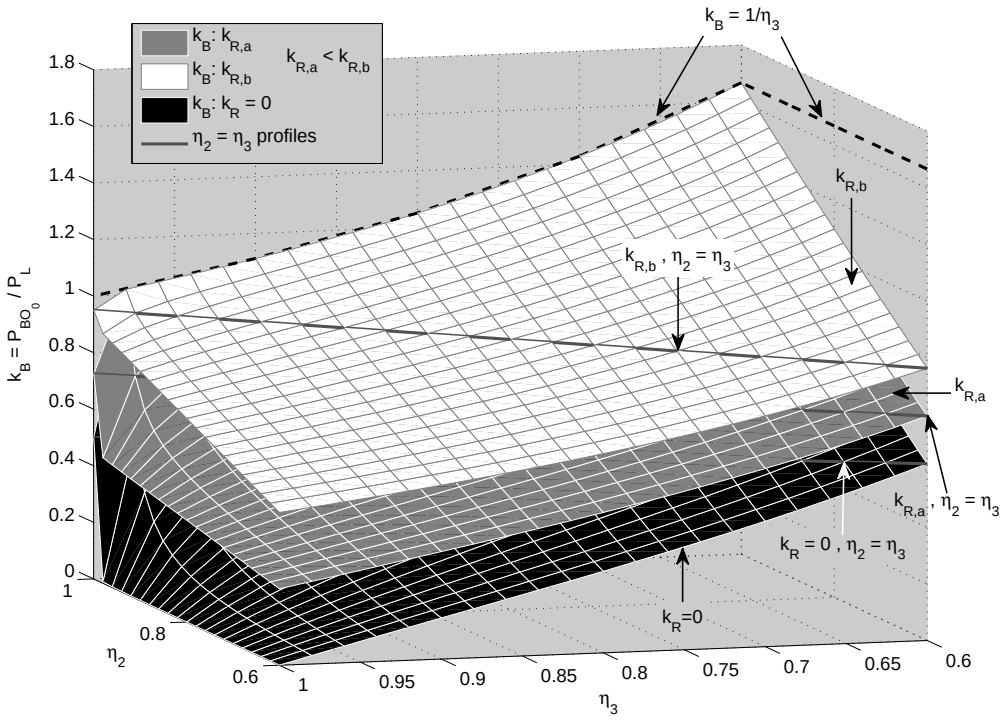


Figure 4-3: $k_B$ functional analysis.

behavior of the efficiency ratio is described by (4.34).

$$\left.\begin{array}{rcl} k_x \leq 1 & \Rightarrow & \dfrac{\partial f_x}{\partial k_R} \leq 0 \\ k_x > 1 & \Rightarrow & \dfrac{\partial f_x}{\partial k_R} > 0 \end{array}\right\} \tag{4.34}$$

From (4.32)-(4.34) it is concluded that $f_x$ is continuous in the range of interest of $k_R$. Also, for any $k_R$, this analysis indicates that $f_x$ is a monotonic function, and the limits calculated in (4.32) constrain the range of $f_x$ according to (4.35).

$$\left.\begin{array}{l} k_x \leq 1 \;\Rightarrow\; k_x \leq f_x \leq (1-\eta_3)\,k_x + \eta_3 \;\Rightarrow\; f_x \leq 1 \\ k_x > 1 \;\Rightarrow\; (1-\eta_3)\,k_x + \eta_3 \leq f_x \leq k_x \;\Rightarrow\; f_x > 1 \end{array}\right\}, \forall\,\{0 \leq k_R < 1\} \tag{4.35}$$

The conditions presented in (4.35) describe the behavior of the topologies efficiency, and using the definition of efficiency ratio $f_x$ given in (4.18), the efficiency comparison of both serial and parallel topologies can be summarized as:

$$\left.\begin{array}{l} k_x \leq 1 \Rightarrow \eta_P \geq \eta_S \\ k_x > 1 \Rightarrow \eta_P < \eta_S \end{array}\right\}, \forall\,\{0 \leq k_R < 1\} \tag{4.36}$$

The results presented in (4.36) can be corroborated by analyzing the first and second partial

ISBN:978-84-692-6902-2/ DL:T-1848-2009

derivatives of $f_x$ with respect to $k_x$, and also calculating the $f_x$ limit values in $k_x \to 0^+$ and $k_x \to 1$ conditions:

$$\frac{\partial f_x}{\partial k_x} = \frac{(1-\eta_3) - \eta_3 (1-\eta_2) k_R}{1 - \eta_2 \cdot \eta_3 \cdot k_R} \tag{4.37}$$

$$\frac{\partial^2 f_x}{\partial k_x^2} = 0 \tag{4.38}$$

$$\left.\begin{array}{l} \lim\limits_{k_x \to 0^+} f_x = \eta_3 \dfrac{1-k_R}{1-\eta_2 \cdot \eta_3 \cdot k_R} \Rightarrow 0 < \lim\limits_{k_x \to 0^+} f_x < 1 \\ \lim\limits_{k_x \to 1} f_x = 1 \end{array}\right\} \Rightarrow \frac{\partial f_x}{\partial k_x} > 0 \tag{4.39}$$

Equations (4.37)-(4.39) demonstrate that $f_x$ is monotonically increasing on $k_x$ with a linear behavior, and since $f_x(1) = 1$, it is also valid the analysis presented in (4.35) and therefore the same conclusion given in (4.36) is obtained.

Finally, the direct effect of $\eta_2$ and $\eta_3$ over $f_x$ can be analyzed in a similar way through partial derivatives of $f_x$ with respect of each variable, but it is more informative to analyze the relative effect of $\eta_2$ and $\eta_3$ over $(\partial f_x / \partial k_x)$, this because it illustrates the behavior of $f_x$ in a defined load profile condition under variations of the converters efficiencies:

$$\frac{\partial^2 f_x}{\partial k_x \partial \eta_3} = -\frac{1-k_R}{(1-\eta_2 \cdot \eta_3 \cdot k_R)^2} \leq 0 \tag{4.40}$$

$$\frac{\partial^2 f_x}{\partial k_x \partial \eta_2} = -\eta_3^2 \cdot k_R \frac{1-k_R}{(1-\eta_2 \cdot \eta_3 \cdot k_R)^2} \leq 0 \tag{4.41}$$

In the common design condition of $\{\eta_2 = \eta_3\}$ it is also interesting to analyze the effect of the efficiencies deviation, and with this objective a new efficiencies deviation variable $\Delta\eta$ that models the deviation of $\eta_2$ from $\eta_3$ is defined:

$$\Delta\eta = \eta_2 - \eta_3 \tag{4.42}$$

The partial derivative of $(\partial f_x / \partial k_x)$ with respect of $\Delta\eta$ is given in (4.43).

$$\frac{\partial^2 f_x}{\partial k_x \partial \Delta\eta} = -\eta_3^2 \cdot k_R \frac{1-k_R}{(1-\eta_3^2 \cdot k_R - \eta_3 \cdot k_R \cdot \Delta\eta)^2} \leq 0 \tag{4.43}$$

This analysis allows to investigate the efficiency relation in the $\{\eta_2,\ \eta_3\}$ regions where $k_B > 1/\eta_3$. From (4.16) it is deduced that $k_B > 0$, and due to the continuity of $f_x$ in the range of interest of $k_x$, the relations given in (4.36), (4.39) and (4.43) imply that, in $k_B > 1/\eta_3$ conditions, $k_x < 1$ because $P_{BOx} \leq P_L/\eta_3$, which is expressed in (4.44).

$$k_B > 1/\eta_3 \Rightarrow f_x < 1 \Rightarrow \eta_P > \eta_S \tag{4.44}$$

ISBN:978-84-692-6902-2/ DL:T-1848-2009

From the analyses performed in (4.40), (4.41), (4.43) and (4.44) it is concluded that increments in $\eta_2$ and $\eta_3$ cause decrements in the variations of $f_x$ with respect to variations on $k_x$. Also, positives unbalances of $\eta_2$ over $\eta_3$ cause decrements in the variations of $f_x$, and negative unbalances cause increments in that derivative.

Finally, the analyses performed on $f_x$ are illustrated in figure 4-4, where practical $k_R$ and $k_x$ ranges are evaluated for different $\eta_2$ and $\eta_3$ relations. It is confirmed that $\eta_1$ does not have influence in the efficiency ratio, and also that $k_R$ does not change the topology selection suggested by $k_x$, this because $k_R$ does not generate transitions across the plane $f_x = 1$. The numerical calculations also demonstrate that $\eta_3$ has a strong influence in the efficiency ratio, which physically indicates that higher values of $\eta_3$ generates lower efficiency discrepancies between the serial and parallel topologies.

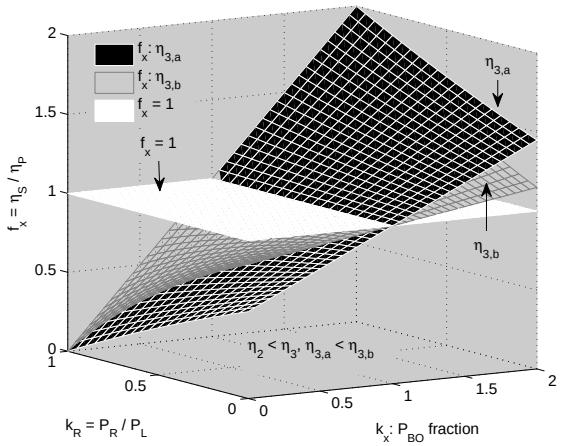


(a) $f_x$ functional analysis, $\eta_2 < \eta_3$.

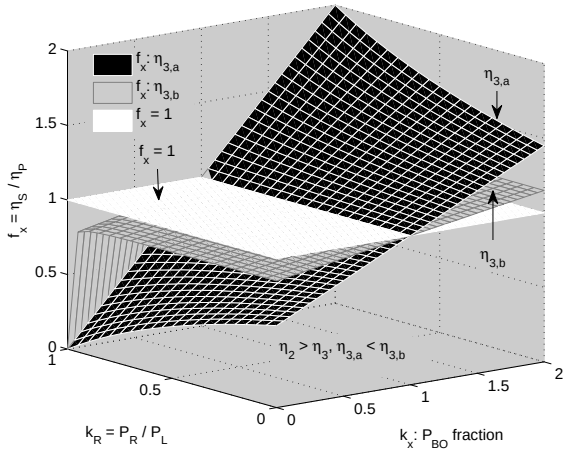


(b) $f_x$ functional analysis, $\eta_2 > \eta_3$.

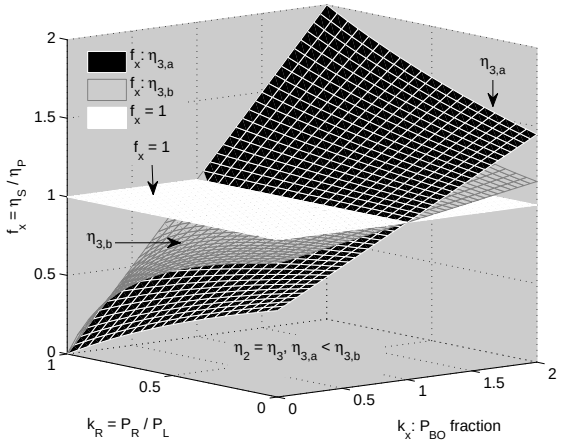


(c) $f_x$ functional analysis, $\eta_2 = \eta_3$.

Figure 4-4: $f_x$ functional analysis in different $\eta_2$ and $\eta_3$ relation.

ISBN:978-84-692-6902-2/ DL:T-1848-2009

### 4.3.1 General considerations and selection criteria

The analytical results presented in (4.23), (4.28), (4.31) give information about $k_B$, and the results presented in (4.36), (4.40), (4.41), (4.43) and (4.44) about $f_x$. The $k_B$ analysis describe the conditions where parallel and serial topologies have the same efficiency, and also defines the limit from which one topology is more efficient than the other. In the same way, the results on $f_x$ describe which topology has the higher efficiency depending on the load power fraction extracted from the ASD.

The mathematical relations (4.23) and (4.28) indicate that variations in the DC/DC converters efficiencies modify the ASD limit power from which one topology is more efficient than the other. The reduction of the $\eta_2$ efficiency causes a lower limit value, and according to the definition of $k_x$ (4.17) and the analysis of the efficiency ratio presented in (4.36), this implies that the region where the serial topology is more efficient grows. This same behavior is obtained when the $\eta_3$ efficiency is incremented, and also a $\eta_3 > \eta_2$ condition has the same effect. This is important because the DC/DC converters efficiencies are not constant with respect to the output power, and considering the limit cases is an effective technique to estimate which is better topology for a given application.

The results presented in (4.31) analyze the effect of the amount of power feed-back from the load on the behavior of the power limit factor $k_B$, from which it can be concluded that higher feed-back power (regenerative ratio) reduces the region where the serial topology is more efficient. This behavior was expected because high feed-back power implies lower fuel cell-ASD power flow. In this condition the parallel topology is more efficient due to the presence of only one converter in the fuel cell-load path instead of the two converters present in the serial topology for the same power flow (fuel cell-load). The power limit factor $k_B$ can be estimated by using the nominal values of the efficiencies and regenerative ratio in equation (4.16).

The results of the efficiency ratio analysis presented in (4.36) imply that for ASD output power $P_{BO_x}$ higher than the power limit $P_{BO_0} = k_B \cdot P_L$, ($k_x = P_{BO_x}/P_{BO_0} > 1$), the serial topology is more efficient, and for lower ASD output power ($k_x < 1$) than the same limit, the parallel topology is more efficient. Also, the analytical results presented in (4.40), (4.41) and (4.43) indicate that increments in $\eta_3$ generate a reduction in the difference of consumption and efficiency between both topologies, and the same effect is caused by increments in $\eta_2$. Moreover, the results obtained in (4.44) indicate that in regions where $k_B > 1/\eta_3$, the parallel topology has higher efficiency (lower fuel cell power request). A numerical approximation to the efficiency ratio can be calculated by using the rated power efficiency of the converters and operating point regenerative ratio in equation (4.19).

In summary, for load profiles that request an ASD power profile higher than an specific limit defined by the load profile, the serial topology is more efficient than the parallel. For other cases, the parallel topology exhibits a better performance in power requested from the fuel cell, and therefore its efficiency is higher. The results of the analyses presented provide mathematical expressions

that can be used to estimate the most efficient topology for a defined load profile through simple calculations.

### 4.3.2 Numerical Examples

Jiang et al. [109] [110] consider a load profile that periodically draws pulse current to test its adaptive control strategy for active power sharing in hybrid fuel cell-battery power sources. The same type of load profile was considered by Gao et al. [111], this work being focused in the supply of pulse demands. Bonnet et al. [112] present a power profile generated by a driving cycle representative of a real railway service as a pulsating demand, and Lam et al. [113] propose pulsating load changes to simulate medium-hybrid vehicle power profiles. To illustrate the methodology and give efficiency comparison, in this example a pulsating load demand with consumption and regeneration intervals has been considered. This periodic load profile is presented in figure 4-5, where the profile is specified by its amplitude $A$ (W), regenerative power $RS$ (W), period $T_s$ (s) and duty cycle $D$ (%). Another important characteristic is the DC component $DC$ (W).

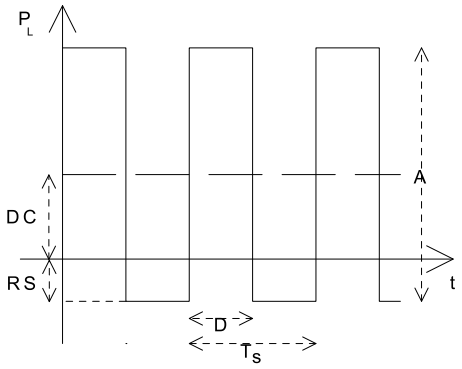


Figure 4-5: Load power profile for numerical examples.

In this analysis the characteristics of the 1.2 kW Nexa power module from Ballard has been considered; according to the model proposed in section 2, it has an air compressor that allows a dynamic response in 150 ms for 1 A perturbations in the stack current. Also, the limitation of the fuel cell power slew-rate has also been considered in order to provide more realistic results. A slow air compressor dynamics can cause oxygen starvation, which can be generally avoided by limiting the slew-rate, as was discussed previously in section 4.2 [114] [115].

The power slew-rate limitation causes a high-frequency filtering in the power requested to the fuel cell, being those high-frequency transients supplied by the ASD. According to the experimental results reported in [114] and the analysis performed in section 4.2, it has been considered a maximum fuel cell power slew-rate of 300 W/s (250 W/s + 20 %), which causes that the fuel cell provides

ISBN:978-84-692-6902-2/ DL:T-1848-2009

mainly the DC component of the pulsating load profile, and therefore the AC components are exchanged with the ASD.

The energy consumed in one period by the load profile is given by (4.45), and the energy feedback from the load in the regenerative stage is given by (4.46). The DC and AC components of the load profile are given in (4.47) and (4.48), respectively. Also, the regenerative ratio can be calculated as in (4.49).

$$E_{L_{con}} = (A - RS)(T_s \cdot D) \quad [J] \tag{4.45}$$

$$E_{L_{reg}} = (RS)(T_s(1 - D)) \quad [J] \tag{4.46}$$

$$P_{L_{DC}} = A \cdot D - RS \quad [W] \tag{4.47}$$

$$P_{L_{AC}} = A \cdot D \cdot (1 - D) \quad [W] \tag{4.48}$$

$$k_{R_{num}} = (E_{L_{reg}})/(E_{L_{con}}) \tag{4.49}$$

**Example 1: Load profile with high DC power component**

The load profile considered in this first example is specified by the following parameters: $A = 1$ kW, $RS = 300$ W, $T_s = 1$ s and $D = 80$ %. Also, the efficiencies of the DC/DC converters are $\eta_1 = \eta_2 = \eta_3 = 0.93 = \eta_{0,num}$. In one period, the energies consumed and returned by the load can be calculated using (4.45) to $E_{L_{con}} = 560\ J$ and (4.46) to $E_{L_{reg}} = 60\ J$, respectively. The regenerative ratio (4.49) in this example is $k_R = 0.1$, and the load consumption profile DC (4.47) and AC (4.48) components are equal to $P_{L_{DC}} = 500\,W$ and $P_{L_{AC}} = 160\,W$, respectively.

$$k_{B_{num}} = \frac{1 + \eta_{0,num} \cdot k_{R_{num}}}{1 + \eta_{0,num}} \tag{4.50}$$

The numerical value of $k_B$ can be calculated from (4.16), but taking into account the equal DC/DC converters efficiency considered in this example, it can be simplified to (4.50). Form this equation it is calculated that $k_{B_{num}} = 0.57$ and, from the $k_B$ definition (4.16), the power exchanged with the ASD that makes equal the efficiencies of both serial and parallel topologies is $P_{BO_0} = 319.2\,W$. Considering that the AC load profile component is exchanged with the ASD, and taking into account the efficiency of the DC/DC converters, it can be obtained $P_{BO_x,num} = P_{L_{AC}}/\eta_{0,num} = 172\ W$. This power is extracted from the ASD in order to supply the high frequency components of the load consumption profile, and it is restored to the ASD by using the fuel cell and feed-back powers in the same period.

From the $k_x$ definition (4.17) it is calculated its numerical value to $k_{x,num} = 0.54$ and, using the

ISBN:978-84-692-6902-2/ DL:T-1848-2009

analytical results presented in (4.36), it is concluded that, for this particular load profile, the parallel topology is more efficient than the serial one, and therefore requests less power power from the fuel cell, minimizing in this way the hydrogen consumption. Moreover, using equations (4.18)-(4.19), it is possible to calculate that the efficiency ratio for this example is $f_{x,num} = 0.962$, which gives the relation between the serial and parallel topologies efficiency.

In order to validate the parallel topology selection suggested by the numerical use of the analytical results, a detailed physical simulation using Matlab/Simulink has been performed. The simulation model considers a detailed and parameterized fuel cell physical model and its control systems (previously described in section 3.2.1 [23] [114]), the recommended fuel cell power slew-rate limitation, the battery model, the DC/DC converters efficiencies, and the same load profile for both topologies. Also, to regulate the SOC of the ASD, a proportional-integral-derivative (PID) controller has been tuned using the Ziegler-Nichols tuning method, which has been widely used in fuel cell control systems [116] [117] [118]. This controller regulates the power requested from the fuel cell in order to achieve a SOC=50 % in each period.

Figure 4-6 shows the load, fuel cell and ASD power profile waveforms of the simulation of both topologies. In the simulations it is observed that the fuel cell DC power profile requested in the parallel topology is lower than the requested in the serial one, and therefore the parallel topology efficiency is higher. In order to provide a better illustration of the topologies efficiency relation for the load profile given in this example, the simulation of the efficiency of both topologies over a time span of 300 s is depicted in figure 4-7(a). In this simulation it is observed an initial transient caused by the start-up of the fuel cell ($0\ \mathsf{s} \leq t \leq 50\ \mathsf{s}$), in which the fuel cell operating point is changed from 0 W to the steady state operating power. In this initial transient, the power requested by the load is mainly extracted from the ASD, which is also later compensated by the SOC controller. The simulation of figure 4-7(a) shows the steady state efficiencies $\eta_{P,sim} = 88.8$ % and $\eta_{S,sim} = 85.1$ % of the parallel and serial topologies, respectively, being the relation between them $f_{x,sim} = \eta_{S,sim}/\eta_{P,sim} = 0.958$.

These simulation results verify the analytical-based conclusion previously obtained by the calculations performed using the nominal values of the power system and load profile. Finally, the small numerical discrepancies between the $f_{x,num}$ and $f_{x,sim}$ values are mainly caused by the low-frequency AC components of the load power supplied by the fuel cell, this because the slew-rate limitation can be approximated by its time response to a second-order low-pass filter with a 2 rad/s cut-off frequency.

ISBN:978-84-692-6902-2/ DL:T-1848-2009

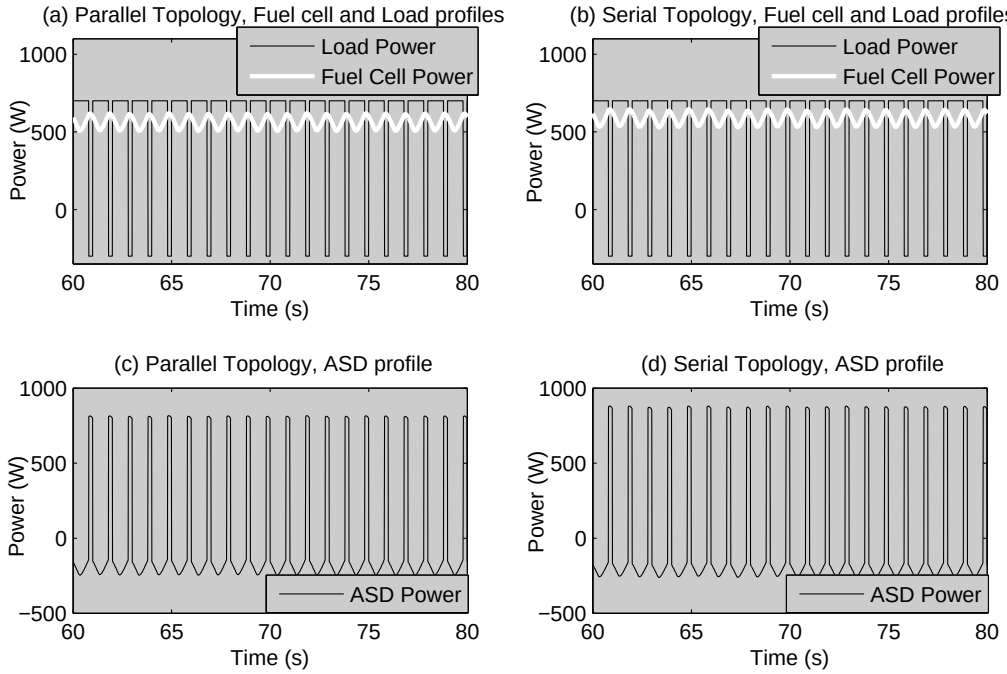


Figure 4-6: Matlab/Simulink-based simulation of example 1 (A = 1 kW, RS = 300 W, Ts = 1 s, D = 80 %).

**Example 2: Load profile with high AC power component**

In this second example it has been considered a similar load profile than in the previous subsection, but in this case the load profile parameters are $A = 1$ kW, $RS = 100$ W, $T_s = 1$ s, and $D = 20$ %. The same efficiencies $\eta_1 = \eta_2 = \eta_3 = 0.93 = \eta_{0,num}$ have also been considered. Following the same procedure presented in example 1, in one period the energies consumed and feed-back by the load can be calculated to $E_{L_{con}} = 180\ J$ and $E_{L_{reg}} = 80\ J$, respectively. The regenerative ratio in this example is $k_R = 0.44$, and the load consumption profile DC and AC components are equal to $P_{L_{DC}} = 100\ W$ and $P_{L_{AC}} = 160\ W$, respectively. Using (4.50) it is calculated $k_{B_{num}} = 0.73$, and from $k_B$ definition (4.16), the power exchanged with the ASD that makes equal the efficiencies of both serial and parallel topologies is $P_{BO_0} = 131.4\ W$. Making the same consideration of example 1, the AC load profile component is exchanged with the ASD, and taking into account the efficiency of the DC/DC converters, it can be calculated as $P_{BO_x,num} = P_{L_{AC}}/\eta_{0,num} = 172\ W$. This power is extracted from the ASD in the consumption stage of the load profile and restored in the regenerative stage.

Using the $k_x$ definition (4.17) $k_{x,num} = 1.31$ and, from the analytical results given in (4.36), it is concluded that the serial topology is more efficient that the parallel one for this new load profile. Also, the numerical value of the efficiencies relation $f_{x,num} = 1.049$ is calculated using (4.18)-(4.19).

ISBN:978-84-692-6902-2/ DL:T-1848-2009

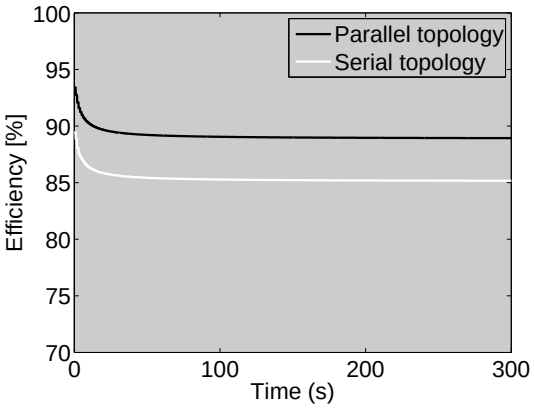


(a) Topologies efficiencies in example 1.

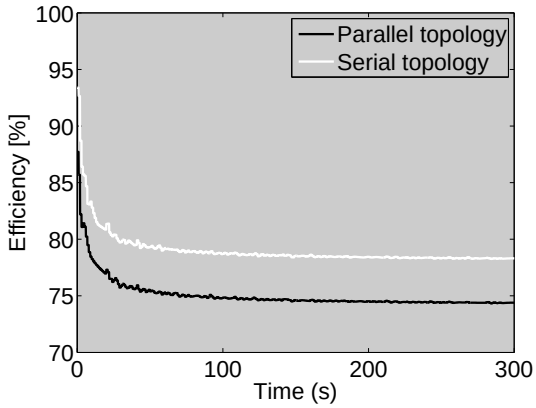


(b) Topologies efficiencies in example 2.

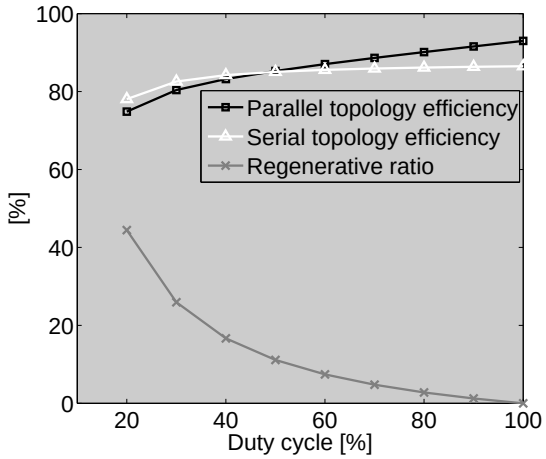


(c) Topologies efficiency and regenerative ratio in {A = 1 kW, RS = 100 W, Ts = 1 s}.

Figure 4-7: Numerical simulation of the serial and parallel hybrid topologies efficiency for pulsating load demands.

A Matlab/Simulink time-based simulation of the efficiency of both topologies, depicted in figure 4-7(b), has been performed considering the new load profile. In this simulation it is again observed an initial transient caused by the start-up of the fuel cell. The steady state efficiencies are $\eta_{P,sim} = 74.65$ % and $\eta_{S,sim} = 78.1$ % for the parallel and serial topologies, respectively, being the relation between them $f_{x,sim} = \eta_{S,sim}/\eta_{P,sim} = 1.046$. Again, the simulation results verify the analytical-based conclusion derived from the calculations performed using the nominal values of the power system and the load profile.

In order to provide a more general validation, additional numerical simulations of the steady-state topologies and regenerative ratio have been performed using a Matlab/Simulink model. Those simulations consider DC/DC converters efficiency of $\eta_1 = \eta_2 = \eta_3 = 0.93 = \eta_{0,num}$, and a load

ISBN:978-84-692-6902-2/ DL:T-1848-2009

profile parameters $A = 1$ kW, $RS = 100$ W, and $T_s = 1$ s. The duty cycle of the load profile has been sequentially modified from 20 % to 100 % in steps of 10 % to cover a wide range of {DC, AC} power profile and regenerative ratio conditions. The simulation results are depicted in figure 4-7(c), where it is observed that for pulsating load profiles with $D < 52.53$ % (high AC component) the serial topology provides a higher efficiency, and with $D > 52.53$ % (high DC component) conditions the parallel topology efficiency is higher. In the figure it is also showed the regenerative ratio for the different duty cycles, which for the load profile considered in this example, can be calculated from equations (4.45), (4.46) and (4.49) as:

$$k_R = \frac{RS}{A - RS} \cdot \frac{1 - D}{D} \tag{4.51}$$

$$\left.\begin{aligned} \lim_{k_R \to 1^-} \eta_S &= \left.\frac{(1 - k_R) \cdot P_L}{P_{fcS}}\right|_{k_R=1} = 0^+ \\ \lim_{k_R \to 1^-} \eta_P &= \left.\frac{(1 - k_R) \cdot P_L}{P_{fcP}}\right|_{k_R=1} = 0^+ \end{aligned}\right\} \tag{4.52}$$

It is observed that the regenerative ratio grows meanwhile the duty cycle decrease, and therefore the net power consumed by the load $\{(1 - k_R) \cdot P_L\}$ also decrease, reducing in this way the power extracted from the fuel cell. This is an important remark because the reduction of both load and fuel cell power profiles generates a reduction in the calculated efficiency, this because the difference between the fuel cell and load powers is more representative with respect to the load net power. In the limit case when the regenerative ratio is near to one, the efficiency of the topologies drops near to zero (4.52) because the net power consumed by the load is near to zero, but the fuel cell still provides a small amount of power in order to compensate the DC/DC converter losses and restore the SOC. But this low efficiency condition at high regenerative ratios does not imply a higher fuel cell power profile than the one requested by the same load consumption in lower regenerative ratio conditions.

Finally, the simulation-based results of the proposed numerical examples verify the analytical results, and therefore also validate the selection criteria proposed in this section, which allows to define the most efficient hybrid topology depending on the application and load profile nominal values.

ISBN:978-84-692-6902-2/ DL:T-1848-2009

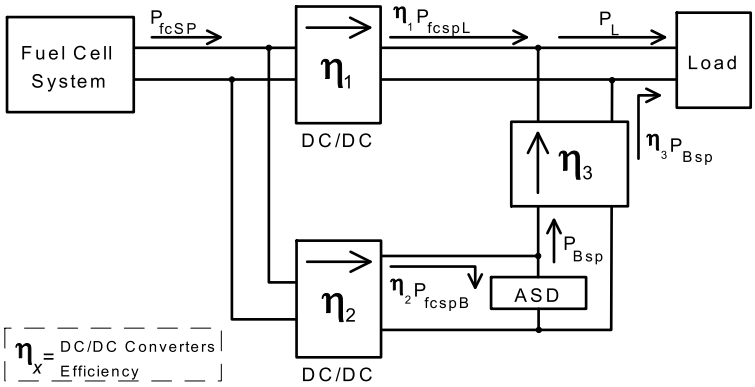


Figure 4-8: Novel serial-parallel hybrid topology

### 4.3.3 Novel Non-regenerative Hybrid Topology Analysis

In the previous section the efficiencies of the most common hybrid topologies considering feed-back power from the load (regenerative load) were analyzed. But there are in the literature several works and applications where non-regenerative hybrid topologies were used [101]-[107]. In this way, the analysis previously presented indicates that the serial topology is more efficient in power profiles that request high ASD energy exchange, and the parallel in the opposite cases. But, the selection criteria proposed require a previous knowledge of the power profile and, moreover, if the load profile suffers changes in its frequency components, the traditional serial or parallel topology selected will not be the most efficient at any time. Therefore, a topology that combines the serial and parallel efficiency advantages for any fuel cell-ASD power profile is desirable. In this way, the topology proposed in figure 4-8 is intended to address this issue, this because it has only one unidirectional converter in any energy flow path considered for non-regenerative applications (fuel cell to load, fuel cell to ASD, and ASD to load).

This novel hybrid topology, named serial-parallel topology, is not considered for regenerative applications because, in that cases, it will require more power converters than parallel and serial options, and therefore the comparisons are not fair.

In non-regerative applications, the regenerative ratio is set to $k_R = 0$, and the fuel cell power requested in parallel ($P_{fc_P}$) and serial ($P_{fc_S}$) topologies are given by (4.53) and (4.54), respectively.

$$P_{fc_P} = \frac{\eta_2 \cdot P_L + (1 - \eta_2 \cdot \eta_3) P_{BO}}{\eta_1 \cdot \eta_2} \tag{4.53}$$

$$P_{fc_S} = \frac{P_L}{\eta_1 \cdot \eta_3} \tag{4.54}$$

Following the methodology presented in the regenerative case for both parallel and serial topologies, and also taking into account the nomenclature of figure 4-8, the fuel cell power requested $P_{fc_{SP}}$

ISBN:978-84-692-6902-2/ DL:T-1848-2009

by the generic power load profile $P_L$ in the serial-parallel topology is given in (4.55)-(4.56), where (4.55) gives the load power equation and the SOC regulation condition.

$$\left.\begin{aligned} P_L &= \eta_1 \cdot P_{fc_{SP}L} + \eta_3 \cdot P_{B_{SP}} \\ P_{B_{SP}} &= \eta_2 \cdot P_{fc_{SP}B} \end{aligned}\right\} \tag{4.55}$$

$$P_{fc_{SP}} = \frac{\eta_2 \cdot P_L + (\eta_1 - \eta_2 \cdot \eta_3)\, P_{BO}}{\eta_1 \cdot \eta_2} \tag{4.56}$$

In order to compare the efficiency of the serial-parallel topology with the parallel and serial options previously presented, two analyses have been carried out. The first comparison is performed between the parallel and serial-parallel topologies, where the conditions for $P_{fc_P} = P_{fc_{SP}}$ derived from (4.57) are: $\{\eta_1 = 1\}$ or $\{P_{BO} = 0\ \mathsf{W}\}$.

$$\left.\begin{aligned} P_{fc_P} &= P_{fc_{SP}} \\ (1 - \eta_2 \cdot \eta_3)\, P_{BO} &= (\eta_1 - \eta_2 \cdot \eta_3)\, P_{BO} \end{aligned}\right\} \tag{4.57}$$

The first condition $\{\eta_1 = 1\}$ is non realistic, and the second one $\{P_{BO} = 0\ \mathsf{W}\}$ assumes null ASD energy flows. Also, from (4.53) and (4.56) it is concluded that in $\{P_{BO} > 0,\ 0 < \eta_1 < 1,\ 0 < \eta_2 < 1,\ 0 < \eta_3 < 1\}$ conditions $P_{fc_P} > P_{fc_{SP}}$. This conclusion can be verified by the reduction of inequation (4.58).

$$\left.\begin{aligned} P_{fc_P} &> P_{fc_{SP}} \\ \frac{\eta_2 \cdot P_L + (1 - \eta_2 \cdot \eta_3)\, P_{BO}}{\eta_1 \cdot \eta_2} &> \frac{\eta_2 \cdot P_L + (\eta_1 - \eta_2 \cdot \eta_3)\, P_{BO}}{\eta_1 \cdot \eta_2} \\ \{1 > \eta_1,\ P_{BO} &> 0\} \end{aligned}\right\} \tag{4.58}$$

In non-regenerative applications, the efficiencies of the parallel ($\eta_P$), serial ($\eta_S$) and serial-parallel ($\eta_{SP}$) topologies are given in (4.59).

$$\left.\begin{aligned} \eta_P &= \frac{P_L}{P_{fc_P}} \\ \eta_S &= \frac{P_L}{P_{fc_S}} \\ \eta_{SP} &= \frac{P_L}{P_{fc_{SP}}} \end{aligned}\right\} \tag{4.59}$$

From (4.53), (4.56), (4.58) and (4.59) it is concluded that for $\{0 < \eta_1 < 1,\ P_{BO} > 0\}$ conditions the serial-parallel topology is more efficient than the parallel option. In the limit case when the load profile is supplied by the fuel cell exclusively ($P_{BO} = 0$ W), equations (4.53) and (4.56) are equal to $\{P_L/\eta_1\}$ and therefore the topologies have the same efficiency. In the other limit case, when the load profile is supplied only by the ASD ($P_{BO} = P_L/\eta_3$), the relation between the efficiencies of the topologies is given by (4.60), and therefore the serial-parallel topology is more efficient. These analyses are summarized in equation (4.61), which implies that in realistic conditions the serial-parallel topology is more efficient than the parallel option, and in the extreme condition when the

ISBN:978-84-692-6902-2/ DL:T-1848-2009

power requested by the load is exclusively supplied by the fuel cell, the topologies exhibit the same efficiency. This means that the lower the power supplied by the ASD, the most comparable the topologies efficiencies.

$$\left.\frac{\eta_{SP}}{\eta_P}\right|_{P_{BO}=P_L/\eta_3} = \frac{1}{\eta_1} > 1 \tag{4.60}$$

$$P_{BO} \geq 0 \Rightarrow \eta_{SP} \geq \eta_P, \quad \forall\ \{0 < \eta_i < 1,\ i = 1..3\} \tag{4.61}$$

A second comparison is performed between the serial and serial-parallel topologies, where the conditions for $P_{fc_S} = P_{fc_{SP}}$ are:

$$\frac{P_L}{\eta_1 \cdot \eta_3} = \frac{\eta_2 \cdot P_L + (\eta_1 - \eta_2 \cdot \eta_3)\, P_{BO}}{\eta_1 \cdot \eta_2} \tag{4.62}$$

$$P_{BO_0} = \frac{\eta_2}{\eta_3} \cdot \frac{1-\eta_3}{\eta_1 - \eta_2 \cdot \eta_3} P_L \tag{4.63}$$

$$k_B = \frac{P_{BO_0}}{P_L} = \frac{\eta_2}{\eta_3} \cdot \frac{1-\eta_3}{\eta_1 - \eta_2 \cdot \eta_3} \quad , \quad 0 \leq k_B \leq 1/\eta_3 \tag{4.64}$$

The same $k_x = (P_{BO_x}/P_{BO_0})$ definition introduced in the previous section has been used to correlate the generic power profile exchanged with the ASD ($P_{BO_x}$) with the equal efficiency limit power ($P_{BO_0}$). Also, the efficiency ratio $f_{x,S-SP}$ between the serial and serial-parallel topologies is given in (4.65). Following the continuity and functional analyses presented in the regenerative case, the efficiency relation (4.66) is obtained.

$$f_{x,S-SP} = \frac{\eta_S}{\eta_{SP}} = (1-\eta_3)k_x + \eta_3 \tag{4.65}$$

$$\left.\begin{array}{l} k_x \leq 1 \ \Rightarrow\ f_{x,S-SP} \leq 1 \ \Rightarrow\ \eta_S \leq \eta_{SP} \\ k_x > 1 \ \Rightarrow\ f_{x,S-SP} > 1 \ \Rightarrow\ \eta_S > \eta_{SP} \end{array}\right\} \tag{4.66}$$

The efficiency comparison between the serial and serial-parallel topologies can be concluded from (4.64) and (4.66). But in order to perform a fair comparison, the efficiencies of the converters that charge the ASD from the fuel cell must be equal in both topologies, and therefore the condition $\eta_1 = \eta_2$ is considered. This implies that $f_{x,S-SP}$ can be simplified to expression (4.67), which depends on the load ($P_L$) and ASD ($P_{BO_x}$) power profiles.

$$f_{x,S-SP} = \frac{\eta_S}{\eta_{SP}} = \eta_3 \left[1 + (1-\eta_3)\frac{P_{BO_x}}{P_L}\right] \leq 1, \quad \forall \left\{0 \leq P_{BO_x} \leq \frac{P_L}{\eta_3}\right\} \tag{4.67}$$

In the limit case when the load power is supplied only by the fuel cell ($P_{BO_x} = 0$ W) the efficiency ratio $\{f_{x,S-SP} = \eta_3 < 1\}$, where $\eta_3$ corresponds to the additional losses between the topologies for this power flow. Also, in the other limit (and non-practical) case, when the load

ISBN:978-84-692-6902-2/ DL:T-1848-2009

power is exclusively extracted from the ASD ($P_{BO_x} = P_L/\eta_3$), the efficiency ratio is unitary and, therefore, the topologies have the same efficiency. These mathematical analyses are summarized in equation (4.68), which implies that in realistic conditions the serial-parallel topology is more efficient than the serial option, and in the extreme case when the load power is exclusively supplied by the ASD, the topologies exhibit the same efficiency. This means that the higher the power supplied by the ASD, the most comparable the topologies efficiencies.

$$\left.\begin{array}{l} 0 \leq P_{BO_x} < \dfrac{P_L}{\eta_3} \Rightarrow \eta_{SP} > \eta_S \\ P_{BO_x} = \dfrac{P_L}{\eta_3} \Rightarrow \eta_{SP} = \eta_S \end{array}\right\}, \quad \forall\ \{0 < \eta_i < 1,\ i = 1..3\} \tag{4.68}$$

**Numerical Examples**

In order to validate the higher efficiency of the proposed serial-parallel topology demonstrated by the analytical results, three numerical examples considering power profiles with different characteristics have been performed. The first profile considers a high AC component represented by a pulsating load power profile ($P_{L1}$) with parameters $A = 500$ W, $RS = 0$ W, $T_s = 1$ s, and $D = 35$ %, and the efficiencies of the considered DC/DC converters are $\eta_1 = \eta_2 = \eta_3 = 0.93 = \eta_{0,num}$. Following the methodology for numerical examples presented in subsection 4.3.2, the DC and AC component of the power profile in one period are $P_{L_{DC}} = 175$ W and $P_{L_{AC}} = 113.75$ W, respectively. The regenerative ratio is set to $k_{R_{num}} = 0$, and using equation (4.50) $k_{B_{num}} = 0.518$ is obtained, which allows to calculate $P_{BO_0} = 90.65$ W and $P_{BO_x} = 122.31$ W.

From the $k_x$ definition (4.17) its numerical value is $k_{x,num} = 1.35$, and from the analytical results given in (4.36) it is concluded that, for this non-regenerative load profile, the serial topology is more efficient than the parallel one. Also, from the analyses summarized in (4.61) and (4.68) it is concluded that the serial-parallel topology is more efficient than both serial and parallel traditional topologies.

By using a Matlab/Simulink-based simulation of the three topologies, the efficiency of each topology for the same load profile has been obtained. The simulation results are depicted in figure 4-9(a), where the steady states efficiencies of the parallel, serial and serial-parallel topologies are $\eta_P = 84.4$ %, $\eta_S = 86.5$ %, and $\eta_{SP} = 88.7$ %, respectively. These simulation results verify both the analytical results and the higher efficiency of the serial-parallel topology in this high AC-dominant power component load profile.

ISBN:978-84-692-6902-2/ DL:T-1848-2009

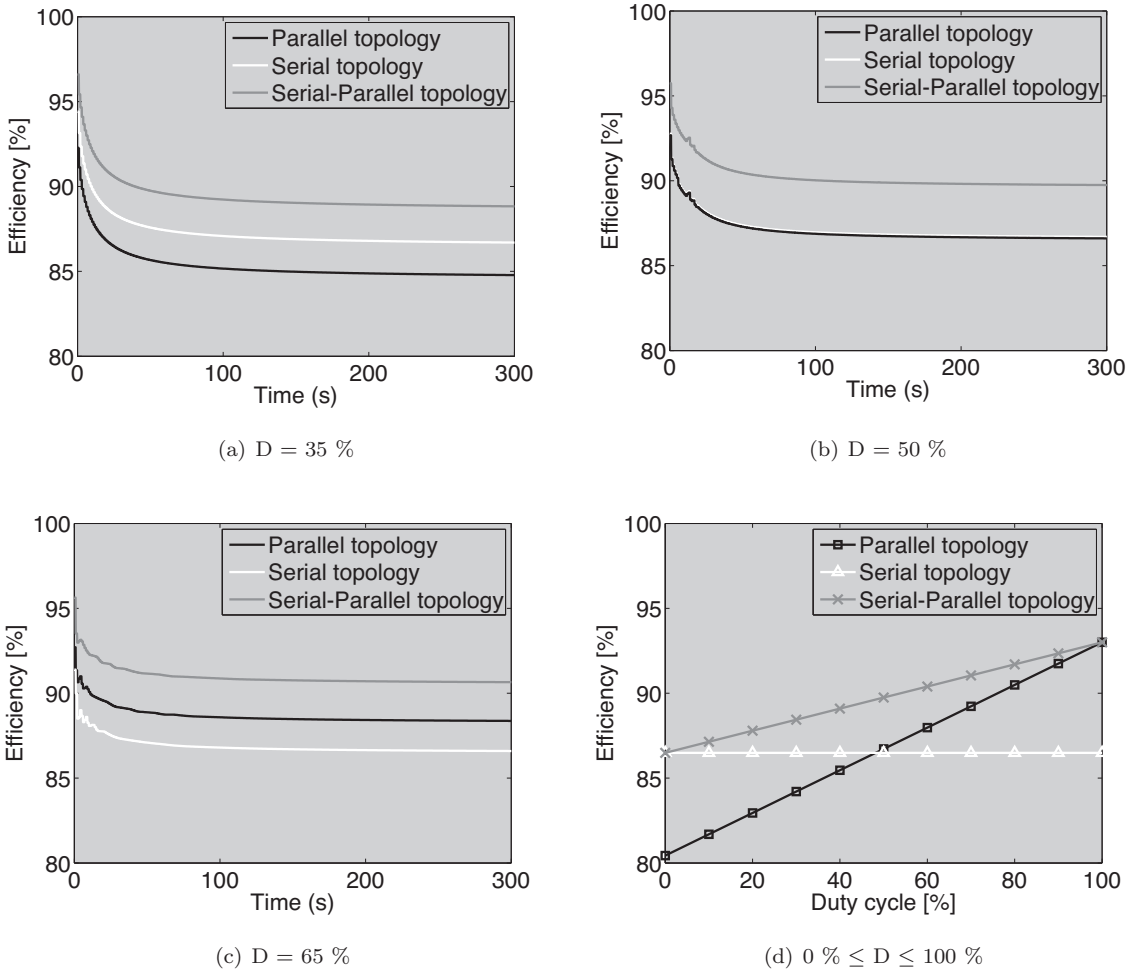


(a) D = 35 %

(b) D = 50 %

(c) D = 65 %

(d) 0 % ≤ D ≤ 100 %

Figure 4-9: Numerical simulation of the serial, parallel and serial-parallel hybrid topologies efficiency for non-regenerative pulsating load demands.

A second numerical example is presented considering a load power profile $P_{L2}$ with the same parameters than $P_{L1}$ but with a different duty cycle $D = 50$ %. In this example, the DC and AC components of the load power profile in one period are $P_{L_{DC}} = 250$ W and $P_{L_{AC}} = 125$ W, respectively. The regenerative ratio is set to $k_{R_{num}} = 0$, and it is calculated that $k_{B_{num}} = 0.518$, $P_{BO_0} = 129.5$ W, $P_{BO_x} = 134.4$ W, and $k_{x,num} = 1.03$. Finally, from (4.36) it is concluded that, for this $P_{L2}$ load profile, the difference in the serial and parallel topologies efficiencies is very small, this because $k_x$ is near to 1, but the serial topology efficiency still slightly higher. Again, from the analyses given in (4.61) and (4.68), it is concluded that the serial-parallel topology is more efficient than both serial and parallel topologies.

The analytical-based results have been validated using a Matlab/Simulink-based simulation of the three topologies for this $P_{L2}$ ($D = 50$ %) load profile. The simulation results are depicted in figure 4-9(b), where the steady state efficiencies of the parallel, serial and serial-parallel topologies

ISBN:978-84-692-6902-2/ DL:T-1848-2009

are $\eta_P = 86.3$ %, $\eta_S = 86.5$ %, and $\eta_{SP} = 89.6$ %, respectively. These simulation results verify the analytical results, and also confirm the improved efficiency of the serial-parallel topology for this load profile. In addition, the duty cycle that makes both serial and parallel topologies efficiency equal ($k_x = 1$) is $D = 51.81$ %, in which the serial and parallel topologies efficiency are $\eta_S = \eta_P = 86.5$ %, instead the serial-parallel topology efficiency is $\eta_{SP} = 89.7$ % for this duty cycle.

The third numerical example considers a load power profile $P_{L3}$ with a duty cycle $D = 65$ %. In this new condition the load power profile DC and AC components, in one period, are $P_{L_{DC}} = 325$ W and $P_{L_{AC}} = 113.75$ W, respectively. The regenerative ratio is set to $k_{R_{num}} = 0$, and also $k_{B_{num}} = 0.518$, $P_{BO_0} = 168.35$ W, and $P_{BO_x} = 122.3$ W are calculated. Since $k_{x,num} = 0.73$, it is concluded that the parallel topology is more efficient than the serial option for this $P_{L3}$ load profile. Finally, the analytical results given in (4.61) and (4.68), indicate that the serial-parallel topology is more efficient than both serial and parallel topologies.

The Matlab/Simulink-based simulation of the three topologies for this $P_{L3}$ load profile are plotted in figure 4-9(c), where the steady state efficiencies of the parallel, serial and serial-parallel topologies are $\eta_P = 88.2$ %, $\eta_S = 86.5$ %, and $\eta_{SP} = 90.6$ %, respectively. These results verify the analytical conclusions, and also confirm that the serial-parallel topology is the most efficient for this load profile.

To cover a wider range of {DC, AC} conditions additional simulations have been performed, in which the duty cycle of the load profile has been changed form 0 % to 100 % in steps of 10 %. The simulations results are plotted in figure 4-9(d), where it is observed that in non-regenerative pulsating load profiles with $D < 51.81$ % (high AC component) the serial topology has higher efficiency than the parallel one, but the novel serial-parallel topology is the most efficient. In the same way, for $D > 51.81$ % (high DC component) conditions the parallel topology efficiency is higher than the serial one, but again the serial-parallel topology efficiency is better.

In conclusion, the mathematical analysis and numerical simulations confirm that the proposed novel serial-parallel hybrid topology has higher efficiency than the typical parallel and serial options in non-regenerative applications, requiring lower fuel cell power to supply a load profile, and therefore generating lower hydrogen consumption. This higher efficiency condition of the novel serial-parallel topology is also non-depending on the load profile, making it ideal for unknown, non-predictable or wide-frequency excursion load profiles. The main disadvantage of this new topology resides in the DC/DC converters control design, since it requires to take into account the non-linear regulation of the converters that interact with the fuel cell, and also the cooperative SOC and load bus regulation. Those are interesting research issues, since the literature offers analytical tools to address those challenges [119] [120]. In this way, the fuel cell control approaches and power electronics anal-

ROVIRA I VIRGILI UNIVERSITY
FUEL CELL MODELING AND CONTROL FOR FUEL CONSUMPTION OPTIMIZATION
Carlos Andres Ramos Paja
ISBN:978-84-692-6902-2/ DL:T-1848-2009

ysis and design presented in the next sections are restricted to the serial and parallel topologies, since the novel serial-parallel topology requires additional analysis of implementation problems and more complex control approaches, and therefore it is proposed for further developments and future works. Similarly, the extension of this serial-parallel topology to consider regenerative power flows will require more DC/DC converter than both serial and parallel options. In this case, the viability analysis considering the higher efficiency provided but the higher cost and weight must be performed.

Finally, the flow chart for the hybrid topology selection procedure is summarized in figure 4-10.

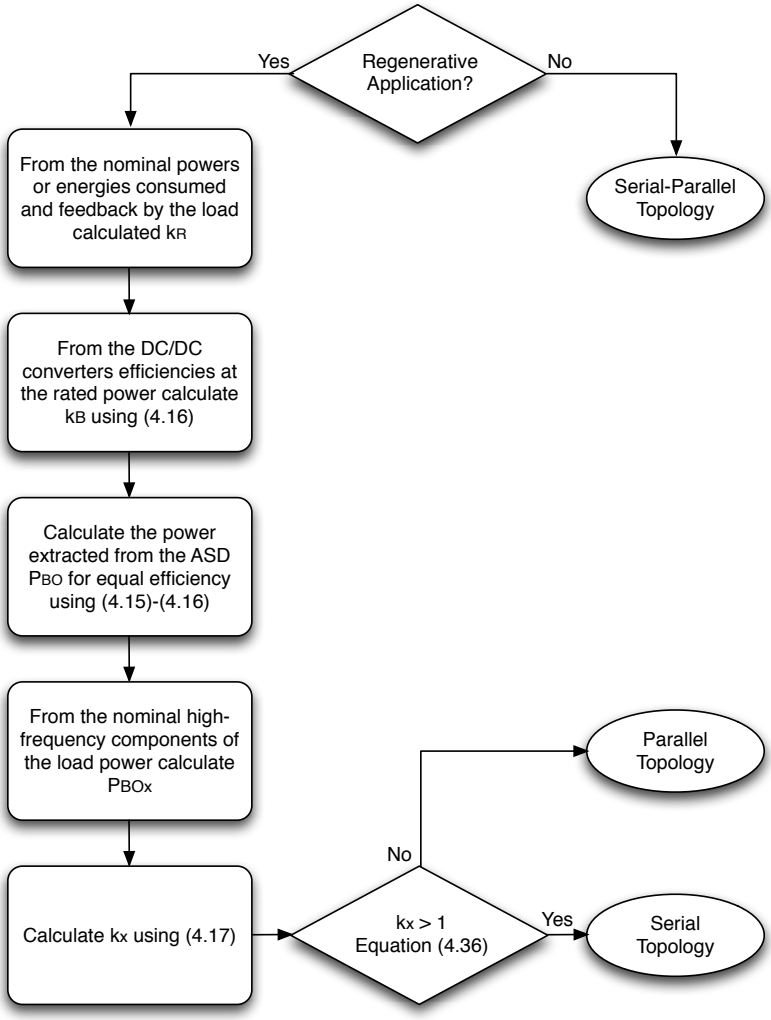


Figure 4-10: Hybrid topology selection flow chart.

ISBN:978-84-692-6902-2/ DL:T-1848-2009

## 4.4 Fuel cell control

In this work, the fuel cell control is designed to regulate the oxygen excess ratio in a safe and efficient state. This $\lambda_{O_2}$ regulation is an important issue since this variable determines the safety of the fuel cell and gives information about the relation of the energy produced and the air compressor consumption to produce it. In this way, Pukrushpan et al. propose to regulate $\lambda_{O_2} = 2$ to guarantee safety and to provide high efficiency [1] in a 75 kW fuel cell, and Arce et al. demonstrate that the maximum constant $\lambda_{O_2}$ value that can be regulated in a 1.2 kW Nexa power module without air pump saturation is $\lambda_{O_2} = 3.29$ [27], and also that this value is near to the maximum efficiency points, this consuming less hydrogen to supply the load. In summary, positive deviations of $\lambda_{O_2}$ from the reference value imply low efficiency and negative deviations increase the oxygen starvation phenomenon probability.

The $\lambda_{O_2}$ control strategies presented in this chapter have been designed using a linearized model of the 1.2 kW Nexa power module, which depends on the fuel cell current $I_{st}$ and on the air pump voltage control $V_{ap}$ obtained in [27] and employed in (4.69). The linearization has been made around an operating point of 15 A and 69.9 % of the maximum air pump control voltage, which is in the middle of the linear zone of the polarization curve.

$$\lambda_{O_2}(s) = \begin{bmatrix} \dfrac{0.01218s^2 + 0.01802s + 0.7242}{s^3 + 3.45s^2 + 7.324s + 5.745} \\ \dfrac{-0.2659s - 0.001432}{s + 0.005318} \end{bmatrix}^T \begin{bmatrix} V_{ap}(s) \\ I_{st}(s) \end{bmatrix} \tag{4.69}$$

In the next subsections PEMFC power systems and control structures for both parallel and serial hybrid topologies are analyzed and designed to achieve the control objectives proposed in section 4.2.

### 4.4.1 Parallel hybrid topology approach

The parallel topology is recommended for load power profiles with a dominant DC component, or also when the power plant includes multiple energy sources. Figure 4-11 shows a typical scheme for a fuel cell-based parallel hybrid topology, where the fuel cell power electronics interface consist on an unidirectional DC/DC converter, which in this case has the main objective of restrict the fuel cell power slew-rate. The ASD is interconnected to the bus by a bidirectional DC/DC converter, where its main objectives are control the DC bus voltage and regulate the ASD SOC. In this application example it is required to provide a 350 V DC bus that support transients of 30 % of the nominal power, which in example is a typical requirement in Advanced Data Centers (ADC) and Telecom systems [121].

ISBN:978-84-692-6902-2/ DL:T-1848-2009

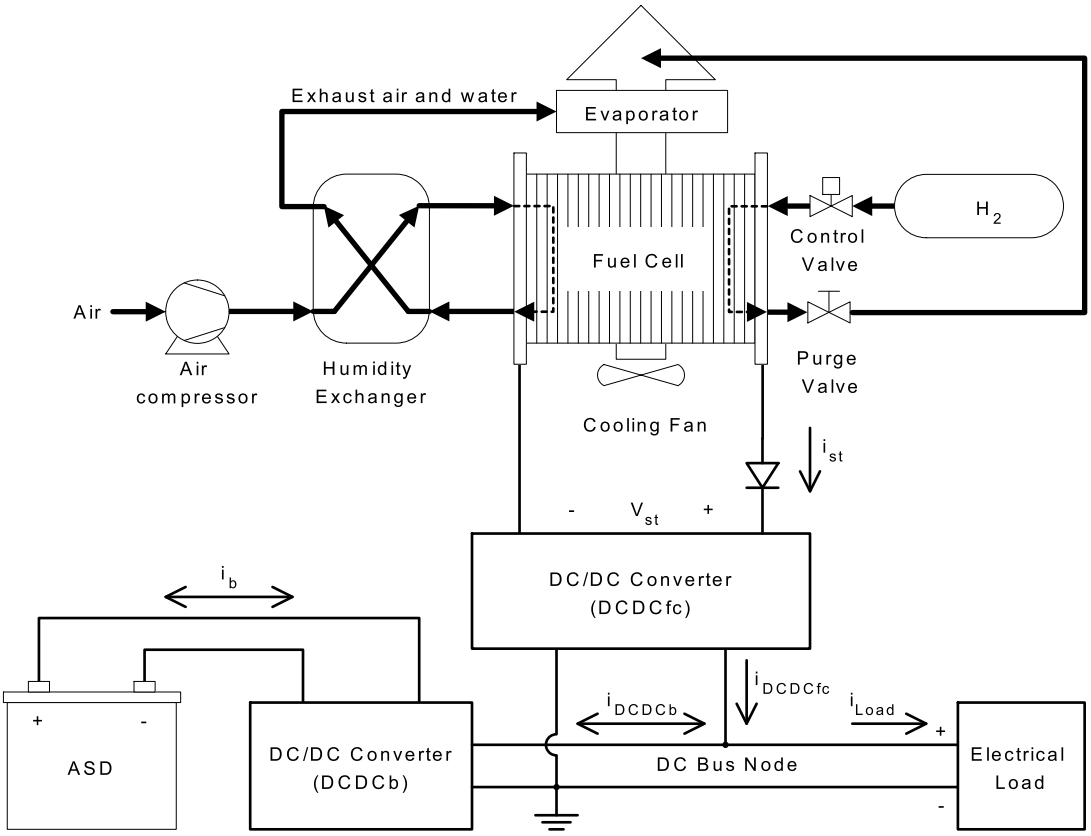


Figure 4-11: Parallel hybrid topology.

Following the Arce et al. recommendation, the $\lambda_{O_2}$ reference is set to 3.29, and a digital fuel cell controller is designed using a discretization of the $\lambda_{O_2}$ control-oriented model given in (4.69). The fuel cell controller was designed in digital domain to allow its implementation in portable and embedded digital processing systems. The selected sampling time was $T_s = 1$ ms, this leading to the follows $\lambda_{O_2}$ discrete model:

$$\lambda_{O_2}(z) = \frac{10^{-5}\left(1.217z^2 - 2.432z + 1.215\right)}{z^3 - 2.997z^2 + 2.993z - 0.9966}\, V_{ap}(z) + \frac{-0.2659z + 0.2659}{z - 1}\, I_{st}(z) \tag{4.70}$$

From (4.70) a digital controller with a response time according with the air compressor constant time and with a maximum over-impulse of 50 % has been designed. This controller has feed-forward and feed-back components, where the first one has a fast response to modify the air flow in agreement with the current demand, and the second one ensures a null steady-state error and limits the over-impulse to avoid oxygen starvation situations ($\lambda_{O_2} < 1$). The designed controller is given in (4.71), where $e_{\lambda_{O_2}}(z)$ represents the $\lambda_{O_2}$ deviations from the reference, and it has the same sampling time of the model (1 ms).

$$V_{ap}(z) = 5.033\left(\frac{z - 0.9976}{z - 1}\, e_{\lambda_{O_2}}(z)\right) + 1.998\, I_{st}(z) + 39.987 \tag{4.71}$$

ISBN:978-84-692-6902-2/ DL:T-1848-2009

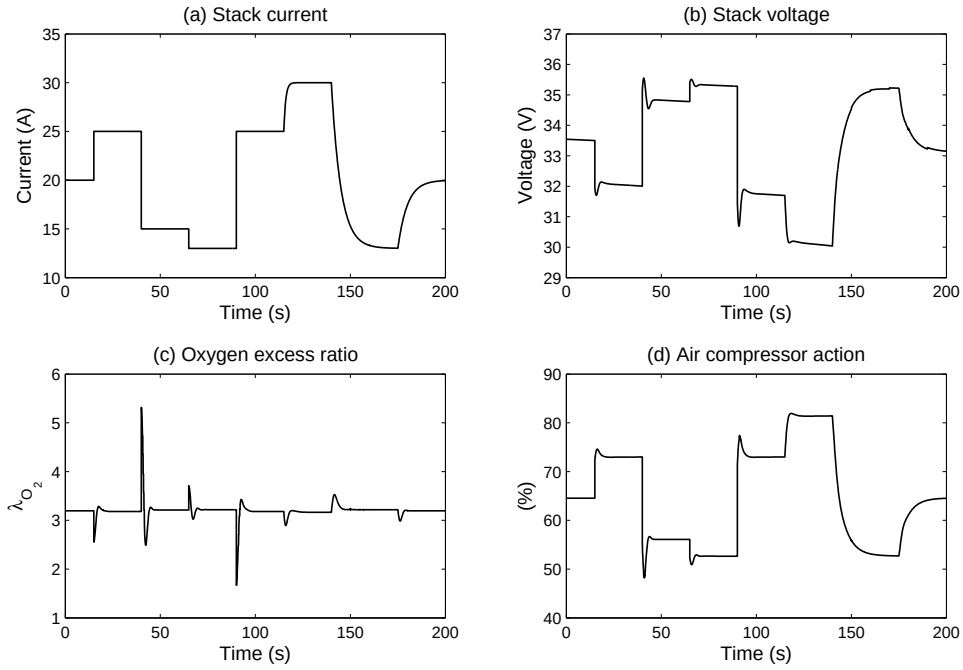


Figure 4-12: Oxygen excess ratio control ($\lambda_{O_2}$).

Figure 4-12 shows the non-linear model behavior under the controller action, where it is observed a satisfactory $\lambda_{O_2}$ regulation (4-12(c)) in response to step-up and step-down stack current transients (4-12(a)). These current transients have high and low frequency ranges, where the first four transients ($0\ \mathsf{s} \leq t \leq 100\ \mathsf{s}$) are high frequency steps and the last tree ones ($100\ \mathsf{s} < t \leq 200\ \mathsf{s}$) are low frequency transitions. Simulations show that in low frequency transients the $\lambda_{O_2}$ deviations are much lower than in the high frequency range (15 % of the deviation). Similarly, in the low frequency range the stack voltage profile is smoother (4-12(b)), which implies lower frequency disturbances in the DC/DC converter interface (DCDCfc). Figure 4-12(d) exhibits the air compressor control signal profile, which has high and low frequency transients in agreement with the current profile, and where the smooth behavior is desirable because it implies less heating in the compressor allowing it to operate in the linear zone.

The fuel cell interface DC/DC converter (DCDCfc) is a boost converter whose parameters are: $L = 3.2$ mH, $C = 100\ \mu\mathsf{F}$, $R_L = 40\ \mathsf{m}\Omega$, $R_C = 33\ \mathsf{m}\Omega$, switching frequency of 100 kHz, $V_g = 40$ V (input voltage), $V_o = 350$ V (output voltage). The control strategy of this converter implements a digital inductor current control, which has a dynamic compensation ramp for the digital PWM (DPWM) current control as is described in [122]. The inductor current reference corresponds to the stack current profile, whose slew-rate restriction is dynamically calculated by dividing the selected stack power slew-rate into the measured stack voltage. In this application the power slew-rate was set to 200 W/s (250 W/s - 20 %) due to the simplicity of the fuel cell and DCDCfc controllers.

ROVIRA I VIRGILI UNIVERSITY
FUEL CELL MODELING AND CONTROL FOR FUEL CONSUMPTION OPTIMIZATION
Carlos Andres Ramos Paja
ISBN:978-84-692-6902-2/ DL:T-1848-2009

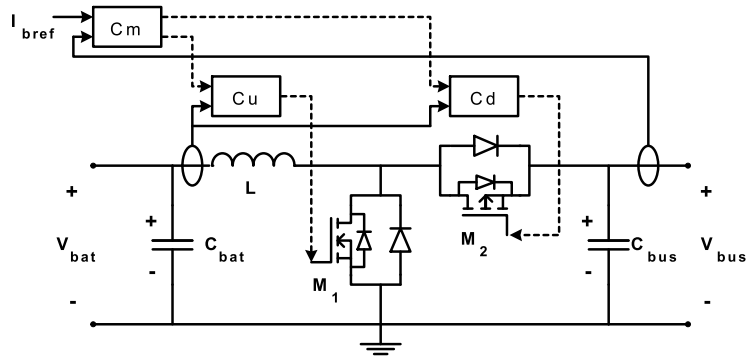


(a) DCDCb circuit and control scheme.

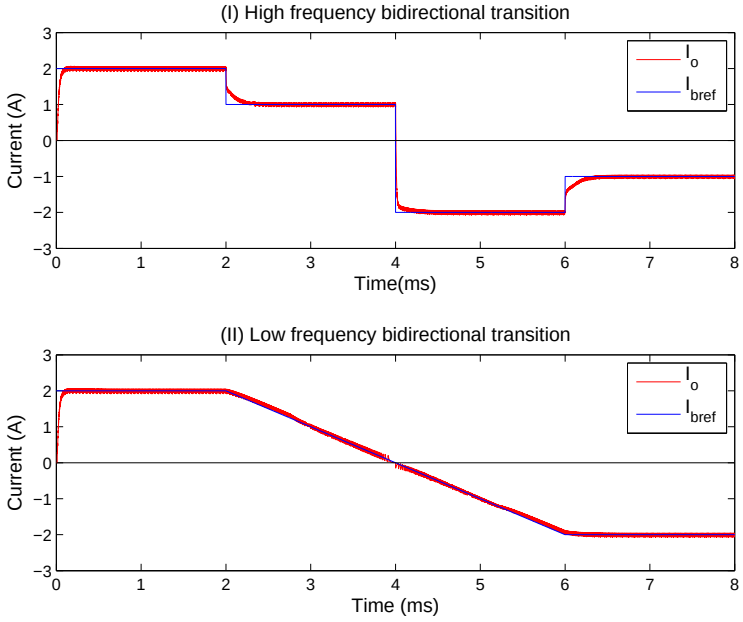


(b) DCDCb dynamic simulation.

Figure 4-13: Bidirectional DC/DC converter DCDCb.

### Bidirectional DC/DC converter control design

The bidirectional DC/DC converter (DCDCb) used to interface the ASD allows to regulate the 350 V DC bus voltage by supplying or absorbing load power. The ASD considered in this theoretical exercise is a 220 V - 10 Ah lead-acid battery constituted by 18 cells of 12 V each one, which is commonly used in industrial environments. The battery model used is a Thevenin model [123].

The DCDCb converter was designed to allow voltage elevation on ASD-Load direction (boost direction) and reduction in Load-ASD direction (buck direction). The circuital scheme is given in figure 4-13(a), which has a boost and buck topologies sharing the inductor L allowing the design

ISBN:978-84-692-6902-2/ DL:T-1848-2009

of conventional current control strategies. The converter operation has two stages: first, the power deliver stage where the MOSFET M2 is inactive and MOSFET M1 is controlled by Cu to follow the current reference in the inductor. Cu is an average current control and its current reference is defined by a cascade supervisor controller Cm. This Cm controller generates the current reference for Cu to follow the given ASD-to-bus current $I_{bref}$.

The second operation stage is the absorption power stage, where M1 is inactive and M2 is controlled by Cd and Cm, Cd is an average current control and the control behavior is equivalent to the described in the power deliver stage, but in this case Cd follows the $I_{bref}$ current reference to define the bus-to-ASD current. Cm controller generates zero current reference for Cu (M1) or Cd (M2) to disable them according to the operation stage definition previously described. Also, Cm controller has a Proportional-Integral (PI) regulation strategy designed to achieve null steady-state error, null maximum over-impulse, and a maximum stabilization time of 0.5 ms in response to 1 A (350 W) load transients. These design characteristics makes the DCDCb constant time two magnitude orders lower than the fuel cell time constant allowing the decoupling of both systems.

The DCDCb parameters are $C_{bat} = 100\ \mu\mathsf{F}$, $C_{bus} = 53.5\ \mu\mathsf{F}$, $L = 47\ \mu\mathsf{H}$, $V_{bat} = 220\,\mathrm{V}$, $V_{bus} = 350$ V and switching frequency of 400 kHz. The transfer function of the reference controller in Cm is $G_{rud}(s) = 2\ (s + 10^4)/(s)$. Figure 4-13(b) depicts the regulation simulation of DCDCb, where the input/output bus-interface current $\mathsf{I_o}$ is controlled in the deliver ($\mathsf{I_o} > 0$) and absorption ($\mathsf{I_o} < 0$) power stages. The control scheme exhibits a satisfactory performance in high frequency reference transients and operation transitions as is showed in figure 4-13(b)(I), and also in low frequency reference transients and operation transitions the behavior is the expected (figure 4-13(b)(II)), which confirms the accomplishment of the control requirements.

The Cm current reference $i_{bref}$ (4.72) is defined to compensate the power difference between the load and fuel cell caused by its power slew-rate restriction, where $P_{Load}$ and $P_{DCDCfc}$ are the electric powers of the load and DCDCfc converter, respectively, and $V_{bus}$ the load (bus) voltage.

$$i_{bref} = \left(P_{Load} - P_{DCDCfc}\right)/V_{bus} = i_{Load} - i_{DCDCfc} \tag{4.72}$$

In this application the SOC of the battery is regulated reducing or incrementing the time taken to make zero the battery current (in both directions), being the SOC estimated through the battery voltage, this allowing to guarantee the nominal charge/discharge cycles. This simple method is enough given the time constant of the fuel cell and the reduced battery model used in the simulations, but in real applications a more accurate SOC estimation will be required, which is not the subject of this section.

ISBN:978-84-692-6902-2/ DL:T-1848-2009

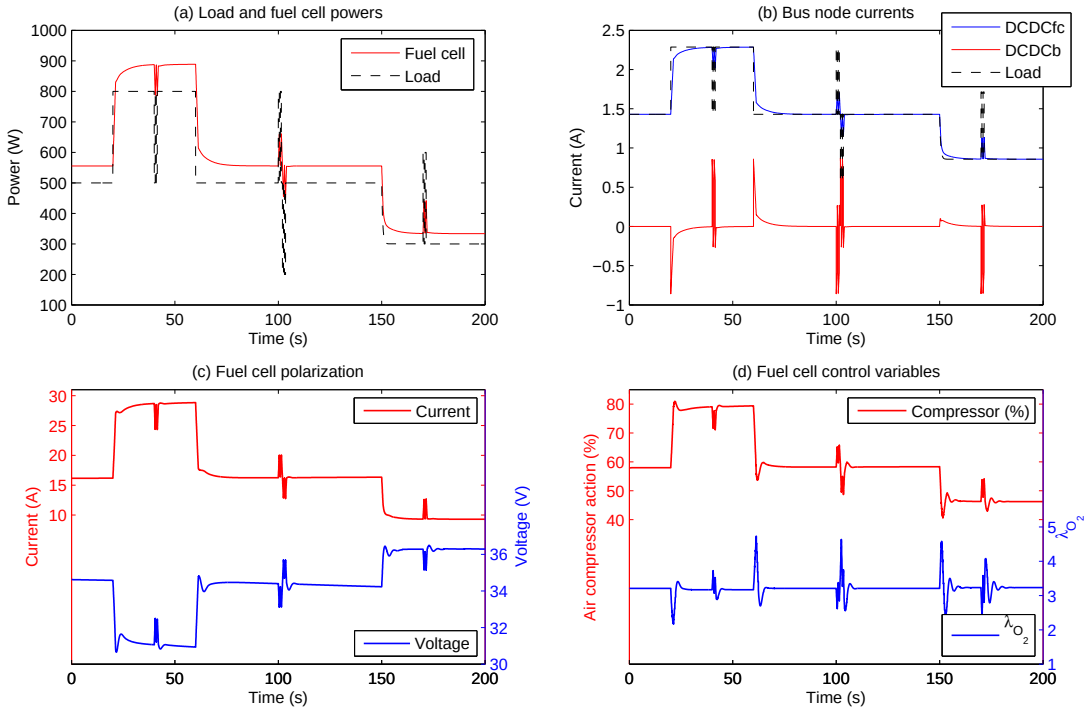


Figure 4-14: Dynamic system response simulation.

### Simulation results

The simulation of the proposed parallel hybrid fuel cell power system is performed by using a power load profile that exhibits transients between 25 % and 30 % of the nominal power. Figure 4-14 depicts the system dynamic response, where figure 4-14(a) shows the load and fuel cell power profiles. The simulation reveals that the fuel cell produces a power in excess of 11 % over the requested by the load to compensate the DCDCfc losses, whose efficiency was considered equal to 90 %. The bus node currents given in figure 4-14(b) illustrate the fuel cell power slew-rate restriction, where the DCDCb converter compensate this effect and adjust its current (supply or absorption) to maintain the bus voltage. Figures 4-14(c) and 4-14(d) show the fuel cell polarization and control, where the $\lambda_{O_2}$ regulation is satisfactory allowing a safe operation near of an acceptable efficiency zone. Figure 4-15 presents a zoom of the simulation results in high and low frequency transients. In this way, figure 4-15(a) shows the load and fuel cell power profiles in high frequency transients, where it can be observed the power slew-rate restriction applied to the fuel cell by DCDCfc converter. Figure 4-15(b) shows the bus node currents in the same conditions, where the battery supply the high frequency components of the load profile. Similarly, figure 4-15(c) depicts the fuel cell and load power profiles for low frequency transients, where the power slew-rate restriction systems affects only in

ISBN:978-84-692-6902-2/ DL:T-1848-2009

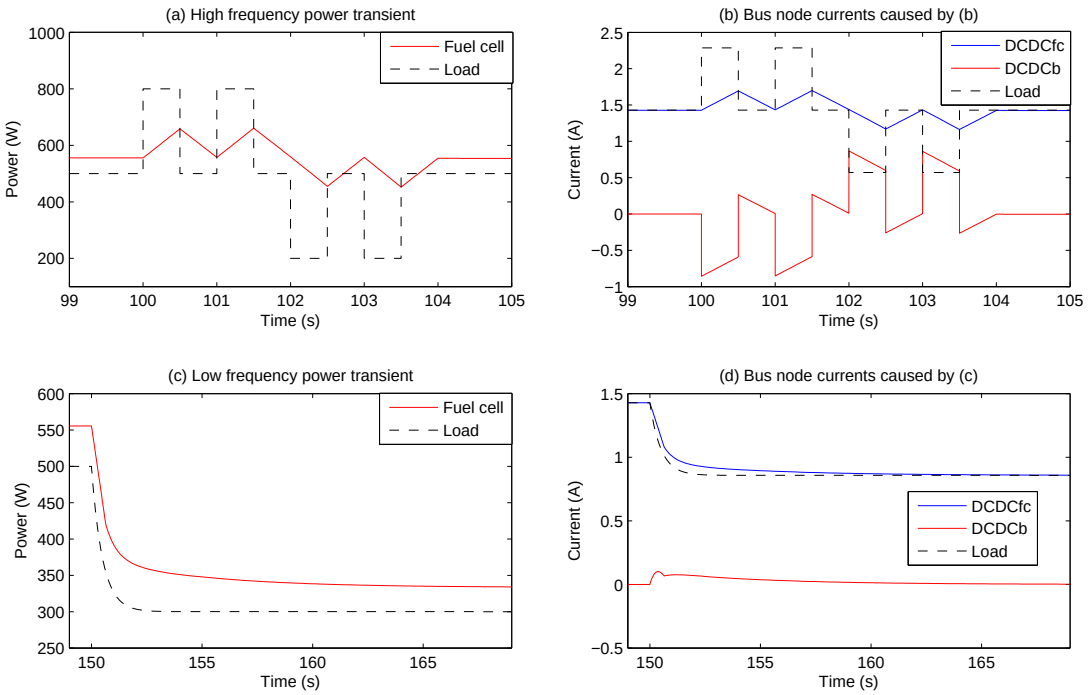


Figure 4-15: High and low frequency power transients response.

the beginning of the transient. This is corroborated by the bus node current profiles given in figure 4-15(d), where the battery supplies a small amount of current and the fuel cell provides almost all the load current.

Finally, the fuel cell power system proposed for a regulated DC bus using batteries as ASD in parallel hybrid topologies allows a safe operation, allowing a satisfactory oxygen excess ratio regulation and a fuel cell operation in an acceptable efficiency zone, this respecting the dynamic limitations of the fuel cell and the control objectives proposed in this chapter.

### 4.4.2 Serial hybrid topology approach

The serial topology presented in figure 4-16 must be used to supply load power profiles with high frequency components (AC component dominant), or also when it is required a semi-regulated DC bus applications where the load regulation converter is owned by the load. This is commonly in automotive applications where the electronic loads (electronic fuel injection system, ABS break system, radio, etc.) have each one its particular supply voltage regulator.

ISBN:978-84-692-6902-2/ DL:T-1848-2009

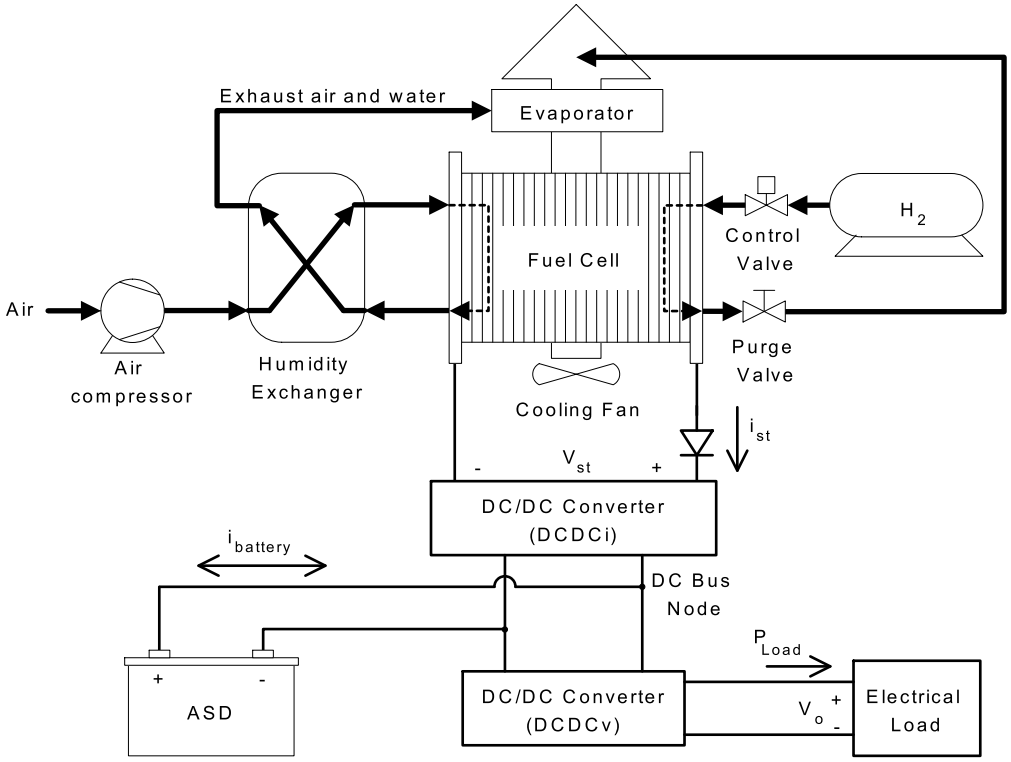


Figure 4-16: Serial hybrid topology.

From the oxygen excess ratio definition it is observed that variations on the stack current are transmitted directly to $\lambda_{O_2}$. In this section it is proposed to filter this current to provide a constrained $\lambda_{O_2}$ regulation, and therefore more safety and efficiency control results. Other important issue is the air pump saturation and heating, since these cause non-linear behaviors and increase power losses. The final consideration is the fuel cell power slew-rate restriction, which has been set to $S_{Rfc} = 300$ W/s (250 W/s + 20 %) based on the mechanical considerations of section 4.2 and on the robust characteristic of the $\lambda_{O_2}$ QFT controller proposed in this section.

From the above considerations, the following design constraints are formulated: a) for current transients lower than 10 A, $\lambda_{O_2}$ deviations must be constrained to $\pm 1$, b) the air pump must not be saturated, c) the air flow must not have high-frequency oscillations to avoid excessive heating.

The control design was performed using the $\lambda_{O_2}$ control-oriented model given in (4.69), and the $\lambda_{O_2}$ reference was set to 3.29 by the same reasons given in the parallel hybrid topology control design of the previous section. The $\lambda_{O_2}$ model can be rewritten as (4.73) to allow a better nomenclature in the controller design, where $V_{ap}$ represents the air compressor control signal and $I_{st}$ the stack current.

$$\left.\begin{aligned} \lambda_{O_2}(s) &= P1(s)I_{st}(s) + P2(s)V_{ap}(s) \\ P1(s) &= -\frac{26.6s + 0.14}{10^2 s + 0.53} \\ P2(s) &= \frac{10^{-2}(1.22s^2 + 1.80s + 72.42)}{s^3 + 3.45s^2 + 7.32s + 5.75} \end{aligned}\right\} \tag{4.73}$$

ISBN:978-84-692-6902-2/ DL:T-1848-2009

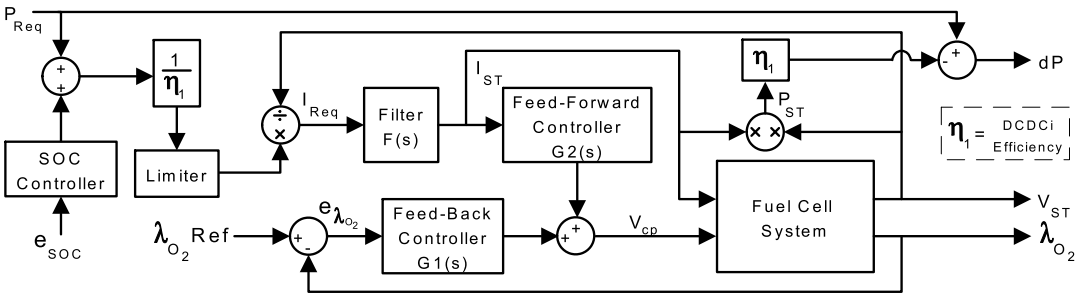


Figure 4-17: Control structure.

The control structure designed in this section is presented in figure 4-17. In this structure the power requested to the fuel cell is regulated to control the SOC of the battery, and it is also limited to avoid damages. The current requested to the fuel cell is defined first to fulfill the power demand, and is later filtered by $F(s)$ in order to suppress high-frequency components, respecting the maximum considered power slew-rate of $S_{Rfc}$. Assuming the lower safe stack voltage condition (26 VDC), the maximum current slew-rate corresponds to the time-domain designed filter transfer function given in (4.74).

$$F(s) = \frac{9}{s^2 + 6s + 9} \tag{4.74}$$

Since the requested filtered current $I_{st}$ can be considered as a known perturbation that must be canceled to regulate $\lambda_{O_2}$, it is proposed to regulate the air compressor action by feed-forward and feed-back controllers. While the feed-forward controller $G2(s)$ provides anticipative action to cancel the effects of the requested current changes [124], the feed-back controller $G1(s)$ provides tight regulation of $\lambda_{O_2}$ whereas maintains robust stability.

The feed-forward transfer function $G2(s)$, given in (4.75), was designed according to the air compressor dynamics to obtain a phase margin of 60° and a gain margin of 10 dB, where $V_{ap,I_{st}}(s)$ is the air compressor control component provided by this controller.

$$\left.\begin{aligned} V_{ap,I_{st}}(s) = G2(s)I_{st}(s) + 39.98 \\ G2(s) = 1.2 \end{aligned}\right\} \tag{4.75}$$

The feed-back controller $G1(s)$ was designed using QFT control theory concepts, in order to robustly satisfy the design constraints. This feed-back controller is described in the next subsection.

The SOC controller regulates the battery charge to guarantee a nominal number of charge cycles, and it maintains the battery in the required conditions for assisting in load transients. This controller modifies the power generated by the fuel cell in two domains: a) In non-saturation conditions, the

ISBN:978-84-692-6902-2/ DL:T-1848-2009

controller makes a fine-tuning using the control-to-output transfer function (4.76), which gives the relation between the change in the power requested $\Delta P_{fc_{SOC}}(s)$ and the error in the SOC $e_{soc}(s)$. This controller was designed to achieve null steady-state error with low frequency response. b) In overload situations, when the battery SOC changes excessively fast, the SOC controller keeps the power request saturated until the SOC reaches the fine-tuning zone.

$$\Delta P_{fc_{SOC}}(s) = 100\frac{15s + 0.7}{s}e_{soc}(s) \tag{4.76}$$

Finally, to avoid fuel cell stress, its maximum power was limited to 1 kW. This limitation and the current filtering generate a difference $dP$ between the power requested and the generated that is supplied by the battery.

### $\lambda_{O_2}$ QFT Control Design

Quantitative feedback theory is a robust control design method, which is based in the frequency response of the system to control. Such frequency response is plotted against the numerical solution of closed loop inequalities which impose stability or performance constraints [125, 126].

In this particular case the requirements of the closed-loop system are: a) reject current perturbations, b) avoid air pump saturation, c) assure robust stability. The first requirement can be expressed as a gain constraint of the closed-loop transfer function between $\lambda_{O_2}$ and the perturbation $I_{st}$:

$$\frac{\lambda_{O_2}(s)}{I_{st}(s)} = F(s)\frac{P1(s) + P2(s)G2(s)}{1 + P2(s)G1(s)} \tag{4.77}$$

For an oxygen excess ratio of $\pm 1$ in front of a step current perturbation of 10 A, it can be approximated the closed loop requirement (perturbation rejection criteria) as

$$\begin{gathered}\left|F(s)\frac{P1(s) + P2(s)G2(s)}{1 + P2(s)G1(s)}\right| \leq \delta_1, \\ \delta_1 := \tfrac{1}{10}, \quad s = j\omega, \quad \forall\ \omega < 0.1\ rad/s.\end{gathered} \tag{4.78}$$

The second requirement refers to the amplitude of the control signal $V_{ap}$, which must be limited to avoid undesired saturations ($V_{ap} \leq 100$) taking into account the maximum current transient considered (10 A). The transfer function between the control signal and the maximum expected perturbation is

$$\frac{V_{ap}(s)}{I_{st}(s)} = F(s)\frac{G2(s) - P1(s)G1(s)}{1 + P2(s)G1(s)}, \tag{4.79}$$

ISBN:978-84-692-6902-2/ DL:T-1848-2009

which has been constrained with the following requirement (control signal limitation criteria):

$$\begin{array}{c}\left|F(s)\dfrac{G2(s)-P1(s)G1(s)}{1+P2(s)G1(s)}\right|\leq\delta_2,\\ \delta_2:=\frac{100}{10},\quad s=j\omega,\quad\forall\,\omega>0\;rad/s.\end{array}\tag{4.80}$$

Besides of the previous performance constraints, the system must also maintain stability and acceptable damping properties. Such properties will be assured maintaining a minimum phase margin of 60° and a gain margin larger than 10 dB. This can be achieved by bouncing the input-output closed-loop transfer function ($\lambda_{O_2Ref}$ is the controller reference) given in (4.81) as described in (4.82).

$$\frac{\lambda_{O_2}(s)}{\lambda_{O_2Ref}(s)}=\frac{P2(s)G1(s)}{1+P2(s)G1(s)}\tag{4.81}$$

$$\begin{array}{c}\left|\dfrac{P2(s)G1(s)}{1+P2(s)G1(s)}\right|\leq\delta_3,\\ \delta_3:=1,\quad s=j\omega,\quad\forall\,\omega>0\;rad/s.\end{array}\tag{4.82}$$

The three previous requirements were numerically solved using CAD tools (see i.e. [127]) to derive bounds that delimit the necessary gain and phase at each frequency of interest. Such bounds form lines that were plotted in a Nichols chart against the transfer function $P2(s)$. A detail of this Nichols chart is depicted in figure 4-18. Once all requirements and plant data were collected in the Nichols chart, the design of controller $G1(s)$ was carried out by using Matlab's QFT Toolbox, which allows to manually select the appropriate controller to satisfy the requirements. In the figure, the open-loop transfer function must be between the solid and dashed lines bounds in order to fulfill the requirements.

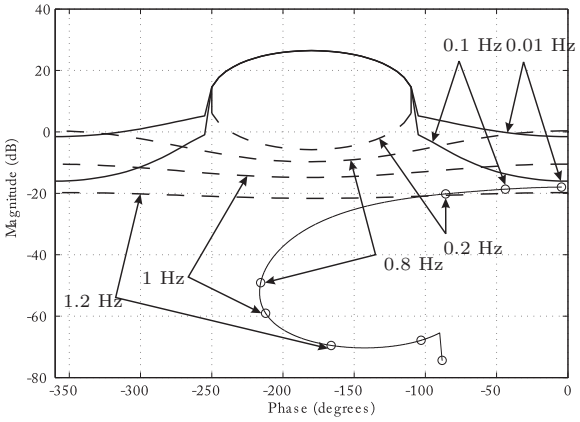


Figure 4-18: Nichols chart of the requirement bounds and the transfer function $P2(s)$. Note that the requirements are not satisfied.

ISBN:978-84-692-6902-2/ DL:T-1848-2009

The designed QFT controller $G1(s)$ is given in (4.83), and the open-loop transfer function $P2(s)G1(s)$ satisfying the requirements is plotted in figure 4-19.

$$G1(s) = \frac{3046.35(s+1.26)}{s(s+4.18)(s+5.36)} \cdot \frac{(13.44s^2+28.80s+59.29)}{(s^2+1.54s+59.29)} \tag{4.83}$$

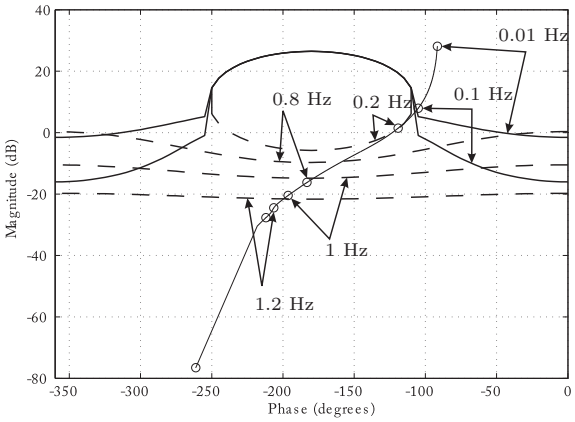


Figure 4-19: Nichols chart of the requirement bounds and the transfer function $P2(s)G1(s)$. Note that with controller $G1(s)$ all requirements are satisfied.

### QFT Controller Simulation

The QFT controller $G1(s)$ was designed to avoid air compressor (pump) saturation and to meet $\lambda_{O_2}$ constraints considering current filtering. Figure 4-20 depicts the responses of the controller to three current profiles, namely unrestricted, limited in slew-rate and filtered. In the interval $0\ s \leq t < 175\ s$ the stack current has high-frequency transients that are not restricted. The response of the QFT controller to 10 A step transients generates oscillations in the air compressor control signal and therefore undesired heating in the compressor, and also the $\lambda_{O_2}$ does not fulfill the $\pm 1$ constraint. This is expected because high-frequency current components affect directly $\lambda_{O_2}$ and the air compressor dynamics does not allow a faster response. In order to protect the fuel cell, in the literature it is reported the restriction of the stack current slew-rate [104], but with this procedure $\lambda_{O_2}$ is still affected by high-frequency components. This can be observed in the interval $175\ s < t \leq 350\ s$, where the stack current slope is limited to 10 A/s, and the QFT controlled air compressor response exhibits high-frequency oscillations. Also, the $\lambda_{O_2}$ constraints are unfulfilled. Finally, in the interval $350\ s < t \leq 530\ s$ there are presented the behaviors of the air flow and $\lambda_{O_2}$ regulated by the QFT controller in response to the current profile filtered by $F(s)$. In this condition, the QFT controller fulfills the constraints in air compressor saturation and control signal ripple, and also the $\lambda_{O_2}$ deviations caused by current transients of 10 A are constrained.

ISBN:978-84-692-6902-2/ DL:T-1848-2009

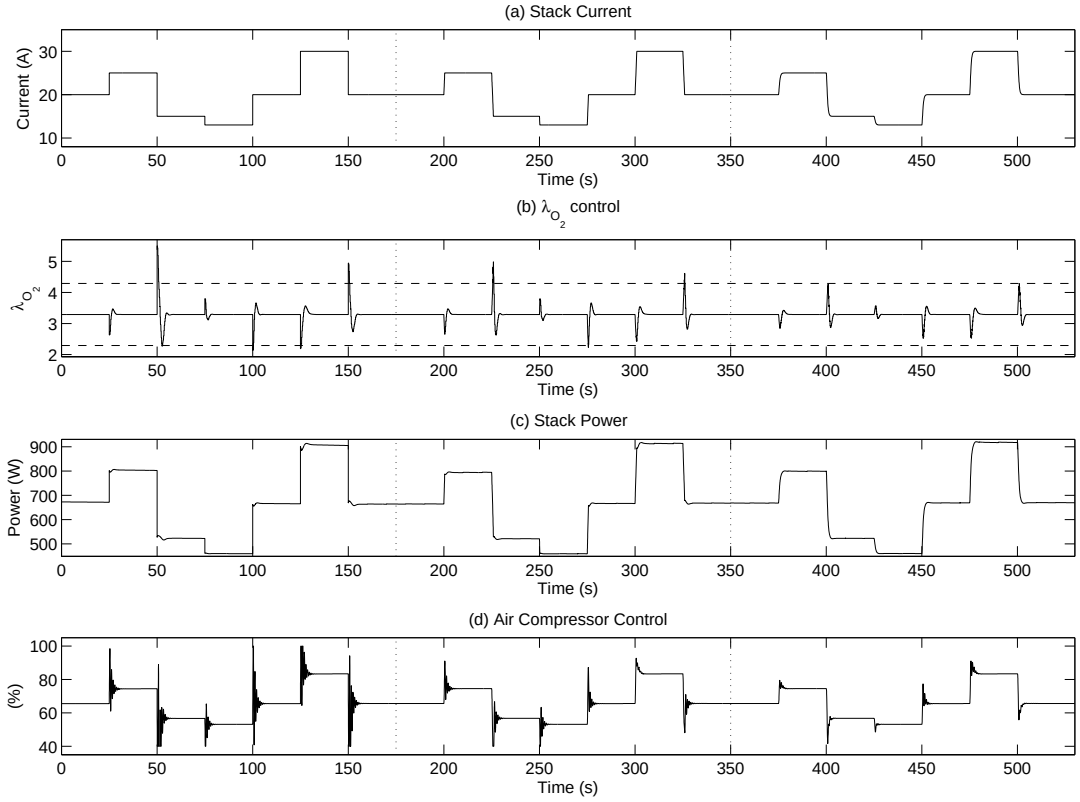


Figure 4-20: Current filtering effect on the $\lambda_{O_2}$ control.

The performance of the QFT controller was also contrasted with a classically designed PI controller $G_{PI}(s)$ presented in (4.84), which was designed to achieve a phase margin of 60° and a gain margin of 10 dB.

$$G_{PI}(s) = 2.68\frac{s+2.3}{s} \tag{4.84}$$

Both controllers were tested under the same filtered current profile that has 10 A and 15 A transients. Figure 4-21 shows the filtered current profile, the air compressor control signal and the $\lambda_{O_2}$ profiles generated by the controllers. It is observed that QFT controller fulfills the $\lambda_{O_2}$ deviation restriction in response to 10 A current transients. The PI controller does not achieve this low $\lambda_{O_2}$ error profile, and only at transients of 5 A it is possible to accomplish the $\pm 1$ restriction. Also, the PI controller does not prevent the oxygen starvation phenomenon in $t = 160$ s when a 15 A step-up transient causes $\lambda_{O_2} < 1$. In this same condition, the QFT controller does not fulfill the constraint of $\lambda_{O_2}$ but avoids oxygen starvation phenomenon. The air compressor control profile generated by the PI controller has saturations and ripples, and these effects heat the air compressor and make its behavior non-linear, increasing the power losses and decreasing the control efficiency. In comparison, the QFT controller arrives near to the saturation limits but the flow is not saturated, and the control

ISBN:978-84-692-6902-2/ DL:T-1848-2009

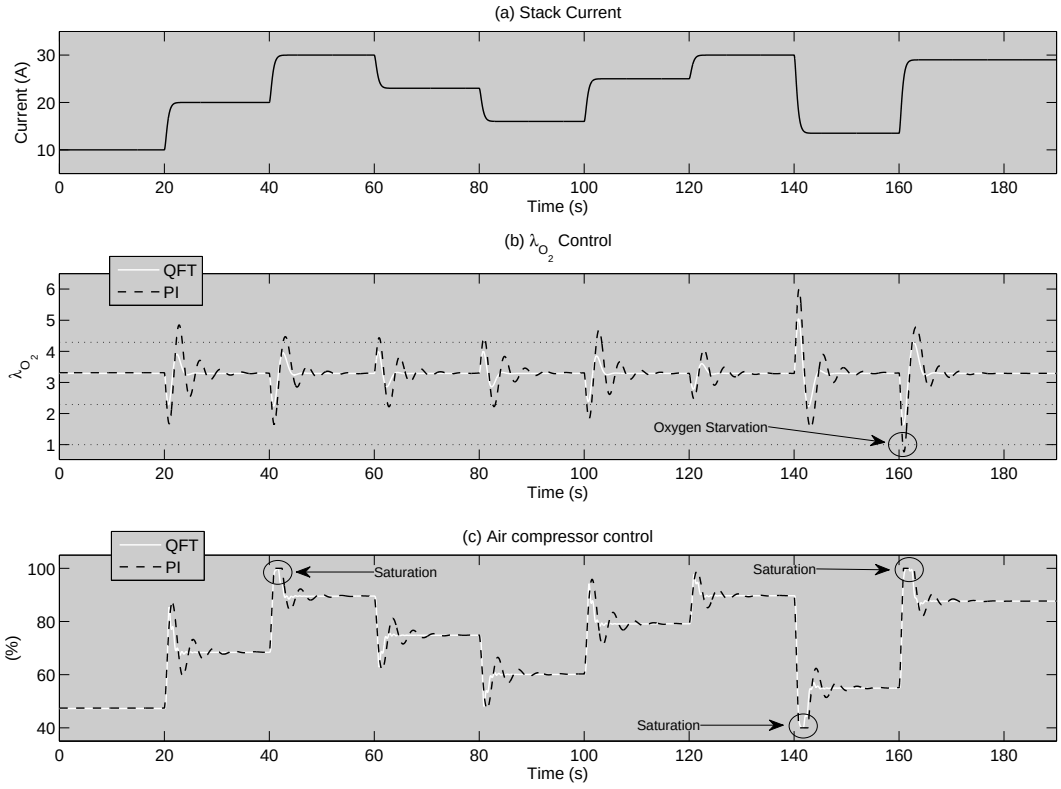


Figure 4-21: QFT and PI controllers comparison.

behavior exhibits low ripple. Also, the $\lambda_{O_2}$ regulation is satisfactory, and even when the current transients exceed the maximum considered in the design process the QFT controller avoids oxygen starvation phenomenon.

In summary, the QFT controller fulfills the design constraints and exhibits better results than a classically designed PI controller. Finally, the QFT controller provides safety against oxygen starvation phenomenon even at higher over-current conditions.

### Filtering and voltage regulation

The stack current filtering was performed controlling the input current of the DC/DC converter *DCDCi* (figure 4-16) according to $F(s)$. The topology selected for *DCDCi* was a DC/DC boost converter [128], controlling the inductor current using a sliding-mode current control strategy [129]. The electrical parameters of the converter are: L = 140 $\mu$H, C = 70 $\mu$F, switching frequency of 100 kHz, an electrical efficiency assumed constant $\eta_1 = 0.95$, and a capacitive filter between the fuel cell and the converter of Ci = 100 $\mu$F. The simulation of the input current control of the *DCDCi* converter is presented in figure 4-22, where a satisfactory correlation between the reference and

ISBN:978-84-692-6902-2/ DL:T-1848-2009

the input current can be observed. The response time to a 12 A step reference is 80 $\mu$s, which is three magnitude orders lower than the fuel cell response time. Also, this response time is enough considering the delay introduced by $F(s)$, which generates the current reference for the sliding-mode controller of the *DCDCi* converter. This current reference depends on the $F(s)$ dynamics and on the current requested by the *DCDCv* converter (figure 4-16). The difference between the fuel cell generated and required powers is exchanged with the battery, altering in this way its SOC and voltage.

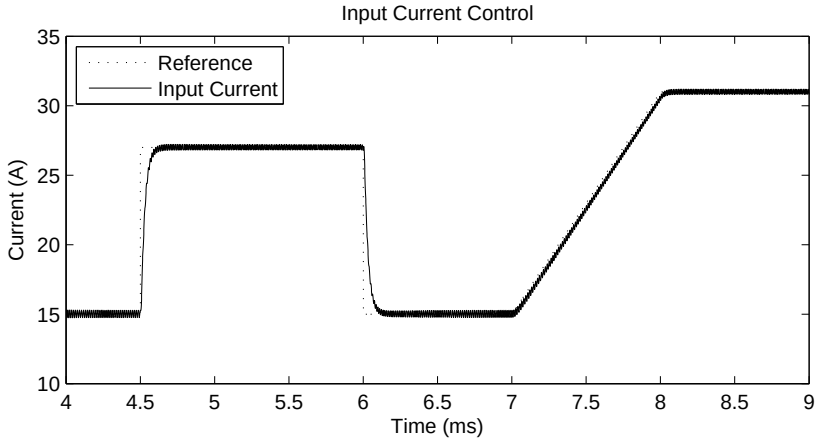


Figure 4-22: DCDCi converter control simulation.

The voltage level considered for the intermediate DC bus is 220 VDC, this due to the extended and documented use of 220 VDC batteries in industrial applications, considering 1 Ah batteries in this case. The load bus has been set to 400 VDC due to its common use in inverters supply and hybrid vehicles. The nominal load power is 1 kW, and the load profile has high-frequency transients and overloads.

The intermediate DC bus (battery) voltage variation and the load power transients are compensated by the *DCDCv* converter in order to regulate the output voltage. The *DCDCv* has a boost topology, and the inductor current is controlled using a PWM current control loop and a linear voltage controller $G_{vo}(s)$, given in (4.85), which ensures a 60° phase margin and a 10 dB gain margin to regulate the output voltage, where $I_{bv}(s)$ is the current reference given to the PWM current control loop and $e_{vo}(s)$ is the error in the output voltage.

$$G_{vo}(s) = \frac{I_{bv}(s)}{e_{vo}(s)} = 10^5 \frac{2.175s + 65.237}{s^2 + 10989s} \tag{4.85}$$

The electrical parameters of the *DCDCv* converter are: L = 400 $\mu$H, C = 440 $\mu$F, switching frequency of 100 kHz, a capacitive input filter Ci = 440 $\mu$F, and a constant electrical efficiency $\eta_3 = 0.95$. The simulation of the controlled converter *DCDCv* is presented in figure 4-23, which

ISBN:978-84-692-6902-2/ DL:T-1848-2009

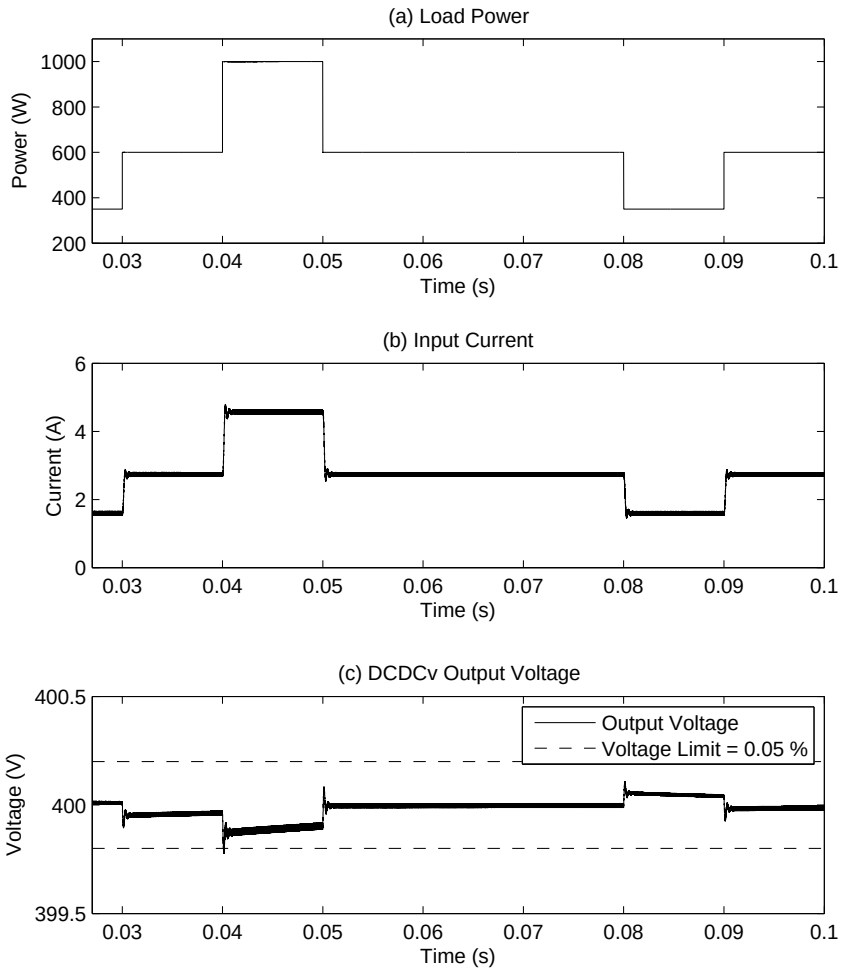


Figure 4-23: DCDCv converter control simulation.

shows the requested load profile, the required input current and the output voltage regulation. The load power profile has high-frequency transients of 40 % of the nominal power, which are transmitted through the input current to the intermediate DC bus. The simulation shows a fast response of the controller regulating the output voltage.

Finally, the switching DC/DC converters *DCDCi* and *DCDCv* permit to regulate the load voltage and to filter the fuel cell requested current.

### Serial topology dynamic simulation

The serial topology has been recommended for pulsating power load profiles, and therefore in this simulation the load profile has a high frequency AC component. Figure 4-24 presents the simulation of the topology controlled by the strategies designed, detailing its response to a pulsating load profile

ISBN:978-84-692-6902-2/ DL:T-1848-2009

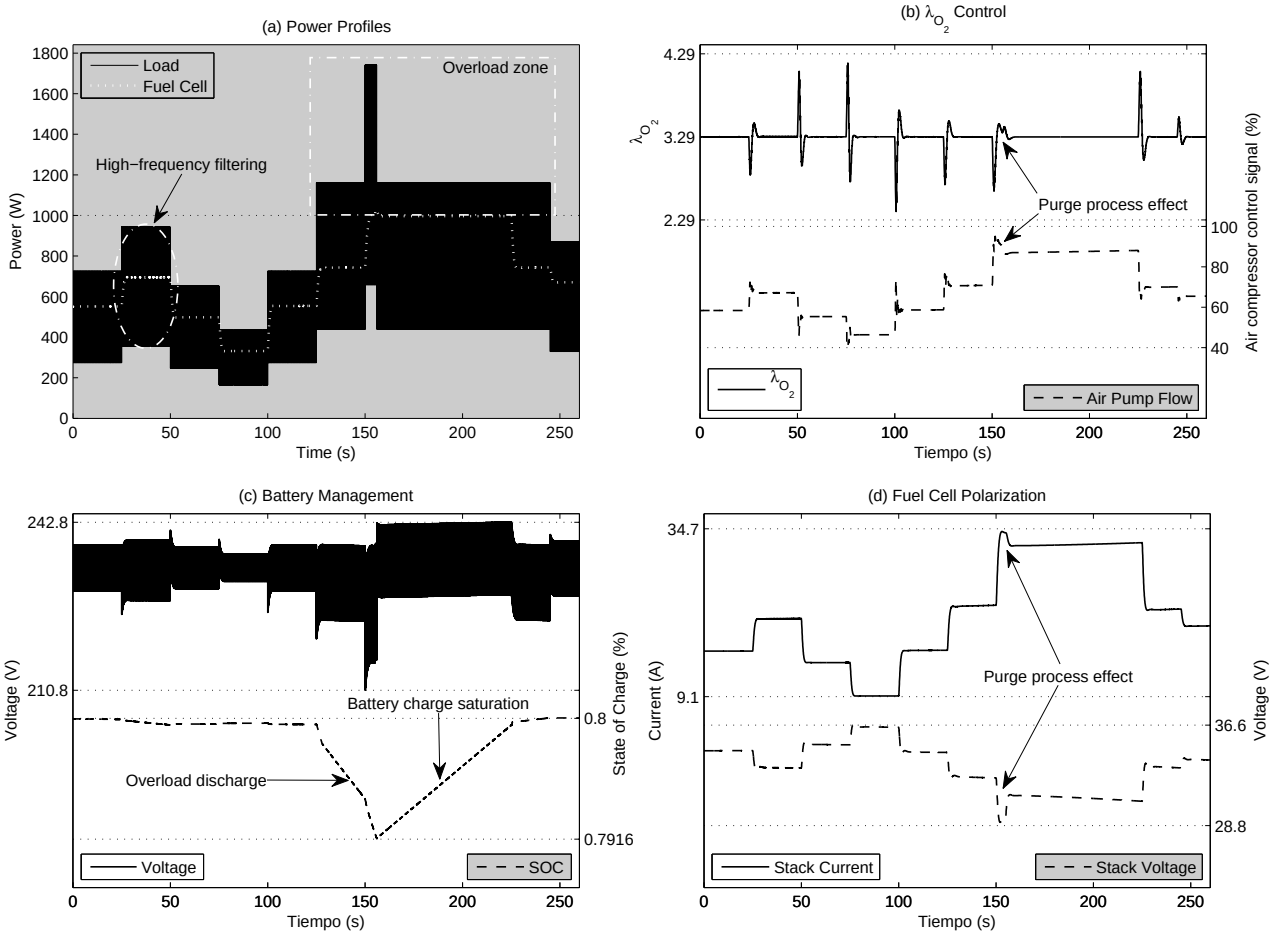


Figure 4-24: Serial topology simulation.

with high-frequency transients and overload demands, which AC components are depicted as a *black zone* due to the small time between plots, which is caused by the high frequency pulses. Figure 4-24(a) shows the load and fuel cell power profiles, where the high-frequency filtering and overload operations are supported by the topology. The regulation of $\lambda_{O_2}$ is depicted in figure 4-24(b), where the design constraints are respected in both $\lambda_{O_2}$ and air compressor control signal. Also, in this figure it is observed the effect of the anode purge process, in which the purge valve is opened to remove water particles and inert gases that deteriorate the output power. This purge process causes an increment in the hydrogen concentration and therefore an increment in the hydrogen partial pressure that generates the rise of the output voltage. This perturbation is compensated by modifying the stack current (figure 4-24(d)). The purge process frequency depends mainly on the amount of water vapor $W_v$ produced, which according to equation (2.8) given in section 2 depends on the stack current. Also, a high current condition requires high hydrogen flows which carry inert gases.

ISBN:978-84-692-6902-2/ DL:T-1848-2009

A purge process in figures 4-24(b) and 4-24(d) occurs at $t = 155$ s because the stack voltage was deteriorated below the purge limit by the water vapor and inert gases accumulation along the load profile. Due to the purge process the stack voltage exhibits a fast rise, but the high current condition at $t > 155$ s increases the production of water vapor and the accumulation of inert gases, and in these conditions the stack voltage begins to drop again. Also, the purge process causes an additional fast perturbation in the stack current due to the purge valve current consumption. The purge process control is implemented in the Nexa power module and also in the simulation model used in this particular simulation, which is based on the Real et al. model [23]. In the simulation results it is observed that the disturbances caused by this purge process are also regulated by the designed $\lambda_{O_2}$ control system.

Finally, the battery management is presented in figure 4-24(c), in which the battery voltage varies according to the power exchanged with the intermediate DC bus by two components: a high-frequency component due to the *DCDCv* current ripple (again depicted as a *black zone* due to the small time difference between plots) and the battery internal resistance, and a low-frequency component due to the SOC variation caused by the average power exchanged with the bus. Also, in figure 4-24(c), it can be observed the fine-tuning of the SOC in a near-to-reference zone, and the saturation of the fuel cell power to restore the SOC after an overload condition as was indicated in the topology control description and in the SOC controller given in (4.76).

In summary, the simulation results of the serial topology and control systems in response to a high-frequency, pulsating and overloaded power load profile, exhibit a satisfactory behavior in the DC intermediate and load buses fulfilling the control constraints.

ISBN:978-84-692-6902-2/ DL:T-1848-2009

## 4.5 Fuel cell power interface system design and experimental setup

The main objective of this chapter is the design of a fuel cell power system that provides a regulated DC bus with safe and efficient fuel cell operation. The fuel cell power interface system designed for this experimental setup considers an unidirectional power flow from the system to the load, and therefore the hybrid serial topology requires simpler power converter implementation. Also, the fuel cell-based DC bus design process developed in this section is intended for automotive, aerospace and telecom applications, where the electrical loads commonly have their own power supply regulation system, being also the serial topology the best option. In order to design a generic bus supply system, it has been considered a DC bus with voltage regulation strategy supplied from the fuel cell following the serial hybrid topology, which can be used for unidirectional applications, but it can be easily extended to bidirectional power flows in order to supply regenerative loads.

In this work is proposed the regulation of the fuel cell stack current using an input current controlled DC/DC switching converter [130]. Similarly, other authors have been proposed this same strategy with different objectives [30] [106] [131]. Also, in this work a capacitor was selected to supply power transients due to its high-frequency capabilities, easy state-of-charge estimation and low serial resistance in contrast to battery-based systems. The use of supercapacitors and fuel cells in hybrid topologies has been analyzed in [132] and [133], whose results are also valid for high capacitive-low serial resistance capacitor banks.

The block diagram of the proposed fuel cell power interface system is depicted in figure 4-25, considering a DC/DC power converter and input filter in series with the fuel cell (1.2 kW Nexa power module), which regulates a capacitive DC bus in order to supply the load. Also, there are considered the power converter input current control and bus overvoltage protection. The power interface system is externally controlled by real-time Matlab-based regulation strategies in order to ensure bus performance and fuel cell safe operation.

### 4.5.1 DC/DC power converter and input filter

The Nexa power system user manual [134] reports a maximum operating limits for stack voltage of 22 V and 50 V, but these limits correspond to extreme conditions, i.e. 22 V at short duration stack current transients (60 A - 70 A for 10 ms - 1 ms, respectively) and 50 V for zero stack current, being these limits also measured at the beginning of fuel cell life at standard operating conditions (sea level, 30 °C). In this work it was considered a real, and experimentally measured, safe stack voltage range between 26 V and 46 V, and due to telecom, aerospace and electric vehicle applications

ISBN:978-84-692-6902-2/ DL:T-1848-2009

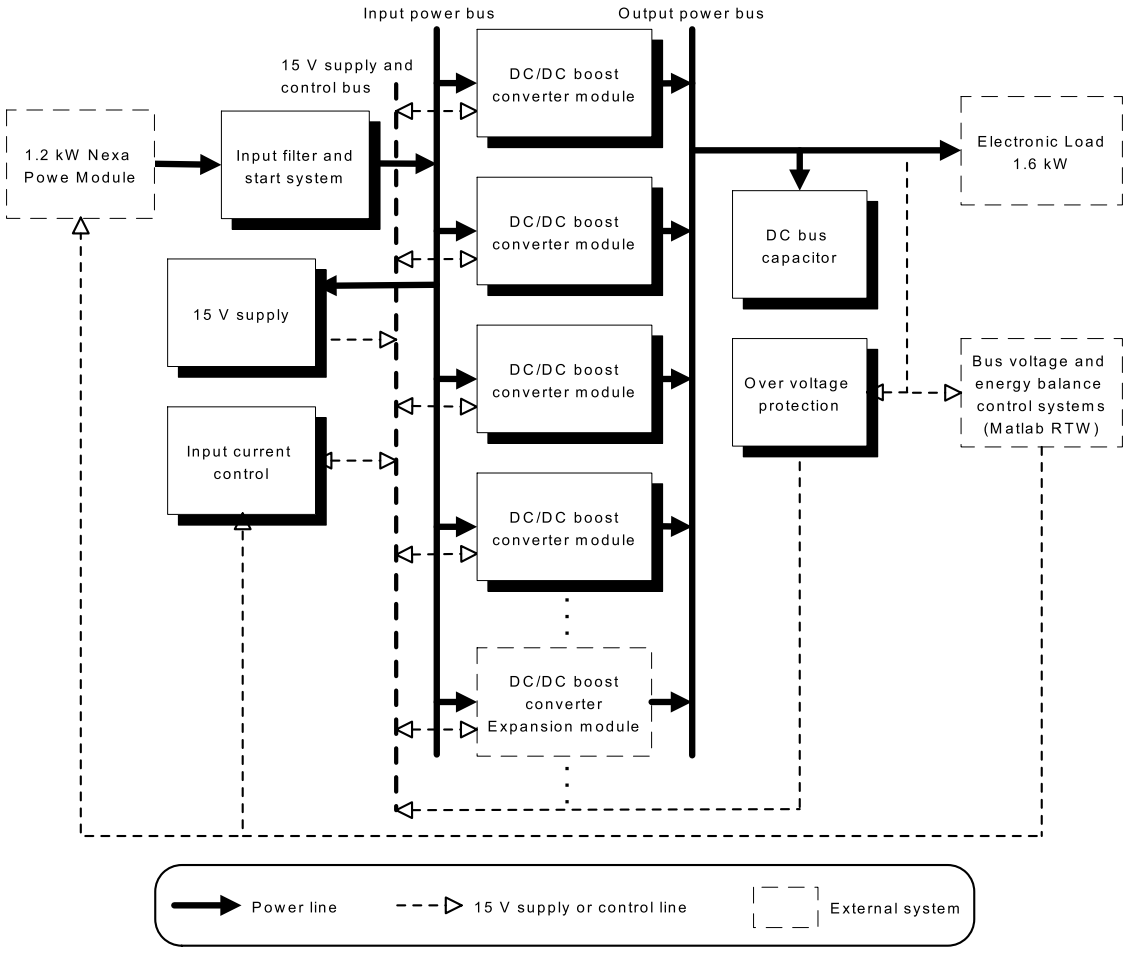


Figure 4-25: Fuel cell power interface system - block diagram.

use 48 V (or above) DC buses, a boost DC/DC switching converter topology was used. Also, the boost topology has the inductor in series with the power supply, allowing in this way a controllable input current ripple, which is not possible in buck converters due to its discontinuous input current, requiring a high input filter for this issue. The designed power converter has a nominal power of 1.2 kW to support the Nexa power module, but in order to make it robust, redundant and scalable, it was developed using several power conversion modules, each one of the with a maximum power of 300 W. This is showed in figure 4-25, where are presented input and output power buses that allow the connection of multiple power conversion modules. In this work were developed four *300 W boost converter modules* to interface the 1.2 kW Nexa power module, but the structure is flexible to support higher or lower power systems using different number of modules.

The circuit scheme of each DC/DC boost converter module is given in figure 4-26, where it is showed the boost converter topology, inductor current sensing and conditioning, and inductor

ISBN:978-84-692-6902-2/ DL:T-1848-2009

current control. The core of the converter module is the DC/DC boost converter, whose basic elements are the inductor L, MOSFET N-channel and SCHOTTKY diode, and also was introduced a Rsense shunt resistor to measure the inductor current.

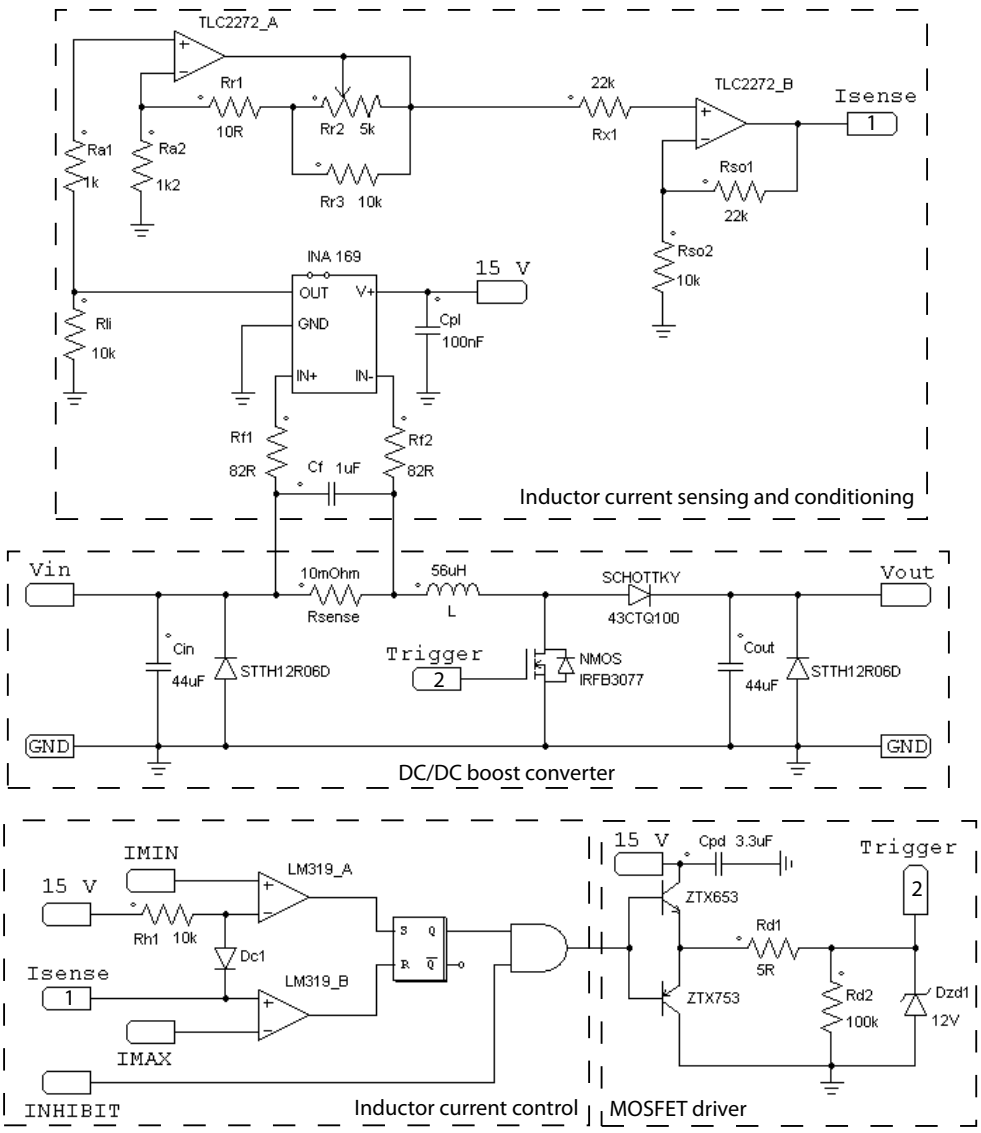


Figure 4-26: DC/DC boost converter module circuit scheme.

The boost converter module has two states: the first one is given with the MOSFET in conduction (ON) causing the inhibition of the diode and therefore the inductor is parallelized with the input voltage. The inductor current grows with an approximately linear waveform due to the small resistance of the inductor and Rsense, incrementing in this way the energy stored in the inductor. The second state is given with the MOSFET in non-conduction (OFF) causing the conduction of the diode and therefore the inductor is now connected between the input and output, transferring its

ISBN:978-84-692-6902-2/ DL:T-1848-2009

stored energy to the load. In steady-state the output voltage is grater than the input voltage causing the reduction of the inductor energy in each cycle. Also, if the output capacitance is dominant, like in this application case, the output voltage can be considered constant in one cycle and therefore the inductor current waveform can be considered linear. The switching of the converter between these two topologies generates a continuos inductor current waveform, and this operating mode is denominated Continuos Conduction Mode (CCM). In cases where the inductor current falls to zero, the diode is inhibited when the MOSFET is OFF and a new state appears, which is characterized by zero inductor current. This operating mode is called Discontinuous Conduction Mode (DCM) due to the discontinuity in the indictor current waveform [128]. Each converter module supports up to 300 W and its inductor was designed for a nominal current of 10 A (for inductor construction, and diode and MOSFET selection see Appendix C).

In order to reduce the electromagnetic radiation generated in the converter, two sets of capacitors of 22 $\mu$F EPCOS MKT (100 V, 10 % tolerance) where placed in the input and output of the converter, being localized near to the inductor and diode, respectively. These capacitors gives a discharge path for the inductor in input source disconnection, but for safety was introduced an antiparallel STTH12R06D diode to support this condition, and which one also avoid negative capacitor voltages. This diode also causes a short circuit condition in cases where the input polarization cables were inverted, this being detectable in Nexa power system software and laboratory power supplies. Another antiparallel STTH12R06D diode was introduced in the converter output to avoid negative voltage conditions in the capacitive bus, i.e. in suddenly disconnection of inductive loads.

The current sensing uses the shunt resistor technique, where the voltage drop in Rsense (10 m$\Omega$) is conditioned to obtain the inductor current value. The Rsense voltage drop range is [0 mV, 100 mV], which is acceptable for the INA169 amplifier used in the implementation. The amplification performed by the INA169 was limited to 10 V/V in order to avoid reduction in its bandwidth, this because the required 100 times amplification to obtain a current sensing relation of 1 A/V constraints the INA169 bandwidth to 44 kHz. This was addressed by using a two stage additional 10 V/V amplification based on operational amplifiers (TLC2272), where the first stage allows a fine tuning of the voltage gain and the second one has a fixed voltage gain of 3.2 V/V. The TLC2272 allows unipolar supply, which simplify the design, and have the two operational amplifiers required for the additional 10 V/V amplification. The voltage signal that represents the inductor current of the boost module is called Isense in figure 4-26.

The power conditioning system input current must be controlled in order to regulate the fuel cell stack current, and therefore the converter modules are controlled in current mode. In this way, the inductor current was controlled using sliding mode control technique. In the current control

ISBN:978-84-692-6902-2/ DL:T-1848-2009

implementation a window comparator was used to detect when the current reaches its maximum and minimum allowed values triggering the RESET or SET signal of a bistable circuit (S-R flip-flop), respectively. The use of this bistable reduces the circuit noise sensibility and it stores the switching state applied to the MOSFET driver.

In CCM the inductor current waveform is approximately triangular, and in general, it is possible to perform an analysis using sliding mode control theory assuming a sliding surface $S(x) = i_L - I_{BRef}$. $I_{BRef}$, the boost converter module average inductor current reference, is considered constant in the cycle and in the middle of the hysteresis band of the comparator, $I_{BRef} = (IMAX + IMIN)/2$ [129]. The converter module was designed to operate between 40 kHz and 100 kHz, but in low reference current cases the switching frequency tends to increase due to the hysteresis reduction caused by the IMIN saturation (to zero). This was addressed by forcing the converter module to operate in DCM extracting the required power in *burst mode* cycles [135], where the converter absorbs the average power in each cycle required to generate the desired average input current; this without incrementing the switching frequency.

The *burst mode* is generated by introducing a diode-resistor network (Dc1 - Rh1, figure 4-26) in the window comparator in order to compare IMIN with $I_{BRef} + V_d$ ($V_d$ is the diode Dc1 voltage drop) while IMAX is still compared with $I_{BRef}$ as depicted in the circuit scheme of figure 4-26. In CCM this diode increments the hysteresis band in $V_d$ and introduces a steady state error in the average current of $V_d/2$, which is compensated by the power conditioning system input current control (PCSICC). In low reference current conditions, $I_{BRef} < (IMAX + IMIN)/2$, the PCSICC changes $I_{BRef}$, and therefore IMAX and IMIN, in order to achieve the desired average current. When IMIN is saturated to zero, the diode Dc1 avoids the SET of the MOSFET when the inductor current drops to zero, this because IMIN comparator has at least a $V_d$ level in its negative input (inductor current zero) which keeps the MOSFET OFF generating the DCM. When the average current decreases from the reference value $I_{Ref}$, PCSICC grows the converter modules reference $I_{BRef}$, and therefore IMAX and IMIN, causing eventually the SET of the MOSFET. Similarly, when the average current is greater than $I_{Ref}$, PCSICC decrease $I_{BRef}$ generating DCM and *burst mode*. This procedure avoids the reduction of the hysteresis band and therefore the switching frequency is not incremented, in fact it is decremented.

Figure 4-27 shows the experimental inductor currents of the four converter modules in CCM and DCM operating modes. The CCM depicted in figures 4-27(a) and 4-27(c) is the normal operating mode, where each module is controlled by its own local current control which reference current $I_{BRef}$ is defined by the supervisory controller PCSICC to obtain a desired average input current $I_{Ref}$. The inductor currents in the converter modules have triangular waveforms, but because the small differences in the converter inductors, capacitors, diodes and MOSFET drivers, the triggering times of the MOSFETs (and even the switching frequencies) are not the same, causing in this way

ISBN:978-84-692-6902-2/ DL:T-1848-2009

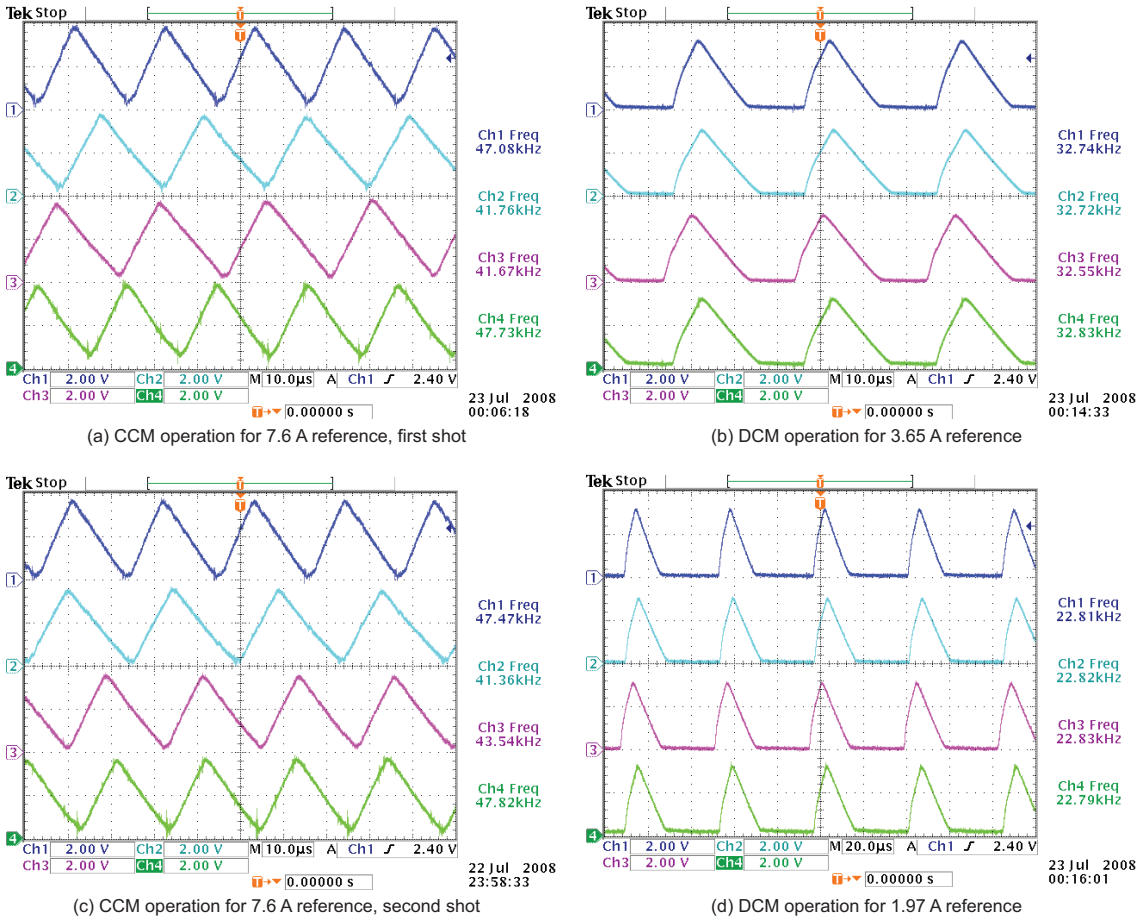


(a) CCM operation for 7.6 A reference, first shot

(b) DCM operation for 3.65 A reference

(c) CCM operation for 7.6 A reference, second shot

(d) DCM operation for 1.97 A reference

Figure 4-27: Converter module CCM and DCM operating modes.

partial current ripple cancelation [136]. The amount of canceled ripple depends on the inductor currents phase differences, which depend on the electric elements differences. These differences do not affect appreciably the system dynamics, and also are a natural condition due to the electric elements tolerance. Figures 4-27(a) and 4-27(c) depict two oscilloscope shots taken in different times, where it is observed the four converter modules inductor currents, each one with different phase and small differences in its switching frequency, being the first shot the better ripple cancelation case. In this way, the four-module power system gives a natural partial input current ripple cancelation which helps the input filter to request a small-ripple current to the fuel cell. An interleaving triggering and control of the four modules for better and regulated input current ripple cancelation can be implemented in further works for system improvement.

The DCM has a different MOSFET triggering behavior than CCM, this because the supervisory controller PCSICC modifies $I_{BRef}$ causing the MOSFET SET, and the MOSFET RESET is triggered by the IMAX comparator. These conditions cause the almost simultaneous SET of the MOSFET in the converter modules because $I_{BRef}$ is common for all them. This is depicted in

ISBN:978-84-692-6902-2/ DL:T-1848-2009

figures 4-27(b) and 4-27(d), where it is observed the inductor currents of the four converter modules operating in DCM for average current references of 3.65 A and 1.97 A, respectively. To obtain these average currents *burst mode* is required in order to avoid sliding-mode switching frequency increasing, which experimental validation given in figures 4-27(b) and 4-27(d) reports an approximated equal switching frequency of 32.7 kHz for the first current reference and 22.8 kHz for the second one. The switching frequency and phase of the modules are approximately the same because the MOSFET SET depends on a common controller, but this synchronization avoids current ripple cancelation generating an increment in the input current ripple. Further improvement of the power system can be performed by redesigning the *burst mode* implementation or using a different technique to address the low reference current-increase switching frequency situation.

The MOSFET driver of the converter modules, depicted in figure 4-26, consist in two high-current fast transistors (ZTX653 and ZTX753) in *totem pole* configuration which drives the MOSFET through an damping resistor of 5 $\Omega$. A 15 V zener diode was connected at the MOSFET gate to avoid damages caused by overvoltage or negative voltages, which are not normal conditions, but these problems can be generated by driver or supply failure. Also, to guarantee the shutdown of the MOSFET if the driver does not have supply, it was placed a 100 $\mathsf{k}\Omega$ resistor between the MOSFET gate and ground (boost converter commonly requires low-side MOSFET configuration where source is connected to ground). The driver supply is locally stabilized using a high-frequency decoupling capacitor of 3.3 $\mu\mathsf{F}$.

In order to reduce the current ripple in the fuel cell, the input filter was designed to absorb the current ripple generated by the converter modules, which in normal operating mode (CCM and DCM) is constrained between 0 A for complete cancelation and 14 A for inductor currents in phase. The probability of experiment the 14 A worst case is small due to the electronic elements differences, but for fuel cell safety it has been considered in the design. Also, in DCM the inductor currents will be in phase but the requested power will be lower than in CCM.

The input filter consist in a L-C network designed to absorb the current ripple in normal operating conditions (input current grater than 10 % of the nominal stack current), being selected a design current of 3.5 A (7.6 %), where it can be found DCM and CCM operating modes. The *burst mode* caused by DCM generates high current ripples (inductor currents in phase) with a minimum switching frequency between 32 kHz and 36 kHz. Using the cut-off frequency of L-C filters (4.86) and commercially available capacitors and inductor cores, the filter depicted in figure 4-28 ($\mathsf{L_f}$, $\mathsf{C_{f1}}$) was designed to has a cut-off frequency around a decade under the minimum switching frequency. This filter has a cut-off frequency of 3.5 kHz, being it enough to filter the high frequency components of the converter current ripple.

ISBN:978-84-692-6902-2/ DL:T-1848-2009

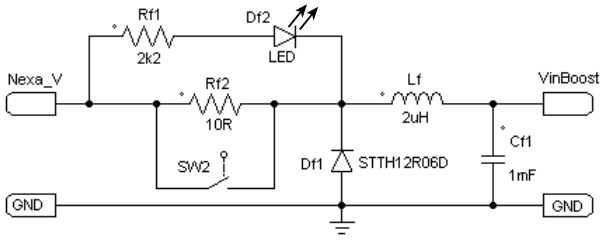


Figure 4-28: Input filter circuit scheme.

$$F_{co} = \frac{1}{2\pi\sqrt{L \cdot C}} \tag{4.86}$$

The circuit scheme of the implemented input filter given in figure 4-28 has an additional resistor-switch network (Rf2, SW2), which is used to charge the capacitive bus and input filter with a constrained current in order to avoid fuel cell damages in the start-up of the system. This is necessary because the power system must be pre-charged using the fuel cell, which implies a fast and high energy request in the system start-up. Rf2 constraints the charge current, indicated by LED diode Df2 ON (charge mode), until the power system energy is the required for normal operation, indicated by Df2 OFF (operating mode), time when SW2 switch is manually closed to exclude Rf2 configuring in this way the power system in its operating structure. In further development this charge system will be automatized with diode or MOSFET circuital structures to improve the power system.

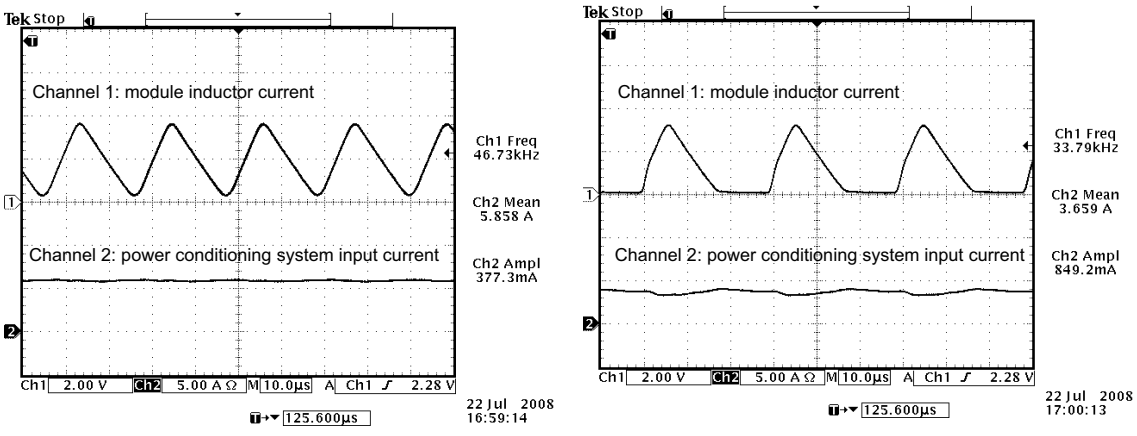


(a) CCM operation for 5.858 A input current

(b) DCM operation for 3.659 A input current

Figure 4-29: CCM and DCM power conditioning system input currents.

ISBN:978-84-692-6902-2/ DL:T-1848-2009

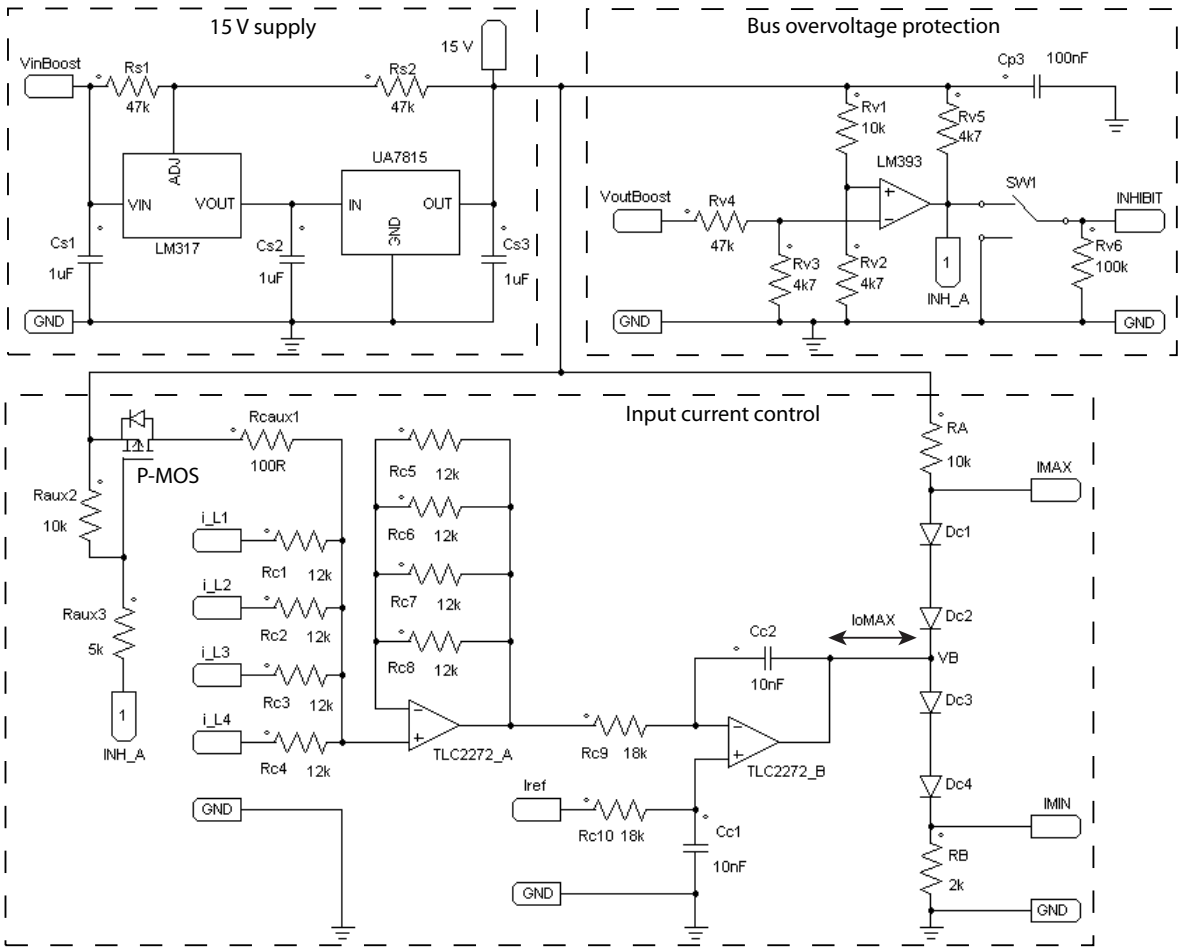


Figure 4-30: Power system control board circuit scheme.

The experimental input filter currents, and therefore fuel cell currents, measured in CCM and DCM operation are depicted in figures 4-29(a) and 4-29(b), respectively. In CCM the input current ripple of the power conditioning system is approximately 377.3 mA and in DCM is 849.2 mA, being these ripples almost constant for each operating mode due to the hysteresis band low variations. These current ripples are acceptable because they represent less than 10 % of the nominal fuel cell current [137], being 0.82 % in CCM and 1.85 % in DCM. Also, in the experiments presented in figure 4-29 the CCM and DCM current ripples corresponds to 6.4 % and 23.2 % of the DC currents, respectively, those being under the recommended 30 % limit for high and low frequency current ripples [134] [138].

The supervisory control of the converter modules includes de average input current control and overvoltage protection, which ones must be applied to all the modules at any time. These were implemented in a single power system control board, which circuit scheme is given in figure 4-30. This control board includes a 15 V voltage source implemented with linear regulators, which allows to supply the integrated circuits for control and operation of the system using the fuel cell without

ISBN:978-84-692-6902-2/ DL:T-1848-2009

additionally power supplies or equipment.

The average input current regulation strategy performed by the PCSICC controller was implemented using a voltage average operational amplifier, which calculates the average input current value from the inductor current sensing signals of the converter modules. Next, the error of the average current from the reference $I_{Ref}$ is calculated to be processed by an integrator operational amplifier that close the control loop. The input current control technique (PCSICC) is therefore an Integral controller that generates the IMIN and IMAX values using a resistor-diode network as given in figure 4-30. The maximum and minimum values of the hysteresis band are defined by the relation between RA and RB. In this application was used the TLC2272 integrated chip, which operational amplifiers are Rail-to-Rail allowing it to generate control signals near to ground and supply levels. This integrated chip, in the control board, has an approximated output current $\mathsf{IoMAX} = \pm 5\ \mathsf{mA}$.

The control board also implements the bus overvoltage protection, which consists in a comparator network that evaluates the bus voltage in front to a preset maximum allowed voltage of 55 V. The comparator generates a INHIBIT signal that forces the MOSFET shutdown in the converter modules (ON for normal operation and OFF for shutdown), reactivating the MOSFET switching control when the overvoltage condition is over. An additional P-MOS MOSFET and resistors network has been introduced in order to minimize the current peaks in converter MOSFET reactivation. These peaks could be normally generated by the integrator saturation caused by the discontinuous zone of the DCM currents, but in an overvoltage condition the additional P-MOS network, activated by the comparator output ($\mathsf{INH\_A}$), forces the fast drop to zero of the integrator output by masking its inputs with a constant high voltage. This condition disappears when the overvoltage condition ended because the P-MOS is inhibited and the integrator recover its control inputs.

The experimental evaluation of this protection is depicted in figure 4-31, where experiment (a) shows one single module normal operation where ripple cancelation does not occur and therefore represents the worst case. This experiment shows a normal CCM operation where the bus voltage fulfills the limit restriction of 55 V, being 48 V in this case. Figure 4-31(b) presents the action of the overvoltage protection when the bus voltage arrives the 55 V limit. This experimental condition was forced by defining a constant high inductor current without supervisory control action, causing in this way a periodic activation of the overvoltage protection. The same procedure was followed using the four converter modules without supervisory input current control, obtaining the inductor current profiles depicted in figure 4-31(c), where it is observer a high frequency in the overvoltage protection activation contrasted with the single module experiment (figure 4-31(b), 8.53 kHz), being approximately 22.5 kHz for all converter modules. In the same way, figure 4-31(d) shows the average input current (input filter current), constrained in this experiment by the activation of the overvoltage protection. This experiment reports a satisfactory behavior of the overvoltage protection, but

ISBN:978-84-692-6902-2/ DL:T-1848-2009

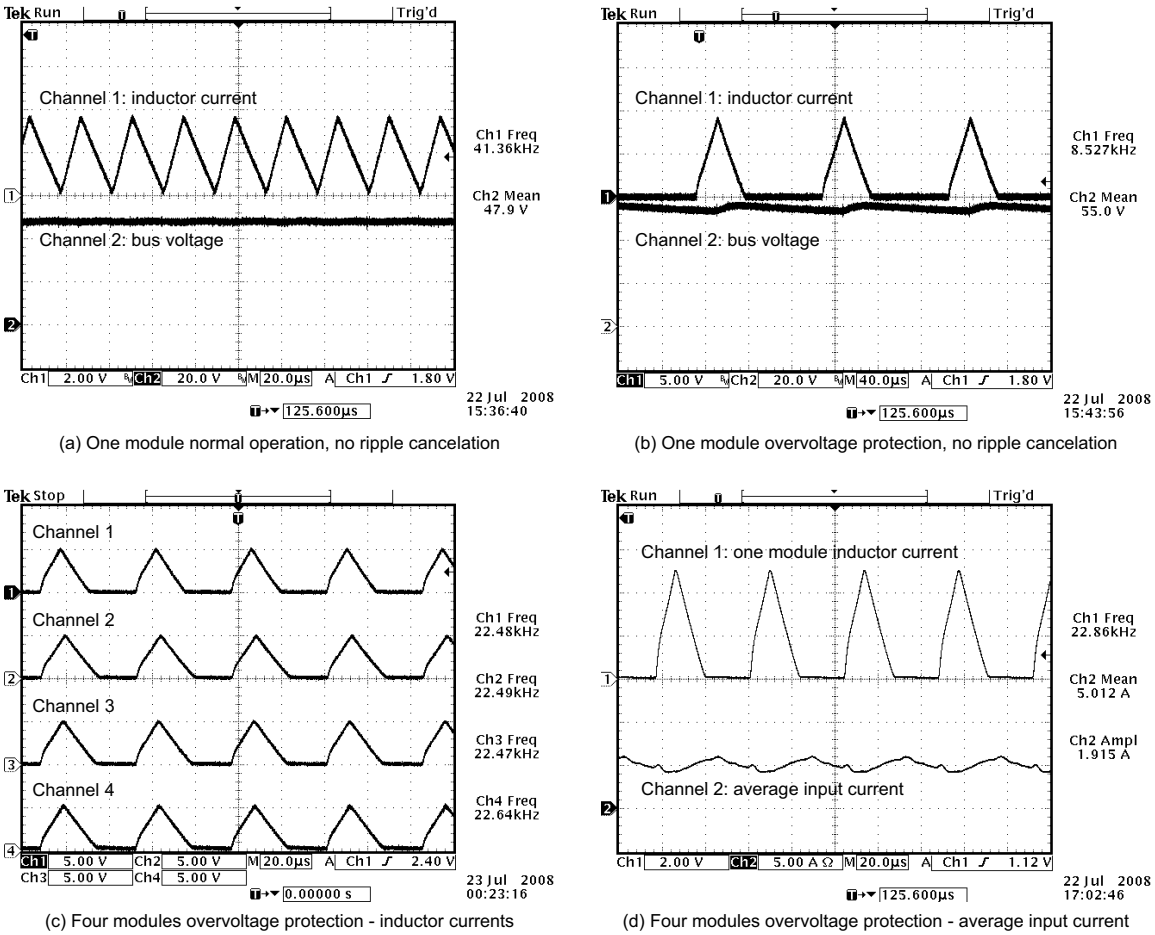


Figure 4-31: Bus overvoltage protection experimental evaluation.

makes evident the high distortion in the input current caused in the activation of the protection, which is mainly generated by the synchronization of the MOSFET activation due to the overvoltage protection system. This input current distortion, analyzed in terms of current ripple, represents a 4.16 % of the fuel cell nominal current and a 38.2 % of the DC current, which respects the maximum current ripple recommended (10 %) but does not respect the maximum ripple-DC relation recommended (30 %) and therefore the fuel cell must not be under this condition unnecessary prolonged time. It is noticed that this is not a normal operating mode, it is a protecting mode that must not be active unless load or power system fail, but its operation can be improved by using interleaving converter modules control to reduce the current distortion.

Finally, this protection circuit has an additional switch (SW1) that is used to safe turn-on/turn-off the power system. The system is turned-on by charging the bus capacitance and next closing SW1, and similarly, is turned-off by opening SW1. Also, SW1 switch is useful to manually inhabitation of the MOSFET, and therefore of the power conversion system, when fuel cell or load undesired operating situations are detected.

ISBN:978-84-692-6902-2/ DL:T-1848-2009

### 4.5.2 DC bus capacitor design and voltage regulation

In order to provide a regulated DC bus, the bus capacitor dimensioning and energy regulation must ensure a system behavior in admissible voltage limits and power transients restoring times. In the power interface system the relations between the switching converter, capacitor and load currents and powers are given by:

$$i_{dc/dc} = i_{cb} + i_{Load} \tag{4.87}$$

$$P_{dc/dc} = P_{cb} + P_{Load} \tag{4.88}$$

where $i_{dc/dc}$ and $P_{dc/dc}$ correspond to the output of the switching converter, $i_{cb}$ and $P_{cb}$ to the capacitor, and $i_{Load}$ and $P_{Load}$ to the load. Also, it is necessary to take into account the switching converter losses, which are represented by a power conversion efficiency of $\eta_{dc/dc}$ considered constant in all the power range.

In a power transient, the capacitor initially supplies the power to the load, then the fuel cell operating point is moved to the new steady-state constraining its maximum power slope to the defined slew-rate limit. If the load current has a high-frequency ripple, this one is supplied by the bus capacitor and the fuel cell provides the low-frequency components.

In order to dimension the capacitor, the following DC bus parameters were defined: maximum load power transient considered $\Delta P_L$ (W), maximum fuel cell power slew-rate admissible $S_{Rfc}$ (W/s), and maximum bus voltage deviation allowed $K_{vb}$ (%). Due to the power converter efficiency, the slew-rate limit that affects the power delivered to the capacitor and load is $S_R = \eta_{dc/dc} \cdot S_{Rfc}$ (W/s).

The most critical load transient case is reached in a power step of $\Delta P_L$, then the fuel cell power will be changed with a slope of $S_{Rfc}$ until it reaches the new steady-state power point at $\Delta t_d = \Delta P_L / S_R$ (s). Therefore, the power $P_{cb}(t)$ supplied by the capacitor in this time interval can be expressed as

$$P_{cb}(t) = \Delta P_L - S_R \cdot t \ , \quad 0 \leq t \leq \Delta t_d \tag{4.89}$$

and the energy $E_{Tcb}$ exchanged between the capacitor and the load is

$$E_{Tcb} = \int_0^{\Delta t_d} P_{cb}(t)\ dt = \frac{\Delta P_L^2}{2 S_R} \tag{4.90}$$

also, this energy difference produces a bus voltage variation of $(K_{vb}/100) \cdot V_{0bus}$ from the steady-state

ISBN:978-84-692-6902-2/ DL:T-1848-2009

value $V_{0bus}$. This voltage change can also be expressed as a function of the capacitor initial energy and the energy remaining at $\Delta t_d$ seconds (when the power exchange with the load has ended) as

$$E_{Tcb} = \frac{1}{2} C_{cb} \cdot V_{0bus}^2 \left| 1 - (1 - K_{vb}/100)^2 \right| \tag{4.91}$$

Finally, the capacitance that ensures the desired maximum bus voltage change at the considered load transient is deduced from equations (4.90) and (4.91) as

$$C_{cb} = \frac{\Delta P_L^2}{\eta_{dc/dc} \cdot S_{Rfc} \cdot V_{0bus}^2 \left| 1 - (1 - K_{vb}/100)^2 \right|} \tag{4.92}$$

Other important parameter of the DC bus behavior is the voltage restitution time $\Delta t_r$ after a load transient. To restore the bus voltage in a desired restitution time, the linear-non-linear (Lnl) control technique was used, which has also been used to regulate DC/DC switching converters in [139] and [140]. The principal characteristic of this technique is a fast recovery after transients because the system supplies the maximum possible energy until the controlled variable reaches a desired limit, where a linear controller makes a smooth regulation. Using the Lnl control technique, the fuel cell will supply a defined power excess $\Delta P_{rbfc}$ over the one required by the load to restore the capacitor energy at the desired restitution time, and therefore the effective power excess that restores the bus voltage is $\Delta P_{rb} = \eta_{dc/dc} \cdot \Delta P_{rbfc}$.

Using the same considerations made in the capacitor dimensioning, recovering the bus voltage from a load power transient of $\Delta P_L$ requires to restore the energy $E_{Tcb}$ exchanged between the capacitor and the load defined in (4.90).

The Lnl control technique saturates the maximum power delivered by the fuel cell to $P_{fc} = (P_{Load} + \Delta P_{rb})/(\eta_{dc/dc})$ in a bus voltage recover operation. However, in the beginning of the voltage recovering the Lnl control does not take any action; instead, the fuel cell power changes respecting the slew-rate limit until it reaches the Lnl limit, which occurs at $\Delta t_{r1} = \Delta P_{rb}/S_R$ seconds after the beginning of the recover operation, and then the fuel cell power is held constant during $\Delta t_{r2} = \Delta t_r - \Delta t_{r1}$ seconds. The power excess over the one required by the load, supplied to restore the capacitor steady-state during the Lnl saturation zone can be expressed as

$$\Delta P_{rcb}(t) = \begin{cases} S_R \cdot t, & 0 \leq t < \Delta t_{r1} \\ \Delta P_{rb}, & \Delta t_{r1} \leq t < \Delta t_r \end{cases} \tag{4.93}$$

and the energy $E_{Trcb}$ exchanged with the bus as

$$E_{Trcb} = \int_0^{\Delta t_r} \Delta P_{rcb}(t) \cdot dt = \Delta P_{rb} \left( \Delta t_r - \frac{\Delta P_{rb}}{2 S_R} \right) \tag{4.94}$$

ISBN:978-84-692-6902-2/ DL:T-1848-2009

Finally, to restore the energy of the capacitor in the desired restitution time $\Delta t_r$ after a load power transient of $\Delta P_L$, a power excess limit $\Delta P_{rbfc}$ is required, obtained from equations (4.90) and (4.94) as

$$\begin{aligned} \Delta P_{rbfc} = S_{Rfc}\left[\Delta t_r - \sqrt{\Delta t_r^2 - \left(\frac{\Delta P_L}{\eta_{dc/dc}\cdot S_{Rfc}}\right)^2}\right] \\ \Delta t_r \geq \left(\frac{\Delta P_L}{\eta_{dc/dc}\cdot S_{Rfc}}\right) \\ \Delta P_{rbfc} \leq \Delta t_r \cdot S_{Rfc} \end{aligned} \tag{4.95}$$

where the constraints on $\Delta t_r$ and $\Delta P_{rbfc}$ are achieved when the fuel cell power slew-rate limit is fulfilled.

The Lnl control technique allows a smooth regulation near the steady-state by means of a linear control system, and therefore the Lnl saturation will affect the fuel cell power control reference in high power transients. In power transients that require a fuel cell power below the defined limit, the linear control defines the power reference, but again respecting the fuel cell power slew-rate limit.

The series resistance of the capacitor generates power losses that can be considerable depending on its ohmic value and bus voltage. For the previous $\Delta P_L$ load transient, the capacitor current is given in (4.96) and the energy dissipated in its serial resistance $R_s$ is described by (4.97).

$$i_{cb}(t) = \frac{\Delta P_L - S_R \cdot t}{V_{bus}}, \quad 0 \leq t \leq \Delta t_d \tag{4.96}$$

$$E_{sr,cb} = \int_0^{\Delta t_d} i_{cb}^2(t)\cdot R_s \, dt = \frac{R_s \cdot \Delta P_L^3}{3\eta_{dc/dc}\cdot S_{Rfc}\cdot V_{bus}^2} \tag{4.97}$$

The dissipation factor $K_{E,R_S}$, defined in (4.98), presents the energy spent in $R_s$ in comparison to the energy exchanged with the capacitor.

$$K_{R_S} = \frac{E_{sr,cb}}{E_{Tcb}} = \frac{2R_s\cdot\Delta P_L}{3V_{bus}^2} \tag{4.98}$$

The power consumption in $R_s$ is reflected as an increment in the restitution time $\Delta t_r$, caused by the excess of energy required to restore the bus voltage. Assuming the energy dissipated in the restitution operation approximately equal to the dissipated in the transient supply, the excess of energy required is $2E_{sr,cb}$. From equations (4.90) and (4.94) it is calculated the increment in the restitution time $\Delta t_{r,R_S}$ given in (4.99), and the relative increment factor $K_{\Delta t,R_S}$ defined in (4.100).

$$\Delta t_{r,R_S} = \frac{2R_s\cdot\Delta P_L^3}{3V_{bus}^2\cdot\eta_{dc/dc}^2\cdot\Delta P_{rbfc}\cdot S_{Rfc}} \tag{4.99}$$

ISBN:978-84-692-6902-2/ DL:T-1848-2009

$$K_{\Delta t,R_S} = \frac{\Delta t_{r,R_S}}{\Delta t_r} = \frac{4R_s \cdot \Delta P_L^3}{3V_{bus}^2 \left(\eta_{dc/dc}^2 \cdot \Delta P_{rbfc}^2 + \Delta P_L^2\right)} \tag{4.100}$$

In this work, a 48 V DC bus has been selected to illustrate the design and control process, due to its common use (i.e. aerospace and telecom power systems, etc.). The DC bus parameters are summarized in table 4.2.

Table 4.2: DC bus parameters.

| Parameter | Value |
|---|---|
| $\eta_{dc/dc}$ | 85 % |
| $V_{0bus}$ | 48 V |
| $K_{vb}$ | 5 % |
| $\Delta P_L$ | 300 W |
| $S_{Rfc}$ | 250 W/s |
| $C$ | 1.9 F |
| $\Delta t_r$ | 2.7 s |
| $\Delta P_{rbfc}$ | 100 W |

The fuel cell power slew-rate has been designed from the mechanical consideration and experimental behavior of the Nexa power module as was previously described in section 4.2. Also, the bus restitution time and fuel cell power excess have been designed to obtain an acceptable response time without an excessive excursion of the fuel cell power from its final steady-state. The capacitor required in this application must support at least 50.4 V, and actually does not exist a single capacitor or supercapacitor that fulfills both voltage and capacitance specifications, and therefore it is necessary to use a module constituted by commercially available capacitors. In this work, the bus capacitor bank was implemented using a parallel array of 7 Nippon Chemi-con U36D capacitors of 0.27 F and 63 V, each one with a serial resistance of 4 mΩ. The capacitor bank theoretical serial resistance is 571 $\mu\Omega$, but the experimental value that considers also the connectors and cables is $R_s$ = 1.87 mΩ. From equations (4.98) and (4.100), and taking into account the accepted variation of the bus voltage defined by $K_{vb}$, the energy dissipated in $R_s$ is between 0.015 % and 0.018 % of the energy exchanged with the load, and the increment in the restitution time is between 0.027 % and 0.033 %. A supercapacitor-based system with the same characteristics can be implemented with commercially available devices, i.e. using a serial array of 27 AN-series LS ultracapacitors of 50 F and 2.7 V. Each one of these supercapacitors has a serial resistance $R_{s_0}$ = 16 mΩ, which results in a total $R_s$ = 432 mΩ that generates an energy dissipation between 3.4 % and 4.2 % of the energy exchanged with the bus, and an increment in the restitution time between 6.3 % and 7.7 %. In terms of resistive losses, for high voltage applications it is more efficient to use high voltage capacitors in parallel instead of low voltage supercapacitors in series.

ROVIRA I VIRGILI UNIVERSITY
FUEL CELL MODELING AND CONTROL FOR FUEL CONSUMPTION OPTIMIZATION
Carlos Andres Ramos Paja
ISBN:978-84-692-6902-2/ DL:T-1848-2009

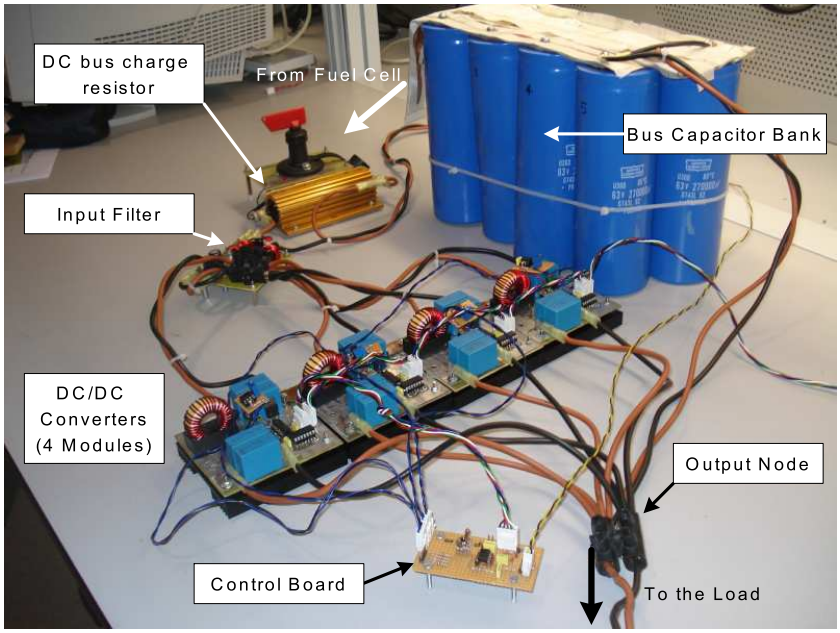


Figure 4-32: Fuel cell power conditioning system.

Finally, the fuel cell power conditioning system implemented is depicted in figure 4-32, where it is observed the output bus 1.9 F capacitor bank, the controlled DC/DC converter modules, the power conditioning control board, the input filter and the bus capacitor charge resistor.

## 4.6 Minimum fuel consumption control strategy for fuel cell-based power systems

The topology used to control the implemented fuel cell-based power system is presented in figure 4-33, where the boost DC/DC converter is controlled to define the fuel cell current and the bus capacitor supplies the power transients. Also, the topology allows to control the capacitor voltage in order to provide a regulated DC bus. These regulations are performed by controlling the fuel cell power production in agreement with the load power and bus voltage, being the fuel cell controlled through its current and $\lambda_{O_2}$ profiles, which controllers were implemented by using the Matlab Real-Time Windows Target and a National Instruments data acquisition card (DAQ) to interface with the sensors and actuators.

The main objective of the control strategy developed in this section is ensure a safe and efficient fuel cell operation in a regulated DC bus, and therefore the first step is define the optimal fuel cell operating points. Next, the controllers that allow the fuel cell operation in that conditions must be designed, implemented and tested. Both procedures are described in the next subsections.

ISBN:978-84-692-6902-2/ DL:T-1848-2009

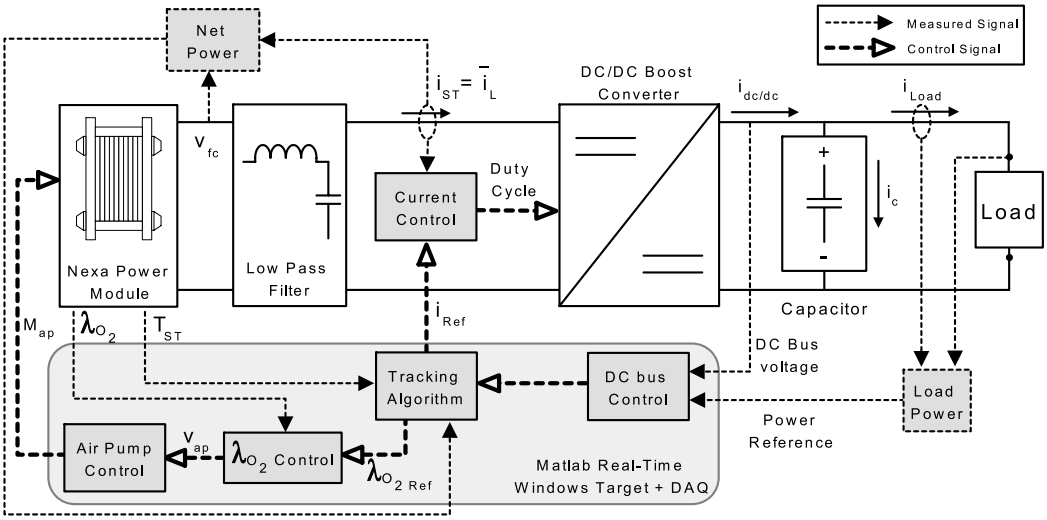


Figure 4-33: Fuel cell-based power system control topology.

### 4.6.1 Fuel cell maximum power points characterization

Fuel cell output power depends on the stack current and air pump flow rate. The stack current is the result of the load and auxiliary system currents, and therefore a higher air pump flow rate implies higher current demand. For constant stack current conditions, this power relationship has an optimal point where the relation between the power generated by the stack and the one spent by the air pump is maximum. In those operating points the power delivered to the load (net power) is the maximum for the load current requested.

The analysis of common control objectives for the fuel cell Nexa power module (Nexa) $\lambda_{O_2}$ profiles is summarized in figure 4-34, where the behavior of the net power as a function of $\lambda_{O_2}$ in constant-stack-current curves is presented. These net power curves describe the effective power delivered to the load, which is the electric power generated by the stack minus the power required by the auxiliary systems. Also, figure 4-34 depicts the $\lambda_{O_2}$ profiles generated by constant voltage, $\lambda_{O_2} = 3.29$ and maximum power control strategies. The constant voltage control is not safe because its profile is near to the oxygen starvation limit ($\lambda_{O_2} = 1$), the constant $\lambda_{O_2} = 3.29$ was chosen because it is the highest $\lambda_{O_2}$ constant value that can be achieved before the air pump saturation, and therefore is the farthest constant value from starvation limit. Finally, the maximum power profile determines the values of $\lambda_{O_2}$ where the relation between the energy delivered to the load and the energy spent by the air pump is maximum, and again this profile is far from the starvation limit.

ISBN:978-84-692-6902-2/ DL:T-1848-2009

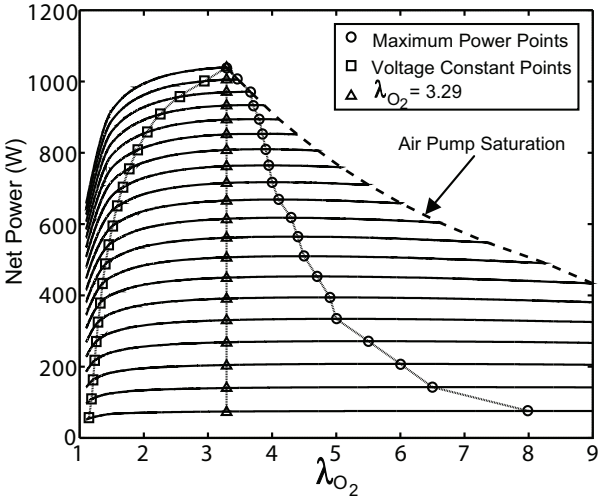


Figure 4-34: Fuel cell Nexa power module $\lambda_{O_2}$ profiles.

In the maximum power points, the stack current requested by the load and auxiliary systems is the minimum possible to produce the particular stack power condition. For example, in figure 4-34 it is observed that the maximum power point corresponding to a 610 W net power is $\{I_{st} = 17.5\ A,\ \lambda_{O_2} = 4.35\}$, but this net power can be also generated in other operating points like $\{I_{st} = 19\ A,\ \lambda_{O_2} = 1.8\}$. From this minimum stack current condition of the maximum power points, and from the hydrogen flow requested in the electrochemical reaction (2.7), it is concluded that the maximum power points correspond to the minimum fuel consumption conditions to provide a particular net power. This work proposes to follow these maximum power points in order to supply the power requested by the load with the minimum fuel consumption, providing safety to the fuel cell and smooth behavior of $\lambda_{O_2}$. In this way, $\lambda_{O_2}$ must be regulated following the maximum power profile and the fuel cell net-current will be also controlled to avoid high-frequency transients that produce fast changes in the oxygen excess ratio and in the output power.

Fuel cell temperature changes cause stack voltage variations, modifying in this way the stack power at the maximum power points. According to the stack voltage variation caused by changes in the stack temperature ($T_{st}$), it described in the model proposed in chapter 2 (2.36), and considering a defined net current and $\lambda_{O_2}$ operating point, the net power variation caused by temperature changes is calculated as follows:

$$\Delta P_{net,T} = dV_T \cdot I_{net} \tag{4.101}$$

where $dV_T$ is the voltage variation caused by thermal effects (2.36), $I_{net}$ the net current and $\Delta P_{net,T}$ the power deviation.

ISBN:978-84-692-6902-2/ DL:T-1848-2009

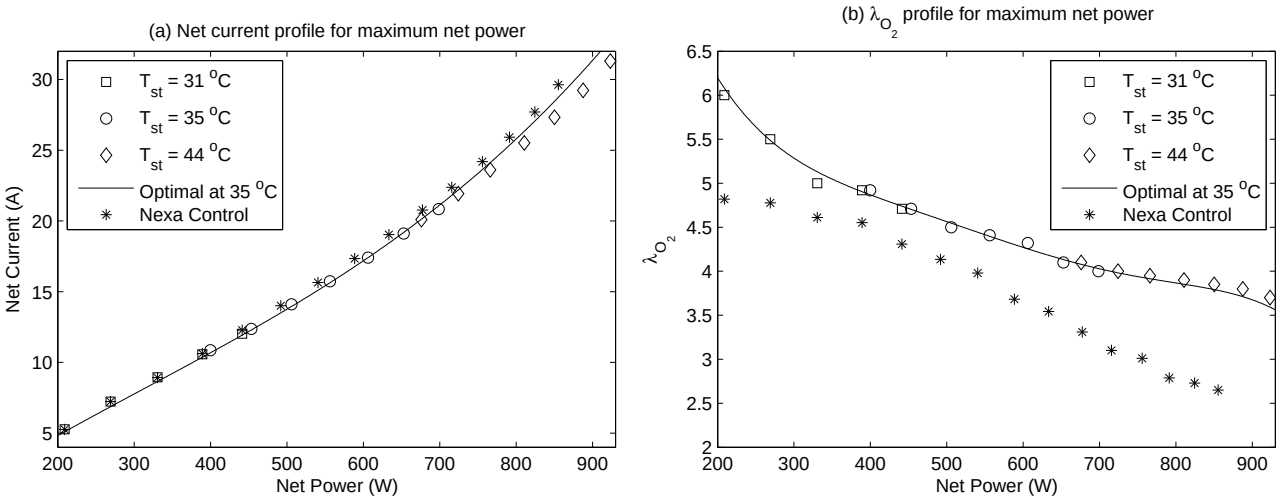


Figure 4-35: Nexa fuel cell current and $\lambda_{O_2}$ optimal profiles for fuel consumption efficiency.

In order to identify the net-current and $\lambda_{O_2}$ optimal profiles for minimum consumption, the maximum power points were experimentally obtained for constant temperatures. This was performed by heating the cooling fan input air to control the stack temperature, being limited up to net power operating points where the stack does not require heating to achieve the desired temperature. Figure 4-35 shows the experimental maximum power points operating conditions at 31 °C, 35 °C and 44 °C. Using the net power deviation given in (4.101), the net power of those maximum power points at 35 °C is calculated, and these conditions are used to identify the net current and $\lambda_{O_2}$ optimal profiles at 35 °C depicted in figure 4-35 (solid line).

From the identified net current and $\lambda_{O_2}$ curves it is calculated the optimal operating conditions to produce a required net power at $T_{st}^0 = 35$ °C. Equations (4.102) and (4.103) allow to calculate the optimal net current ($I_{net,op}$) and $\lambda_{O_2,op}$ to generate a requested net power $P_{net,35}$ when $T_{st} = T_{st}^0$. The equations parameters are given in table 4.3.

$$I_{net,op} = \sum_{k=0}^{3} \left[ a_k \cdot (P_{net,35})^k \right] \tag{4.102}$$

$$\lambda_{O_2,op} = \sum_{k=0}^{5} \left[ b_k \cdot (P_{net,35})^k \right] \tag{4.103}$$

To obtain $I_{net,op}$ and $\lambda_{O_2,op}$ at different stack temperatures, it is necessary to take into account the power deviation caused by the temperature. The required net power $P_{net}$ can be expressed as the power $P_{net,35}$ generated with the same net current and $\lambda_{O_2}$ at $T_{st}^0$ plus the power deviation caused by the temperature difference:

$$P_{net} = P_{net,35} + \Delta P_{net,T} \tag{4.104}$$

ISBN:978-84-692-6902-2/ DL:T-1848-2009

Table 4.3: $I_{net,op}$ and $\lambda_{O_2,op}$ equations parameters.

| k | $a_k$ | $b_k$ |
|---|---|---|
| 0 | $-1.868$ | $13.323$ |
| 1 | $3.802 \times 10^{-2}$ | $-6.878 \times 10^{-2}$ |
| 2 | $-2.888 \times 10^{-5}$ | $2.352 \times 10^{-4}$ |
| 3 | $3.072 \times 10^{-8}$ | $-4.139 \times 10^{-7}$ |
| 4 | | $3.566 \times 10^{-10}$ |
| 5 | | $-1.194 \times 10^{-13}$ |

From (4.101) it is noted that the power deviation also depends on the net current. Replacing (4.101) in (4.104) it is obtained the polynomial equation presented in (4.105), whose solution describes the $P_{net,35}$ value used to calculate the optimal operating point $\{I_{net,op}\ ,\ \lambda_{O_2,op}\}$ that produces the required net power at the given stack temperature.

$$P_{net,35} + \Delta V_{fc,T} \cdot I_{net,op} - P_{net} = 0 \tag{4.105}$$

Equation (4.105) is a third order polynomial equation with at least one real solution. In cases where more than one real solution exist, the selection criteria given in (4.106) is used, and also constrained to the power slew-rate restriction.

$$\left.\begin{array}{r} P_{net,35} > 0 \\ if\ T_{st} > T_{st}^0 \Rightarrow P_{net,35} < P_{net} \\ if\ T_{st} < T_{st}^0 \Rightarrow P_{net,35} > P_{net} \end{array}\right\} \tag{4.106}$$

The procedure to obtain the optimal operating point for any required power and stack temperature is: calculate the required net power $P_{net,35}$ at $T_{st}^0$ (35 °C) solving equation (4.105), and next calculate the optimal net current and $\lambda_{O_2}$ values using equations (4.102) and (4.103).

Finally, to allow a comparison with the internal control system of the 1.2 kW Nexa Power Module, its experimental net current and $\lambda_{O_2}$ profiles at the same temperatures of the maximum power points profiles are also depicted in figure 4-35. The Nexa internal control system describes non-optimal $\lambda_{O_2}$ values that require higher net currents and therefore higher fuel consumption.

### 4.6.2 Minimum fuel consumption point tracking and control algorithm

Equations (4.102) and (4.105) define the reference of the fuel cell net-current control, as function of the power requested and stack temperature. Due to the effect of the current in the behavior of $\lambda_{O_2}$, this net current regulation is a feed-forward control system that allows fast responses to power transients and smooth $\lambda_{O_2}$ behavior. Similarly, equation (4.103) defines the reference of the

ISBN:978-84-692-6902-2/ DL:T-1848-2009

$\lambda_{O_2}$ feedback control system to achieve the same minimum consumption condition. Also, a slew-rate power regulation is designed to minimize the transient effects in $\lambda_{O_2}$, and this is done by the current slope constraint and the coupling with a capacitor that provides energy in high-frequency transients. In this way, the air pump control voltage and DC/DC converter input current are regulated to produce the demanded electric power while tracking the minimum fuel consumption points.

The fuel cell current is controlled to follow the profile defined in (4.102), which allows the fast tracking of the operating points that produce the requested power with maximum efficiency. Also, the current is affected by the power slew-rate regulation system, constraining the maximum current slope and therefore reducing the $\lambda_{O_2}$ control transients that deviate it from its optimal profile.

The controller developed to regulate $\lambda_{O_2}$ has been designed using the linearized model given in (4.69). This controller has a feedback component designed to obtain a gain margin of 10 dB and a phase margin of 60°. Also, the controller has a feed-forward component that depends on the current, designed to obtain the same gain margin. The transfer function that defines the behavior of the air pump voltage to control $\lambda_{O_2}$ in a desired profile is summarized in (4.107), where $e_{\lambda_{O_2}}(s)$ is the deviation of $\lambda_{O_2}$ from the desired value.

$$V_{ap}(s) = \begin{bmatrix} 158.1\dfrac{1+0.44s}{1+26s} & 1.2 \end{bmatrix} \begin{bmatrix} e_{\lambda_{O_2}}(s) \\ I_{st}(s) \end{bmatrix} + 40 \tag{4.107}$$

The model described in (4.69) considers a controlled air pump that produces the desired air flow, and its control strategy corresponds to the Nexa regulation system for this device. In order to perform an experimental validation of the proposed $\lambda_{O_2}$ control and minimum consumption strategies, an externally accessible controller for the air pump has been developed. This controller has been designed to reproduce the closed loop behavior of the air pump controlled by the Nexa control board. Following the identified Nexa control strategy, the feed-forward controller given in (4.108) has been implemented. The controller defines the air pump motor speed reference $M_{ap}$ to obtain an air flow equal to the one generated by the Nexa air pump controller at the same control voltage $V_{ap}$ condition.

$$M_{ap}(s) = 1.315\frac{s^2+11.3s+13}{s^2+16.7s+25.5}V_{ap}(s) \tag{4.108}$$

The designed $\lambda_{O_2}$ and air pump controllers were used to evaluate the behavior of the fuel cell and DC bus systems in response to high-frequency load power transients, this following the control topology previously described in figure 4-33. The change in the load power requested determines the reference of the fuel cell current controlled by the DC/DC converter, and for the air pump voltage control system to follow the optimal profiles that ensure a minimum hydrogen consumption for the load profile.

ISBN:978-84-692-6902-2/ DL:T-1848-2009

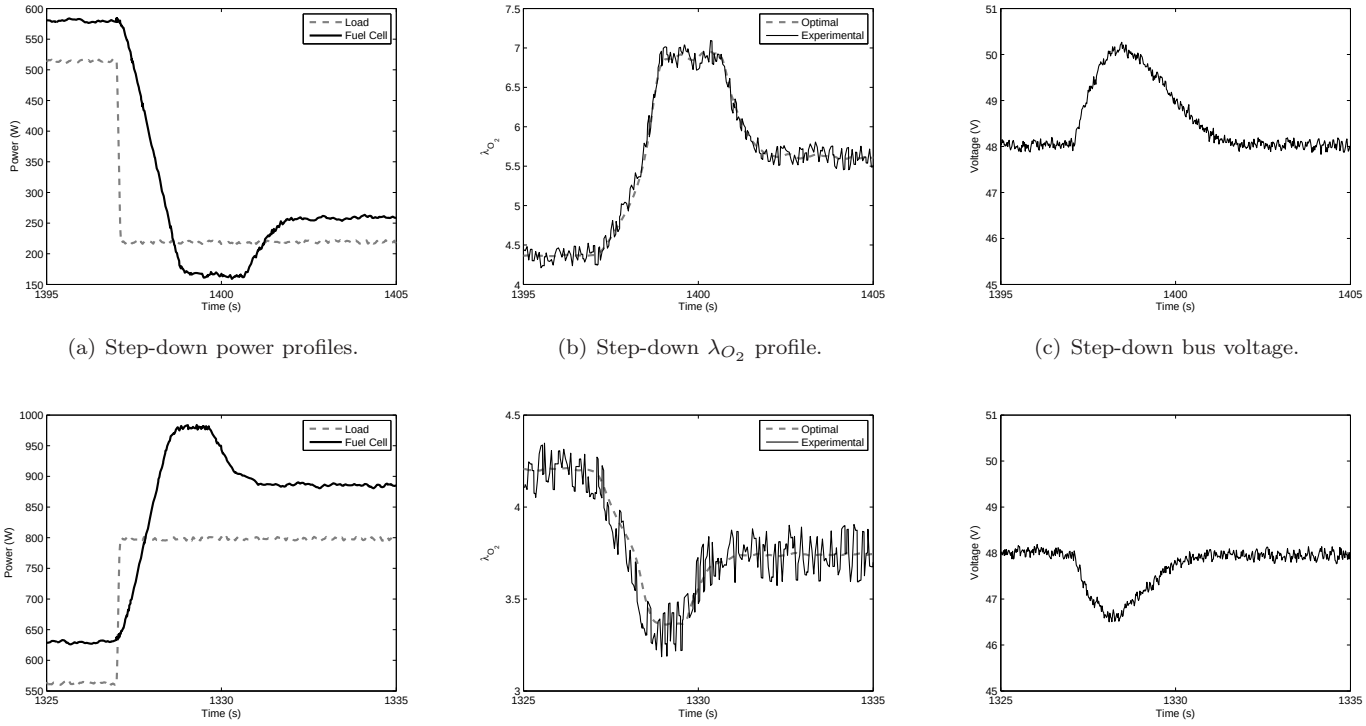


(a) Step-down power profiles. (b) Step-down $\lambda_{O_2}$ profile. (c) Step-down bus voltage.

(d) Step-up power profiles. (e) Step-up $\lambda_{O_2}$ profile. (f) Step-up bus voltage.

Figure 4-36: Fuel cell and DC Bus control in load power transients.

Figure 4-36(a) presents the experimental behavior of the fuel cell control system in response to a 300 W step-down load power transient. It is observed the action of the 250 W/s slew-rate regulation system and the bus restoring system that saturates the power excess over the one required by the load to the designed value. The corresponding $\lambda_{O_2}$ optimal reference and experimentally controlled profiles for the fuel cell power delivered are depicted in figure 4-36(b), where a satisfactory performance and smooth transitions are observed. Finally, figure 4-36(c) depicts the measured bus voltage profile, where the capacitor-bank supplies the high-frequency transient and therefore its voltage is modified in the expected deviation, and it is also restored by the bus control system in the specified restitution time. Similarly, figures 4-36(d)-4-36(f) present the experimental behaviors of the fuel cell and DC bus control system in response to a 250 W step-up power transient. It is observed the expected performance of the control system and a satisfactory $\lambda_{O_2}$ regulation in the tracking of the minimum fuel consumption points. Also, it is noted a small $\lambda_{O_2}$ ripple caused by the air flow system.

ISBN:978-84-692-6902-2/ DL:T-1848-2009

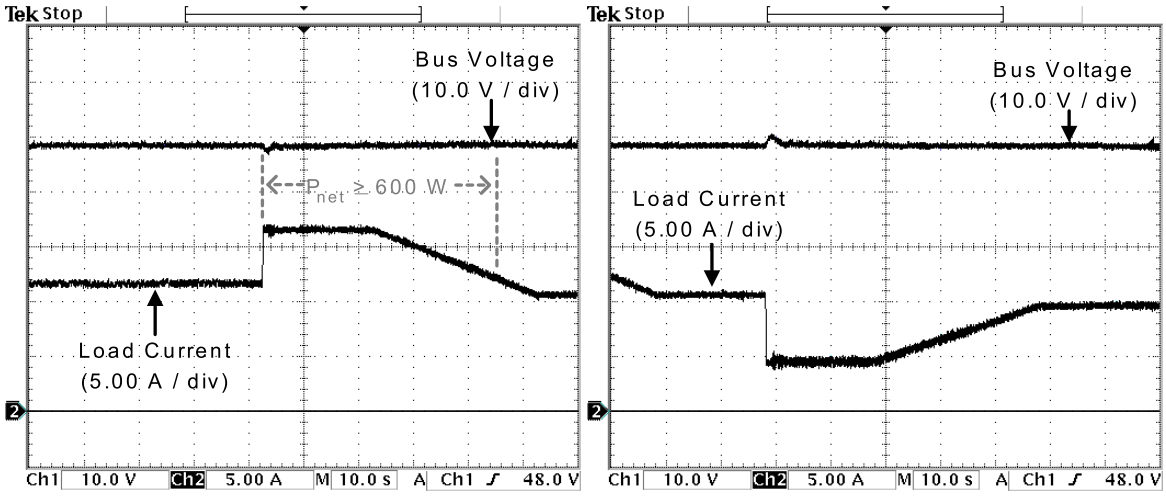


(a) Load and fuel cell power profiles.

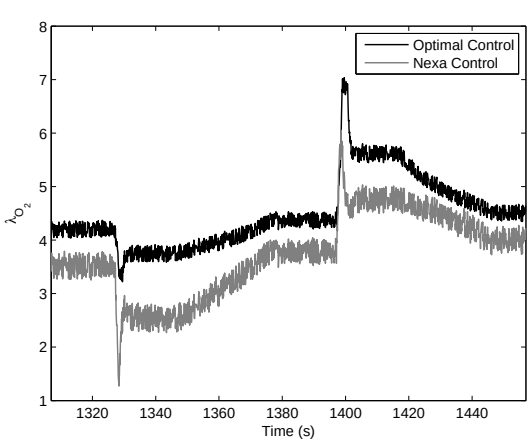


(b) Nexa and optimal $\lambda_{O_2}$ profiles.

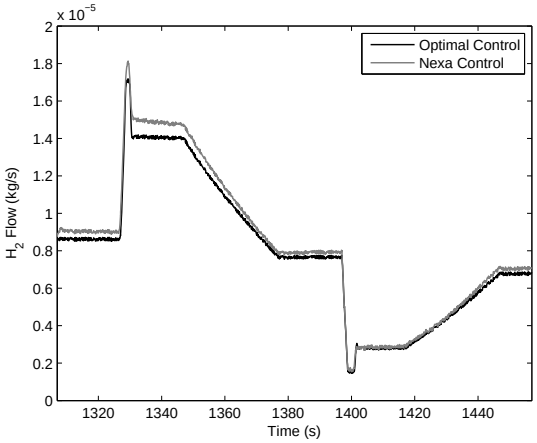


(c) Nexa and optimal $H_2$ flow profiles.

Figure 4-37: Hydrogen consumption comparison in a load profile.

### 4.6.3 Fuel consumption and efficiency analysis

To analyze the fuel consumption efficiency of the fuel cell system with the proposed $\lambda_{O_2}$ control profile, its hydrogen flow profile was compared with the one generated by the internal control system implemented in the Nexa control board. This was performed by controlling an electronic load to obtain the load current profile depicted in figure 4-37(a), which requests high and low frequency transients meanwhile the bus control system regulates the load voltage. The capacitor bank provides the energy to the load in the transients that does not fulfill the selected power slew-rate. In the same figure the experimental behavior of the DC bus voltage is presented, which corroborates the expected capacitor bank energy control and the constraint of its voltage to the maximum admissible deviation limits.

ISBN:978-84-692-6902-2/ DL:T-1848-2009

The defined load profile was applied to the fuel cell system working with both Nexa and optimal profile controllers. The fuel cell net power profile in both cases was the same due to the decoupling performed by the DC/DC converter and its power slope limitation. The experimental $\lambda_{O_2}$ profiles performed by Nexa and optimal profile controllers are depicted in figure 4-37(b), where the last one performs an accurate tracking of the minimum consumption points. This was done because of the satisfactory performance of the $\lambda_{O_2}$ and air pump control systems at the optimal profile. The $\lambda_{O_2}$ profile generated by the Nexa module internal control follows a similar behavior compared with the optimal profile but has significant differences in the steady-state values. Also, the Nexa controlled profile presents lower regulation in load power transients, which could be dangerous for the fuel cell because this implies a high probability of entering in an oxygen starvation condition. Figure 4-37(c) presents the experimental hydrogen flows generated by both control strategies to supply the load power. It is observed a significant reduction of the hydrogen flow requested at high power using the optimal profile control instead of the Nexa internal control, and also a small reduction at low power. These behaviors are in agreement with the corresponding $\lambda_{O_2}$ profiles and the fuel cell power characterization presented in figure 4-35, where at $\lambda_{O_2}$ values far from the maximum power points higher currents are required to produce the desired net power and therefore higher hydrogen consumption.

Finally, considering an hydrogen cylinder of 240 gr, the presented load power profile of figure 4-37(a) could be supplied by the electrical power generation system during 8 hours using the Nexa internal control. Using the optimal profile control, this load power profile can be supplied during additionally 18.7 minutes with the same hydrogen cylinder. This supply time excesses can be also expressed in terms of fuel use efficiency, the optimal profile control being 3.87 % more efficient than the Nexa internal control in this particular case. The analysis shows a higher efficiency of the optimal profile control compared with the Nexa internal control for high power profiles. In this way, in the high power component of the requested net power profile ($P_{net} \geq 600$ W), the optimal profile control is 4.43 % more efficient than the Nexa internal control. Similarly, in the low power component ($P_{net} < 600$ W), the optimal profile control is 2.89 % more efficient than the other strategy. Finally, for a constant fuel cell net power of 885 W, the optimal profile control is 5.2 % more efficient than the Nexa internal control.

With these results, the optimal profile control allows to supply the load for a longer time with the same hydrogen storage than other strategies which generate non-optimal $\lambda_{O_2}$ profiles. This implies an increment in the efficiency of the overall electrical energy generation system based on fuel cells. Also, the developed control strategies protects the stack by decreasing the probability of oxygen starvation.

ISBN:978-84-692-6902-2/ DL:T-1848-2009

## 4.7 Conclusions

This chapter has defined the most critical mechanical restrictions and control objectives for fuel cell-based power system controllers. The analysis reports that an auxiliary storage device is needed to supply high-frequency load transients and to avoid fuel cell damages caused by oxygen starvation phenomenon. In the specialized literature typical serial or parallel fuel cell-ASD hybrid topologies are used to fulfill this requirement. This chapter has analyzed the efficiency of both topologies, and given a selection criterion that depends on the load power profile: for load power profiles that request a higher ASD power than the limit defined by the consumption and regenerative power profiles, it should be processed by the serial hybrid topologies because they are more efficient than the parallel topologies in these conditions. Likewise, high regenerative ratios increase the minimum ASD power when the serial topology is more efficient. This indicates that the parallel topology is more efficient in DC dominant component profiles.

The selection criteria proposed requires a previous knowledge of the frequency components or dynamic behavior of the load profile, so the most efficient topology cannot be selected in unknown load profile cases. This chapter also proposes a novel serial-parallel topology for these cases because, in practical conditions, it is more efficient than both serial and parallel options. In extreme cases, when the load power is supplied exclusively by the ASD or the fuel cell, the serial-parallel topology is as efficient as the best of both serial and parallel topologies in these conditions. Since there are numerous non-regenerative applications, and for the comparison in terms of number of DC/DC converters between the three topologies to be fair, the serial-parallel topology was mathematically analyzed considering non-regenerative conditions. In future developments, the analysis can be extended to address other applications or considerations. Another interesting future development is the design and implementation of the control systems required to operate this novel serial-parallel topology, which is a challenge for the non-linear regulation of the converters that interact with the fuel cell, and also for the cooperative SOC and load bus regulation.

Control strategies for the fuel cell in both traditional parallel and serial topologies were also proposed, and the relation between the fuel cell maximum power slew-rate and controller robustness was presented. The parallel topology uses a small slew-rate because the controller considered is a common lineal design. The serial application, however, uses a robust QFT controller that allows a more aggressive power slew-rate and gives higher bandwidth to the system. Next, an experimental system was designed in order to test the theoretical control approach. In this setup, a power interface system based on four DC/DC boost converter modules was designed, in which the average input current was controlled to define the fuel cell stack current. Also, the capacitor bus dimensioning process allows to select it depending on the applications parameters, being in this case a 48 VDC bus with voltage deviations and restitution time restrictions. The serial resistance effect of the capacitor

ISBN:978-84-692-6902-2/ DL:T-1848-2009

bank was also analyzed, and the losses in a parallel capacitor bank were compared with the losses in a serial array of supercapacitors.

Then the fuel cell maximum power points were characterized as a function of the oxygen excess ratio $\lambda_{O_2}$ and stack temperature. The net current and $\lambda_{O_2}$ optimal profiles that produce lower losses to supply a desired power and prevent oxygen starvation phenomenon have also been identified. In the same way, the fuel cell net current control was implemented by using the power interface system fulfilling the fuel cell power slew-rate obtained experimentally, allowing a smooth control of the air pump voltage and an efficient and safe $\lambda_{O_2}$ regulation. In order to regulate the DC bus, the capacitor bank supplies the load power transients while the control algorithm modifies the fuel cell power to the new steady-state.

In addition, $\lambda_{O_2}$ and air pump control strategies were developed to evaluate the proposed optimal profiles. The prevention of oxygen starvation and the hydrogen flow profiles of the proposed strategy and the Nexa internal control were experimentally compared. These evaluations demonstrated that the minimum fuel consumption points can be tracked by using the identified optimal profiles to control the net current and $\lambda_{O_2}$. This allows smooth transitions of the oxygen excess ratio and decreases the probability of oxygen starvation phenomenon even more. Notice that the combination of a safe $\lambda_{O2}$ control strategy and a constraint on the slew-rate of the power supplied by the fuel cell can increase the lifetime of the fuel cell. This control strategy also makes it possible to use the same amount of hydrogen to supply the power required by the load for longer time than other non-optimal $\lambda_{O_2}$ profiles. This can also be expressed as an increase in fuel consumption efficiency, which is extremely useful in portable applications such as aerospace, telecom, vehicles, etc.

Finally, the minimum consumption control approach presented in this chapter requires the fuel cell maximum power points to be characterized offline, and the aging of the stack and auxiliary systems can change these points. Taking into account the rejuvenation procedures performed by the control board of the Nexa power module, however, the aging effects will be perceptible only in the long term. In this case, the fuel cell can be characterized for the new fuel cell behavior and the model proposed in chapter 2 can be parameterized again. Studies have been made of the effect of fuel cell aging [141] [142], which means that the control technique can be improved in the future to take this issue into account.

ROVIRA I VIRGILI UNIVERSITY
FUEL CELL MODELING AND CONTROL FOR FUEL CONSUMPTION OPTIMIZATION
Carlos Andres Ramos Paja
ISBN:978-84-692-6902-2/ DL:T-1848-2009

# Chapter 5

# Conclusions and Future Works

This thesis reviews the basic theory on fuel cell control and power interfacing for real applications. The revision illustrates the characteristics of the modeling approaches reported in the literature, and makes it possible to select the most appropriate approach for individual applications. It also identifies a need for two fuel cell modeling approaches. The first is a model with a circuit-based load connection which can predict important internal states such as the oxygen excess ratio or stack temperature. This model is required because the existing circuit-based models do not predict internal states that are important in fuel cell operation and protection, and the physical models available represent the fuel cell as a non-linear voltage source difficult to analyze and implement for power electronics design and simulation. The second approach required is a low-computation consuming model intended for real-time applications, such as emulator design, which gives an easy and accurate parameterization procedure to represent real prototypes.

The first need has been addressed in chapter 2. A mixed model has been designed that predicts internal states using physical and identified equations, and makes load interaction through a diode-based circuit. This model estimates the oxygen excess ratio using electrochemical relations, and computes the thermal model of the fuel cell to predict the output voltage deviation caused by stack temperature changes. The output circuit models the fuel cell electrical impedance to achieve a more realistic load interaction. The modeling procedure, which includes estimating the compressor dynamics and losses, identifying the control system and calculating the output impedance has been presented. The model parameterization procedure can be applied to any fuel cell prototype by performing simple experimental tests such as load current step response and recording the stack current, voltage and temperature changes, as well as the air flow and air temperature profiles. The model was parameterized using experimental data from a state-of-the-art-prototype (Ballard 1.2 kW Nexa power system), and implemented in a standard power electronics simulator (PSIM) for validation. This implemented model makes it possible to analyze and estimate the effects of power

ISBN:978-84-692-6902-2/ DL:T-1848-2009

electronic designs (DC/DC converters, inverters, filters, etc.) on fuel cell health and performance. The oxygen excess ratio and stack current ripple are particularly important for these aspects.

In the same research line, the fuel cell system was also analyzed to document the causes of stack voltage ripple in ripple free current conditions, which is not predicted by reported models. The results show that this voltage ripple is mainly caused by oscillations in the compressor control system, and is particularly critical in resistive loads where it causes current ripple, which degrades the stack power. Similarly, the procedure for estimating membrane water content, focused on the sensors required for its reproduction, was analyzed. This analysis has identified the minimum set of sensors that allow to calculate the membrane water content. This estimation is useful for designing stack protection systems and evaluating the safety of control strategies.

This model can be improved, in future works, by considering more complex models for compressor dynamics and losses, and a more detailed model for thermal-based voltage changes. Theoretical equations should be included to explain the voltage ripple inside the model, which is also desirable in order to reproduce the fuel cell dynamics more accurately. Finally, the results found for the estimation of the membrane water content make it possible to design on-line estimation systems, which can protect the fuel cell against insufficient-membrane-wetted conditions that degrade the stack.

The second modeling need has also been addressed in this thesis, and a fuzzy-based modeling technique has been developed intended to reproduce fuel cell dynamics with minimum calculation requirements. This model is described in chapter 3, where the theoretical background of the modeling technique is given, and justified by a state-of-the-art analysis.

Basically, the fuzzy-based modeling technique considers three main physical phenomena of the fuel cell. The first is the variation of the polarization curve, which depends on the fuel flow applied. It is represented as static stack current-voltage ratios for different fuel flow ratio operating points, where the fuel flow ratio is a normalization relative to the maximum fuel flow applicable to the stack. The second phenomenon modeled is the *charge double layer* effect caused by the electrode-membrane structure, which has a capacitor-like behavior. The third phenomenon is the *instantaneous ohmic* effect generated by stack current transients, which is absorbed by the steady-state model when the current transient ends.

Chapter 3 uses a new approach based on fuzzy estimators trained by the ANFIS algorithm to describe the modeled phenomena. The fuel cell polarization reproduction is based on a fuzzy-ANFIS model obtained from stack current, voltage and fuel flow experimental data, and the polarization curve depends on the fuel flow ratio condition. This approach makes it possible to parameterize this model to real prototypes by performing simple ramp-like current profiles measuring stack voltage and fuel flow control signal. The *instantaneous ohmic* effect is modeled by a non-linear resistor, the resistive value of which is given by a fuzzy-ANFIS model, trained using fuel cell equivalent

ISBN:978-84-692-6902-2/ DL:T-1848-2009

resistance calculated from experimental measurements of the instantaneous voltage deviations caused by defined current transients. This approach makes it easy to parameterize the model by performing controlled current transients in the desired operating range, and obtaining a resistive value for each operating condition. Similarly, the *charge double layer* effect is modeled by a capacitive system, represented by a first order delay, where the capacitance is given by a fuzzy-ANFIS model. This fuzzy-ANFIS system is trained by a set of time constants calculated from simple current and fuel flow ratio transients performed on the prototype, so the model reproduces this dynamic component in the desired operating range. Finally, a discrete transfer function of the dynamic stack voltage, supported by the three fuzzy-ANFIS models, has been described. This model is contrasted with a previously parameterized fuel cell physical model and validated with experimental data from a real prototype, which leads to the satisfactory reproduction of fuel cell behavior.

The main discrepancy between the fuzzy-based model and the prototype behavior is in the voltage ripple presented in the experimental data, which is not predicted by the parameterized physical and fuzzy-based models. The fuzzy-based model can be improved in future work by considering the voltage ripple effect, and modeling it with oscillators which frequency can be also fuzzified. Another important future improvement for this model is the inclusion of a thermal model, which can be also modeled by a first order delay where the constant-time be fuzzied. Finally, the consideration of the oxygen excess ratio is a useful improvement that could be make this model suitable for fuel cell control strategies evaluation, and also it is interesting to perform it in a future development.

This thesis has also presented the advantages of using emulators to test fuel cell control devices and strategies, and to evaluate power electronic implementations intended to interact with fuel cells. A fuel cell emulator structure has been proposed for designing a low-cost emulation system, which reproduces different prototypes by modifying the fuel cell model, where portability and low cost are also valuable characteristics.

The emulator design has been developed using the fuzzy-based fuel cell modeling technique, which provides satisfactory accuracy with few calculation requirements, so it is ideal for real-time applications. The model has been implemented in a low-cost microcontroller, which also computes the control of the power stage. Chapter 3 describes linear and switching power stages for fuel cell emulation, and analyses their advantages and drawbacks. The main conclusions are: the switching power stage requires a small power supply, but introduces a non-modeled voltage ripple, which is not correlated with the real fuel cell voltage ripple. In contrast, the linear power stage does not introduce a considerable voltage ripple, which means that it can be emulated by modeling approaches. Its main drawback, however, is that it requires a high power supply. The implementation and control considerations of the emulator and its different power stages have been described, analyzed and experimentally validated, and the behavior of a real fuel cell prototype has been satisfactorily

ISBN:978-84-692-6902-2/ DL:T-1848-2009

reproduced. Also, the switching and linear power stages proposed improve the state of the art of fuel cell emulation in terms of voltage ripple analysis and reproduction capability, which makes it possible to emulate a wide range of fuel cell prototypes with detailed or simplified models.

The emulator can be improved by taking into account the strategy for controlling the air flow rate in the fuel cell system that is to be reproduced, which mainly causes the output voltage ripple. Also, powerful calculation devices, like DSP or FPGA, can be used to improve the emulator by using more complex physical fuel cell models, thus making it possible to emulate on-line such important internal states as the stack temperature and oxygen excess ratio.

The next step in using fuel cell systems in real applications is to control the stack in safe and efficient operating conditions, and to design a power electronics interface system to interact with real loads. This thesis has taken into account both issues by designing a power system interface and fuel cell control. Chapter 4 has defined important physical restrictions on fuel cell operation and control objectives that guarantee safe fuel cell power generation. A control oriented non-linear relation that describes the behavior of the oxygen excess ratio has also been presented (4.1), and it was concluded that the main delays in regulating the oxygen excess ratio are caused by the compressor, and that the stack power slew-rate must be limited to avoid oxygen starvation. Next, the most common fuel cell-auxiliary storage device topologies have been reviewed, and their efficiency for the different load power profiles analyzed. This analysis provided a selection criteria that depends on the load power profile: the serial hybrid topology must be selected for load profiles with high frequency transients or dominant AC components, and the parallel topology is most efficient at low frequency load profiles or when the DC component is high, where the threshold depends on the fuel cell bandwidth and on the consumption and regenerative power profiles. This criterion can be used to select a topology when the application does not constrain this freedom (i.e. when each load has its own power converter). Likewise, a novel serial-parallel hybrid topology has been proposed, which is more efficient than the reviewed topologies in practical load conditions. It is, therefore, suitable for fuel cell-auxiliary storage device applications whose load profiles have not previously been identified. Its advantages and higher efficiency have been analytically demonstrated and validated through numerical simulations in non-regenerative conditions, but its analysis can be extended to different considerations in future developments.

The fuel cell control system is the core of a power supply system, and chapter 4 has presented control approaches for both parallel and serial hybrid topologies. Since the serial-parallel topology requires additional control and implementation analyses, it has not been considered for control design here, but it is an interesting future development.

The parallel and serial approaches presented in this study demonstrate that the fuel cell can be controlled in a desired oxygen excess ratio set point, so that the operating conditions are safe and the

ISBN:978-84-692-6902-2/ DL:T-1848-2009

load can be supplied at the same time. The control structure presented includes linear and robust designs (i.e. QFT controllers), which constrains air flow oscillations and stack current slew-rate in order to maintain the compressor in its linear zone and the fuel cell far from the oxygen starvation boundary.

The next step in the control of the fuel cell power system is to define the control profiles. This thesis has presented a methodology for modeling the optimal operating conditions, represented by the oxygen excess ratio and the load current profiles that depend on the stack temperature, so that the fuel consumption can be minimized and the load supplied. This methodology obtains these profiles by performing simple steady-state tests on different load conditions. They can be applied to any fuel cell power system. Using the optimal operating points identified, an optimal regulation strategy has been proposed for controlling the fuel cell based power system: a DC bus voltage is regulated and the power requested by the load is supplied with minimum hydrogen consumption.

In order to validate the control systems and fuel minimization strategy proposed, an experimental, fuel cell-based power system has been designed and implemented, in which new theoretical developments have been used to design the bus capacitance. This power system consists of a four boost module converter, an input filter, a bus capacitor bank, and an input current controller. The experimental results corroborate that this implementation regulates the DC bus voltage and constrains the stack power slew-rate. Chapter 4 also gives practical considerations about the control and implementation of the system, which are valuable for further designs.

The experimental validation of the minimum consumption strategy has also been presented. The methodology for estimating the optimal operating points, the system for correcting thermal deviations and the overall control structure have all been discussed. The experimental results show that the proposed minimization strategy consumes less hydrogen than the manufacturers control system, and, because it is more efficient, it supplies the load for longer time. This system and its control strategy can be applied to any autonomous fuel cell-based power system, particularly in automobile or telecom applications, to increase the overall system efficiency.

The main limitation of the proposed strategy is that the optimal control profiles must be identified off-line, so they can be deviated by stack or compressor aging. The system for minimizing fuel consumption, then, can be improved in future developments by considering the effect of aging on the maximum power points of the stack. Likewise, another useful improvement to the system would be to develop and implement a strategy for identifying optimal control profiles on-line. This would compensate for aging and make the system able to control fuel cell array systems instead of a single prototype.

In conclusion, this thesis gives theoretical background on fuel cell analysis and control. It also gives practical and experimental considerations to improve fuel cell operation and offers theoretical

ISBN:978-84-692-6902-2/ DL:T-1848-2009

tools for designing fuel cell-based power systems. Its use is illustrated with practical and validated examples. Finally, this thesis proposes a novel strategy for regulating fuel cell power systems which minimizes fuel consumption, and improves the state of the art in this field.

The results and conclusions presented here identify future research lines that will be investigated in future work by the author. Two direct developments will be addressed. The first is the experimental validation of the criterion for selecting hybrid topologies given in chapter 4, and of the advantages of the proposed serial-parallel topology described in the same chapter. The power electronics design and control for the novel serial-parallel topology are also possible issues for future work. The second is the on-line estimation of the maximum power points of fuel cell systems, which aims to improve the fuel minimization strategy proposed in this thesis.

In general, the modeling of fuel cells for power electronics applications is an open field, as is the modeling of fuel cell power systems that take into account the power conversion stage. Likewise, fuel cell emulation requires a deeper analysis of modeling considerations and operating conditions, and a design methodology must also be proposed and standardized. These open research fields are work opportunities. This same aspect has been identified for the design of fuel cell control systems, where non-linear control techniques could be a better solution for achieving safe operation and higher efficiency, because fuel cell power systems are non-linear in nature. These fuel cell power systems also require a specific power electronics design that takes into account the mechanical restrictions of fuel cells, and the restrictions in power electronics control strategies.

ROVIRA I VIRGILI UNIVERSITY
FUEL CELL MODELING AND CONTROL FOR FUEL CONSUMPTION OPTIMIZATION
Carlos Andres Ramos Paja
ISBN:978-84-692-6902-2/ DL:T-1848-2009

# Appendix A

# Adaptive-Network-Based Fuzzy Inference System (Anfis)

In order to illustrate the Fuzzy-Anfis structure, its the mathematical analysis is presented using a multiple-input-single-output (MISO) system. This does not imply less generality because a multiple-input-multiple-output (MIMO) system can be modeled as MISO systems interconnected.

In literature are reported different MISO fuzzy reasoning systems, and in the Fuzzy-Anfis application of this thesis, the Takagi-Sugeno if-then rules are used. These rules has premise conditions that implies consequent outputs. A typical if-then rule of a MISO system with $n$ inputs and $m$ rules is:

$$\text{if } x_1 \text{ is } C_{1j} \text{ and } x_2 \text{ is } C_{2j} \text{ and } \cdots\ x_i \text{ is } C_{ij} \text{ and } \cdots\ x_n \text{ is } C_{nj} \text{ then } f_j = \left[\sum_{i=1}^{n} (p_{ij} \cdot x_i) + r_j\right] \quad \text{(A.1)}$$

where $\{x_i,\ i = 1 \cdots n\}$ are the inputs, $\{C_{ij},\ i = 1 \cdots n,\ j = 1 \cdots m\}$ the fuzzy sets and $\{p_{ij},\ r_j,\ i = 1 \cdots n,\ j = 1 \cdots m\}$ the output function or consequent parameters. The output $f_j$ of a rule computation is a linear combination of the input variables plus a constant parameter $r_j$ [77].

Each rule has an absolute firing strength $\{w_j,\ j = 1 \cdots m\}$ that defines the weight of its value in the final output. The function to calculate this weight depends on the T-S fuzzy system implementation, and in this application the product function was used. The final output of the MISO fuzzy system is a weighted average of each rule output [77], calculated as follows:

$$f = \sum_{j=1}^{m} (\bar{w}_j f_j) \quad \text{(A.2)}$$

ISBN:978-84-692-6902-2/ DL:T-1848-2009

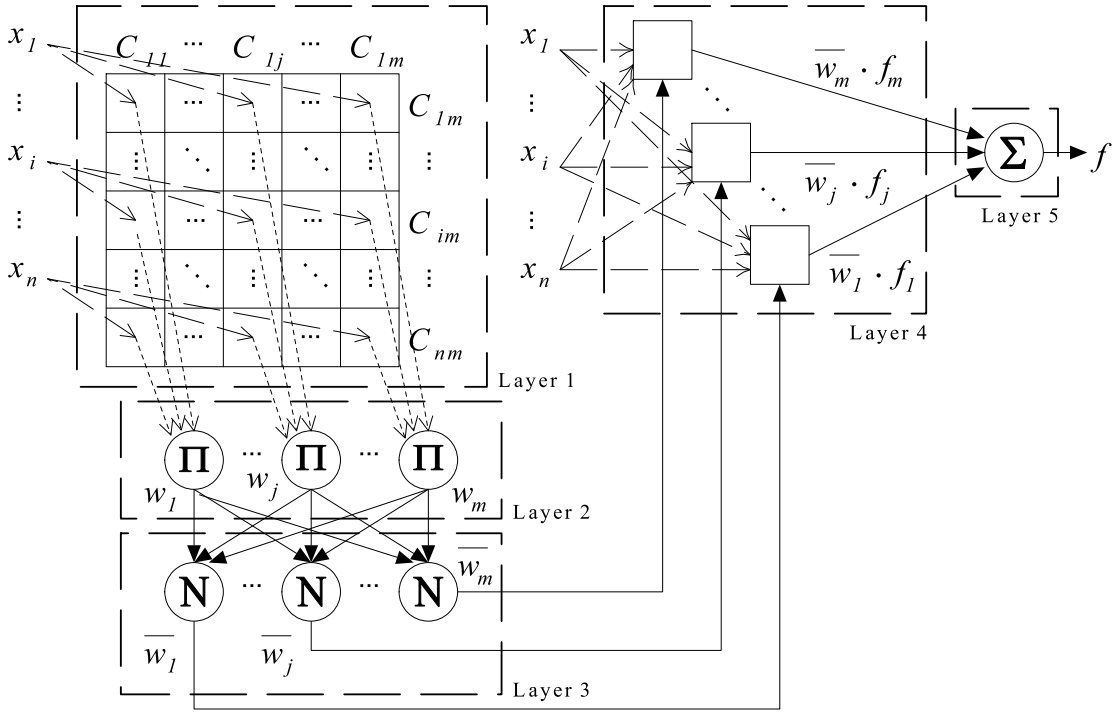


Figure A-1: Fuzzy-Anfis network structure.

where $\{\bar{w_j},\ j = 1 \cdots m\}$ are the normalized firing strengths of each rule defined as

$$\bar{w_j} = \frac{w_j}{\sum_{j=1}^{m} w_j} \tag{A.3}$$

The Fuzzy-Anfis systems used in this application are trained off-line as five-layers adaptive neural networks and used in the estimation process as T-S fuzzy systems. In this way, the network structure of the Fuzzy-Anfis systems used is presented in figure A-1, where its different layers are observed. The outputs of *Layer 1* are the fuzzy sets membership grades of the inputs, and these are obtained by using a defined membership function (MF) $\mu(x)$. The most common MF are the generalized bell function (A.4) and the gausian function (A.5) [77] [78], where $\{a_{ij},\ b_{ij}, c_{ij},\ i = 1 \cdots n,\ j = 1 \cdots m\}$ are the MF or premise parameters. In this work was selected the gausian MF for the Fuzzy-Anfis systems.

$$\mu_{b,C_{ij}}(x) = \frac{1}{1 + \left|\frac{x - c_{ij}}{a_{ij}}\right|^{2 \cdot b_{ij}}} \tag{A.4}$$

$$\mu_{g,C_{ij}}(x) = e^{-\left(\frac{x - c_{ij}}{a_{ij}}\right)^2} \tag{A.5}$$

The outputs of *Layer 2* are the absolute firing strengths $\{w_j,\ j = 1 \cdots m\}$, which are calculated

ISBN:978-84-692-6902-2/ DL:T-1848-2009

using a generalized AND operation. In this work was selected the product operator and therefore $w_j$ is calculated as follows:

$$w_j = \prod_{i=1}^{n} \left[ \mu_{g,C_{ij}} (x_i) \right] \tag{A.6}$$

where $\mu_{g,C_{ij}}(x_i)$ is the $C_{ij}$ fuzzy set MF that evaluates the input $x_i$.

The outputs of *Layer 3* are the normalized firing strengths defined in (A.3). The outputs of *Layer 4* are the if-then rules results $\{f_j,\ j = 1 \cdots m\}$ defined in (A.1) weighted by the normalized firing strengths:

$$\bar{w_j} \cdot f_j = \bar{w_j} \cdot \left[ \sum_{i=1}^{n} (p_{ij} \cdot x_i) + r_j \right] \tag{A.7}$$

Finally, the output of *Layer 5* is the summation of the outputs of *Layer 4*, and corresponds with the T-S fuzzy output previously defined in (A.2). The structure of figure A-1 has static and adaptive layers. The adaptive layers have variable parameters and therefore require training, and this is contrarily in the static layers that not have changing parameters. The adaptive layers in this structure are *Layer 1* due to its premise parameters, and *Layer 4* due to its consequent parameters. This network is trained using the hybrid learning algorithm described in [77], which uses the least-squares method to identify the consequent parameters and gradient descent to update the premise parameters according to the errors backward propagated.

Due to the Anfis network structure and the hybrid learning algorithm, the Fuzzy-Anfis systems can approximate any non-linear function in a defined input range as was demonstrated by Jang [77]. Also, different real-time implementation techniques for T-S fuzzy systems have been reported, those with different accuracy and computation load levels that allow to adjust the real-time implementation to the application requirements and hardware specifications.

ROVIRA I VIRGILI UNIVERSITY
FUEL CELL MODELING AND CONTROL FOR FUEL CONSUMPTION OPTIMIZATION
Carlos Andres Ramos Paja
ISBN:978-84-692-6902-2/ DL:T-1848-2009

ROVIRA I VIRGILI UNIVERSITY
FUEL CELL MODELING AND CONTROL FOR FUEL CONSUMPTION OPTIMIZATION
Carlos Andres Ramos Paja
ISBN:978-84-692-6902-2/ DL:T-1848-2009

# Appendix B

# Evaluation of Fixed-Step Differential Equations Solution Methods for Real-Time Simulation and Emulation

For Real-Time implementation, numerical methods for differential equations solution must be *step by step*, which takes information from previous iterations to generate the new states. In real-time simulation and emulation systems, the input data generally comes from *Analog to Digital Converters (ADC)* and the output interaction is performed through *Digital to Analog Converters (DAC)* or *Pulse-width modulation (PWM) outputs*. In this appendix, a review of common differential equations solution methods for Real-Time implementations is presented. Also, an accuracy and computational load analysis oriented to fuel cell applications is performed.

## B.1 Fixed-step differential equations solution methods

The discrete nature of the differential equation solution methods input and output data, in real-time simulation and emulation systems, implies that the solution methods must have *fixed step size*.

$$\frac{dy}{dx} = f(x, y) \tag{B.1}$$

The most common solution methods for the differential equation (B.1) in real-time are the *Ex-*

ISBN:978-84-692-6902-2/ DL:T-1848-2009

*plicit Euler* and *Runge-Kutta* methods [143].

### B.1.1 Explicit Euler Method

The Euler method require to transform the differential equations into integral equations:

$$y(x) = \int f(x,y)dx$$
$$y_1 = y_0 + \int_{x_0}^{x_1} f(x,y)dx \tag{B.2}$$

The solution of equation (B.2) is intended to obtain the future value of the function by using its present value and an integration of the signal: $f(x,y) = f(x_0,y_0)$, $\forall x \in (x_0,x_1) \Rightarrow y_1 = y_0 + hf(x_0,y_0)$, where $h = x_1 - x_0$ is the integration step:

$$y_{n+1} = y_n + hf(x_n,y_n) \tag{B.3}$$

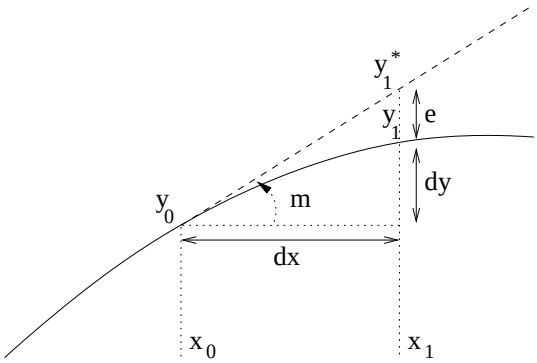


Figure B-1: Explicit Euler Method.

In figure B-1, the Explicit Euler Method is presented, where the *tendency* of the curve in the point $(x_0,y_0)$ is calculated through a linear approximation with slope $m = f(x_0,y_0)$, obtaining a variation of the function $y(x)$ in the interval $dx = x_1 - x_0 = h$ of $(y_1^* - y_0)$. The real variation of the function in the interval $dx$ is $dy = y_1 - y_0$ and the error of the Euler approximation is:

$$e = y_1^* - y_1$$
$$e = h \cdot f(x_0,y_0) - dy \tag{B.4}$$

Analyzing (B.4), it is deduced that the error is directly proportional to the integration step size; and making a physical interpretation of the variation $dy$, it is concluded that this one depends directly of $h$. These analyses allow to affirm that the Explicit Euler Method requires small integration

ISBN:978-84-692-6902-2/ DL:T-1848-2009

step size to obtain solutions with acceptable errors.

### B.1.2 Runge-Kutta Methods

Runge-Kutta method represent a standard in commercial simulation systems, because it virtually converges in all cases that it is applied. A basic analysis of the Runge-Kutta method can be done from the second order method (RK2), in which is carried out an intermediate step of size $\frac{h}{2}$, with the objective to obtain a better estimation of the slope to carry out a more accurate lineal approach of the function.

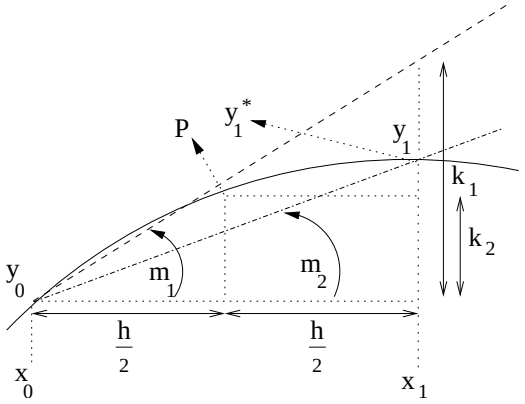


Figure B-2: Second Order Runge-Kutta Method.

In figure B-2 the RK2 method is represented, where the first step consists on an Explicit Euler approach to find the *mid point* $(x_1, y_0 + k_1)$, and then the slope of the straight line is calculated at this point like $m_2 = f(x_0 + \frac{h}{2}, y_0 + \frac{k_1}{2})$, which is used to estimate the final estimation of the function $y(x)$:

$$\begin{aligned} k_1 &= h \cdot f(x_n, y_n) \\ k_2 &= h \cdot f\left(x_n + \tfrac{h}{2}, y_n + \tfrac{k_1}{2}\right) \\ y_{n+1} &= y_n + k_2 \end{aligned} \tag{B.5}$$

This method calculates a slope $m_1$ to approach an intermediate point of the function, where a new slope $m_2$ is calculated, which is used to estimate the variation of the function in the interval $h$, and therefore this method is also known as *Mid Point Method*. Carrying out an error analysis in $t = n + 1$, where $y(t) \mid_{t=n+1} = y(n+1)$, is obtained that $e = k_2 + y_n - y(n+1)$, arriving to:

$$e = h \cdot f\left(x_n + \frac{h}{2}, y_n + \frac{h \cdot f(x_n, y_n)}{2}\right) + y_n - y(n+1) \tag{B.6}$$

From the equation (B.6), it is deduced that the error depends on a high order expression of the

ISBN:978-84-692-6902-2/ DL:T-1848-2009

integration step size ($h^3$), completing the expression of RK2:

$$y(n+1) = y_{n+1} + O(h^3) \tag{B.7}$$

where $O(h^3)$ represents the error in the approximation of $y(n+1)$ through $y_{n+1}$.

**Fixed Step 4th Order Runge-Kutta Method (RK4)**

This method requires four evaluations of the derivation function for each integration step (four times the Euler evaluation), obtaining an error in terms of $h^5$, which indicates that the error decreases drastically when the step size $h$ is reduced. Its calculation steps are given in (B.8).

$$\left.\begin{array}{l} k_1 = h \cdot f(x_n, y_n) \\ k_2 = h \cdot f\left(x_n + \frac{h}{2}, y_n + \frac{k_1}{2}\right) \\ k_3 = h \cdot f\left(x_n + \frac{h}{2}, y_n + \frac{k_2}{2}\right) \\ k_4 = h \cdot f\left(x_n + h, y_n + k_3\right) \\ y_{n+1} = y_n + \frac{k_1}{6} + \frac{k_2}{3} + \frac{k_3}{3} + \frac{k_4}{6} \\ y_{n+1} - y(n+1) = O(h^5) \end{array}\right\} \tag{B.8}$$

The high convergency ratio and satisfactory approximation in the solution makes of this method a standard in the simulation and emulation industry. In this way, in [144] a power systems real-time simulator is presented, which uses the Runge-Kutta method for the simulation of the mathematical models, being executed in a DSP. Also, in [145] an implementation of the RK4 algorithm in a parallel simulation system is presented, focused on power systems simulation, and exposing the possibility of using the system in real time simulations.

In summary, it is possible to affirm that the Runge-Kutta methods have satisfactory accuracy, good convergence and a moderate calculation volume [42].

### B.1.3 Real-Time Considerations

In [146], an analysis of the precision of these two methods is presented, which is summarized in the tables B.1 and B.2. In table B.1, the deviations of the Euler and RK4 methods with respect to an analogical integrator is presented, it depending on the number of steps that each method takes to process the highest frequency of the signal. For example, the RK4 method reaching a precision of 0.001 dB with 8 integration steps.

In table B.2, the approximation error is analyzed depending on the number of steps that each method takes to process the highest frequency in the signal, and it is compared with the error of

ISBN:978-84-692-6902-2/ DL:T-1848-2009

Table B.1: Deviations in Euler and RK4 Methods.

| $\frac{f_{integration}}{f_{signal}}$ | Euler | RK4 |
|---|---|---|
| 32 | 0.01 dB | 0.000004 dB |
| 16 | 0.06 dB | 0.00007 dB |
| 8 | 0.2 dB | 0.001 dB |
| 4 | 0.9 dB | 0.02 dB |
| 2 | 3.9 dB | 0.4 dB |

Table B.2: Equivalent errors to discretization errors.

| Resolution | 1 part in | Euler $\frac{f_{integration}}{f_{signal}}$ | RK4 $\frac{f_{integration}}{f_{signal}}$ |
|---|---|---|---|
| 8 | 256 | 21 | 3.5 |
| 10 | 1024 | 41 | 4.9 |
| 12 | 4096 | 83 | 6.9 |
| 14 | 16384 | 170 | 9.7 |
| 16 | 65535 | 360 | 14.0 |

discretization in an analog to digital converter (ADC). This information is very useful in the selection of the processing system. i.e. using a 10 bits ADC to acquire the input signals, it is necessary to use 5 RK4 integration steps to obtain the same error of 1 part in 1024, or 41 Euler integration steps to achieve the same precision. The use of more integration steps than the ones suggested by table B.2 is useless because the error introduced by the ADC masks the additional numerical integration precision, and therefore, the increment in the computational time required by the additional steps do not generate more precision in the overall system (ADC+processing).

In conclusion, Runge-Kutta methods are appropriate for systems with high variability in the simulation/emulation signals, since they can provide an acceptable approximation without compromising strongly the sampling time. On the other hand, Euler methods enable a fast approximation of the system behavior, being adequate for systems with low variability in the signals. Due to Euler method requires small calculation power, it is suitable to be implemented in low-calculation-power embedded systems.

## B.2 Real-Time simulation of Fuel Cell systems

Real-Time simulations of the non-linear model proposed by Pukrushpan et al. [1] have been performed, this in order to analyze the behavior of Euler and RK4 methods in fuel cell states calculation for real-time implementations. The processing environments used are Personal Computes (PC) and Embedded systems. The PC environments use the MATLAB Real-Time Windows Target Toolbox and RTAI-Linux Target Application, looking for emulate the fuel cell stack and its auxiliary systems. The Embedded environments used are the DS1104© dSPACE PowerPC Target and a TMS320C6711

Texas Instruments DSP (DSK Starter Kit).

The Real-Time Windows Target [41] allows the real-time execution of simulink models on Windows 2000/XP environments. Likewise, the RTAI-Lab Linux Target [147] allows the *Hard Real-Time* execution of simulink models implementing the *Real-Time POSIX standards* [148]. These implementation platforms can coexist with another applications and it is possible to develop graphic user interfaces (GUI) without additional hardware.

The high-performance embedded system DS1104© dSPACE [149] allows the hard real-time execution of complex simulink models that require high calculation power. For signal monitoring, dSPACE provide the *ControlDesk* tool [150] that allows the visualization and interaction with internal and external signals in run-time. DS1104 characteristics: PCI Interface, PowerPC main processor, TMS320F240 secondary processor, 32 Mb of DRAM, USB programming interface, 4×16-bits ADC, 4×12-bits ADC, 8×16 DAC, 2×12 DAC, 20×DIO, $3\phi$ PWM coder.

The last implementation platform evaluated was the TMS320C6711 DSK [151], which has a high-performance floating point DSP-processor. The programming is performed through the *Matlab DSP TM320C6000 Target* and has the characteristic of operating autonomously, being possible to programming the real-time model from an external memory. This characteristic makes it ideal for prototyping of emulators, since it is easy to transport, low cost and do not require additional hardware.

The procedure of selecting the numerical methods for real-time implementations has been trivialized in many developments, but the appropriate selection of the numerical method has definitive influence in the final prototype characteristics like: size, power request, complexity and cost. In this appendix the analyses are focused on a fuel cell model, which was also simulated using the variable step size algorithm *ode45 (Dormand-Prince)* of Matlab/Simulink to analyze the precision and computational loads of the fixed-step approximation methods, this because the *ode45* algorithm implements a step size control to minimize the integration errors. The mathematical model was implemented with Euler and RK4 methods, evaluating their performance for real-time simulations. The programming was developed in Matlab/simulink using the Real-Time Workshop Toolbox and the *Targets* required for each implementation platform.

### B.2.1 Real-Time Simulation Results

Figure B-3 shows the comparison between the outputs of the dynamic-step-size method (green line) and the outputs of the real-time simulations of the Euler method (red line) and RK4 method (blue line). The real-time evaluation was made using the processing of the physical variables: cathode air mass flow (figure B-3(a)), membrane water content (figure B-3(b)) and stack voltage (figure B-3(c)).

ISBN:978-84-692-6902-2/ DL:T-1848-2009

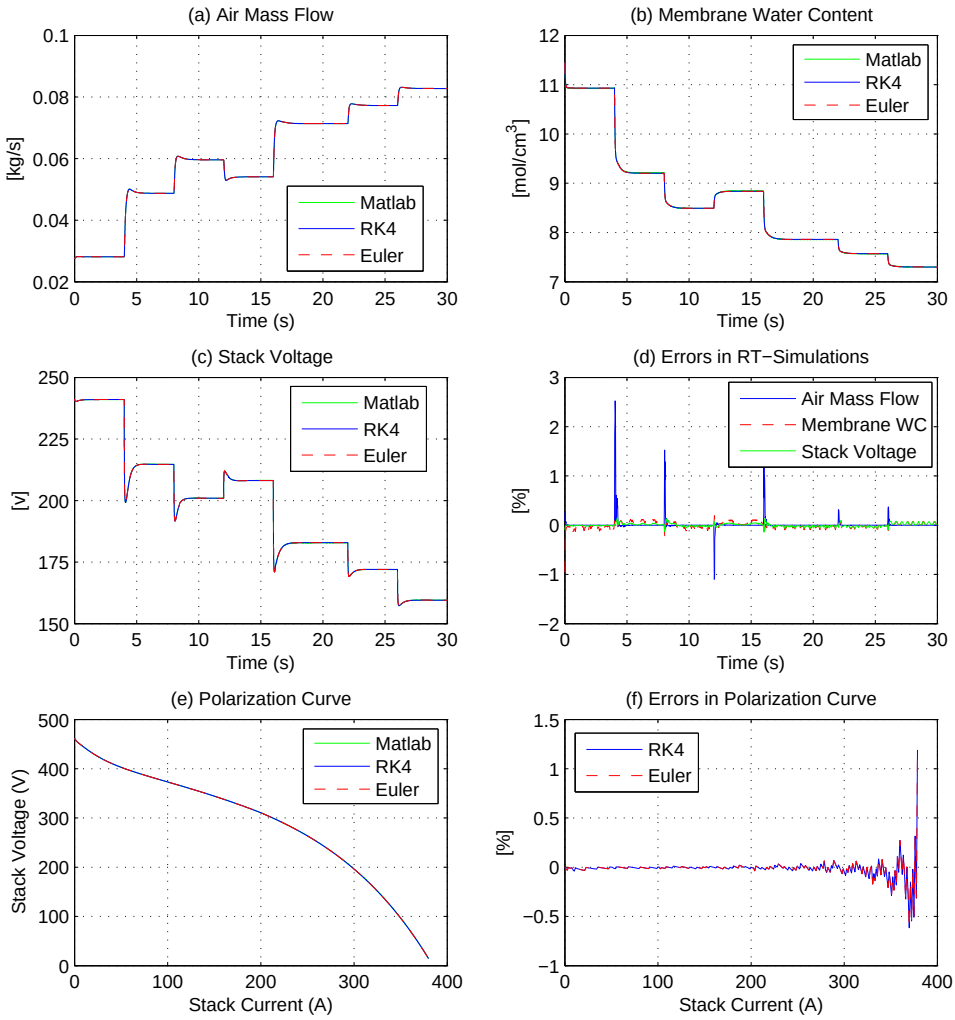


Figure B-3: Comparison of the simulations.

Figure B-3(d) depicts the errors in the estimations of the previous variables, where it is observer a 3% band in the approximation errors.

The absolute average errors of the cathode air mass flow calculation generated with the Euler and RK4 methods (fixed step) with respect to the variable step method, and between the Euler and RK4 methods, can be calculated as follows:

$$E_{Adeu} = 100 \cdot \sqrt{\sum_{i=1}^{N} e_{deu\_i}^2} = 0.962\% \tag{B.9}$$

ISBN:978-84-692-6902-2/ DL:T-1848-2009

$$E_{Adr4} = 100 \cdot \sqrt{\sum_{i=1}^{N} e_{dr4\_i}^2} = 0.961\% \tag{B.10}$$

$$E_{AReu} = 100 \cdot \sqrt{\sum_{i=1}^{N} e_{Reu\_i}^2} = 0.001\% \tag{B.11}$$

where $e_{deu\_i}$, $e_{dr4\_i}$ and $e_{Reu\_i}$ are the errors in each interval time of Euler Method, RK4 Method and Euler-RK4 Methods, respectively. It is observed that Euler Method error ($E_{Adeu}$) and RK4 Method error ($E_{Adr4}$) are almost equal, which is confirmed with the error between these two methods ($E_{AReu}$).

In figure B-3(e) the polarization curves are presented, these obtained with the variable step-size simulation and with real-time simulations of Euler and RK4 methods. The errors in the polarization curve are depicted in figure B-3(f), being enclosed in a 1.5 % band. It is also noticed that the errors of the methods executed in real-time are similar.

### B.2.2 Computational loads comparison

The real-time implementations of the mathematical model using the numerical methods were made with 10 different sampling times (0.1 ms to 1.0 ms, with intervals of 0.1 ms). In figure B-4 are presented the average computational loads for each sampling time in the selected implementation platforms. The reduction in the computational load when Euler method is used is remarkable: with a sampling time of 0.1 ms, RK4 demands 70% of the processor and Euler requires less than 30% (Real-Time Windows Target, figure B-4(a)). In the RTAI-Lab Linux Target implementation, it can be noticed that the processor load decreases, which also provides the execution in hard-real-time keeping the real-time POSIX standards.

A satisfactory performance of the two numerical methods in the embedded platforms can be also observed (figures B-4 (c) and (d)), where the Euler method presents a small computational load, allowing the realization of additional operations in the processor. In the particular case of the TMS320C6711, which is the most adequate for an emulator implementation due to its autonomy, it is possible to combine both numerical methods for different parts of the mathematical model, using Euler for small-variance signals and RK4 for high-precision signals. Equally, taking into account the information of tables B.1 and B.2, it is possible to adjust the numerical methods and sampling times to do not deteriorate the resolution fixed by the data acquisition systems.

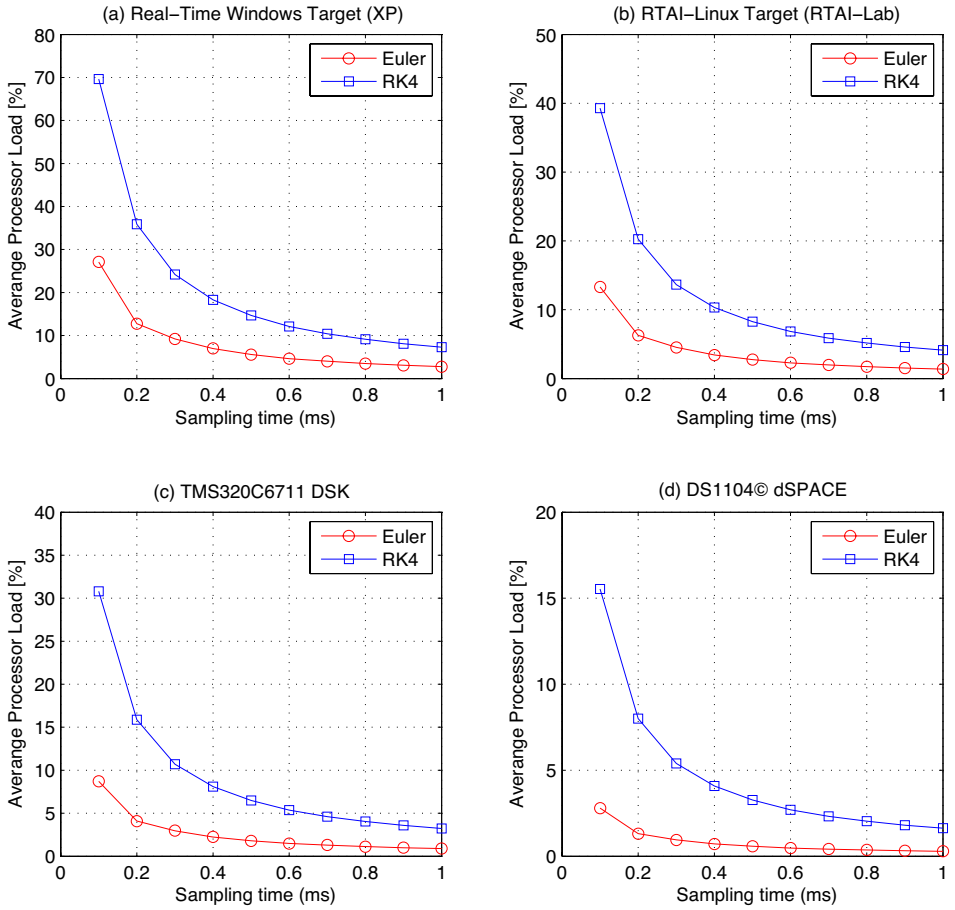


Figure B-4: Computational loads comparison.

## B.3 Final remarks

In the selection of a numerical method for the solution of physical equations, it intended for emulation of dynamical systems, it is necessary to keep in mind the quantization errors of the ADC and DAC systems. Similarly, it is necessary to evaluate the volume of numerical calculation required in function of the reached precision. These analyses allow to choose the most appropriate algorithm avoiding to waste *time of calculation* without obtaining a substantial increment in the precision of the solutions.

It is observed that Euler method precision is virtually the same that the RK4 method in some of the states of the particular case analyzed (fuel cell model), and noticing that RK4 requires more calculation volume (200 %), it is possible to affirm that Euler method is acceptable for real-time emulation of the fuel cell stack. In the same way, due to the fuel cell system dynamics, it is possible

ROVIRA I VIRGILI UNIVERSITY
FUEL CELL MODELING AND CONTROL FOR FUEL CONSUMPTION OPTIMIZATION
Carlos Andres Ramos Paja
ISBN:978-84-692-6902-2/ DL:T-1848-2009

to use the Euler method for real-time emulation of the air supply system. This implies a smaller cost in the hardware implementation in comparison to the requirements of RK4 or superior methods. Using commercial hardware it is possible to implement real-time emulators in embedded devices, such as the TMS320C6711 DSK evaluated. This system can work stand alone, requiring a minimal additional hardware and permitting an easy transportation and turn-on of the emulator. Finally, the TMS320C6711 DSK has a high-calculation power processor, which makes possible to emulate additional components of the energy generation system such gas refinement system, DC/DC or DC/AC converters and control, fuel cell and fuel flow control systems, etc.

ROVIRA I VIRGILI UNIVERSITY
FUEL CELL MODELING AND CONTROL FOR FUEL CONSUMPTION OPTIMIZATION
Carlos Andres Ramos Paja
ISBN:978-84-692-6902-2/ DL:T-1848-2009

# Appendix C

# DC/DC boost modules construction considerations

In this appendix some important construction information and considerations for the DC/DC boost modules are given.

## C.1 Inductor construction

The inductors for the DC/DC boost modules have been constructed using commercially available toroidal cores *Kool Mμ 77076-A7* from Magnetics [152]. Next, using the Magnetics software design, it was defined a minimum section of the inductor wires of $1.3\ \mathrm{mm}^2$ (AWG16), which was obtained by using 20 copper wires with sections of $0.07\ \mathrm{mm}^2$ interleaved to generate lower ESR at high frequencies. The average values of the four modules characterization, measured using a QUADTECH LCR 1910 inductance analyzer and a QUADTECH 1320 current source [153], are: $\mathsf{L} = 56\ \mu\mathsf{H}$ ($\mathsf{Ibias} = 8\ \mathsf{A}$), $\mathsf{R}_{\mathsf{DC}} = 12\ \mathrm{m}\Omega$, $\mathsf{ESR}_{20\ \mathsf{kHz}} = 145\ \mathrm{m}\Omega$, $\mathsf{ESR}_{50\ \mathsf{kHz}} = 175\ \mathrm{m}\Omega$ and $\mathsf{ESR}_{100\ \mathsf{kHz}} = 300\ \mathrm{m}\Omega$.

## C.2 Diode and MOSFET selection

The selected diode was a Schottky diode 43CTQ100PBF with characteristics: IF(AV) = 40 A using two diode in parallel, VR = 100V, VF = 0.67 V. It has a TO 220 packing case with thermal resistance of $1\ ^\circ\mathsf{C/W}$ (junction-case).

The MOSFET used was a IRFB3077PBF, which characteristics are: VDSS =75 V, RDS(on) = $3\ \mathrm{m}\Omega$, ID =120 A. Its TO 220 packing case has a $0.5\ ^\circ\mathsf{C/W}$ junction-case thermal resistance, and an additional $0.5\ ^\circ\mathsf{C/W}$ case-heat sink thermal resistance.

ISBN:978-84-692-6902-2/ DL:T-1848-2009

Both diode and MOSFET are over-dimensioned to generate circuit robustness. Also, in this application it was used a heat sink with $2.9\,°C/W$ thermal resistance (heat sink-ambient), which due to the switches over-dimensioned, must maintain its temperature near to the ambient without forced convection.

ROVIRA I VIRGILI UNIVERSITY
FUEL CELL MODELING AND CONTROL FOR FUEL CONSUMPTION OPTIMIZATION
Carlos Andres Ramos Paja
ISBN:978-84-692-6902-2/ DL:T-1848-2009

# Appendix D

# Publications

The main results of my Ph.D. research have been or are intended to be published in journal papers and conference proceedings. The next journal papers and conference papers are published or accepted for publication, and they contribute to the divulgation of my research results.

## D.1 Journal Papers

C.A. Ramos-Paja, A. Romero, R. Giral, E. Vidal-Idiarte, L. Martínez-Salamero, "Fuzzy-based modelling technique for PEMFC electrical power generation systems emulation", *IET Power Electronics*, Vol. 2, no. 3, pp. 241-255, 2009.

C.A. Ramos-Paja, C. Bordons, A. Romero, R. Giral, L. Martínez-Salamero, "Minimum Fuel Consumption Strategy for PEM Fuel Cells", *IEEE Transactions on Industrial Electronics*, Vo. 56, no. 3, pp. 685-696, 2009.

C.A. Ramos-Paja, R. Giral, L. Martínez-Salamero, J. Romano, A. Romero, G. Spagnuolo, "A PEM fuel cell model featuring oxygen excess ratio estimation and power electronics interaction", *IEEE Transactions on Industrial Electronics*, Accepted for publication in 2009.

ISBN:978-84-692-6902-2/ DL:T-1848-2009

## D.2 Conference Papers

C.A. Ramos, A. Romero, R. Giral, "Métodos Numéricos en la Emulación de Sistemas de Potencia", *Seminario Anual de Automática, Electrónica Industrial e Instrumentación (SAAEI'06)*, Gijón-Spain, September 2006.

E. Arango, C.A. Ramos-Paja, J. Calvente, R. Giral, A. Romero, L. Martnez-Salamero, "Fuel Cell Power Output Using a LQR Controlled AIDB Converter", *International Conference on Clean Electrical Power (ICCEP '07)*, Carpi-Italy. May 2007.

C.A. Ramos-Paja, A. Romero, R. Giral, "Evaluation of Fixed-Step Differential Equations Solution Methods for Fuel Cell Real-Time Simulation", *International Conference on Clean Electrical Power (ICCEP '07)*, Carpi-Italy. May 2007.

C.A. Ramos-Paja, A. Romero, R. Giral, L. Martnez-Salamero, "Maximum Power Point Tracking Strategy for Fuel Cell Power Systems", *IEEE International Symposium on Industrial Electronics (ISIE07)*, Vigo-Spain, June 2007.

C.A. Ramos-Paja, A. Romero, R. Giral, "Modelado, Control y Diseño de Sistemas de Potencia para Optimización de Consumo en Pilas de Combustible", *Graduated Student Meeting on Electronic Engineering*, Tarragona-Spain, July 2008.

J. Ríos-Torres, C.A. Ramos-Paja, C. Pinedo, A. Romero, R. Giral, "Plataforma para evaluación y monitoreo del funcionamiento de una pila de combustible FCPUV", *I Simpósio Ibérico de Hidrógeno, Pilas de combustible y Baterías avanzadas*, Bilbao-Spain, July 2008.

C.A. Ramos-Paja, C. Olalla, C. Bordons, A. Romero, R. Leyva, R. Giral, "Hybrid topologies analysis for fuel cell QFT control design", *15th Interantional Congress of Electrical, Electronic and Systems Engineering (Intercon 2008)*, Trujillo-Peru, August 2008.

C.A. Ramos-Paja, C. Carrejo, A. Romero, E. Vidal-Idiarte, R. Giral, C. Bordons, M. Milanovic, "Control suave del exceso de oxígeno en una pila de combustible limitando la razón de cambio de la potencia con una rampa de compensación dinámica", *Seminario Anual de Automática, Electrónica Industrial e Instrumentación (SAAEI'08)*, Cartagena-Spain, September 2008.

ISBN:978-84-692-6902-2/ DL:T-1848-2009

C.A. Ramos-Paja, J. Ríos-Torres, A. Romero, R. Giral, "Análisis de los sensores requeridos para el desarrollo de estimadores del comportamiento dinámico de la humedad en la membrana de una pila de combustible", *XIII Simposio de tratamiento de señales, imágenes y visión artificial (STSIVA 2008)*, Bucaramanga-Colombia, September 2008.

C.A. Ramos-Paja, J. Ríos-Torres, A. C. Pinedo, E. Franco-Mejía, "Implementación de una plataforma modular para monitoreo y caracterización de pilas de combustible", *XIII Simposio de tratamiento de señales, imágenes y visión artificial (STSIVA 2008)*, Bucaramanga-Colombia, September 2008.

ROVIRA I VIRGILI UNIVERSITY
FUEL CELL MODELING AND CONTROL FOR FUEL CONSUMPTION OPTIMIZATION
Carlos Andres Ramos Paja
ISBN:978-84-692-6902-2/ DL:T-1848-2009

ISBN:978-84-692-6902-2/ DL:T-1848-2009

# Bibliography

[1] J. Pukrushpan, A. Stefanopoulou, and H. Peng, "Control of fuel cell breathing," *IEEE Control Systems Magazine*, vol. 24, pp. 30 – 46, 2004.

[2] J. Correa, F. Farret, L. Canha, and M. Simoes, "An electrochemical-based fuel-cell model suitable for electrical engineering automation approach," *IEEE Transactions on Industrial Electronics*, vol. 51, pp. 1103 – 1112, 2004.

[3] F. Barbir and T. Gomez, "Efficiency and economics of proton exchange membrane (pem) fuel cells," *International Journal of Hydrogen Energy*, vol. 22, pp. 1027–1037, 1997.

[4] R. Gemmen, "Analysis for the effect of inverter ripple current on fuel cell operating condition," *Journal of Fluids Engineering*, vol. 125, no. 3, pp. 576–585, 2003.

[5] W. Choi, J. Howze, , and P. Enjeti, "Development of an equivalent circuit model of a fuel cell to evaluate the effects of inverter ripple current," *Journal of Power Sources*, vol. 158, no. 2, pp. 1324–1332, 2006.

[6] J. Pukrushpan, A. Stefanopoulou, and H. Peng, "Modeling and control for pem fuel cell stack system," *Proceedings of the 2002 American Control Conference*, vol. 4, pp. 3117 – 3122, 2002.

[7] J. Adams, W. C. Yang, K. A. Oglesby, and K. D. Osborne, "The development of ford's p2000 fuel cell vehicle," 2000.

[8] W. Friede, S. Rael, and B. Davat, "Mathematical model and characterization of the transient behavior of a pem fuel cell," *IEEE Trans. on Power Electronics*, vol. 19, no. 5, pp. 1234–1241, 2004.

[9] K. J. Runtz and M. Lyster, "Fuel cell equivalent circuit models for passive mode testing and dynamic mode design," in *Electrical and Computer Engineering, 2005. Canadian Conference on*, 2005, pp. 794–797.

[10] J. R. J. Larminie, "Current interrupt techniques for circuit modelling," in *Electrochemical Measurement, IEE Colloquium on*, 1994, pp. 12/1–12/6.

[11] D. Yu and S. Yuvarajan, "A novel circuit model for pem fuel cells," in *Applied Power Electronics Conference and Exposition, 2004. APEC '04. Nineteenth Annual IEEE*, vol. 1, 2004, pp. 362–366 Vol.1.

[12] R. G. Capel, J. Calvente, H. Valderrama-Blavi, A. Romero, and L. Martínez-Salamero, "Modelling of a fuel cell as an energy source power system," in *Seminario Anual de Automtica, Electrnica industrial e Instrumentación - SAAEI06*, 2006.

[13] P. Famouri and R. Gemmen, "Electrochemical circuit model of a pem fuel cell," in *Power Engineering Society General Meeting, 2003, IEEE*, vol. 3, 2003, p. 1440 Vol. 3.

[14] A. Hernandez, D. Hissel, and R. Outbib, "Non linear state space modelling of a pemfc," *Fuel Cells*, vol. 6, no. 1, pp. 38–46, 2006, 10.1002/fuce.200500102.

[15] X. Xue, K. Cheng, and D. Sutanto, "Unified mathematical modelling of steady-state and dynamic voltage-current characteristics for pem fuel cells," *Electrochimica Acta*, vol. 52, no. 3, pp. 1135–1144, 2006.

ISBN:978-84-692-6902-2/ DL:T-1848-2009

[16] S. Ogaji, R. Singh, P. Pilidis, and M. Diacakis, "Modelling fuel cell performance using artificial intelligence," *Journal of Power Sources*, vol. 154, no. 1, pp. 192–197, 2006.

[17] J. Golbert and R. Lewin, "Model-based control of fuel cells: (1) regulatory control," *Journal of Power Sources*, vol. 135, no. 1-2, pp. 135–151, 2004.

[18] ——, "Model-based control of fuel cells (2): Optimal efficiency," *Journal of Power Sources*, vol. 173, no. 1, pp. 298–309, 2007.

[19] M. J. Khan and M. T. Iqbal, "Dynamic modelling and simulation of a fuel cell generator," *Fuel Cells*, vol. 5, no. 1, pp. 97–104, 2005, 10.1002/fuce.200400054.

[20] ——, "Modelling and analysis of electro-chemical, thermal, and reactant flow dynamics for a pem fuel cell system," *Fuel Cells*, vol. 5, no. 4, pp. 463–475, 2005, 10.1002/fuce.200400072.

[21] S.-Y. Choe, J.-G. Lee, J.-W. Ahn, and S.-H. Baek, "Integrated modeling and control of a pem fuel cell power system with a pwm dc/dc converter," *Journal of Power Sources*, vol. 164, no. 2, pp. 614–623, 2007.

[22] J. M. Correa, F. A. Farret, L. N. Canha, and M. G. Simoes, "An electrochemical-based fuel-cell model suitable for electrical engineering automation approach," *Industrial Electronics, IEEE Transactions on*, vol. 51, no. 5, pp. 1103–1112, 2004.

[23] A. J. del Real, A. Arce, and C. Bordons, "Development and experimental validation of a pem fuel cell dynamic model," *Journal of Power Sources*, vol. 173, no. 1, pp. 310–324, 2007.

[24] A. Hernandez, D. Hissel, and R. Outbib, "Fuel cell fault diagnosis: A stochastic approach," *IEEE International Symposium on Industrial Electronics ISIE-2006*, vol. 6, pp. 1984–1989, 2006.

[25] C. Bordons, A. Arce, and A. del Real, "Constrained predictive control strategies for pem fuel cells," *American Control Conference*, pp. 2486–2491, 2006.

[26] Powersim, "Psim: Power electronics simulation software, http://www.powersys.fr/psimpresent.php," 2008.

[27] A. Arce, D. Ramirez, A. del Real, and C. Bordons, "Constrained explicit predictive control strategies for pem fuel cell systems," *46th IEEE Conference on Decision and Control*, pp. 6088–6093, 2007.

[28] J. T. Pukrushpan, A. G. Stefanopoulou, and H. Peng, *Control of Fuel Cell Power Systems: Principles, Modeling, Analysis and Feedback Design*. Springer-Verlag London, 2004.

[29] K.-W. Suh and A. G. Stefanopoulou, "Performance limitations of air flow control in power-autonomous fuel cell systems," *IEEE Transactions on Control Systems Technology*, vol. 15, no. 3, pp. 465–473, 2007.

[30] A. Vahidi, A. G. Stefanopoulou, and H. Peng, "Current management in a hybrid fuel cell power system: A model-predictive control approach," *IEEE Transactions on Control Systems Technology*, vol. 14, no. 6, pp. 1047–1057, 2006.

[31] P. Buasr and Z. Salameh, "An electrical circuit model for a proton exchange membrane fuel cell (pemfc)," in *IEEE Power Engineering Society General Meeting*, 2006.

[32] D. Yu and S. Yuvarajan, "Electronic circuit model for proton exchange membrane fuel cells," *Journal of Power Sources*, vol. 142, pp. 238–242, 2005.

[33] P. Bevington and D. K. Robinson, *Data Reduction and Error Analysis for the Physical Sciences*. McGraw-Hill Education, 2002.

[34] S. Gelfi, A. Stefanopoulou, J. Pukrushpan, and H. Peng, "Dynamics of low-pressure and high-pressure fuel cell air supply systems," *Proceedings of the 2003 - American Control Conference*, vol. 3, pp. 2049 – 2054, 2003.

[35] P. Thounthong and P. Sethakul, "Analysis of a fuel starvation phenomenon of a pem fuel cell," *Power Conversion Conference - Nagoya, 2007. PCC '07*, pp. 731–738, 2007.

ISBN:978-84-692-6902-2/ DL:T-1848-2009

[36] S. Shimpalee, S. Greenway, and J. V. Zee, "The impact of channel path length on pemfc flow-field design," *Journal of Power Sources*, vol. 160, no. 1, p. 398406, 2006.

[37] J. T. Pukrushpan, A. G. Stefanopoulou, and S. Varigonda, "Control-oriented model of fuel processor for hydrogen generation in fuel cell applications," *IFAC Symposium in Adavnces in Automotive Systems 2004*, 2004.

[38] I. Jolliffe, *Principal Component Analysis*. Springer; 2nd edition, 2002.

[39] J. Ding, A. V. Gribok, J. W. Hines, and B. Rasmussen, "Redundant sensor calibration monitoring using independent component analysis and principal component analysis," *Real-Time Systems*, vol. 27, pp. 27 – 47, 2004.

[40] I. E. Research. (2008) Pls_toolbox. [Online]. Available: http://software.eigenvector.com/

[41] I. MathWorks. (2008) Real time windows target toolbox. [Online]. Available: http://www.mathworks.com/products/rtwt/

[42] M. C. Chandorkar, "A survey of real time integration methods for systems of ordinary differential equations," *M. Tech. Credit Seminar Report, Electronic Systems Group, EE Dept, IIT Bombay*, 2003.

[43] H. Mosskull, J. Galic, and B. Wahlberg, "Stabilization of induction motor drives with poorly damped input filters," *IEEE Transactions on Industrial Electronics*, vol. 54, no. 5, pp. 2724–2734, 2007.

[44] H. Koizumi, T. Mizuno, T. Kaito, Y. Noda, N. Goshima, M. Kawasaki, K. Nagasaka, and K. Kurokawa, "A novel microcontroller for grid-connected photovoltaic systems," *IEEE Transactions on Industrial Electronics*, vol. 53, no. 6, pp. 1889–1897, 2006.

[45] J. Arellano-Padilla, G. Asher, and M. Sumner, "Control of an ac dynamometer for dynamic emulation of mechanical loads with stiff and flexible shafts," *IEEE Transactions on Industrial Electronics*, vol. 53, no. 4, pp. 1250–1260, 2006.

[46] Z. Hakan Akpolat, G. Asher, and J. Clare, "Dynamic emulation of mechanical loads using a vector-controlled induction motor-generator set," *IEEE Transactions on Industrial Electronics*, vol. 46, no. 2, pp. 370–379, 1999.

[47] M. Rodic, K. Jezernik, and M. Trlep, "Control design in mechatronic systems using dynamic emulation of mechanical loads," *Proceedings of the IEEE International Symposium on Industrial Electronics*, vol. 4, pp. 1635–1640, 2005.

[48] R. Bettendorf, "Winder software testing with real-time dynamic simulation," *IEEE Transactions on Industrial Electronics*, vol. 52, no. 2, pp. 489–498, 2005.

[49] B. Lu, X. Wu, H. Figueroa, and A. Monti, "A low-cost real-time hardware-in-the-loop testing approach of power electronics controls," *IEEE Transactions on Industrial Electronics*, vol. 54, no. 2, pp. 919–931, 2007.

[50] V. Dinavahi, R. Iravani, and R. Bonert, "Design of a real-time digital simulator for a d-statcom system," *IEEE Transactions on Industrial Electronics*, vol. 51, no. 5, pp. 1001–1008, 2004.

[51] H. Li, M. Steurer, K. Shi, S. Woodruff, and D. Zhang, "Development of a unified design, test, and research platform for wind energy systems based on hardware-in-the-loop real-time simulation," *IEEE Transactions on Industrial Electronics*, vol. 53, no. 4, pp. 1144–1151, 2006.

[52] A. Vath, Z. Lems, H. Mncher, M. Shn, N. Nicoloso, and T. Hartkopf, "Dynamic modelling and hardware-in-the-loop testing of pemfc," *Journal of Power Sources*, vol. 157, pp. 816–827, 2006.

[53] A. Prabha, E. Prasad, and I. Pitel, "An advanced fuel cell simulator," in *Nineteenth Annual IEEE Applied Power Electronics Conference and Exposition - APEC '04*, 2004.

[54] C. Dufour, T. Das, and S. Akella, "Real time simulation of proton exchange membrane fuel cell hybrid vehicle," in *Proceeding of the Congress on Global Powetrain 2005*, 2005, pp. 1554–1558.

ISBN:978-84-692-6902-2/ DL:T-1848-2009

[55] J.-G. Lim, S.-H. Kim, E.-K. Seo, H.-B. Shin, S.-K. Chung, and H.-W. Lee, "Implementation of fuel cell dynamic simulator," *37th IEEE Power Electronics Specialists Conference*, vol. 4, pp. 1–5, 2006.

[56] L. Tae-Won, L. Byoung-Kuk, J. Su-Jin, K. Sung-Ho, and W. Chung-Yuen, "Development of a 3 kw fuel cell generation system with an active fuel cell simulator: topology, control, and design," *IEEE 35th Annual Power Electronics Specialists Conference (PESC04)*, vol. 6, pp. 4743–4748, 2004.

[57] L. Tae-Won, K. Sung-Ho, Y. Yong-Ho, J. Su-Jin, and W. Chung-Yuen, "A 3 kw fuel cell generation system using the fuel cell simulator," *IEEE International Symposium on Industrial Electronics*, vol. 2, pp. 833–837, 2004.

[58] M. Ordonez, M. T. Iqbal, and J. E. Quaicoe, "Development of a fuel cell simulator based on an experimentally derived model," *Canadian Conference on Electrical and Computer Engineering*, pp. 1449–1452, 2005.

[59] M. Cirrincione, M. C. Di Piazza, G. Marsala, M. Pucci, and G. Vitale, "Real time simulation of renewable sources by model-based control of dc/dc converters," *IEEE International Symposium on Industrial Electronics (ISIE)*, pp. 1548–1555, 2008.

[60] S. Sirisukprasert and T. Saengsuwan, "The modeling and control of fuel cell emulators," *5th International Conference on Electrical Engineering, Electronics, Computer, Telecommunications and Information Technology (ECTI-CON)*, vol. 2, pp. 985–988, 2008.

[61] A. Gebregergis and P. Pillay, "The development of solid oxide fuel cell (sofc) emulator," *IEEE Power Electronics Specialists Conference (PESC)*, pp. 1232–1238, 2007.

[62] M. Ordonez, M. T. Iqbal, and J. E. Quaicoe, "A novel fuel cell simulator," *IEEE 36th Power Electronics Specialists Conference (PESC05)*, pp. 178–184, 2005.

[63] N. A. Parker-Allotey, C. Y. Leong, R. McMahon, P. R. Palmer, A. T. Bryant, and W. Dunford, "Development and testing of a drive system for electric vehicles," *42nd IAS Annual Meeting and Industry Applications Conference*, pp. 1718–1725, 2007.

[64] R. Wai and R. Duan, "High-efficiency dc/dc converter with high voltage gain," *IEE Proceedings-Electric Power Applications*, vol. 152, no. 4, pp. 793–802, 2005.

[65] R.-J. Wai and C.-Y. Lin, "High-efficiency, high-step-up dc-dc convertor for fuel-cell generation system," *IEE Proceedings-Electric Power Applications*, vol. 152, no. 5, pp. 1371–1378, 2005.

[66] R. Wai, C. Lin, L. Liu, and Y. Chang, "High-efficiency single-stage bidirectional converter with multi-input power sources," *IET Electric Power Applications*, vol. 1, no. 5, pp. 763–777, 2007.

[67] C. Liu, A. Johnson, and J.-S. Lai, "Modeling and control of a novel six-leg three-phase high-power converter for low voltage fuel cell applications," vol. 6, 2004, pp. 4715–4721.

[68] J. Anzicek and M. Thompson, "Dc-dc boost converter design for kettering universitys gem fuel cell vehicle," 2005, pp. 307–316.

[69] X. Kong, A. Khambadkone, and S. K. Thum, "A hybrid model with combined steady-state and dynamic characteristics of pemfc fuel cell stack," *Industry Applications Conference, 2005. Fourtieth IAS Annual Meeting. Conference Record of the 2005*, vol. 3, pp. 1618 – 1625, 2005.

[70] K. Stanton and L. Jih-Sheng, "A thermally dependent fuel cell model for power electronics design," 2005, pp. 1647–1651.

[71] J.-N. Marie-Francoise, H. Gualous, and A. Berthon, "Supercapacitor thermal- and electrical-behaviour modelling using ann," *IEE Proceedings-Electric Power Applications*, vol. 153, no. 2, pp. 255–262, 2006.

[72] S. Jemei, D. Hissel, M. Pera, and J. Kauffmann, "On-board fuel cell power supply modelling on the basis of neural network methodology," *Journal of Power Sources*, vol. 124, pp. 479–486, 2003.

ISBN:978-84-692-6902-2/ DL:T-1848-2009

[73] S. Ogaji, R. Singh, P. Pilidis, and M. Diacakis, "Modelling fuel cell performance using artificial intelligence," *Journal of Power Sources*, vol. 154, pp. 192–197, 2006.

[74] F. Yang, X.-J. Zhu, and G.-Y. Cao, "Nonlinear fuzzy modeling of a mcfc stack by an identification method," *Journal of Power Sources*, vol. 166, no. 2, pp. 354–361, 2007.

[75] E. Entchev and L. Yang, "Application of adaptive neuro-fuzzy inference system techniques and artificial neural networks to predict solid oxide fuel cell performance in residential microgeneration installation," *Journal of Power Sources*, vol. 170, no. 1, pp. 122–129, 2007.

[76] X. Yu, M. Starke, L. Tolbert, and B. Ozpineci, "Fuel cell power conditioning for electric power applications: a summary," *IET Electric Power Applications*, vol. 1, no. 5, pp. 643–656, 2007.

[77] Jyh-Shing and R. Jang, "Anfis : Adap tive-ne twork-based fuzzy inference system," *IEEE Transactions on Systems, Man, and Cybernetics*, vol. 23, no. 3, pp. 665 – 685, 1993.

[78] M. F. Azeem, M. Hanmandlu, and N. Ahmad, "Generalization of adaptive neuro-fuzzy inference systems," *IEEE Transactions on Neural Networks*, vol. 11, no. 6, pp. 1332 – 1346, 2000.

[79] J. T. Pukrushpan, A. G. Stefanopoulou, and S. Varigonda, "Control-oriented model of an integrated fuel cell stack and fuel processor system," *IFAC Symposium on Advances in Automotive Control 2004*, 2004.

[80] Electrochem. (2008) Ecl 150 electronic load. [Online]. Available: http://www.electrocheminc.com

[81] F. Zenith and S. Skogestad, "Control of fuel cell power output," *Journal of Process Control*, vol. 17, no. 4, pp. 333–347, 2007.

[82] K. Ogata, *Discrete-Time Control Systems (2nd Edition)*. Prentice Hall, 1994.

[83] B. C. Kuo and F. Golnaraghi, *Automatic Control Systems*. Wiley, 2002.

[84] M. Viswanathan, *Measurement Error and Research Design*. Sage Publications, 2005.

[85] R. Tymerski and V. Vorperian, "Generation and classification of pwm dc-to-dc converters," *IEEE Trans. on Aerospace and Electronics Systems*, vol. 24, no. 6, pp. 743–754, 1988.

[86] B. J. Patella, A. Prodic, A. Zirger, and D. Maksimovic, "High-frequency digital pwm controller ic for dc-dc converters," *IEEE Transactions on Power Electronics*, vol. 18, no. 1, pp. 438–446, 2003.

[87] T.-W. Lee, J. Hur, B.-K. Lee, and C.-Y. Won, "Design of a fuel cell generation system using a pemfc simulator," *Electric Power Systems Research*, vol. 77, no. 10, pp. 1257–1264, 2007.

[88] C. Park, J. Liu, and P. H. Chou, "B#: a battery emulator and power-profiling instrument," *IEEE Design & Test of Computers*, vol. 22, no. 2, pp. 150–159, 2005, 0740-7475.

[89] I. Texas, "Opa549: High-voltage, high-current operational amplifier," *Texas Instruments Datasheet*, 2003.

[90] G. Marsala, M. Pucci, G. Vitale, M. Cirrincione, and A. Miraoui, "A prototype of a fuel cell pem emulator based on a buck converter," *Applied Energy, doi:101016/japenergy200812028*, pp. 1–9, 2009.

[91] J. Wishart, Z. Dong, and M. Secanell, "Optimization of a pem fuel cell system based on empirical data and a generalized electrochemical semi-empirical model," *Journal of Power Sources*, vol. 161, no. 2, pp. 1041–1055, 2006.

[92] M.-J. Kim and H. Peng, "Power management and design optimization of fuel cell/battery hybrid vehicles," *Journal of Power Sources*, vol. 165, no. 2, pp. 819–832, 2007.

[93] E. Muller, A. Stefanopoulou, and L. Guzzella, "Optimal power control of hybrid fuel cell systems for an accelerated system warm-up," *IEEE Transactions on Control Systems Technology*, vol. 15, no. 2, pp. 290–305, 2007.

ISBN:978-84-692-6902-2/ DL:T-1848-2009

[94] A. Vega-Leal, R. Palomo, F. Barragan, C. Garcia, and J. Brey, "Design of control systems for portable pem fuel cells," *Journal of Power Sources*, vol. 169, no. 1, pp. 194–197, 2007.

[95] D.-K. Choi, B.-K. Lee, S.-W. Choi, C.-Y. Won, and D.-W. Yoo, "A novel power conversion circuit for cost-effective battery-fuel cell hybrid systems," *Journal of Power Sources*, vol. 152, no. 1, pp. 245–255, 2005.

[96] W. Rong-Jong and D. Rou-Yong, "High-efficiency power conversion for low power fuel cell generation system," *IEEE Transactions on Power Electronics*, vol. 20, no. 4, pp. 847–856, 2005.

[97] D. Marquezini, D. Ramos, R. Machado, and F. Farret, "Interaction between proton exchange membrane fuel cells and power converters for ac integration," *IET Renewable Power Generation*, vol. 2, pp. 151 – 161, 2008.

[98] E. L. Yong Wang, Seeyoung Choi, "Fuel cell power conditioning system design for residential application," *International Journal of Hydrogen Energy*, vol. 34, no. 5, pp. 2340–2349, 2009.

[99] A. A. Ferreira, J. A. Pomilio, G. Spiazzi, and L. de Araujo Silva, "Energy management fuzzy logic supervisory for electric vehicle power supplies system," *IEEE Transactions on Power Electronics*, vol. 23, no. 1, pp. 107–115, 2008.

[100] P. Thounthong, S. Rael, and B. Davat, "Control algorithm of fuel cell and batteries for distributed generation system," *IEEE transactions on Energy conversion*, vol. 23, no. 1, pp. 148–155, 2008.

[101] J. J. Brey, C. R. Bordallo, J. M. Carrasco, E. Galvn, A. Jimenez, and E. Moreno, "Power conditioning of fuel cell systems in portable applications," *International Journal of Hydrogen Energy*, vol. 32, no. 10-11, pp. 1559–1566, 2007.

[102] P. Fontela, A. Soria, J. Mielgo, J. F. Sierra, J. de Blas, L. Gauchia, and J. M. Martnez, "Airport electric vehicle powered by fuel cell," *Journal of Power Sources*, vol. 169, no. 1, pp. 184–193, 2007.

[103] F. Segura, E. Durán, and J. Andújar, "Design, building and testing of a stand alone fuel cell hybrid system," *Journal of Power Sources, doi:10.1016/j.jpowsour.2008.12.111*, pp. 1–9, 2009.

[104] P. Thounthong, S. Rael, B. Davat, and I. Sadli, "A control strategy of fuel cell/battery hybrid power source for electric vehicle applications," *37th IEEE Power Electronics Specialists Conference-PESC06*, pp. 1–7, 2006.

[105] K. Jin, X. Ruan, M. Yang, and M. Xu, "A novel hybrid fuel cell power system," *37th IEEE Power Electronics Specialists Conference-PESC06*, pp. 1–7, 2006.

[106] P. Thounthong, S. Rael, and B. Davat, "Control strategy of fuel cell and supercapacitors association for a distributed generation system," *IEEE Transactions on Industrial Electronics*, vol. 54, no. 6, pp. 3225–3233, 2007.

[107] D. Ramirez, L. F. Beites, F. Blazquez, and J. C. Ballesteros, "Distributed generation system with pem fuel cell for electrical power quality improvement," *International Journal of Hydrogen Energy*, vol. 33, no. 16, pp. 4433–4443, 2008.

[108] R. Moore, K. Hauer, S. Ramaswamy, and J. Cunningham, "Energy utilization and efficiency analysis for hydrogen fuel cell vehicles," *Journal of Power Sources*, vol. 159, no. 2, pp. 1214–1230, 2006.

[109] Z. Jiang, L. Gao, and R. Dougal, "Adaptive control strategy for active power sharing in hybrid fuel cell/battery power sources," *IEEE Transaction on Energy Conversion*, vol. 22, no. 2, pp. 507–515, 2007.

[110] Z. Jiang, L. Gao, M. J. Blackwelder, and R. A. Dougal, "Design and experimental tests of control strategies for active hybrid fuel cell/battery power sources," *Journal of Power Sources*, vol. 130, no. 1-2, pp. 163–171, 2004.

[111] L. Gao, Z. Jiang, and R. Dougal, "An actively controlled fuel cell/battery hybrid to meet pulsed power demands," *Journal of Power Sources*, vol. 130, no. 1-2, pp. 202–207, 2004.

ISBN:978-84-692-6902-2/ DL:T-1848-2009

[112] C. Bonnet, S. Didierjean, N. Guillet, S. Besse, T. Colinart, and P. Carre, "Design of an 80 kwe pem fuel cell system: Scale up effect investigation," *Journal of Power Sources, doi:10.1016/j.jpowsour.2007.12.100*, vol. 130, 2008.

[113] L. Lam, R. Louey, N. Haigh, O. Lim, D. Vella, C. Phyland, L. Vu, J. Furukawa, T. Takada, D. Monma, and T. Kano, "Vrla ultrabattery for high-rate partial-state-of-charge operation," *Journal of Power Sources*, vol. 174, no. 1, pp. 16–29, 2007.

[114] C. Ramos-Paja, C. Bordons, A. Romero, R. Giral, and L. Martinez-Salamero, "Minimum fuel consumption strategy for pem fuel cells," *IEEE Transactions on Industrial Electronics*, vol. 56, no. 3, pp. 685–696, 2009.

[115] P. Thounthong, S. Rael, and B. Dava, "Energy management of fuel cell/battery/supercapacitor hybrid power source for vehicle applications," *Journal of Power Sources, doi:10.1016/j.jpowsour.2008.12.120*, pp. 1–43, 2009.

[116] M. Iqbal, "Modeling and control of a wind fuel cell hybrid energy system," *Renewable Energy*, vol. 28, no. 2, pp. 223–237, 2003.

[117] M. Serra, A. Husar, D. Feroldi, and J. Riera, "Performance of diagonal control structures at different operating conditions for polymer electrolyte membrane fuel cells," *Journal of Power Sources*, vol. 158, no. 2, pp. 1317–1323, 2006.

[118] C. H. Woo and J. Benziger, "Pem fuel cell current regulation by fuel feed control," *Chemical Engineering Science*, vol. 62, no. 4, pp. 957–968, 2007.

[119] C. Tse and M. D. Bernardo, "Complex behavior in switching power converters," *Proceedings of the IEEE*, vol. 90, no. 5, pp. 768–781, 2002.

[120] R. Strzelecki and G. S. Zinoviev, *Power Electronics in Smart Electrical Energy Networks - Overview of Power Electronics Converters and Controls*. Springer-Verlag London, 2008.

[121] A. Pratt, "Dc voltage level overview," *DC for Data Centers Workshop*, 2007.

[122] C. Ramos-Paja, C. Carrejo, A. Romero, E. Vidal-Idiarte, R. Giral, C. Bordons, and M. Milanovic, "Control suave del exceso de oxigeno en una pila de combustible limitando la razon de cambio de la potencia con una rampa de compensacion dinamica," in *Seminario Anual de Automatica, Electronica Industrial e Instrumentacion - SAAEI08*, 2008.

[123] Y.-H. Kim and H.-D. Ha, "Design of interface circuits with electrical battery models," *IEEE Transactions on Industrial Electronics*, vol. 44, no. 1, pp. 81–86, 1997.

[124] J.-J. Slotine and W. Li, *Applied Nonlinear Control*. Prentice Hall, 1991.

[125] I. M. Horowitz, *Quantitative Feedback Design Theory*. QFT Publications, 1993.

[126] C. H. Houpis, S. J. Rasmussen, and M. Garcia-Sanz, *Quantitative feedback theory. Fundamentals and Applications.*, 2nd ed. New York: Marcel Dekker, 2005.

[127] C. Borghesani, Y. Chait, and O. Yaniv, *The Quantitative Feedback Theory Toolbox for MATLAB*, 1995.

[128] B. Williams, "Basic dc-to-dc converters," *IEEE Transactions on Power Electronics*, vol. 23, no. 1, pp. 387–401, 2008.

[129] M. Lopez, L. de Vicuna, M. Castilla, P. Gaya, and O. Lopez, "Current distribution control design for paralleled dc/dc converters using sliding-mode control," *IEEE Transactions on Industrial Electronics*, vol. 51, no. 2, pp. 419–428, 2004.

[130] C. Ramos, A. Romero, R. Giral, and L. Martinez-Salamero, "Maximum power point tracking strategy for fuel cell power systems," *IEEE International Symposium on Industrial Electronics ISIE-2007*, pp. 2613–2618, 2007.

ISBN:978-84-692-6902-2/ DL:T-1848-2009

[131] Z. Jiang and R. Dougal, "A compact digitally controlled fuel cell/battery hybrid power source," *IEEE Transactions on Industrial Electronics*, vol. 53, no. 4, pp. 1094–1104, 2006.

[132] J. Moreno, M. Ortuzar, and J. Dixon, "Energy-management system for a hybrid electric vehicle, using ultracapacitors and neural networks," *IEEE Transactions on Industrial Electronics*, vol. 53, no. 2, pp. 614–623, 2006.

[133] M. Ortuzar, J. Moreno, and J. Dixon, "Ultracapacitor-based auxiliary energy system for an electric vehicle: Implementation and evaluation," *IEEE Transactions on Industrial Electronics*, vol. 54, no. 4, pp. 2147–2156, 2007.

[134] *Ballard Nexa Power Module Users manual*, 2006.

[135] M. Budaes and L. Goras, "Burst mode switching mechanism for an inductorless dc-dc converter," in *International Semiconductor Conference (CAS-2007)*, 2007, pp. 463–466.

[136] D. Perreault and J. Kassakian, "Distributed interleaving of paralleled power converters," *IEEE Transactions on Circuits and Systems I: Fundamental Theory and Applications*, vol. 44, no. 8, pp. 728–734, 1997.

[137] Y. Novaes, R. Zapelini, and I. Barbi, "Design considerations of a long-term single-phase uninterruptible power supply based on fuel cells," in *IEEE 36th Power Electronics Specialists Conference - PESC '05*, 2005, pp. 1628–1634.

[138] H.-J. Chiu, C.-J. Yao, and Y.-K. Lo, "A dc/dc converter topology for renewable energy systems," *International journal of circuit theory and applications - DOI: 10.1002/cta.475*, 2008.

[139] J. Quintero, A. Barrado, M. Sanzand, C. Ragaand, and A. Lazaro, "Bandwidth and dynamic response decoupling in a multi-phase vrm by applying linear-non-linear control," *IEEE International Symposium on Industrial Electronics ISIE-2007*, pp. 3373–3378, 2007.

[140] A. Barrado, A. Lazaro, R. Vazquez, V. Salas, and E. Olias, "The fast response double buck dc-dc converter (frdb): operation and output filter influence," *IEEE Transactions on Power Electronics*, vol. 20, no. 6, pp. 1261–1270, 2005.

[141] E. Laffly, M.-C. Pera, and D. Hissel, "Polymer electrolyte membrane fuel cell modelling and parameters estimation for ageing consideration," *IEEE International Symposium on Industrial Electronics ISIE-2007*, pp. 180–185, 2007.

[142] B. Wahdame, D. Candusso, X. Franois, F. Harel, M.-C. Pera, D. Hissel, and J.-M. Kauffmann, "Comparison between two pem fuel cell durability tests performed at constant current and under solicitations linked to transport mission profile," *International Journal of Hydrogen Energy*, vol. 32, no. 17, pp. 4523–4536, 2007.

[143] W. H. Press, S. A. Teukolsky, W. T. Vetterling, and B. P. Flannery, *Numerical Recipes in C*. Cambridge University Press, 1992.

[144] S. Siala, C. Bordas, J. Pouliquen, and M. Benkhoris, "Embedded real time simulator for complex power system," *2004 IEEE 35th Annual Power Electronics Specialists Conference, 2004. PESC 04.*, 2004.

[145] W. F. Z. J. L. Chen, "Convergence and stability of a parallel computation algorithm in power systems," *International Conference on Power System Technology, 2002. Proceedings. PowerCon 2002.*, 2002.

[146] X. Corporation, "How much simulation speed do you need? the answer might surprise you," *White Paper from XANALOG Corporation (www.xanalog.com)*, 2002.

[147] P. RTAI-Lab. (2006) Rtai-lab linux target.

[148] LynuxWorks. (2006) What is posix? [Online]. Available: http://www.lynuxworks.com/products/posix/posix.php3

[149] I. dSpace. (2006) Ds1104 r&d controller board. [Online]. Available: http://www.dspaceinc.com/ww/en/inc/home/products/hw/singbord/ds1104.cfm

[150] ——. (2006) Controldesk. [Online]. Available: http://www.dspaceinc.com/ww/en/inc/home/products/sw/expsoft/contrdes.cfm

[151] I. T. Instruments. (2006) Tms320c6711. [Online]. Available: http://focus.ti.com/docs/prod/folders/print/tms320c6711d.html

[152] I. Magnetics. (2008) Magnetics web page. [Online]. Available: http://www.mag-inc.com/

[153] I. Quadtech. (2008) Quadtech web page. [Online]. Available: http://www.quadtech.com/